From Nuclei to Compact Stars

Contents

1 Topics

The study of compact objects such as white dwarfs, neutron stars and black holes requires the interplay between nuclear and atomic physics together with relativistic field theories, e.g., general relativity, quantum electrodynamics, quantum chromodynamics, as well as particle physics. In addition to the theoretical physics aspects, the study of astrophysical scenarios characterized by the presence of a compact object has also started to be focus of extensive research within our group. The research which has been done and is currently being developed within our group can be divided into the following topics:

- **Nuclear and Atomic Astrophysics**. Within this subject of research we study the properties and processes occurring in compact stars in which nuclear and atomic physics have to be necessarily applied. We focus on the properties of nuclear matter under extreme conditions of density and pressure found in these objects. The equation of state of the matter in compact star interiors is studied in detail taking into account all the interactions between the constituents within a full relativistic framework.

- **White Dwarfs Physics and Structure**. The aim of this part of our research is to construct the structure of white dwarfs within a self-consistent description of the equation of state of the interior together with the solution of the hydrostatic equilibrium equations in general relativity. Both non-magnetized and magnetized white dwarfs are studied.

- **White Dwarfs Astrophysics**. We are interested in the astrophysics of white dwarfs both isolated and in binaries. Magnetized white dwarfs, soft gamma repeaters, anomalous X-ray pulsars, white dwarf pulsars, cataclysmic variables, binary white dwarf mergers, and type Ia supernovae are studied. The role of a realistic white dwarf interior structure is particularly emphasized.

- **Neutron Stars Physics and Structure**. We calculate the properties of the interior structure of neutron stars using realistic models of the nuclear matter equation of state within the general relativistic equations of equilibrium. Strong, weak, electromagnetic and gravitational interactions have to be jointly taken into due account within a self-consistent fully relativistic framework. Both non-magnetized and magnetized neutron stars are studied.

- **Neutron Stars Astrophysics**. We study astrophysical systems harboring neutron stars such as isolated and binary pulsars, low and intermediate X-ray binaries, inspiraling and merging double neutron stars. Most extreme cataclysmic events involving neutron stars and their role in the explanation of extraordinarily energetic astrophysical events such as gamma-ray bursts are analyzed in detail.

- **Radiation Mechanisms of White Dwarfs and Neutron Stars**. We here study the possible emission mechanisms of white dwarfs and neutron stars. We are thus interested in both electromagnetic and gravitational radiation at work in astrophysical systems such as compact star magnetospheres, inspiraling and merging relativistic double neutron stars, neutron star-white dwarfs, and neutron star-black hole binaries represent some examples.

- **Exact and Numerical Solutions of the Einstein and Einstein-Maxwell Equations in Astrophysics**. We analyze the ability of analytic exact solutions of the Einstein and Einstein-Maxwell equations to describe the exterior spacetime of compact stars such as white dwarfs and neutron stars. For this we compare and contrast exact analytic with numerical solutions of the stationary axisymmetric Einstein equations. The problem of matching between interior and exterior spacetime is addressed in detail. The effect of the quadrupole moment on the properties of the spacetime is also investigated. Particular attention is given to the application of exact solutions in astrophysics, e.g. the dynamics of particles around compact stars and its relevance in astrophysical systems such as X-ray binaries and gamma-ray bursts.

- **Critical Fields and Non-linear Electrodynamics Effects in Astrophysics**. We study the conditions under which ultrastrong electromagnetic fields can develop in astrophysical systems such as neutron stars and in the process of gravitational collapse to a black hole. The effects of nonlinear electrodynamics minimally coupled to gravity are investigated. New analytic and numeric solutions to the Einstein-Maxwell equations representing black holes or the exterior field of a compact star are obtained and analyzed. The consequences on extreme astrophysical systems, for instance gamma-ray bursts, are studied.

2 Participants

2.1 ICRANet

- C. L. Bianco (ICRANet; University of Rome, Italy)
- J. A. Rueda (ICRANet; Sapienza University of Rome, Italy)
- R. Ruffini (ICRANet; University of Rome, Italy)
- G. Vereschagin (ICRANet; Sapienza University of Rome, Italy)
- S.-S. Xue (ICRANet; Sapienza University of Rome, Italy)

2.2 External on going collaborations

- C. G. Bernal (Universidade Federal do Rio Grande, Brazil)
- K. Boshkayev (Al-Farabi Kazakh National University, Kazakhstan)
- R. Camargo (Universidade do Estado de Santa Catarina, Florianópolis, Brazil)
- C. Cherubini (Università Campus Biomedico, Rome, Italy)
- S. Chiapparini (Universidade do Estado do Rio de Janeiro, Brazil)
- S. B. Duarte (Centro Brasileiro de Pesquisas Físicas, Brazil)
- S. Filippi (Università Campus Biomedico, Rome, Italy)
- C. L. Fryer (University of Arizona; Los Alamos National Laboratory, USA)
- E. Gacía-Berro (Universitat Politècnica de Catalunya, Spain)

- P. Lorén Aguilar (University of Exeter, United Kingdom)
- S. O. Kepler (Universidade Federal do Rio Grande do Sul, Brazil)
- M. Malheiro (Instituto Tecnológico de Aeronáutica, Brazil)
- R. M. Jr. Marinho (Instituto Tecnológico de Aeronáutica, Brazil)
- S. M. de Carvalho (Universidade Federal do Tocantins, Brazil)
- M. M. Guzzo (Universidade Estadual de Campinas, Brazil)
- G. Mathews (University of Notre Dame, USA)
- D. P. Menezes (Universidade Federal de Santa Catarina, Brazil)
- R. Negreiros (Universidade Federal de Fluminense, Brazil)
- L. Pachón (Universidad de Antioquia, Colombia)
- H. Quevedo (Universidad Nacional Autónoma de México, Mexico)
- C. V. Rodrigues (Instituto Nacional de Pesquisas Espaciais, Brazil)
- F. Torres (Universidade Estadual de Campinas, Brazil)
- C. Valenzuela (Universidad del Valle, Colombia)
- C. A. Z. Vasconcellos (Universidade Federal do Rio Grande do Sul, Brazil)
- B. Wiggins (Los Alamos National Laboratory, USA)

2.3 Postdocs

- B. S. Arsioli (Agenzia Spaziale Italiana; ASI Space Data Center, Italy)
- R. Belvedere (Centro Brasileiro de Pesquisas Físicas; ICRANet-Rio, Brazil)
- J. G. Coelho (Instituto Nacional de Pesquisas Espaciais, Brazil)
- C. L. Ellinger (Los Alamos National Laboratory, USA)

- M. Muccino (ICRANet; University of Rome, Italy)
- J. P. Pereira (Universidade Federal do ABC, Brazil)
- Y. Wu (Max Planck Institute for Nuclear Physics, Germany)

2.4 Graduate Students

- L. Becerra (ICRANet; Sapienza University of Rome, Italy)
- D. L. Cáceres (ICRANet; Sapienza University of Rome, Italy)
- S. Campion (ICRANet; Sapienza University of Rome, Italy)
- R. V. Lobato (ICRANet; Sapienza University of Rome, Italy; Instituto Tecnológico de Aeronáutica, Brazil)
- R. Riahi (Isfahan University of Technology, Iran)
- J. F. Rodriguez (ICRANet; Sapienza University of Rome, Italy)
- J. D. Uribe (ICRANet; Sapienza University of Rome, Italy)

3 Publications 2017

3.1 Refereed Journals

3.1.1 Printed

1. Gómez, L. Gabriel; Rueda, J. A., *Dark matter dynamical friction versus gravitational wave emission in the evolution of compact-star binaries*, Physical Review D 96, 063001, 2017.

   The measured orbital period decay of relativistic compact-star binaries, with characteristic orbital periods 0.1 days , is explained with very high precision by the gravitational wave (GW) emission of an inspiraling binary in a vacuum predicted by general relativity. However, the binary gravitational binding energy is also affected by an usually neglected phenomenon, namely the dark matter dynamical friction (DMDF) produced by the interaction of the binary components with their respective DM gravitational wakes. Therefore, the inclusion of the DMDF might lead to a binary evolution which is different from a purely GW-driven one. The entity of this effect depends on the orbital period and on the local value of the DM density, hence on the position of the binary in the Galaxy. We evaluate the DMDF produced by three different DM profiles: the Navarro-Frenk-White (NFW) profile, the nonsingular-isothermal-sphere (NSIS) and the Ruffini-Argüelles-Rueda (RAR) DM profile based on self-gravitating keV fermions. We first show that indeed, due to their Galactic position, the GW emission dominates over the DMDF in the neutron star (NS)-NS, NS-(white dwarf) WD and WD-WD binaries for which measurements of the orbital decay exist. Then, we evaluate the conditions (i.e. orbital period and Galactic location) under which the effect of DMDF on the binary evolution becomes comparable to, or overcomes, the one of the GW emission. We find that, for instance for 1.3–0.2 $M_\odot$ NS-WD, 1.3–1.3 $M_\odot$ NS-NS, and 0.25–0.50 $M_\odot$ WD-WD, located at 0.1 kpc, this occurs at orbital periods around 20-

30 days in a NFW profile while, in a RAR profile, it occurs at about 100 days. For closer distances to the Galactic center, the DMDF effect increases and the above critical orbital periods become interestingly shorter. Finally, we also analyze the system parameters (for all the DM profiles) for which DMDF leads to an orbital widening instead of orbital decay. All the above imply that a direct/indirect observational verification of this effect in compact-star binaries might put strong constraints on the nature of DM and its Galactic distribution.

2. Cipolletta, Federico; Cherubini, Christian; Filippi, Simonetta; Rueda, Jorge A.; Ruffini, Remo, *Equilibrium Configurations of Classical Polytropic Stars with a Multi-Parametric Differential Rotation Law: A Numerical Analysis*, Communications in Computational Physics 22, 863, 2017.

   In this paper we analyze in detail the equilibrium configurations of classical polytropic stars with a multi-parametric differential rotation law of the literature using the standard numerical method introduced by Eriguchi and Mueller. Specifically we numerically investigate the parameters space associated with the velocity field characterizing both equilibrium and non-equilibrium configurations for which the stability condition is violated or the mass-shedding criterion is verified.

3. Cipolletta, F.; Cherubini, C.; Filippi, S.; Rueda, J. A.; Ruffini, R., *Last stable orbit around rapidly rotating neutron stars*, Physical Review D 96, 024046, 2017.

   We compute the binding energy and angular momentum of a test particle at the last stable circular orbit (LSO) on the equatorial plane around a general relativistic, rotating neutron star (NS). We present simple, analytic, but accurate formulas for these quantities that fit the numerical results and which can be used in several astrophysical applications. We demonstrate the accuracy of these formulas for three different equations of state (EOS) based on nuclear relativistic mean-field theory models and argue that they should remain still valid for any NS EOS that satisfy current astrophysical constraints. We compare and contrast our numerical results with the corresponding ones for the Kerr metric characterized by the same mass and angular momentum.

4. Coelho, Jaziel G.; Cáceres, D. L.; de Lima, R. C. R.; Malheiro, M.; Rueda,

J. A.; Ruffini, R., *The rotation-powered nature of some soft gamma-ray repeaters and anomalous X-ray pulsars*, A&A 599, A87, 2017.

Soft gamma-ray repeaters (SGRs) and anomalous X-ray pulsars (AXPs) are slow rotating isolated pulsars whose energy reservoir is still matter of debate. Adopting neutron star (NS) fiducial parameters; mass $M = 1.4\ M_{\odot}$, radius $R = 10$ km, and moment of inertia, $I = 10^{45}$ g cm^2, the rotational energy loss, $\dot{E}_{\rm rot}$, is lower than the observed luminosity (dominated by the X-rays) L_X for many of the sources. We investigate the possibility that some members of this family could be canonical rotation-powered pulsars using realistic NS structure parameters instead of fiducial values. We compute the NS mass, radius, moment of inertia and angular momentum from numerical integration of the axisymmetric general relativistic equations of equilibrium. We then compute the entire range of allowed values of the rotational energy loss, $\dot{E}_{\rm rot}$, for the observed values of rotation period P and spin-down rate $\dot{P}$. We also estimate the surface magnetic field using a general relativistic model of a rotating magnetic dipole. We show that realistic NS parameters lowers the estimated value of the magnetic field and radiation efficiency, $L_X/\dot{E}_{\rm rot}$, with respect to estimates based on fiducial NS parameters. We show that nine SGRs/AXPs can be described as canonical pulsars driven by the NS rotational energy, for LX computed in the soft (2–10 keV) X-ray band. We compute the range of NS masses for which $L_X/\dot{E}_{\rm rot} < 1$. We discuss the observed hard X-ray emission in three sources of the group of nine potentially rotation-powered NSs. This additional hard X-ray component dominates over the soft one leading to $L_X/\dot{E}_{\rm rot} > 1$ in two of them. We show that 9 SGRs/AXPs can be rotation-powered NSs if we analyze their X-ray luminosity in the soft 2–10 keV band. Interestingly, four of them show radio emission and six have been associated with supernova remnants (including Swift J1834.9–0846 the first SGR observed with a surrounding wind nebula). These observations give additional support to our results of a natural explanation of these sources in terms of ordinary pulsars. Including the hard X-ray emission observed in three sources of the group of potential rotation-powered NSs, this number of sources with $L_X/\dot{E}_{\rm rot} < 1$ becomes seven. It remains open to verification 1) the accuracy of the estimated distances and 2) the possible contribution of the associated supernova remnants to the hard X-ray emission.

5. Cáceres, D. L.; de Carvalho, S. M.; Coelho, J. G.; de Lima, R. C. R.; Rueda, J. A., *Thermal X-ray emission from massive, fast rotating, highly magnetized white dwarfs*, MNRAS 465, 4434, 2017.

   There is solid observational evidence on the existence of massive, $M \sim 1\ M_{\odot}$, highly magnetized white dwarfs (WDs) with surface magnetic fields up to $B \sim 10^9$ G. We show that, if in addition to these features, the star is fast rotating, it can become a rotation-powered pulsar-like WD and emit detectable high-energy radiation. We infer the values of the structure parameters (mass, radius, moment of inertia), magnetic field, rotation period and spin-down rates of a WD pulsar death-line. We show that WDs above the death-line emit blackbody radiation in the soft X-ray band via the magnetic polar cap heating by back flowing pair-created particle bombardment and discuss as an example the X-ray emission of soft gamma-repeaters and anomalous X-ray pulsars within the WD model.

6. Rueda, Jorge A.; Aimuratov, Y.; de Almeida, U. Barres; Becerra, L.; Bianco, C. L.; Cherubini, C.; Filippi, S.; Karlica, M.; Kovacevic, M.; Fuksman, J. D. Melon; Moradi, R.; Muccino, M.; Penacchioni, A. V.; Pisani, G. B.; Primorac, D.; Ruffini, R.; Sahakyan, N.; Shakeri, S.; Wang, Y., *The binary systems associated with short and long gamma-ray bursts and their detectability*, IJMPD 26, 1730016, 2017.

   Short and long-duration gamma-ray bursts (GRBs) have been recently sub-classified into seven families according to the binary nature of their progenitors. For short GRBs, mergers of neutron star binaries (NSNS) or neutron star-black hole binaries (NS-BH) are proposed. For long GRBs, the induced gravitational collapse (IGC) paradigm proposes a tight binary system composed of a carbon-oxygen core (CO_{core}) and a NS companion. The explosion of the CO_{core} as supernova (SN) triggers a hypercritical accretion process onto the NS companion which might reach the critical mass for the gravitational collapse to a BH. Thus, this process can lead either to a NS-BH or to NSNS depending on whether or not the accretion is sufficient to induce the collapse of the NS into a BH. We shall discuss for the above compact object binaries: (1) the role of the NS structure and the equation-of-state on their final fate; (2) their occurrence rates as inferred from the X and gamma-ray observations; (3) the expected number of detections of their gravitational-wave emission by the Advanced LIGO interferometer.

3.1.2 Accepted for publication or in press

1. Becerra, Laura; Guzzo, Marcelo M.; Rossi-Torres, Fernando; Rueda, Jorge A.; Ruffini, Remo; Uribe, Juan D., *Neutrino Oscillations Within the Induced Gravitational Collapse Paradigm of Long Gamma-Ray Bursts*, to appear in ApJ.

   The induced gravitational collapse (IGC) paradigm of long gamma-ray bursts (GRBs) associated with supernovae (SNe) predicts a copious neutrino-antineutrino ($\nu\bar{\nu}$) emission owing to the hypercritical accretion process of SN ejecta onto a neutron star (NS) binary companion. The neutrino emission can reach luminosities of up to 10^{57} MeV s^{-1}, mean neutrino energies 20 MeV, and neutrino densities 10^{31} cm^{-3}. Along their path from the vicinity of the NS surface outward, such neutrinos experience flavor transformations dictated by the neutrino to electron density ratio. We determine the neutrino and electron on the accretion zone and use them to compute the neutrino flavor evolution. For normal and inverted neutrino-mass hierarchies and within the two-flavor formalism ($\nu_e\nu_x$), we estimate the final electronic and non-electronic neutrino content after two oscillation processes: (1) neutrino collective effects due to neutrino self-interactions where the neutrino density dominates and, (2) the Mikheyev-Smirnov-Wolfenstein (MSW) effect, where the electron density dominates. We find that the final neutrino content is composed by $\sim$55% ($\sim$62%) of electronic neutrinos, i.e. $\nu_e + \bar{\nu}_e$, for the normal (inverted) neutrino-mass hierarchy. The results of this work are the first step toward the characterization of a novel source of astrophysical MeV-neutrinos in addition to core-collapse SNe and, as such, deserve further attention.

3.1.3 Submitted

1. Rodriguez, J. F.; Rueda, J. A.; Ruffini, R., *Comparison and contrast of test-particle and numerical-relativity waveform templates*, submitted to JCAP; arXiv:1706.07704.

   We compare and contrast the emission of gravitational waves and waveforms for the recently established "helicoidal-drifting-sequence" of a test particle around a Kerr black hole with the publicly available waveform templates of numerical relativity simulations. The merger of two black holes of comparable mass are considered. We outline a final smooth merging of the test particle into the Kerr black hole. We find a surprising and unexpected agreement between the two treatments if we adopt for the mass of the particle and for the spin of the Kerr black hole, respectively, the Newtonian-center-of-mass description and the spin of the Kerr black hole formed in the merger.

2. Rodriguez, J. F.; Rueda, J. A.; Ruffini, R., *Strong-field gravitational-wave emission in Schwarzschild and Kerr geometries: some general considerations*, submitted to Physical Review D.

   We show how the concurrent implementation of the exact solutions of the Einstein equations, of the equations of motion of the test particles, and of the relativistic estimate of the emission of gravitational waves from test particles, can establish a priori constraints on the possible phenomena occurring in Nature. Two examples of test particles starting at infinite distance or from finite distance in a circular orbit around a Kerr black hole are considered: the first leads to a well defined gravitational-wave burst the second to a smooth merging into the black hole. We notice a difference between our treatment and the one by Ori and Thorne (2000) which will affect the gravitational-wave signal. This analysis is necessary for the study of the waveforms in merging binary systems.

3. R. Ruffini, J. F. Rodriguez, M. Muccino, J. A. Rueda, Y. Aimuratov, U. Barres de Almeida, L. Becerra, C. L. Bianco, C. Cherubini, S. Filippi, D. Gizzi, M. Kovacevic, R. Moradi, F. G. Oliveira, G. B. Pisani, and Y. Wang, *On the rate and on the gravitational wave emission of short and long GRBs*, submitted to ApJ; arXiv:1602.03545.

   GRBs, traditionally classified as “long” and “short”, have been often assumed, till recently, to originate from a single black hole (BH) with an ultrarelativistic jetted emission. There is evidence that both long and short bursts have as progenitors merging and/or accreting binaries, each composed by a different combination of carbon-oxygen cores (CO_{core}), neutron stars (NSs), BHs and white dwarfs (WDs). Consequently, the traditional long bursts have been sub-classified as (I) X-ray flashes (XRFs), (II) binary-driven hypernovae (BdHNe), and (III) BH-supernovae (BH-SNe). They are framed within the induced gravitational collapse (IGC) paradigm which envisages as progenitor a tight binary composed of a CO_{core} and a NS or BH companion. The SN explosion of the CO_{core}, originating a new NS (νNS), triggers a hypercritical accretion process onto the companion NS or BH. If the accretion is not sufficient for the NS to reach its critical mass, an XRF occurs, leading to a νNS-NS system. Instead, when the BH is already present or formed by the hypercritical accretion, a BdHN occurs, leading to a νNS-BH system. Similarly, the traditional short bursts, originating in NS-NS mergers, are sub-classified as (IV) short gamma-ray flashes (S-GRFs) and (V) short GRBs (S-GRBs), respectively when the merging process does not lead or leads to BH formation. Two additional families are (VI) ultra-short GRBs (U-GRBs) and (VII) gamma-ray flashes (GRFs), respectively formed in νNS-BH and NS-WD mergers. We use the estimated occurrence rate of the above sub-classes to assess the gravitational wave emission in the merging process and its detectability by Advanced LIGO, Advanced Virgo, eLISA, and resonant bars.

4. L. Becerra, J. A. Rueda, P. Lorén-Aguilar, E. García-Berro, *The Spin Evolution of Fast-Rotating, Magnetized Super-Chandrasekhar White Dwarfs in the Aftermath of White Dwarf Mergers*, submitted to ApJ.

   The evolution of the remnant of the merger of two white dwarfs is still an open problem. Furthermore, few studies have studied the case in which the remnant is a magnetic white dwarf with a mass larger than the Chandrasekhar limiting mass. Angular momentum losses might bring the remnant of the merger to the physical conditions suitable for developing a thermonuclear explosion. Alternatively, the remnant may be prone to gravitational and/or rotational instabilities, depending on the initial conditions reached after the coalescence. Dipole magnetic braking is one of the mechanisms that can drive such losses of angular momentum. However, the timescale on which these losses occur depend on several parameters, like the strength of the magnetic field, the inclination angle with respect to the rotation axis of the remnant, and the properties of the white dwarf. In addition, the coalescence leaves a surrounding Keplerian disk that can be accreted by the newly formed white dwarf. Here we compute the post-merger evolution of a super-Chandrasekhar magnetized white dwarf taking into account all the relevant physical processes. These include magnetic torques acting on the star, accretion from the Keplerian disk, the threading of the magnetic field lines through the disk, as well as the thermal evolution of the white dwarf core. We find that the central remnant can reach the conditions suitable to develop a thermonuclear explosion before other instabilities, such as the inverse beta-decay instability or the secular axisymmetric instability, are reached which would instead lead to gravitational collapse of the magnetized remnant.

5. Rueda, Jorge A.; Wu, Yuan-Bin; Xue, She-Sheng, *Surface tension of compressed, superheavy atoms*, submitted to Physical Review C.

   Based on the relativistic mean-field theory and the Thomas-Fermi approximation, we study the surface properties of compressed, superheavy atoms. By compressed, superheavy atom we mean an atom composed by a superheavy nuclear core (superheavy nucleus) with mass number of the order of 10^4, and degenerate electrons that neutralize the system. Some electrons penetrate into the superheavy nuclear core and the rest surround it up to a distance that depends upon the compression level. Taking into account the strong, weak, and electromagnetic interactions, we numerically study the structure of compressed, superheavy atoms and calculate the nuclear surface tension and Coulomb energy. We analyze the influence of the electron component and the background matter on the nuclear surface tension and Coulomb energy of compressed, superheavy atoms. We also compare and contrast these results in the case of compressed, superheavy atoms with phenomenological results in nuclear physics and the results of the core-crust interface of neutron stars with global charge neutrality. Based on the numerical results we study the instability against Bohr-Wheeler surface deformations in the case of compressed, superheavy atoms. The results in this article show the possibility of the existence of such compressed, superheavy atoms, and provide the evidence of strong effects of the electromagnetic interaction and electrons on the structure of compressed, superheavy atoms.

3.1.4 To be submitted or work in progress

1. Becerra, L. M.; Ellinger, C. L., Fryer, C. L.; Rueda, J. A.; Ruffini, R.,*SPH simulations of the induced gravitational collapse scenario for long gamma-ray bursts associated with supernovae.*

We present the first full 3D smoothed-particle hydrodynamics (SPH) simulations of the the induced gravitational collapse (IGC) scenario for the explanation of long-duration gamma-ray bursts (GRBs) associated with supernovae (SNe). We simulate the SN explosion and subsequent evolution of the ejecta expansion in presence of a neutron star (NS) binary companion. The NS companion accretes matter from the SN ejecta at hypercritical (highly super-Eddington) rates allowed by a copious neutrino-antineutrino pair emission near the NS surface. We show: 1) that the NS can reach the critical mass for black-hole (BH) formation in this process; 2) 3D profiles of the SN ejecta thermodynamical properties (e.g. density, pressure and temperature) influenced by the gravitational field of the nearby NS companion and the accretion process onto it; 3) the relevance of our results for a high-precision analysis of GRB data.

2. Rodriguez, J. F.; Rueda, J. A.; Ruffini, R., *Some general considerations on the aftermath of neutron star binary mergers*.

   On the basis of the conservation of energy, angular momentum and baryon number we determine the general properties of the configuration left by the merger of a neutron star (NS) binary. We analyze the conditions under which the central remnant left by the NS-NS merger is purely a supra-massive NS or a black hole with/without surrounding material. The role of the NS equation of state is addressed in detail.

3. Vieira Lobato, R.; Coelho, J. G.; Otoniel, E.; Malheiro, M.; Rueda, J. A., *Radio emission in SGRs/AXPs and white dwarf pulsars*.

   Soft gamma-ray repeaters (SGRs) and anomalous X-ray pulsars (AXPs) have been traditionally assumed to be a class of neutron stars powered by magnetic energy (magnetars) and not by rotation as normal radio pulsars (rotation-powered). The discovery of radio-pulsed emission, expected in ordinary pulsars but not within the magnetar model, in four sources of this class opens the question of the nature of these sources in comparison to the other SGRs/AXPs. We investigate the condition for electron-positron pair creation (death-line) in the pulsar magnetosphere to establish the consistency with the absence/presence of radio emission in SGRs/AXPs. We perform this analysis both for the model of SGRs/AXPs based on neutron stars and for the model based on white dwarfs.

3.2 Conference Proceedings

1. Becerra, L. M.; Fryer, C. L.; Rueda, J. A.; Ruffini, R., *Hypercritical Accretion in the Induced Gravitational Collapse*, XV Latin American Regional IAU Meeting, Cartagena 2016, Revista Mexicana de Astronomía y Astrofísica (Serie de Conferencias) 49, 83, 2017.

   We present the induced gravitational collapse paradigm that have been applied to explain the long gamma-ray burst associated with type Ic supernovae and recently to the X-ray flashes.

2. Malheiro, M.; Coelho, Jaziel G.; Cáceres, D. L.; de Lima, R. C. R.; Lobato, R. V.; Rueda, J. A.; Ruffini, R., *Possible rotation-power nature of SGRs and AXPs*, JPCS, 861, 012003, 2017.

   We investigate the possibility of some Soft Gamma-ray Repeaters (SGRs) and Anomalous X-ray Pulsars (AXPs) could be described as rotation-powered neutron stars (NSs). The analysis was carried out by computing the structure properties of NSs, and then we focus on giving estimates for the surface magnetic field using both realistic structure parameters of NSs and a general relativistic model of a rotating magnetic dipole. We show that the use of realistic parameters of rotating neutron stars obtained from numerical integration of the self-consistent axisymmetric general relativistic equations of equilibrium leads to values of the magnetic field and radiation efficiency of SGRs/AXPs very different from estimates based on fiducial parameters. This analysis leads to a precise prediction of the range of NS masses, obtained here by making use of selected up-to-date nuclear equations of state (EOS). We show that 40% (nine) of the entire observed population of SGRs and AXPs can be described as canonical pulsars driven by the rotational energy of neutron stars, for which we give their possible range of masses. We also show that if the blackbody component in soft X-rays is due to the surface temperature of NSs, then 50% of the sources could be explained as ordinary rotation-powered pulsars. Besides, amongst these sources we find the four SGRs/AXPs with observed radio emission and six that are possibly associated with supernova remnants (including Swift J1834.9-0846 as the first magnetar to show a surrounding wind nebula), suggesting as well a natural explanation as ordinary pulsars.

3. de Lima, Rafael C. R.; Coelho, Jaziel G.; Malheiro, Manuel; Rueda, Jorge

A.; Ruffini, Remo, *SGRs/AXPs as Rotation-Powered Neutron Stars*, IJMPCS 45, 1760030, 2017.

We show that nine soft gamma repeaters (SGRs) and Anomalous X-ray Pulsars (AXPs) of the twenty three known sources can be described as rotation-powered canonical pulsars. To accomplish this we use realistic parameters of rotating neutron stars obtained from numerical integration of the self-consistent axisymmetric general relativistic equations of equilibrium. We present limits to the NS mass where the sources can be rotation-powered.

Draft version December 21, 2017
Preprint typeset using LaTeX style emulateapj v. 12/16/11

NEUTRINO OSCILLATIONS WITHIN THE INDUCED GRAVITATIONAL COLLAPSE PARADIGM OF LONG GAMMA-RAY BURSTS

L. Becerra[1,2], M. M. Guzzo[3], F. Rossi-Torres[3], J. A. Rueda[1,2,4], R. Ruffini[1,2,4] and J. D. Uribe[1,2]

(Dated: December 21, 2017)
Draft version December 21, 2017

ABSTRACT

The induced gravitational collapse (IGC) paradigm of long gamma-ray bursts (GRBs) associated with supernovae (SNe) predicts a copious neutrino-antineutrino ($\nu\bar{\nu}$) emission owing to the hypercritical accretion process of SN ejecta onto a neutron star (NS) binary companion. The neutrino emission can reach luminosities of up to 10^{57} MeV s^{-1}, mean neutrino energies 20 MeV, and neutrino densities 10^{31} cm^{-3}. Along their path from the vicinity of the NS surface outward, such neutrinos experience flavor transformations dictated by the neutrino to electron density ratio. We determine the neutrino and electron on the accretion zone and use them to compute the neutrino flavor evolution. For normal and inverted neutrino-mass hierarchies and within the two-flavor formalism ($\nu_e\nu_x$), we estimate the final electronic and non-electronic neutrino content after two oscillation processes: (1) neutrino collective effects due to neutrino self-interactions where the neutrino density dominates and, (2) the Mikheyev-Smirnov-Wolfenstein (MSW) effect, where the electron density dominates. We find that the final neutrino content is composed by $\sim$55% ($\sim$62%) of electronic neutrinos, i.e. $\nu_e + \bar{\nu}_e$, for the normal (inverted) neutrino-mass hierarchy. The results of this work are the first step toward the characterization of a novel source of astrophysical MeV-neutrinos in addition to core-collapse SNe and, as such, deserve further attention.

1. INTRODUCTION

The emergent picture of gamma-ray burst (GRB) is that both, short-duration and long-duration GRBs, originate from binary systems (Ruffini et al. 2016b).

Short bursts originate from neutron star-neutron star (NS-NS) or neutron star-black hole (NS-BH) mergers (see, e.g., Goodman 1986; Paczynski 1986; Eichler et al. 1989; Narayan et al. 1991). For this case Narayan et al. (1992) introduced the role of neutrino-antineutrino ($\nu\bar{\nu}$) annihilation leading to the formation of an electron-positron plasma (e^-e^+) in NS-NS and NS-BH mergers. Such a result triggered many theoretical works, including the general relativistic treatment by Salmonson & Wilson (2002) of the $\nu\bar{\nu}$ annihilation process giving rise to the e^-e^+ plasma in a NS-NS system.

For long bursts we stand on the induced gravitational collapse (IGC) paradigm (Ruffini et al. 2006, 2008; Izzo et al. 2012; Rueda & Ruffini 2012; Fryer et al. 2014; Ruffini et al. 2015a), based on the hypercritical accretion process of the supernova (SN) ejecta of the explosion of a carbon-oxygen core (CO_{core}) onto a NS binary companion. In the above processes, the emission of neutrinos is a key ingredient.

We focus hereafter on the neutrino emission of long bursts within the IGC scenario. The role of neutrinos in this paradigm has been recently addressed Fryer et al. (2014); Fryer et al. (2015); Becerra et al. (2015, 2016). The hypercritical accretion of the SN ejecta onto the NS companion can reach very high rates of up to $10^{-2}\,M_\odot$ s^{-1} and its duration can be of the order of 10–10^4 s depending on the binary parameters. The photons become trapped within the accretion flow and thus do not serve as an energy sink. The high temperature developed on the NS surface leads to e^-e^+ pairs that, via weak interactions, annihilate into $\nu\bar{\nu}$ pairs with neutrino luminosities of up to 10^{52} erg s^{-1} for the highest accretion rates. Thus, this process dominates the cooling and give rise to a very efficient conversion of the gravitational energy gained by accretion into radiation. We refer to Becerra et al. (2016) for further details on this process.

The above hypercritical accretion process can lead the NS to two alternative fates, leading to the existence of two long GRB sub-classes (Fryer et al. 2014; Fryer et al. 2015; Becerra et al. 2015, 2016; Ruffini et al. 2016b):

I. The hypercritical accretion leads to a more massive NS companion but not to a black hole (BH). These binaries explain the X-ray flashes (XRFs); long bursts with isotropic energy $E_{\rm iso} \lesssim 10^{52}$ erg and rest-frame spectral peak energy $E_{p,i} \lesssim 200$ keV (see Ruffini et al. 2016b, for further details). The local observed number density rate of this GRB sub-class is (Ruffini et al. 2016b): $\rho_{\rm GRB} = 100^{+45}_{-34}$ Gpc^{-3}yr^{-1}.

II. The hypercritical accretion is high enough to make the NS reach its critical mass triggering its gravitational collapse with consequent BH formation. These binaries explain the binary-driven hypernovae (BdHNe); long bursts with $E_{\rm iso} \gtrsim 10^{52}$ erg and $E_{p,i} \gtrsim 200$ keV (see Ruffini et al. 2016b, for further details). The local observed number density rate of this GRB sub-class is (Ruffini et al. 2016b): $\rho_{\rm GRB} = 0.77^{+0.09}_{-0.08}$ Gpc^{-3}yr^{-1}.

Simulations of the hypercritical accretion process in the above binaries have been presented in Fryer et al. (2014); Fryer et al. (2015); Becerra et al. (2015, 2016). It has been shown how, thanks to the development of a copious neutrino emission near the NS surface, the NS is allowed to accrete matter from the SN at very high rates. The specific conditions leading to XRFs and BdHNe as well as a detailed analysis of the neutrino production in these systems have been presented

[1] Dipartimento di Fisica and ICRA, Sapienza Università di Roma, P.le Aldo Moro 5, I–00185 Rome, Italy
[2] ICRANet, P.zza della Repubblica 10, I–65122 Pescara, Italy
[4] ICRANet-Rio, i Centro Brasileiro de Pesquisas Físicas, Rua Dr. Xavier Sigaud 150, 22290–180 Rio de Janeiro, Brazil
[3] Instituto de Física Gleb Wataghin, Universidade Estadual de Campinas, Rua Sérgio Buarque de Holanda 777, 13083-859 Campinas SP Brazil

in Becerra et al. (2016). Neutrino emission can reach luminosities of 10^{52} erg s^{-1} and the mean neutrino energy of the order of 20 MeV. Under these conditions, XRFs and BdHNe become astrophysical laboratories for MeV-neutrino physics additional to core-collapse SNe.

On the other hand, the emission of TeV-PeV neutrinos is relevant for the observations of detectors such as the IceCube (Aartsen et al. 2013). High-energy neutrino emission mechanisms have been proposed within the context of the traditional model of long GRBs. In the traditional "collapsar" scenario (Woosley 1993; Paczyński 1998; MacFadyen & Woosley 1999) the gravitational collapse of a single, fast rotating, massive star originates a BH surrounded by a massive accretion disk (see, e.g., Piran 2004, for a review), and the GRB dynamics follows the "fireball" model that assumes the existence of an ultra-relativistic collimated jet with Lorentz factor $\Gamma \sim 10^2$–10^3 (see e.g. Shemi & Piran 1990; Piran et al. 1993; Meszaros et al. 1993; Mao & Yi 1994). This scenario has been adopted for the explanation of the prompt emission, as well as both the afterglow and the GeV emission of long GRBs. The GRB light-curve structures are there described by (internal or external) shocks (see, e.g., Rees & Meszaros 1992, 1994). The high-energy neutrinos in this context are produced from the interaction of shock-accelerated cosmic-rays (e.g. protons) with the interstellar medium (see e.g. Agostini et al. 2017; Kumar & Zhang 2015, and references therein). A recent analysis of the thermal emission of the X-ray flares observed in the early afterglow of long GRBs (at source rest-frame times $t \sim 10^2$ s) show that it occurs at radii $\sim 10^{12}$ cm and expands with a mildly-relativistic $\Gamma \lesssim 4$ (see Ruffini et al. 2017, for further details). This rules out the ultra-relativistic expansion in the GRB afterglow traditionally adopted in the literature. Interestingly, the aforementioned mechanisms of high-energy neutrino production conceived in the collapsar-fireball model can still be relevant in the context of BdHNe and authentic short GRBs (S-GRBs, NS-NS mergers with $E_{\rm iso} \gtrsim 10^{52}$ erg leading to BH formation; see Ruffini et al. 2016b, for the classification of long and short bursts in seven different sub-classes). The emission in the 0.1–100 GeV energy band observed in these two GRB sub-classes has been shown to be well explained by a subsequent accretion process onto the newly-born BH (Ruffini et al. 2015a,b, 2016a,b; Aimuratov et al. 2017; see also Aimuratov et al. in preparation). Such GeV emission is not causally connected either with the prompt emission or with the afterglow emission comprising the flaring activity (Ruffini et al. 2017). An ultra-relativistic expanding component is therefore expected to occur in BdHNe and S-GRBs which deserves to be explored in forthcoming studies as a possible source of high-energy neutrinos. Specifically, this motivates the present article to identify the possible additional channels to be explored in the hypercritical accretion not around a NS but around a BH.

The aim of this article is to extend the analysis of the MeV-neutrino emission in the hypercritical accretion process around a NS in the XRFs and BdHNe to assess the possible occurrence of neutrino flavor oscillations.

We shall show in this work that, before escaping to the outer space, i.e. outside the Bondi-Hoyle accretion region, the neutrinos experience an interesting phenomenology. The neutrino density near the NS surface is so high that the neutrino self-interaction potential, usually negligible in other very well-known scenarios like the Sun, the upper layers of Earth's atmosphere and terrestrial reactor and accelerator experiments, becomes more relevant than the matter potential responsible for the famous Mikheyev-Smirnov-Wolfenstein (MSW) effect (Wolfenstein 1978; Mikheev & Smirnov 1986). A number of papers have been dedicated to the consequences of the neutrino self-interaction dominance (Notzold & Raffelt 1988; Pantaleone 1992; Qian & Fuller 1995; Pastor & Raffelt 2002; Duan et al. 2006b; Sawyer 2005; Fuller & Qian 2006; Fogli et al. 2007; Duan et al. 2007; Raffelt & Sigl 2007; Esteban-Pretel et al. 2007, 2008; Chakraborty et al. 2008; Duan et al. 2008a,b; Dasgupta et al. 2008a; Dasgupta & Dighe 2008; Sawyer 2009; Duan et al. 2010; Wu & Qian 2011), most of them focused on SN neutrinos. In these cases, the SN induces the appearance of collective effects such as synchronized and bipolar oscillations leading to an entirely new flavor content of emitted neutrinos when compared with the spectrum created deep inside the star. The density of neutrinos produced in the hypercritical accretion process of XRFs and BdHNe is such that the neutrino self-interactions, as in the case of SNe, dominate the neutrino flavor evolution, giving rise to the aforementioned collective effects. The main neutrino source, in this case, is the $\nu\bar{\nu}$ pair production from e^-e^+ annihilation (Becerra et al. 2016) which leads to an equal number of neutrinos and antineutrinos of each type. This equality does not happen in the SN standard scenario. We will show that bipolar oscillations, inducing very quick flavor pair conversions $\nu_e\bar{\nu}_e \leftrightarrow \nu_\mu\bar{\nu}_\mu \leftrightarrow \nu_\tau\bar{\nu}_\tau$, can occur with oscillation length as small as $O(0.05$–$1)$ kilometers. However, the ν–$\bar{\nu}$ symmetry characterizing our system leads to the occurrence of kinematic decoherence making the neutrino flavor content to reach equipartition deep inside the accretion zone. In the regions far from the NS surface where the neutrino density is not so high, the matter potential turns to dominate and MSW resonances can take place. As a result, an entirely different neutrino flavor content emerges from the Bondi-Hoyle surface when compared with what was originally created in the bottom of the accretion zone.

This article is organized as follows. In Sec. 2 we outline the general features of the accretion process onto the NS within the IGC paradigm and present the processes responsible for the neutrino creation. From these features, we obtain the distribution functions that describe the neutrino spectrum near the NS surface. Sec. 3 shows a derivation of the equations that drive the evolution of neutrino oscillations closely related to the geometrical and physical characteristics of our system. We discuss some details on the neutrino oscillation phenomenology. Since we have to face a nonlinear integro-differential system of equations of motion, we introduce the single-angle approximation to later recover the full realistic phenomenology after generalizing our results to the multi-angle approach and, consequently, de-coherent picture. In Sec. 5 the final neutrino emission spectra are presented and compared with those ones in which neutrinos are created in the accretion zone. Finally, we present in Sec. 6 the conclusions and some perspectives for future research on this subject.

2. NEUTRINO CREATION DURING HYPERCRITICAL ACCRETION

The SN material first reaches the gravitational capture region of the NS companion, namely the Bondi-Hoyle region. The infalling material shocks as it piles up onto the NS surface forming an accretion zone where it compresses and eventually becomes sufficiently hot to trigger a highly efficient neutrino emission process. Neutrinos take away most of the infalling matter's gravitational energy gain, letting it reduce its entropy

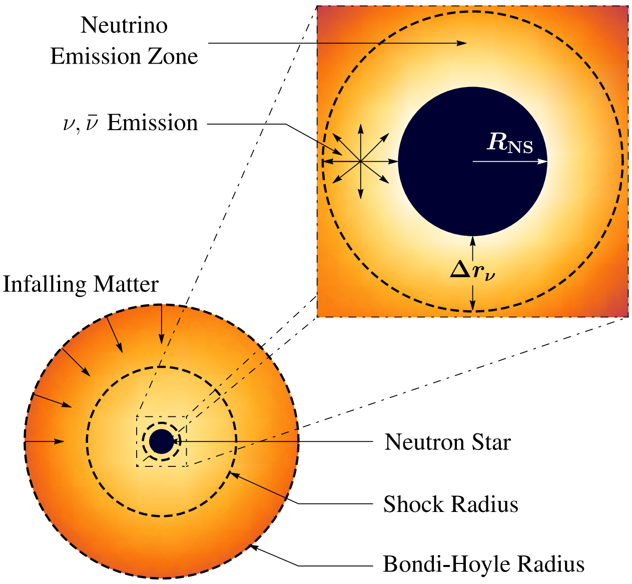

FIG. 1.— Schematic representation of the accretion process onto the NS and the neutrino emission. The supernova ejected material reaches the NS Bondi-Hoyle radius and falls onto the NS surface. The material shocks and decelerates as it piles over the NS surface. At the neutrino emission zone, neutrinos take away most of the infalling matter's energy. The neutrino emission allows the material to reduce its entropy to be incorporated to the NS. The image is not to scale. For binary system with $M_{NS} = 2M_\odot$ and $R_{NS} = 10$ km, and a $M_{ZAMS} = 20M_\odot$ progenitor, at $\dot{M} = 10^{-2} M_\odot/\mathrm{s}$, the position of the Bondi-Hoyle and Shock radii are 2.3×10^5 km and 31 km, respectively. The neutrino emission zone's thickness is $\Delta r_\nu = 0.8$ km.

and be incorporated into the NS. Fig. 1 shows a sketch of this entire hypercritical accretion process.

It was shown in Becerra et al. (2016) that the matter in the accretion zone near the NS surface develops conditions of temperature and density such that it is in a non-degenerate, relativistic, hot plasma state. The most efficient neutrino emission channel under those conditions becomes the electron positron pair annihilation process:

$$e^- e^+ \rightarrow \nu \bar{\nu}. \tag{1}$$

The neutrino emissivity produced by this process is proportional to the accretion rate to the 9/4 power (see below). This implies that the higher the accretion rate the higher the neutrino flux, hence the largest neutrino flux occurs at the largest accretion rate.

We turn now to estimate the accretion rate and thus the neutrino emissivity we expect in our systems.

2.1. *Accretion rate in XRFs and BdHNe*

We first discuss the amount of SN matter per unit time reaching the gravitational capture region of the NS companion, namely the Bondi-Hoyle accretion rate. It has been shown in Bayless et al. (2015); Becerra et al. (2016) that the shorter (smaller) the orbital period (separation) the higher the peak accretion rate $\dot{M}_{peak}$ and the shorter the time at which it peaks, t_{peak}.

The Bondi-Hoyle accretion rate is proportional to the density of the accreted matter and inversely proportional to its velocity. Thus, we expect the accretion rate to increase as the denser and slower inner layers of the SN reach the accretion region. Based on these arguments, Becerra et al. (2016) derived simple, analytic formulas for $\dot{M}_{peak}$ and t_{peak} as a function of the orbital period (given all the other binary parameters) that catch both the qualitatively and quantitatively behaviors of these two quantities obtained from full numerical integration. We refer the reader to the Appendix A of that article for further details. For the scope of this work these analytic expressions are sufficient to give us an estimate of the hypercritical accretion rates and related time scale developed in these systems:

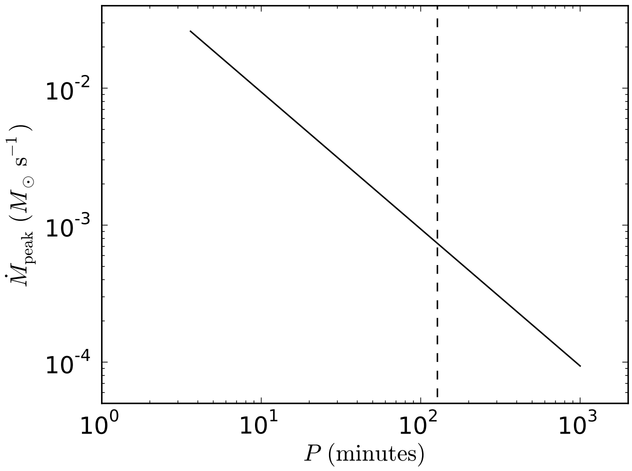

FIG. 2.— Peak accretion rate, $\dot{M}_{peak}$, as a function of the binary orbital period, as given by Eq. (2). This example corresponds to the following binary parameters: a CO_{core} formed by a $M_{ZAMS} = 20\ M_\odot$ progenitor, i.e. $M_{CO} = 5.4\ M_\odot$, an initial NS mass $2.0\ M_\odot$, $v_{star,0} = 2 \times 10^9$ cm s^{-1}, $\eta \approx 0.41$ and index $m = 2.946$ (see Becerra et al. 2016, for further details). For these parameters the largest orbital period for the induced collapse of the NS to a BH by accretion is $P_{max} \approx 127$ min which is represented by the vertical dashed line.

$$t_{peak} \approx \left(1 - \frac{2M_{NS}}{M}\right)\left(\frac{GM}{4\pi^2}\right)^{1/3}\left(\frac{R^0_{star}}{\eta R_{core}}\right)\frac{P^{2/3}}{v_{star,0}}, \tag{2a}$$

$$\dot{M}_{peak} \approx 2\pi^2 \frac{(2M_{NS}/M)^{5/2}}{(1-2M_{NS}/M)^3}\eta^{3-m}\frac{\rho_{core} R^3_{core}}{P}, \tag{2b}$$

where P is the orbital period, m is the index of the power-law density profile of the pre-SN envelope, $v_{star,0}$ is the velocity of the outermost layer of the SN ejecta, $M = M_{CO} + M_{NS}$ is the total binary mass, $M_{CO} = M_{env} + M_{\nu NS}$ is the total mass of the CO_{core} given by the envelope mass and the mass of the central remnant, i.e. the new NS (hereafter νNS) formed from the region of the CO_{core} which undergoes core-collapse (i.e. roughly speaking the iron core of density ρ_{core} and radius R_{core}). We here adopt $M_{\nu NS} = 1.5\ M_\odot$. The parameter η is given by

$$\eta \equiv \frac{R^0_{star}}{R_{core}} \frac{1+m}{1+m(R^0_{star}/\hat{R}_{core})}, \tag{3}$$

where R^0_{star} is the total radius of the pre-SN CO_{core}; $\hat{\rho}_{core}$ and $\hat{R}_{core}$ are parameters of the pre-SN density profile introduced to account of the finite size of the envelope, and m is the power-law index followed by the density profile at radii $r > R_{core}$ (see Becerra et al. 2016, for further details).

Fig. 2 shows the peak accretion rate in Eq. (2) as a function of the orbital period. In this example, we consider the following binary parameters (see Becerra et al. 2016, for details): a CO_{core} produced by a zero-age main-sequence (ZAMS) progenitor with $M_{ZAMS} = 20\ M_\odot$, i.e. $M_{CO} = 5.4\ M_\odot$, an initial NS mass $2.0\ M_\odot$, and a velocity of the outermost ejecta layer

$v_{\rm star,0} = 2\times10^9$ cm s^{-1}. For these parameters, $\eta \approx 0.41$.

It was shown in Becerra et al. (2015, 2016) the existence of a maximum orbital period, $P_{\rm max}$, over which the accretion onto NS companion is not high enough to bring it to the critical mass for gravitational collapse to a BH. As we have recalled in the Introduction, CO$_{\rm core}$-NS binaries with $P > P_{\rm max}$ lead to XRFs while the ones with $P \lesssim P_{\rm max}$ lead to BdHNe. For the binary parameters of the example in Fig. 2, $P_{\rm max} \approx 127$ min (vertical dashed line). We can therefore conclude that BdHNe can have peak accretion rates in the range $\dot{M}_{\rm peak} \sim 10^{-3}$– few 10^{-2} $M_\odot$ s^{-1} while XRFs would have $\dot{M}_{\rm peak} \sim 10^{-4}$–$10^{-3}$ $M_\odot$ s^{-1}.

2.2. *Neutrino emission at maximum accretion*

For the accretion rate conditions characteristic of our models at peak $\sim 10^{-4}$–10^{-2} $M_\odot$ s^{-1}, pair annihilation dominates the neutrino emission and electron neutrinos remove the bulk of the energy (Becerra et al. 2016). The e^+e^- pairs producing the neutrinos are thermalized at the matter temperature. This temperature is approximately given by:

$$T_{\rm acc} \approx \left(\frac{3P_{\rm shock}}{4\sigma/c}\right)^{1/4} = \left(\frac{7}{8}\frac{\dot{M}_{\rm acc}v_{\rm acc}c}{4\pi R_{\rm NS}^2\sigma}\right)^{1/4}, \tag{4}$$

where $P_{\rm shock}$ is the pressure of the shock developed on the accretion zone above the NS surface, $\dot{M}_{\rm acc}$ is the accretion rate, $v_{\rm acc}$ is the velocity of the infalling material, σ is the Stefan-Boltzmann constant and c the speed of light. It can be checked that, for the above accretion rates, the system develops temperatures and densities ($T \gtrsim 10^{10}$ K and $\rho \gtrsim 10^6$ g cm^{-3}; see e.g. Fig. 16 in Becerra et al. 2016) for which the neutrino emissivity of the e^+e^- annhiliation process can be estimated by the simple formula (Yakovlev et al. 2001):

$$\epsilon_{e^-e^+} \approx 8.69\times10^{30}\left(\frac{k_BT}{1\,{\rm MeV}}\right)^9\ {\rm MeV\,cm^{-3}\,s^{-1}}, \tag{5}$$

where k_B is the Boltzmann constant.

The accretion zone is characterized by a temperature gradient with a typical scale height $\Delta r_{\rm ER} = T/\nabla T \approx 0.7\,R_{\rm NS}$. Owing to the strong dependence of the neutrino emission on temperature, most of the neutrinos are emitted from a spherical shell around the NS of thickness (see Fig. 1)

$$\Delta r_\nu = \frac{\epsilon_{e^-e^+}}{\nabla\epsilon_{e^-e^+}} = \frac{\Delta r_{\rm ER}}{9} \approx 0.08 R_{\rm NS}. \tag{6}$$

Eqs. (4) and (5) imply the neutrino emissivity satisfies $\epsilon_{e^-e^+} \propto \dot{M}_{\rm acc}^{9/4}$ as we had anticipated. These conditions lead to the neutrinos to be efficient in balancing the gravitational potential energy gain, allowing the hypercritical accretion rates. The effective accretion onto the NS can be estimated as

$$\dot{M}_{\rm eff} \approx \Delta M_\nu \frac{L_\nu}{E_g}, \tag{7}$$

where ΔM_ν, L_ν are, respectively, the mass and neutrino luminosity in the emission region, and $E_g = (1/2)GM_{\rm NS}\Delta M_\nu/(R_\nu + \Delta r_\nu)$ is half the gravitational potential energy gained by the material falling from infinity to the $R_{\rm NS} + \Delta r_\nu$. The neutrino luminosity is

$$L_\nu \approx 4\pi R_{\rm NS}^2 \Delta r_\nu \epsilon_{e^-e^+}. \tag{8}$$

with $\epsilon_{e^-e^+}$ being the neutrino emissivity in Eq. (5). For $M_{\rm NS} = 2\,M_\odot$ and temperatures 1–10 MeV, the Eqs. (7) and (8) result $\dot{M}_{\rm eff} \approx 10^{-10}$–$10^{-1}$ $M_\odot$ s^{-1} and $L_\nu \approx 10^{48}$–10^{57} MeV s^{-1}.

2.3. *Neutrino spectrum at the NS surface*

After discussing the general features of neutrino emission during the accretion process, it is necessary for our analysis of the neutrino oscillations to determine the neutrino spectrum at the NS surface. Specifically, we need to determine the ratios at which the neutrinos of each flavor are created and their average energy so that we can find a fitting distribution function f_ν with these characteristics.

Since the main source of neutrinos is the e^-e^+ pair annihilation process we can conclude that neutrinos and antineutrinos are created in equal number. Furthermore, the information about the neutrino and antineutrino emission of a given flavor i can be calculated from the integral (Yakovlev et al. 2001):

$$\varepsilon_i^m = \frac{2G_F^2\left(m_ec^2\right)^4}{3\,(2\pi\hbar)^7\,(\hbar c)^3}\int f_{e^-}f_{e^+}\frac{\left(E_{e^-}^m + E_{e^+}^m\right)}{E_{e^-}E_{e^+}}\sigma_i\, d^3\mathbf{p}_{e^-}d^3\mathbf{p}_{e^+} \tag{9}$$

where $G_F = 8.963\times10^{-44}$ MeV cm^3 is the Fermi constant of weak interactions. Here $m = 0, 1, \ldots$ and should not be confused with the index of the power-law density profile of the pre-SN envelope in Sec. 2.1). $f_{e^\pm}$ are the Fermi-Dirac distributions for electron and positrons

$$f_{e^\mp} = \frac{1}{1+\exp\left(\frac{E_{e^\mp}}{k_BT} \mp \eta_{e^\mp}\right)}. \tag{10}$$

$\eta_{e^\mp}$ is the electron (positron) degeneracy parameter including it's rest mass. The Dicus cross section σ_i is written in terms of the electron and positron four-momenta $p_{e^\pm} = (E_{e^\pm}/c, \mathbf{p}_{e^\pm})$ as (Dicus 1972)

$$\sigma_i = C_{+,i}^2\left(1 + 3\frac{p_{e^-}\cdot p_{e^+}}{(cm_e)^2} + 2\frac{(p_{e^-}\cdot p_{e^+})^2}{(cm_e)^4}\right) + 3C_{-,i}^2\left(1+\frac{p_{e^-}\cdot p_{e^+}}{(cm_e)^2}\right). \tag{11}$$

The factors $C_{\pm,i}^2$, are written in terms of the weak interaction vector and axial-vector constants: $C_{\pm,i}^2 = C_{V_i}^2 \pm C_{A_i}^2$, where $C_{V_e} = 2\sin^2\theta_{\rm W} + 1/2$, $C_{A_e} = 1/2$, $C_{V_\mu} = C_{V_\tau} = C_{V_e} - 1$ and $C_{A_\mu} = C_{A_\tau} = C_{A_e} - 1$ with the numerical value of the Weinberg angle approximated by $\sin^2\theta_{\rm W} \approx 0.231$ (Patrignani et al. 2016).

For $m = 0$ and $m = 1$ Eq. (9) gives the neutrino and antineutrino number emissivity (neutrino production rate), and the neutrino and antineutrino energy emissivity (energy per unit volume per unit time) for a certain flavor i, respectively. Hence, not only we are able to calculate the total number emissivity with

$$n = \sum_{i\in\{e,\tau,\mu\}}\varepsilon_i^0, \tag{12}$$

but we can also calculate the neutrino or antineutrino energy moments with

$$\langle E_{\nu_i(\bar{\nu}_i)}^m\rangle = \frac{\varepsilon_i^m}{\varepsilon_i^0},\ \text{for } m \geq 1. \tag{13}$$

We wish to construct a Fermi-Dirac like fitting formula for the neutrino spectrum as it is usually done in supernovae neutrino emission (Janka & Hillebrandt 1989a,b). That is, a function like Eq. (10) in terms of two parameters: the effective

$\dot{M}$ ($M_\odot$ s^{-1})	ρ (g cm^{-3})	k_BT (MeV)	$\eta_{e^\mp}$	$n_{e^-}-n_{e^+}$ (cm^{-3})	$k_BT_{\nu\bar{\nu}}$ (MeV)	$\langle E_\nu\rangle$ (MeV)	$F^C_{\nu_e,\bar{\nu}_e}$ (cm^{-2}s^{-1})	$F^C_{\nu_x,\bar{\nu}_x}$ (cm^{-2}s^{-1})	$n^C_{\nu_e\bar{\nu}_e}$ (cm^{-3})	$n^C_{\nu_x\bar{\nu}_x}$ (cm^{-3})	$\sum_i n^C_{\nu_i\bar{\nu}_i}$ (cm^{-3})
10^{-8}	1.46×10^{6}	1.56	∓0.325	4.41×10^{29}	1.78	6.39	4.17×10^{36}	1.79×10^{36}	2.78×10^{26}	1.19×10^{26}	3.97×10^{26}
10^{-7}	3.90×10^{6}	2.01	∓0.251	1.25×10^{30}	2.28	8.24	3.16×10^{37}	1.36×10^{37}	2.11×10^{27}	9.00×10^{26}	3.01×10^{27}
10^{-6}	1.12×10^{7}	2.59	∓0.193	3.38×10^{30}	2.93	10.61	2.40×10^{38}	1.03×10^{38}	1.60×10^{28}	6.90×10^{27}	2.29×10^{28}
10^{-5}	3.10×10^{7}	3.34	∓0.147	9.56×10^{30}	3.78	13.69	1.84×10^{39}	7.87×10^{38}	1.23×10^{29}	5.20×10^{28}	1.75×10^{29}
10^{-4}	8.66×10^{7}	4.30	∓0.111	2.61×10^{31}	4.87	17.62	1.39×10^{40}	5.94×10^{39}	9.24×10^{29}	3.96×10^{29}	1.32×10^{30}
10^{-3}	2.48×10^{8}	5.54	∓0.082	7.65×10^{31}	6.28	22.70	1.04×10^{41}	4.51×10^{40}	7.00×10^{30}	3.00×10^{30}	1.00×10^{31}
10^{-2}	7.54×10^{8}	7.13	∓0.057	2.27×10^{32}	8.08	29.22	7.92×10^{41}	3.39×10^{41}	5.28×10^{31}	2.26×10^{31}	7.54×10^{31}

TABLE 1
CHARACTERISTICS INSIDE THE NEUTRINO EMISSION ZONE AND THE NEUTRINO SPECTRUM FOR SELECTED VALUES OF THE ACCRETION RATE $\dot{M}$. THE ELECTRON FRACTION IS $Y_e = 0.5$, THE PINCHING PARAMETER FOR THE NEUTRINO SPECTRUM IS $\eta_{\nu\bar{\nu}} = 2.0376$ AND THE.

neutrino temperature $T_{\nu\bar{\nu}}$ and the effective neutrino degeneracy parameter $\eta_{\nu\bar{\nu}}$ otherwise known as the *pinching* parameter (Raffelt 1996; Keil et al. 2003). To that end, it is enough to calculate the first two moments. In particular, for a relativistic non-degenerate plasma ($k_BT > 2m_ec^2$ and $1 > \eta_{e^\mp}$ see table 1) Eq. (9) can be approximated with a very good accuracy by (Yakovlev et al. 2001)

$$\varepsilon_i^m \approx \frac{2G_F^2\,(k_BT)^{8+m}}{9\pi^5\hbar\,(\hbar c)^9}C^2_{+,i}\left[\mathcal{F}_{m+1}(\eta_{e^+})\mathcal{F}_1(\eta_{e^-})\right.$$
$$\left.+\mathcal{F}_{m+1}(\eta_{e^-})\mathcal{F}_1(\eta_{e^+})\right] \tag{14}$$

where $\mathcal{F}_k(\eta) = \int_0^\infty dx\, x^k/\left[1+\exp(x-\eta)\right]$ are the Fermi-Dirac integrals. For $m = 1$, $\eta_{e^\pm} = 0$ and adding over every flavor this expression reduces to Eq. (5). With Eqs. (13) and (14) we find

$$\langle E_\nu\rangle = \langle E_{\bar{\nu}}\rangle \approx 4.1\,k_BT \tag{15a}$$
$$\langle E_\nu^2\rangle = \langle E_{\bar{\nu}}^2\rangle \approx 20.8\,(k_BT)^2\,, \tag{15b}$$

regardless of the neutrino flavor. Furthermore, we can calculate the ratio of emission rates between electronic and non-electronic neutrino flavors in terms of the weak interaction constants

$$\frac{\varepsilon_e^0}{\varepsilon_x^0} = \frac{\varepsilon_e^0}{\varepsilon_\mu^0+\varepsilon_\tau^0} = \frac{C^2_{+,e}}{C^2_{+,\mu}+C^2_{+,\tau}} \approx \frac{7}{3}. \tag{16}$$

Some comments must be made about the results we have obtained:

- It is well known that, within the Standard Model of Particles, there are three neutrino flavors $\nu_e, \bar{\nu}_e$, $\nu_\mu, \bar{\nu}_\mu$ and $\nu_\tau, \bar{\nu}_\tau$. However, as in Eq. (16), we will simplify our description using only two flavors: the electronic neutrinos and antineutrinos $\nu_e, \bar{\nu}_e$, and a superposition of the other flavors $\nu_x, \bar{\nu}_x$ ($x = \mu + \tau$). This can be understood as follows. Since the matter in the accretion zone is composed by protons, neutrons, electrons and positrons, ν_e and $\bar{\nu}_e$ interact with matter by both charged and neutral currents, while ν_μ, ν_τ, $\bar{\nu}_\mu$ and $\bar{\nu}_\tau$ interact only by neutral currents. Therefore, the behavior of these states can be clearly divided into electronic and non-electronic. This distinction will come in handy when studying neutrino oscillations.

- Representing the neutrino (antineutrino) density and flux in the moment of their creation with $n^c_{\nu_i(\bar{\nu}_i)}$ and $F^c_{\nu_i(\bar{\nu}_i)}$ respectively and using Eq. (16) we can recollect two important facts:

$$n^C_{\nu_i} = n^C_{\bar{\nu}_i},\;\; F^C_{\nu_i} = F^C_{\bar{\nu}_i}\;\; \forall i \in \{e,\mu,\tau\} \tag{17a}$$
$$\frac{n^C_{\nu_e}}{n^C_{\nu_x}} = \frac{n^C_{\bar{\nu}_e}}{n^C_{\bar{\nu}_x}} = \frac{F^C_{\nu_e}}{F^C_{\nu_x}} = \frac{F^C_{\bar{\nu}_e}}{F^C_{\bar{\nu}_x}} \approx \frac{7}{3}. \tag{17b}$$

  Eqs. (17) imply that, in the specific environment of our system, of the total number of neutrinos+antineutrinos emitted, $N_\nu + N_{\bar{\nu}}$, 70% are electronic neutrinos ($N_{\nu_e} + N_{\bar{\nu}_e}$), 30% are non-electronic ($N_{\nu_x} + N_{\bar{\nu}_x}$), while the total number of neutrinos is equal to the total number of antineutrinos, i.e. $N_\nu = N_{\bar{\nu}}$, where $N_\nu = N_{\nu_e} + N_{\nu_x}$ and $N_{\bar{\nu}} = N_{\bar{\nu}_e} + N_{\bar{\nu}_x}$.

- Bearing in mind such high neutrino energies as the ones suggested by Eqs. (15) , from here on out we will use the approximation

$$E_\nu \approx c|\mathbf{p}| \gg m_\nu c^2, \tag{18}$$

  where $\mathbf{p}$ is the neutrino momentum.

- From Eq. (13) we obtain the same energy moments for both neutrinos and antineutrinos but, as Misiaszek et al. (2006) points out, these energies should be different since, in reality, this expression returns the arithmetic mean of the particle and antiparticle energy moments, that is $\left(\langle E_\nu^m\rangle + \langle E_{\bar{\nu}}^m\rangle\right)/2$. However, if we calculate the differences between the energy moments with equations (41) and (46) in Misiaszek et al. (2006) for the values of T and $\eta_{e^\pm}$ we are considering, we get $\Delta\langle E\rangle \sim 10^{-2}$–$10^{-3}$ MeV and $\Delta\langle E^2\rangle \sim 10^{-3}$–$10^{-4}$ MeV^2. These differences are small enough that we can use the same effective temperature and pinching parameter for both neutrinos and antineutrinos.

Solving the equations

$$4.1k_BT = k_BT_{\nu\bar{\nu}}\frac{\mathcal{F}_3(\eta_{\nu\bar{\nu}})}{\mathcal{F}_2(\eta_{\nu\bar{\nu}})} \tag{19a}$$
$$20.8\,(k_BT)^2 = (k_BT_{\nu\bar{\nu}})^2\,\frac{\mathcal{F}_4(\eta_{\nu\bar{\nu}})}{\mathcal{F}_2(\eta_{\nu\bar{\nu}})} \tag{19b}$$

for any value of T in table (1) we find $T_{\nu\bar{\nu}} = 1.1331T$ and $\eta_{\nu\bar{\nu}} = 2.0376$. Integrating Eq. (10) over the neutrino momentum space using these values should give the neutrino number density. To achieve this we normalize it with the factor $1/\left(2\pi^2\,(k_BT_{\nu\bar{\nu}})^3\,\mathcal{F}_2(\eta_{\nu\bar{\nu}})\right)$ and then we multiply by

$$n^C_{\nu_i(\bar{\nu}_i)} = w_{\nu_i(\bar{\nu}_i)}\frac{L_\nu}{4\pi R^2_{\rm NS}\langle E_\nu\rangle\langle v\rangle} = w_{\nu_i(\bar{\nu}_i)}\frac{\varepsilon_i^0\Delta r_\nu}{c/2}, \tag{20}$$

where the neutrino's average radial velocity at $r = R_{\rm NS}$ is $\langle v \rangle = c/2$ (Dasgupta et al. 2008b) and $w_{\nu_e} = w_{\bar{\nu}_e} = 0.35$ and $w_{\nu_x} = w_{\bar{\nu}_x} = 0.15$. To calculate the neutrino fluxes we simply $F^C_{\nu(\bar{\nu}_i)} = \langle v \rangle n^c_{\nu_i(\bar{\nu}_i)}$. Gathering our results we can finally write the distribution functions as

$$f_{\nu_e} = f_{\bar{\nu}_e} = \frac{2\pi^2 (\hbar c)^3 n^C_{\nu_e}}{(k_B T_{\nu\bar{\nu}})^3 \mathcal{F}_2(\eta_{\nu\bar{\nu}})} \frac{1}{1+\exp(E/k_B T_{\nu\bar{\nu}} - \eta_{\nu\bar{\nu}})} \quad (21a)$$

$$f_{\nu_x} = f_{\bar{\nu}_x} = \frac{2\pi^2 (\hbar c)^3 n^C_{\nu_x}}{(k_B T_{\nu\bar{\nu}})^3 \mathcal{F}_2(\eta_{\nu\bar{\nu}})} \frac{1}{1+\exp(E/k_B T_{\nu\bar{\nu}} - \eta_{\nu\bar{\nu}})} \quad (21b)$$

It can be checked that these distributions obey

$$\int f_{\nu_i} \frac{d^3\mathbf{p}}{(2\pi\hbar)^3} = n^C_{\nu_i} \quad (22a)$$

$$\int E f_{\nu_i} \frac{d^3\mathbf{p}}{(2\pi\hbar)^3} = \langle E_\nu \rangle n^C_{\nu_i} = \varepsilon^1_i \quad (22b)$$

and with these conditions satisfied we can conclude that Eqs. (21) are precisely the ones that emulate the neutrino spectrum at the NS surface. In Table 1 we have collected the values of every important quantity used in the calculations within this section for the range of accretion rates in which we are interested.

Considering that the problem we attacked in this section reduces to finding a normalized distribution whose first two moments are fixed, the choice we have made with Eqs. (21) is not unique. The solution depends on how many moments are used to fit the distribution and what kind of function is used as an ansatz. A different solution based on a Maxwell-Boltzmann distribution can be found in Keil et al. (2003); Fogli et al. (2005); Misiaszek et al. (2006).

At this stage, we can identify two main differences between neutrino emission in SNe and in the IGC process of XRFs and BdHNe, within the context of neutrino oscillations. The significance of these differences will become clearer in next sections but we mention them here to establish a point of comparison between the two systems since SN neutrino oscillations have been extensively studied.

- Neutrinos of all flavors in XRFs and BdHNe have the same temperature, which leads to equal average energy. The neutrinos produced in SNe are trapped and kept in thermal equilibrium within their respective neutrinosphere. The neutrino-spheres have different radii, causing different flavors to have different average energies. This energy difference leads to a phenomenon called *spectral stepwise swap* which, as we will show below, is not present in our systems (see, e.g., Raffelt 1996; Fogli et al. 2007; Dasgupta & Dighe 2008, and references therein).

- As we have discussed above, in XRFs and BdHNe neutrinos and antineutrinos are emitted in equal number. Due to this fact, kinematical decoherence occurs (up to a number difference of 30% this statement is valid; see Sec. 4 for further details). Instead, SN neutrino and antineutrino fluxes differ such that $F_{\nu_e} > F_{\bar{\nu}_e} > F_{\nu_x} = F_{\bar{\nu}_x}$. It has been argued that this difference between neutrinos and antineutrinos is enough to dampen kinematical decoherence, so that bipolar oscillations are a feature present in SN neutrinos (see, e.g., Esteban-Pretel et al. 2007).

In the next section, we will use the results presented here to determine the neutrino flavor evolution in the accretion zone.

3. NEUTRINO OSCILLATIONS

In recent years the picture of neutrino oscillations in dense media, based only on MSW effects, has undergone a change of paradigm by the insight that the refractive effects of neutrinos on themselves due to the neutrino self-interaction potential are crucial (Notzold & Raffelt 1988; Pantaleone 1992; Qian & Fuller 1995; Pastor & Raffelt 2002; Duan et al. 2006b; Sawyer 2005; Fuller & Qian 2006; Fogli et al. 2007; Duan et al. 2007; Raffelt & Sigl 2007; Esteban-Pretel et al. 2007, 2008; Chakraborty et al. 2008; Duan et al. 2008a,b; Dasgupta et al. 2008a; Dasgupta & Dighe 2008; Sawyer 2009; Duan et al. 2010; Wu & Qian 2011).

As we discussed in Sec. 2, in our physical system of interest neutrinos are mainly created by electron-positron pair annihilation and so the number of neutrinos is equal to the number of antineutrinos. Such a fact creates an interesting and unique physical situation, different from, for example, SN neutrinos for which traditional models predict a predominance of electron neutrinos mainly due to the deleptonization caused by the URCA process (see, e.g., Esteban-Pretel et al. 2007).

The neutrino self-interaction potential decays with the radial distance from the neutron star faster than the matter potential. This is a direct consequence of the usual $1/r^2$ flux dilution and the collinearity effects due to the neutrino velocity dependence of the potential. Consequently, we identify three different regions along the neutrino trajectory in which the oscillations are dominated by intrinsically different neutrino phenomenology. Fig. 3 illustrates the typical situation of the physical system we are analyzing. Just after the neutrino creation in the regions of the accretion zone very close to the surface of the NS, neutrinos undergo kinematic decoherence along the same length scale of a single cycle of the so-called bipolar oscillations. Bipolar oscillations imply very fast flavor conversion between neutrino pairs $\nu_e\bar{\nu}_e \leftrightarrow \nu_\mu\bar{\nu}_\mu \leftrightarrow \nu_\tau\bar{\nu}_\tau$ and, amazingly, the oscillation length in this region can be so small as of the order tens of meters. Note that kinematic decoherence is just the averaging over flavor neutrino states process resulting from quick flavor conversion which oscillation length depends on the neutrino energy. It does not imply quantum decoherence and, thus, neutrinos are yet able to quantum oscillate if appropriate conditions are satisfied. In fact, as it can be observed from Figs. 4 and 5 below, bipolar oscillations preserve the characteristic oscillation pattern, differently from quantum decoherence which would lead to a monotonous dumping figure.

Kinematic decoherence is relevant when three conditions are met: (i) The self-interaction potential dominates over the vacuum potential. (ii) The matter potential does not fulfill the MSW condition. (iii) There is a low asymmetry between the neutrino and antineutrino fluxes. We will see that our system satisfies all three conditions.

As the self-interaction potential becomes small and the matter potential becomes important, oscillations are suppressed and we do not expect significant changes in the neutrino flavor content along this region. This situation changes radically when the matter potential is so small that it is comparable with neutrino vacuum frequencies $\Delta m^2/2p$, where Δm^2 is the neutrino squared mass difference and p is the norm of the neutrino momentum $\mathbf{p}$. In this region, the neutrino self-interaction potential is negligible and the usual MSW resonances can occur. Therefore, we can expect a change in the neutrino spectrum.

We dedicate this section to a detailed derivation of the equations of motion (EoM) of flavor evolution. In later sections, we will analyze the neutrino oscillation phenomenology to build the neutrino emission spectrum from a binary hyper-accretion system.

3.1. *Equations of motion*

The equations of motion (EoM) that govern the evolution of an ensemble of mixed neutrinos are the quantum Liouville equations

$$i\dot{\rho}_{\mathbf{p}} = [H_{\mathbf{p}}, \rho_{\mathbf{p}}] \tag{23a}$$
$$i\dot{\bar{\rho}}_{\mathbf{p}} = [\bar{H}_{\mathbf{p}}, \bar{\rho}_{\mathbf{p}}] \tag{23b}$$

where we have adopted the natural units $c = \hbar = 1$. In these equations $\rho_{\mathbf{p}}$ ($\bar{\rho}_{\mathbf{p}}$) is the matrix of occupation numbers $(\rho_{\mathbf{p}})_{ij} = \langle a_j^\dagger a_i \rangle_{\mathbf{p}}$ for neutrinos ($(\bar{\rho}_{\mathbf{p}})_{ij} = \langle \bar{a}_i^\dagger \bar{a}_j \rangle_{\mathbf{p}}$ for antineutrinos), for each momentum $\mathbf{p}$ and flavors i, j. The diagonal elements are the distribution functions $f_{\nu_i(\bar{\nu}_i)}(\mathbf{p})$ such that their integration over the momentum space gives the neutrino number density n_{ν_i} of a determined flavor i. The off-diagonal elements provide information about the *overlapping* between the two neutrino flavors.

Taking into account the current-current nature of the weak interaction in the standard model, the Hamiltonian for each equation is (Dolgov 1981; Sigl & Raffelt 1993; Hannestad et al. 2006)

$$H_{\mathbf{p}} = \Omega_{\mathbf{p}} + \sqrt{2}G_F \int \left(l_{\mathbf{q}} - \bar{l}_{\mathbf{q}}\right)\left(1 - \mathbf{v}_{\mathbf{q}} \cdot \mathbf{v}_{\mathbf{p}}\right) \frac{d^3\mathbf{q}}{(2\pi)^3} + \sqrt{2}G_F \int \left(\rho_{\mathbf{q}} - \bar{\rho}_{\mathbf{q}}\right)\left(1 - \mathbf{v}_{\mathbf{q}} \cdot \mathbf{v}_{\mathbf{p}}\right) \frac{d^3\mathbf{q}}{(2\pi)^3} \tag{24a}$$
$$\bar{H}_{\mathbf{p}} = -\Omega_{\mathbf{p}} + \sqrt{2}G_F \int \left(l_{\mathbf{q}} - \bar{l}_{\mathbf{q}}\right)\left(1 - \mathbf{v}_{\mathbf{q}} \cdot \mathbf{v}_{\mathbf{p}}\right) \frac{d^3\mathbf{q}}{(2\pi)^3} + \sqrt{2}G_F \int \left(\rho_{\mathbf{q}} - \bar{\rho}_{\mathbf{q}}\right)\left(1 - \mathbf{v}_{\mathbf{q}} \cdot \mathbf{v}_{\mathbf{p}}\right) \frac{d^3\mathbf{q}}{(2\pi)^3} \tag{24b}$$

$\Delta m_{21}^2 = 7.37\,(6.93 - 7.97) \times 10^{-5}$ eV^2
$\lvert\Delta m^2\rvert = 2.50\,(2.37 - 2.63) \times 10^{-3}$ eV^2 Normal Hierarchy
$\lvert\Delta m^2\rvert = 2.46\,(2.33 - 2.60) \times 10^{-3}$ eV^2 Inverted Hierarchy
$\sin^2\theta_{12} = 0.297\,(0.250 - 0.354)$
$\sin^2\theta_{23}(\Delta m^2 > 0) = 0.437\,(0.379 - 0.616)$
$\sin^2\theta_{23}(\Delta m^2 < 0) = 0.569\,(0.383 - 0.637)$
$\sin^2\theta_{13}(\Delta m^2 > 0) = 0.0214\,(0.0185 - 0.0246)$
$\sin^2\theta_{13}(\Delta m^2 < 0) = 0.0218\,(0.0186 - 0.0248)$

TABLE 2
Mixing and squared mass differences as they appear in Patrignani et al. (2016). Error values in parenthesis are shown in 3σ interval. The squared mass difference is defined as $\Delta m^2 = m_3^2 - \left(m_2^2 + m_1^2\right)/2$.

where $\Omega_{\mathbf{p}}$ is the matrix of vacuum oscillation frequencies, $l_{\mathbf{p}}$ and $\bar{l}_{\mathbf{p}}$ are matrices of occupation numbers for charged leptons built in a similar way to the neutrino matrices, and $\mathbf{v}_{\mathbf{p}} = \mathbf{p}/p$ is the velocity of a particle with momentum $\mathbf{p}$ (either neutrino or charged lepton).

As in Sec. 2 we will only consider two neutrino flavors: e and $x = \mu + \tau$. Three-flavor oscillations can be approximated to two-flavor oscillations as a result of the strong hierarchy of the squared mass differences $|\Delta m_{13}^2| \approx |\Delta m_{23}^2| \gg |\Delta m_{12}^2|$ (see Table 2). In this case, only the smallest mixing angle θ_{13} is considered. We will drop the suffix for the rest of the discussion. Consequently, the relevant oscillations are $\nu_e \rightleftharpoons \nu_x$ and $\bar{\nu}_e \rightleftharpoons \bar{\nu}_x$, and each term in the Hamiltonian governing oscillations becomes a 2×2 Hermitian matrix.

Let us first present the relevant equations for neutrinos. Due to the similarity between $H_{\mathbf{p}}$ and $\bar{H}_{\mathbf{p}}$, the corresponding equations for antineutrinos can be obtained in an analogous manner. In the two-flavor approximation, ρ in Eq. (23) can be written in terms of Pauli matrices and the polarization vector $\mathsf{P}_{\mathbf{p}}$ as:

$$\rho_{\mathbf{p}} = \begin{pmatrix} \rho_{ee} & \rho_{ex} \\ \rho_{xe} & \rho_{xx} \end{pmatrix}_{\mathbf{p}} = \frac{1}{2}\left(f_{\mathbf{p}}\mathbb{1} + \mathsf{P}_{\mathbf{p}} \cdot \vec{\sigma}\right), \tag{25}$$

where $f_{\mathbf{p}} = \mathrm{Tr}[\rho_{\mathbf{p}}] = f_{\nu_e}(\mathbf{p}) + f_{\nu_x}(\mathbf{p})$ is the sum of the distribution functions for ν_e and ν_x. Note that the z component of the polarization vector obeys

$$\mathsf{P}_{\mathbf{p}}^z = f_{\nu_e}(\mathbf{p}) - f_{\nu_x}(\mathbf{p}). \tag{26}$$

Hence, this component tracks the fractional flavor composition of the system and appropriately normalizing $\rho_{\mathbf{p}}$ allows to define a survival and mixing probability

$$P_{\nu_e \leftrightarrow \nu_e} = \frac{1}{2}\left(1 + \mathsf{P}_{\mathbf{p}}^z\right), \tag{27a}$$
$$P_{\nu_e \leftrightarrow \nu_x} = \frac{1}{2}\left(1 - \mathsf{P}_{\mathbf{p}}^z\right). \tag{27b}$$

On the other hand, the Hamiltonian can be written as a sum of three interaction terms:

$$\mathsf{H} = \mathsf{H}_{\text{vacuum}} + \mathsf{H}_{\text{matter}} + \mathsf{H}_{\nu\nu}. \tag{28}$$

where H is the two-flavor Hamiltonian. The first term is the Hamiltonian in vacuum (Qian & Fuller 1995):

$$\mathsf{H}_{\text{vacuum}} = \frac{\omega_{\mathbf{p}}}{2}\begin{pmatrix} -\cos 2\theta & \sin 2\theta \\ \sin 2\theta & \cos 2\theta \end{pmatrix} = \frac{\omega_{\mathbf{p}}}{2}\vec{B} \cdot \vec{\sigma} \tag{29}$$

where $\omega_{\mathbf{p}} = \Delta m^2/2p$, $\vec{B} = (\sin 2\theta, 0, -\cos 2\theta)$ and θ is the smallest neutrino mixing angle in vacuum.

The other two terms in Eqs. (24) are special since they make the evolution equations non-linear. Even though they are very similar, we are considering that the electrons during the accretion form an isotropic gas; hence, the vector $\mathbf{v}_{\mathbf{q}}$ in the first integral is distributed uniformly on the unit sphere and the factor $\mathbf{v}_{\mathbf{q}} \cdot \mathbf{v}_{\mathbf{p}}$ averages to zero. After integrating the matter Hamiltonian is given by:

$$\mathsf{H}_{\text{matter}} = \frac{\lambda}{2}\begin{pmatrix} 1 & 0 \\ 0 & -1 \end{pmatrix} = \frac{\lambda}{2}\vec{L} \cdot \vec{\sigma} \tag{30}$$

where $\lambda = \sqrt{2}G_F\,(n_{e^-} - n_{e^+})$ is the charged current matter potential and $\vec{L} = (0, 0, 1)$.

Such simplification cannot be made with the final term. Since neutrinos are responsible for the energy loss of the infalling material during accretion, they must be escaping the accretion zone and the net neutrino and antineutrino flux is non-zero.In this case the factor $\mathbf{v_q}\cdot\mathbf{v_p}$ cannot be averaged to zero. At any rate, we can still use Eq. (25) and obtain (Pantaleone 1992; Zhu et al. 2016; Malkus et al. 2016):

$$\mathsf{H}_{\nu\nu} = \sqrt{2}G_F\left[\int\left(1 - \mathbf{v_q}\cdot\mathbf{v_p}\right)\left(\mathsf{P_q} - \bar{\mathsf{P}}_\mathbf{q}\right)\frac{d^3\mathbf{q}}{(2\pi)^3}\right]\cdot\vec{\sigma} \tag{31}$$

Introducing every Hamiltonian term in Eqs. (23), and using the commutation relations of the Pauli matrices, we find the EoM for neutrinos and antineutrinos for each momentum mode $\mathbf{p}$:

$$\dot{\mathsf{P}}_\mathbf{p} = \left[\omega_\mathbf{p}\vec{B} + \lambda\vec{L} + \sqrt{2}G_F\int\left(1 - \mathbf{v_q}\cdot\mathbf{v_p}\right)\left(\mathsf{P_q} - \bar{\mathsf{P}}_\mathbf{q}\right)\frac{d^3\mathbf{q}}{(2\pi)^3}\right]\times\mathsf{P_p} \tag{32a}$$

$$\dot{\bar{\mathsf{P}}}_\mathbf{p} = \left[-\omega_\mathbf{p}\vec{B} + \lambda\vec{L} + \sqrt{2}G_F\int\left(1 - \mathbf{v_q}\cdot\mathbf{v_p}\right)\left(\mathsf{P_q} - \bar{\mathsf{P}}_\mathbf{q}\right)\frac{d^3\mathbf{q}}{(2\pi)^3}\right]\times\bar{\mathsf{P}}_\mathbf{p}. \tag{32b}$$

Solving the above equations would yield the polarization vectors as a function of time. However, in our specific physical system, both the matter potential λ and the neutrino potential vary with the radial distance from the NS surface as well as the instant t of the physical process which can be characterized by the accretion rate $\dot{M}$. As we will see later, the time dependence can be ignored. This means that Eqs. (32) must be written in a way that makes explicit the spatial dependence, i.e. in terms of the vector $\mathbf{r}$. For an isotropic and homogeneous neutrino gas or a collimated ray of neutrinos the expression $dt = dr$ would be good enough, but for radiating extended sources the situation is more complicated. In Eqs. (23) we must replace the matrices of occupation numbers by the space dependent Wigner functions $\rho_{\mathbf{p},\mathbf{r}}$ (and $\bar{\rho}_{\mathbf{p},\mathbf{r}}$) and the total time derivative by the Liouville operator (Cardall 2008; Strack & Burrows 2005)

$$\dot{\rho}_{\mathbf{p},\mathbf{r}} = \frac{\partial\rho_{\mathbf{p},\mathbf{r}}}{\partial t} + \mathbf{v_p}\cdot\nabla_\mathbf{r}\,\rho_{\mathbf{p},\mathbf{r}} + \dot{\mathbf{p}}\cdot\nabla_\mathbf{p}\,\rho_{\mathbf{p},\mathbf{r}} \tag{33}$$

We will ignore the third term of the Liouville operator since we won't consider the gravitational deflection of neutrinos. For peak accretion rates $\dot{M} \approx 10^{-8}$–$10^{-2}\ M_\odot$/s the characteristic accretion time is $\Delta t_{acc} = M/\dot{M} \approx M_\odot/\dot{M} \approx 10^8$–$10^2$ s. The distances traveled by a neutrino in these times are $r \approx 3\times10^{12}$–3×10^{18} cm. These distances are much larger than the typical binary separation a. As a consequence, we can consider the neutrino evolution to be a stationary process. This fact allows us to neglect the first term in Eq. (33). Putting together these results, the EoM become:

$$i\mathbf{v_p}\cdot\nabla_\mathbf{r}\,\rho_{\mathbf{p},\mathbf{r}} = [H_{\mathbf{p},\mathbf{r}}, \rho_{\mathbf{p},\mathbf{r}}] \tag{34a}$$

$$i\mathbf{v_p}\cdot\nabla_\mathbf{r}\,\bar{\rho}_{\mathbf{p},\mathbf{r}} = [\bar{H}_{\mathbf{p},\mathbf{r}}, \bar{\rho}_{\mathbf{p},\mathbf{r}}], \tag{34b}$$

where $H_{\mathbf{p},\mathbf{r}}$ and $\bar{H}_{\mathbf{p},\mathbf{r}}$ are the same as (24) but the matrices of densities (as well as the polarization vectors) depend on the position $\mathbf{r}$. Note, however, that the electrons in the accretion zone still form an isotropic gas and Eq. (30) is still valid and the matter Hamiltonian depends on $\mathbf{r}$ through $n_{e^-}(\mathbf{r}) - n_{e^+}(\mathbf{r})$. The first two terms in the Hamiltonian remain virtually unchanged. On the other hand, projecting the EoM onto the radial distance from the NS and using the axial symmetry of the system, the integral in the neutrino-neutrino interaction term can be written as

$$\frac{\sqrt{2}G_F}{(2\pi)^2}\int\left(1 - v_{\vartheta'_r}v_{\vartheta_r}\right)\left(\rho_{q,\vartheta',r} - \bar{\rho}_{q,\vartheta',r}\right)q^2dq|d\cos\vartheta'_r|. \tag{35}$$

Since the farther from the NS the interacting neutrinos approach a perfect collinearity, the projected velocities v_{ϑ_r} become decreasing functions of the position. In this particular geometry the diagonal elements of the matrix of densities are written as a product of independent distributions over each variable p, ϑ, ϕ, where the ϕ dependence has been integrated out. The one over p is the normalized Fermi-Dirac distribution and the one over ϑ is assumed uniform due to symmetry. The r dependence is obtained through the geometrical flux dilution. Knowing this, the diagonal elements of matrices of densities at the NS surface are

$$\left(\rho_{\mathbf{p},\mathbf{R}_{\rm NS}}\right)_{ee} = \left(\bar{\rho}_{\mathbf{p},\mathbf{R}_{\rm NS}}\right)_{ee} = f_{\nu_e}(\mathbf{p}) \tag{36a}$$

$$\left(\rho_{\mathbf{p},\mathbf{R}_{\rm NS}}\right)_{xx} = \left(\bar{\rho}_{\mathbf{p},\mathbf{R}_{\rm NS}}\right)_{xx} = f_{\nu_x}(\mathbf{p}) \tag{36b}$$

where the functions f_{ν_i} are given by Eqs. (21).

3.2. *Single-angle approximations*

The integro-differential Eqs. (32) and (34) are usually numerically solved for the momentum $\mathbf{p}$ and the scalar $\mathbf{v_q}\cdot\mathbf{v_p}$. Such simulation are quite time-consuming and the result is frequently too complicated to allow for a clear interpretation of the underlying physics. For this reason, the analytic approximation called the *single-angle limit* is made. Such approximation consists in *imposing* a self-maintained coherence in the neutrino system, i.e. it is assumed that the flavor evolution of all neutrinos emitted from an extended source is the same as the flavor evolution of the neutrinos emitted from the source along a particular path. Under this premise, the propagation angle between the test neutrino and the background neutrinos is fixed. In expression (35) this is equivalent to dropping the ϑ' dependence of ρ and replacing the projected velocity v_{ϑ_r} either by an appropriate average at each r (as in Dasgupta & Dighe 2008) or by a representative angle (usually 0 or $\pi/4$). We will follow the former approach and apply the *bulb model* described in Duan et al. (2006a). Within this model it is shown that the projected velocity at a distance r from the neutrino emission zone is

$$v_r = \sqrt{1 - \left(\frac{R_{\rm NS}}{r}\right)^2\left(1 - v_{R_{\rm NS}}^2\right)}. \tag{37}$$

where $v_{R_{\rm NS}}$ is the projected velocity at the NS surface. By redefining the matrices of density with a change of variable $u = 1 - v_{R_{\rm NS}}^2$ in the integral (35)

$$\rho_{p,u,r}\frac{p^2}{2\,(2\pi)^2} \to \rho_{p,u,r}, \tag{38}$$

and using Eq. (25), we can write the full equations of motion

$$\frac{\partial}{\partial r}\mathsf{P}_{p,r} = \left[\omega_{p,r}\vec{B} + \lambda_r\vec{L} + \mu_r\int_0^\infty \left(\mathsf{P}_{q,r} - \bar{\mathsf{P}}_{q,r}\right) dq\right] \times \mathsf{P}_{p,r} \quad (39a)$$

$$\frac{\partial}{\partial r}\bar{\mathsf{P}}_{p,r} = \left[-\omega_{p,r}\vec{B} + \lambda_r\vec{L} + \mu_r\int_0^\infty \left(\mathsf{P}_{q,r} - \bar{\mathsf{P}}_{q,r}\right) dq\right] \times \bar{\mathsf{P}}_{p,r} \quad (39b)$$

where we have replaced v_r by it's average value

$$\langle v_r \rangle = \frac{1}{2}\left[1 + \sqrt{1 - \left(\frac{R_{\rm NS}}{r}\right)^2}\right]. \quad (40)$$

All the interaction potentials now depend on r and each effective potential strength is parametrized as follows (Dasgupta & Dighe 2008)

$$\omega_{p,r} = \frac{\Delta m^2}{2p\langle v_r \rangle}, \quad (41)$$

$$\lambda_r = \sqrt{2}G_F\left(n_{e^-}(r) - n_{e^+}(r)\right)\frac{1}{\langle v_r \rangle}, \quad (42)$$

$$\mu_r = \frac{\sqrt{2}G_F}{2}\left(\sum_{i\in\{e,x\}} n^C_{\nu_i\bar{\nu}_i}\right)\left(\frac{R_{\rm NS}}{r}\right)^2\left(\frac{1-\langle v_r\rangle^2}{\langle v_r \rangle}\right). \quad (43)$$

It is worth mentioning that all the effective potential strengths are affected by the geometry of the extended source through the projected velocity on the right side of Eqs. (34). For the neutrino-neutrino interaction potential, we have chosen the total neutrino number density as parametrization. This factor comes from the freedom to re-normalize the polarization vectors in the EoM. A different choice has been made in Esteban-Pretel et al. (2007). Of the other two r dependent factors, one comes from the geometrical flux dilution and the other accounts for collinearity in the single-angle approximation. Over all μ_r decays as $1/r^4$.

In Fig. 3 the behavior of the effective potentials within the single-angle formalism is shown for $\dot{M} = 10^{-2}M_\odot$ s^{-1}, $10^{-4}M_\odot$ s^{-1}, $10^{-6}M_\odot$ s^{-1} and $10^{-8}M_\odot$ s^{-1}. In all cases, the neutrino energy is the corresponding average reported in Table 1. Since the oscillatory dynamics of the neutrino flavors are determined by the value of the potentials, and the value of the potentials depends on the data in Table 1, it is important to establish how sensible is this information to the model we have adopted. In particular, to the pre-SN envelope density profile index m. The reported accretion rates can be seen as different states in the evolution of a binary system or as peak accretion rates of different binary systems. For a given accretion rate, the temperature and density conditions on the neutron star surface are fixed. This, in turn, fixes the potentials involved in the equations of flavor evolution and the initial neutrino and antineutrino flavor content. To see the consequences of changing the index m we can estimate the peak accretion rates for new values using Eqs. (2). Since we are only interested in type Ic supernovae, we shall restrict these values to the ones reported in Table 1 of Becerra et al. (2016) (that is $m = 2.771$, 2.946 and 2.801), and in each case, we consider the smallest binary separation such that there is no Roche-Lobe overflow. For these parameters, we find peak accretion rates $\dot{M}_{\rm peak} \sim 10^{-2}$–$10^{-4}M_\odot$ s^{-1} with peak times at $t_{\rm peak} \approx 7$–35 min. Because these accretion rates are still within the range in Table 1, the results contained in Sec. 4 apply also to these cases with different value of the m-index.

The profiles for the electron and positron number densities were adopted from the simulations presented in Becerra et al. (2016). Due to the dynamics of the infalling matter, close to the NS, the behavior of $n_{e^-}(r) - n_{e^+}(r)$ is similar to μ_r. At the shock radius, the electron density's derivative presents a discontinuity and its behavior changes allowing for three distinct regions inside the Bondi-Hoyle radius. The matter potential is always higher than the neutrino potential yet, in most cases, both are higher than the vacuum potential, so we expect neutrino collective effects (neutrino oscillations) and MSW resonances to play a role in the neutrino flavor evolution inside the Bondi-Hoyle radius. Outside the capture region, as long as the neutrinos are not directed towards the SN, they will be subjected to vacuum oscillations.

4. SINGLE-ANGLE SOLUTIONS AND MULTI-ANGLE EFFECTS

The full dynamics of neutrino oscillations is a rather complex interplay between the three potentials discussed in Sec. 3, yet the neutrino-antineutrino symmetry allows us to generalize our single-angle calculations for certain accretion rates using some numerical and algebraic results obtained in Hannestad et al. (2006); Fogli et al. (2007); Esteban-Pretel et al. (2007) and references therein. Specifically, we know that if $\mu_r \gg \omega_r$, as long as the MSW condition $\lambda_r \simeq \omega_r$ is not met, collective effects should dominate the neutrino evolution even if $\lambda_r \gg \mu_r$. On the other hand, if $\mu_r \lesssim \omega_r$, the neutrino evolution is driven by the relative values between the matter and vacuum potentials. With this in mind, we identify two different ranges of values for the accretion rate: $\dot{M} \gtrsim 5\times10^{-5}M_\odot$ s^{-1} and $\dot{M} \lesssim 5\times10^{-5}M_\odot$ s^{-1}.

4.1. *High accretion rates*

For accretion rates $\dot{M} \gtrsim 5\times10^{-5}M_\odot$ s^{-1} the potentials obey the following hierarchy

$$\lambda_r \gtrsim \mu_r \gg \omega_r, \quad (44)$$

hence, we expect strong effects of neutrino self-interactions. In order to appreciate the interesting physical processes which happen with the neutrinos along their trajectory in the accretion zone, we begin this analysis with a simplified approach to the EoM for a monochromatic spectrum with the same energy for both neutrinos and antineutrinos. Let us introduce the following definitions

$$\vec{D} = \mathsf{P}_r - \bar{\mathsf{P}}_r \quad (45)$$

$$\vec{Q} = \mathsf{P}_r + \bar{\mathsf{P}}_r - \frac{\omega_r}{\mu_r}\vec{B}. \quad (46)$$

The role of the matter potential is to logarithmically extend the period of the bipolar oscillations so we can ignore it for now. Also, we will restrict our analysis to a small enough region at $R_{\rm NS} + \Delta r_\nu$ so that we can consider $\frac{d}{dr}(\omega_r/\mu_r) \approx 0$ (adiabatic approximation). Then, By summing and subtracting Eqs. (39) and using definitions (45) and (46), we obtain

$$\frac{d}{dr}\vec{Q} = \mu\vec{D} \times \vec{Q} \quad (47)$$

$$\frac{d}{dr}\vec{D} = \omega\vec{B} \times \vec{Q}. \quad (48)$$

We are now able to build a very useful analogy. The equations above are analogous to the EoM of a simple mechanical pendulum with a vector position given by $\vec{Q}$, precessing

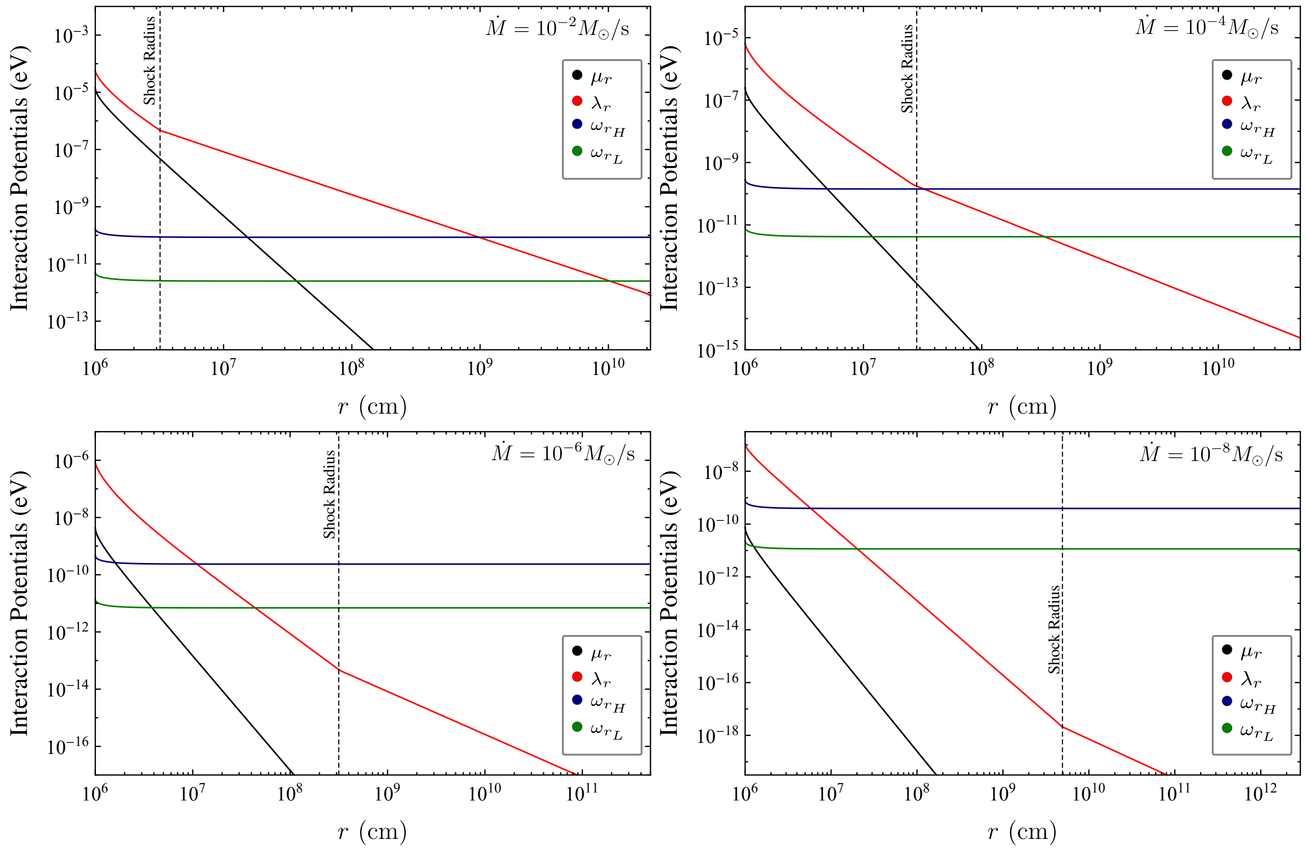

FIG. 3.— Interaction potentials as functions of the radial distance from the NS center for selected accretion rates $\dot{M}$ (see Table 1). Each plot runs from the NS surface to the Bondi-Hoyle surface. μ_r stands for the self-interaction neutrino potential, λ_r is the matter potential and ω_H and ω_L are the higher and lower resonances corresponding to the atmospheric and solar neutrino scales, respectively, defined in Eq. (59). Outside the Bondi-Hoyle region the neutrino and electron densities depend on the direction of their path relative to the SN and the particular ejecta density profile.

around an angular momentum $\vec{D}$, subjected to a force $\omega\mu\vec{B}$ with a moment of inertia proportional to the inverse of μ. With Eqs. (17) and (26) the initial conditions for the polarization vectors are

$$\mathsf{P}(R_{\rm NS}) = \bar{\mathsf{P}}(R_{\rm NS}) = (0, 0, 0.4) \qquad (49)$$

We can easily show that $|\vec{Q}(R_{\rm NS})| = |\mathsf{P}(R_{\rm NS}) + \bar{\mathsf{P}}(R_{\rm NS})| + O(\omega/\mu) \approx 0.8$. Calculating $\frac{d}{dr}(\vec{Q}\cdot\vec{Q})$ it can be checked that this value is conserved.

The analogous angular momentum is $\vec{D}(R_{\rm NS}) = \mathsf{P}(R_{\rm NS}) - \bar{\mathsf{P}}(R_{\rm NS}) = 0$. Thus, the pendulum moves initially in a plane defined by $\vec{B}$ and the z-axis, i.e., the plane xz. Then, it is possible to define an angle φ between $\vec{Q}$ and the z-axis such that

$$\vec{Q} = |\vec{Q}|\,(\sin\varphi, 0, \cos\varphi)\,. \qquad (50)$$

Note that the only non-zero component of $\vec{D}$ is y-component and from (47) and (48) we find

$$\frac{d\varphi}{dr} = \mu|\vec{D}| \qquad (51)$$

and

$$\frac{d|\vec{D}|}{dr} = -\omega|\vec{Q}|\cos(2\theta+\varphi). \qquad (52)$$

The above equations can be equivalently written as

$$\frac{d^2\varphi}{dr^2} = -k^2\sin(2\theta+\varphi), \qquad (53)$$

where we have introduced the inverse characteristic distance k by

$$k^2 = \omega\mu|\vec{Q}|, \qquad (54)$$

which is related to the anharmonic oscillations described by the non-linear EoM (51) and (52). The logarithmic correction to the oscillation length due to matter effects is (Hannestad et al. 2006)

$$\tau_{\dot{M}} = -k^{-1}\ln\left[\left(\frac{\pi}{2}-\theta\right)\frac{k}{(k^2+\lambda^2)^{1/2}}\left(1+\frac{\omega}{|\vec{Q}|\mu}\right)\right]. \qquad (55)$$

The initial conditions (49) imply

$$\varphi\,(R_{\rm NS}) = \arcsin\left(\frac{\omega}{|\vec{Q}|\mu}\sin 2\theta\right). \qquad (56)$$

To investigate the physical meaning of the above equation, let us assume for a moment that 2θ is a small angle. In this case $\varphi\,(R_{\rm NS})$ is also a small angle. If $k^2 > 0$, which is true for the normal hierarchy $\Delta m^2 > 0$, we expect small oscillations around the initial position since the system begins in a stable position of the potential associated with Eqs. (51) and (52). No strong flavor oscillations are expected. On the contrary, for the inverted hierarchy $\Delta m^2 < 0$, $k^2 < 0$ and the initial $\varphi(R_{\rm NS})$ indicates that the system begins in an unstable position and we expect very large anharmonic oscillations. P^z (as well as $\bar{\mathsf{P}}^z$) oscillates between two different maxima passing through a minimum $-\mathsf{P}^z$ $(-\bar{\mathsf{P}}^z)$ several times. This behavior

Inverted Hierarchy

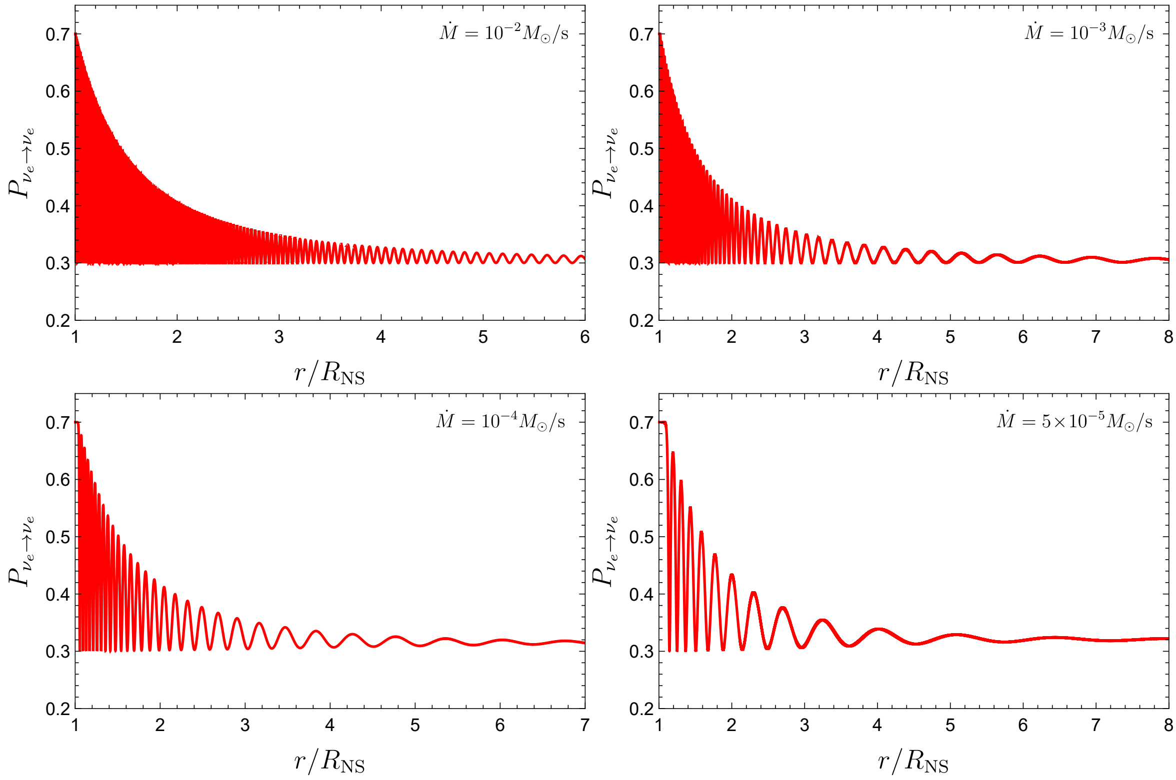

FIG. 4.— Neutrino flavor evolution for inverted hierarchy. Electron neutrino survival probability is shown as a function of the radial distance from the NS surface. The curves for the electron antineutrino match the ones for electron neutrinos.

implies total flavor conversion: all electronic neutrinos (antineutrinos) are converted into non-electronic neutrinos (antineutrinos) and vice-versa. This has been called bipolar oscillations in the literature (Duan et al. 2010).

We solved numerically Eqs. (39) for both normal and inverted hierarchies using a monochromatic spectrum dominated by the average neutrino energy for $\dot{M} = 10^{-2}, 10^{-3}, 10^{-4}$ and $5{\times}10^{-5} M_\odot\ \mathrm{s}^{-1}$, and the respective values reported in Table 1 with the initial conditions given by Eqs. (17) and (36). The behavior of the electronic neutrino survival probability inside the accretion zone is shown in Figs. 4 and 5 for inverted hierarchy and normal hierarchy, respectively. For the inverted hierarchy, there is no difference between the neutrino and antineutrino survival probabilities. This should be expected since for these values of r the matter and self-interaction potentials are much larger than the vacuum potential, and there is virtually no difference between Eqs. (39). Also, note that the antineutrino flavor proportions discussed in Sec. 2.3 remain virtually unchanged for normal hierarchy while the neutrino flavor proportions change drastically around the point $\lambda_r \sim \omega_r$. The characteristic oscillation length of the survival probability found on these plots is

$$\tau \approx (0.05 - 1)\ \mathrm{km} \tag{57}$$

which agree with the ones given by Eq. (55) calculated at the NS surface up to a factor of order one. Such a small value of τ suggests extremely quick $\nu_e\bar{\nu}_e \leftrightarrow \nu_x\bar{\nu}_x$ oscillations.

Clearly, the full EoM are highly nonlinear so the solution may not reflect the real neutrino flavor evolution. Concerning the single-angle approximation, it is discussed in Hannestad et al. (2006); Raffelt & Sigl (2007); Fogli et al. (2007) that in the more realistic multi-angle approach, kinematic decoherence happens. And in Esteban-Pretel et al. (2007) the conditions for decoherence as a function of the neutrino flavor asymmetry have been discussed. It is concluded that if the symmetry of neutrinos and antineutrinos is broken beyond the limit of $O(25\%)$, i.e., if the difference between emitted neutrinos and antineutrinos is roughly larger than 25% of the total number of neutrinos in the medium, decoherence becomes a sub-dominant effect.

As a direct consequence of the peculiar symmetric situation we are dealing with, in which neutrinos and antineutrinos are produced in similar numbers, bipolar oscillations happen and, as we have already discussed, they present very small oscillation length as shown in Eq. (57). Note also that the bipolar oscillation length depends on the neutrino energy. Therefore, the resulting process is equivalent to an averaging over the neutrino energy spectrum and an equipartition among different neutrino flavors is expected Raffelt & Sigl (2007). Although, for simplicity, we are dealing with the two neutrino hypothesis, this behavior is easily extended to the more realistic three neutrino situation. We assume, therefore, that at few kilometers from the emission region neutrino flavor equipartition is a reality:

$$\nu_e : \nu_\mu : \nu_\tau = 1 : 1 : 1. \tag{58}$$

Note that the multi-angle approach keeps the order of the characteristic length τ of Eq. (55) unchanged and kinematics decoherence happens within a few oscillation cycles (Sawyer 2005; Hannestad et al. 2006; Raffelt & Sigl 2007). Therefore, we expect that neutrinos created in regions close to the emission zone will be equally distributed among different fla-

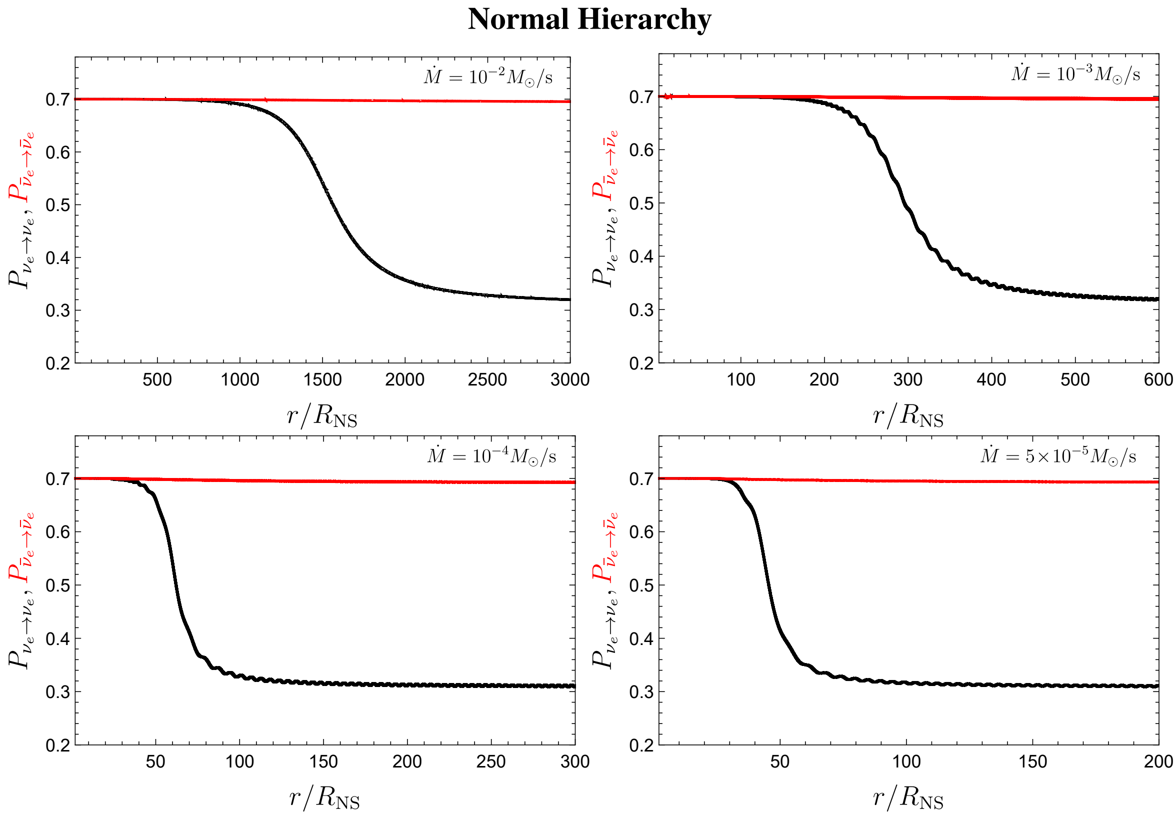

FIG. 5.— Electron neutrino and antineutrino flavor evolution for normal hierarchy.The survival probability is shown as a function of the radial distance from the NS surface.

vors in less than few kilometers after their creation. Once the neutrinos reach this maximally mixed state, no further changes are expected up until the matter potential enters the MSW resonance region. We emphasize that kinematics decoherence does not mean quantum decoherence. Figs. 4 and 5 clearly show the typical oscillation pattern which happens only if quantum coherence is still acting on the neutrino system. Differently from quantum decoherence, which would reveals itself by a monotonous dumping in the oscillation pattern, kinematics decoherence is just the result of averaging over the neutrino energy spectrum resulting from quick flavor conversion which oscillation length depends on the neutrino energy. Therefore, neutrinos are yet able to quantum oscillate if appropriate conditions are satisfied.

We discuss now the consequences of the matter potential.

4.1.1. *Matter Effects*

After leaving the emisison region, beyond $r \approx R_{\rm NS} + \Delta r_\nu$, where Δr_ν is the width defined in Eq. (6), the effective neutrino density quickly falls in a asymptotic behavior $\mu_r \approx 1/r^4$. The decay of λ_r is slower. Hence, very soon the neutrino flavor evolution is determined by the matter potential. Matter suppresses neutrino oscillations and we do not expect significant changes in the neutrino flavor content along a large region. Nevertheless, the matter potential can be so small that there will be a region along the neutrino trajectory in which it can be compared with the neutrino vacuum frequencies and the higher and lower resonant density conditions will be satisfied, i.e.:

$$\lambda(r_H) = \omega_H = \frac{\Delta m^2}{2\langle E_\nu\rangle} \quad \text{and} \quad \lambda(r_L) = \omega_L = \frac{\Delta m^2_{21}}{2\langle E_\nu\rangle}, \tag{59}$$

where Δm^2 and Δm^2_{21} are, respectively, the squared-mass differences found in atmospheric and solar neutrino observations. Table 2 shows the experimental values of mixing angles and mass-squared differences taken from Patrignani et al. (2016). The definition of Δm^2 used is: $\Delta m^2 = m_3^2 - (m_2^2 + m_1^2)/2$. Thus, $\Delta m^2 = \Delta m^2_{31} - \Delta m^2_{21}/2 > 0$, if $m_1 < m_2 < m_3$, and $\Delta m^2 = \Delta m^2_{32} + \Delta m^2_{21}/2 < 0$ for $m_3 < m_1 < m_2$. When the above resonance conditions are satisfied the MSW effects happen and the flavor content of the flux of electronic neutrinos and antineutrinos will be again modified. The final fluxes can be written as

$$F_{\nu_e}(E) = P_{\nu_e\to\nu_e}(E)F^0_{\nu_e}(E) + \left[1 - P_{\nu_e\to\nu_e}(E)\right]F^0_{\nu_x}(E) \tag{60a}$$
$$F_{\bar{\nu}_e}(E) = P_{\bar{\nu}_e\to\bar{\nu}_e}(E)F^0_{\bar{\nu}_e}(E) + \left[1 - P_{\bar{\nu}_e\to\bar{\nu}_e}(E)\right]F^0_{\bar{\nu}_x}(E) \tag{60b}$$

where $F^0_{\nu_e}(E)$, $F^0_{\nu_x}(E)$, $F^0_{\bar{\nu}_e}(E)$ and $F^0_{\bar{\nu}_x}(E)$ are the fluxes of electronic and non-electronic neutrinos and antineutrinos after the bipolar oscillations of the emission zone and $P_{\nu_e\to\nu_e}(E)$ and $P_{\bar{\nu}_e\to\bar{\nu}_e}(E)$ are the survival probability of electronic neutrinos and antineutrinos during the resonant regions.

In order to evaluate $F_{\nu_e}(E)$ and $F_{\bar{\nu}_e}(E)$ after matter effects, we have to estimate the survival probability at the resonant regions. There are several articles devoted to this issue; for instance we can adopt the result in Fogli et al. (2003), namely, for normal hierarchy

$$P_{\nu_e\to\nu_e}(E) = X \sin^2\theta_{12} \tag{61a}$$
$$P_{\bar{\nu}_e\to\bar{\nu}_e}(E) = \cos^2\theta_{12} \tag{61b}$$

and, for inverted hierarchy

$$P_{\nu_e\to\nu_e}(E) = \sin^2\theta_{12} \tag{62a}$$

$$P_{\bar{\nu}_e\to\bar{\nu}_e}(E) = X\cos^2\theta_{12} \tag{62b}$$

The factor X, the conversion probability between neutrino physical eigenstates, is given by Petcov (1987); Fogli et al. (2003); Kneller & McLaughlin (2006)

$$X = \frac{\exp(2r_{\rm res}k_{\rm res}\cos 2\theta_{13}) - 1}{\exp(2r_{\rm res}k_{\rm res}) - 1}, \tag{63}$$

where $r_{\rm res} = r_L$ or $r_{\rm res} = r_H$, defined according to Eq. (59) and

$$\frac{1}{k_{\rm res}} = \left|\frac{d\ln\lambda_r}{dx}\right|_{r=r_{\rm res}}. \tag{64}$$

The factor X is related to how fast physical environment features relevant for neutrino oscillations change, such as neutrino and matter densities.

For slow and adiabatic changes $X \to 0$ while for fast and non-adiabatic, $X \to 1$. In our specific cases, the MSW resonances occur very far from the accretion zone where the matter density varies very slow and therefore $X \to 0$, as can be explicitly calculated from Eq. (63). Consequently, it is straightforward to estimate the final fluxes of electronic and non-electronic neutrinos and antineutrinos.

4.2. *Low accretion rates*

For accretion rates $\dot{M} < 5\times10^{-5}M_\odot$ s^{-1}, either the matter potential is close enough to the vacuum potential and the MSW condition is satisfied, or both the self-interaction and matter potentials are so low that the flavor oscillations are only due to the vacuum potential. In both cases, bipolar oscillations are not present. In Fig. (6) we show the survival probability for $\dot{M} = 10^{-6}M_\odot$ s^{-1} as an example. We can see that neutrinos and antineutrinos follow different dynamics. In particular, for antineutrinos there are two decreases. The first one, around $r \approx (1\text{–}2)R_{\rm NS}$, is due to bipolar oscillations which are rapidly damped by the matter potential as discussed in Sec. 4.1.1. The second one happens around $r \approx (10\text{–}20)R_{\rm NS}$. It can be seen from the bottom left panel of Fig. 3 (that one for $\dot{M} = 10^{-6}M_\odot$ s^{-1}), that around $r \approx (1\text{–}2)\times10^7$ cm (or, equivalently, $r \approx (10\text{–}20)\,R_{\rm NS}$) the higher MSW resonance occurs ($\lambda_r \sim \omega_{r_H}$). For inverted hierarchy, such resonance will affect antineutrinos depleting its number, as can be seen from Eq. (60). Without bipolar oscillations, it is not possible to guarantee that decoherence will be complete and Eq. (58) is no longer valid. The only way to know the exact flavor proportions is to solve the full Eqs. (32).

5. NEUTRINO EMISSION SPECTRA

Using the the calculations of last section we can draw a comparison between the creation spectra of neutrinos and antineutrinos at the NS surface (F^c_ν, n^c_ν), initial spectra after kinematic decoherence (F^0_ν, n^0_ν) and emission spectra after the MSW resonances (F_ν, n_ν). Table 3 contains a summary of the flavor content inside the Bondi-Hoyle radius. With these fractions and Eqs. (21) it is possible to reproduce the spectrum for each flavor and for accretion rates $\dot{M} \geq 5\times10^{-5}M_\odot$ s^{-1}.

The specific cases for $\dot{M} = 10^{-2}M_\odot$ s^{-1} are shown in Fig. 7. In such figures, the left column corresponds to normal hierarchy and the right corresponds to inverted hierarchy. The first two rows show the number fluxes after each process studied. The last row shows the relative fluxes F_ν/F^C_ν between the creation and emission fluxes. For the sake of clarity, we have normalized the curves to the total neutrino number at the NS surface

$$n = 2\sum_{i\in\{e,x\}} n_{\nu_i}. \tag{65}$$

so that each one is a normalized Fermi-Dirac distribution multiplied by the appropriate flavor content fraction. To reproduce any other case, it is enough to use Eqs. (21) with the appropriate temperature.

At this point two comments have to be made about our results:

- As we mentioned before, the fractions in Table 3 were obtained by assuming a monochromatic spectrum and using the single-angle approximation. This would imply that the spectrum dependent phenomenon called the *spectral stepwise swap* of flavors is not present in our analysis even though it has been shown that it can also appear in multi-angle simulations (Fogli et al. 2007). Nevertheless, we know from our calculations in Sec. 2.3 that neutrinos and antineutrinos of all flavors are created with the exact same spectrum up to a multiplicative constant. Hence, following Raffelt & Smirnov (2007a,b), by solving the equation

$$\int_{E_c}^{\infty}(n_{\nu_e} - n_{\nu_x})\,dE = \int_0^{\infty}(n_{\bar{\nu}_e} - n_{\bar{\nu}_x})\,dE, \tag{66}$$

  we find that the critical (split) energy is $E_c = 0$. This means that the resulting spectrum should still be unimodal and the spectral swap in our system could be approximated by a multiplicative constant that is taken into account in the decoherence analysis of Sec. 4.

- The fluxes of electronic neutrinos and antineutrinos shown in these figures and in Eqs. (60) represent fluxes at different positions up to a geometrical $1/r^2$ factor, r being the distance from the NS radius. Also, since we are considering the fluxes before and after each oscillatory process, the values of r are restricted to $r = R_{\rm NS}$ for F^C_ν, $\tau_{\dot{M}} < r < r_H$ for F^0_ν, and $r > r_L$ for F_ν. To calculate the number flux at a detector, for example, much higher values of r have to be considered and it is necessary to study vacuum oscillations in more detail. Such calculations will be presented elsewhere.

From Fig. 7 one can observe that the dominance of electronic neutrinos and antineutrinos found at their creation at the bottom of the accretion zone is promptly erased by kinematic decoherence in such a way that the content of the neutrinos and antineutrinos entering the MSW resonant region is dominated by non-electronic flavors. After the adiabatic transitions provoked by MSW transitions, electronic neutrinos and antineutrinos dominate again the emission spectrum except for non-electronic antineutrinos in the normal hierarchy. Although no energy spectrum distortion is expected, the flavor content of neutrinos and antineutrinos produced near the NS surface escape to the outer space in completely different spectra when compared with the ones in which they were created, as shown in the last row of Fig. 7.

6. CONCLUDING REMARKS

We can now proceed to draw the conclusions and some astrophysical consequences of this work:

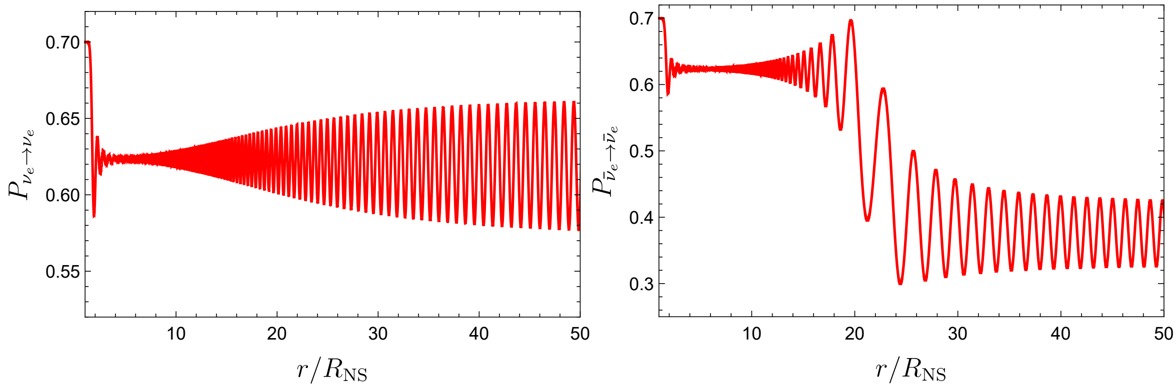

FIG. 6.— Electron neutrino and antineutrino flavor evolution for inverted hierarchy and $\dot{M} = 10^{-6} M_\odot$ s^{-1}. The survival probability is shown as a function of the radial distance from the NS surface.

	$n^0_{\nu_e}/n$	$n^0_{\bar\nu_e}/n$	$n^0_{\nu_x}/n$	$n^0_{\bar\nu_x}/n$	n_{ν_e}/n	$n_{\bar\nu_e}/n$	n_{ν_x}/n	$n_{\bar\nu_x}/n$
Normal Hierarchy	$\frac{1}{6}$	$\frac{1}{6}$	$\frac{1}{3}$	$\frac{1}{3}$	$\frac{1}{3}$	$\frac{1}{6}+\frac{1}{6}\sin^2\theta_{12}$	$\frac{1}{6}$	$\frac{1}{3}-\frac{1}{6}\sin^2\theta_{12}$
Inverted Hierarchy	$\frac{1}{6}$	$\frac{1}{6}$	$\frac{1}{3}$	$\frac{1}{3}$	$\frac{1}{6}+\frac{1}{6}\cos^2\theta_{12}$	$\frac{1}{3}$	$\frac{1}{3}-\frac{1}{6}\cos^2\theta_{12}$	$\frac{1}{6}$

TABLE 3
FRACTION OF NEUTRINOS AND ANTINEUTRINOS FOR EACH FLAVOR AFTER DECOHERENCE AND MATTER EFFECTS. $n = 2\sum_i n_{\nu_i}$.

1. The main neutrino production channel in XRFs and BdHNe in the hypercritical accretion process is pair annihilation: $e^-e^+ \to \nu\bar\nu$. This mechanism produces an initial equal number of neutrino and antineutrino and an initial 7/3 relative fraction between electronic and other flavors. These features lead to a different neutrino phenomenology with respect to the typical core-collapse SN neutrinos produced via the URCA process.

2. The neutrino density is higher than both the electron density and the vacuum oscillation frequencies for the inner layers of the accretion zone and the self-interaction potential dictates the flavor evolution along this region, as it is illustrated by Fig. 3. This particular system leads to very fast pair conversions $\nu_e\bar\nu_e \leftrightarrow \nu_{\mu,\tau}\bar\nu_{\mu,\tau}$ induced by bipolar oscillations with oscillation length as small as $O(0.05$–$1)$ km. However, due to the characteristics of the main neutrino production process, neutrinos and antineutrinos have very similar fluxes inside the neutrino emission zone and kinematic decoherence dominates the evolution of the polarization vectors.

3. The kinematic decoherence induces a fast flux equipartition among the different flavors that then enters the matter dominated regions in which MSW resonances take place.

4. Therefore, the neutrino flavor content emerging from the Bondi-Hoyle surface to the outer space is different from the original one at the bottom of the accretion zone. As shown in Table 3, The initial 70% and 30% distribution of electronic and non-electronic neutrinos becomes 55% and 45% or 62% and 38% for normal or inverted hierarchy, respectively. Since the $\nu \leftrightarrow \bar\nu$ oscillations are negligible (Pontecorvo 1957, 1968; Xing 2013) the total neutrino to antineutrino ratio is kept constant.

We have shown that such a rich neutrino phenomenology is uniquely present in the hypercritical accretion process in XRFs and BdHNe. This deserves the appropriate attention since it paves the way for a new arena of neutrino astrophysics besides SN neutrinos. There are a number of issues which have still to be investigated:

1. We have made some assumptions which, albeit being a first approximation to a more detailed picture, have allowed us to set the main framework to analyze the neutrino oscillations phenomenology in these systems. We have shown in Becerra et al. (2015) that the SN ejecta carry enough angular momentum to form a disk-like structure around the NS before being accreted. However, the knowledge of the specific properties of such possible disk-like structure surrounding the neutron star is still pending of more accurate numerical simulations at such distance scales. For instance, it is not clear yet if such a structure could be modeled via thin-disk or thick-disk models. We have adopted a simplified model assuming isotropic accretion and the structure of the NS accretion region used in Becerra et al. (2016) which accounts for the general physical properties of the system. In order to solve the hydrodynamics equations, the neutrino-emission region features, and the neutrino flavor-oscillation equations, we have assumed: spherically symmetric accretion onto a nonrotating NS, a quasi-steady-state evolution parametrized by the mass accretion rate, a polytropic equation of state, and subsonic velocities inside the shock radius. The matter is described by a perfect gas made of ions, electrons, positrons and radiation with electron and positron obeying a Fermi-Dirac distribution. The electron fraction was fixed and equal to 0.5. We considered pair annihilation, photo-neutrino process, plasmon decay and bremsstrahlung to calculate neutrino emissivities. Under the above conditions we have found that the pair annihilation dominates the neutrino emission for the accretion rates involved in XRFs and BdHNe (see Becerra et al. 2016, for further details). The photons are trapped within the infalling material and the neutrinos

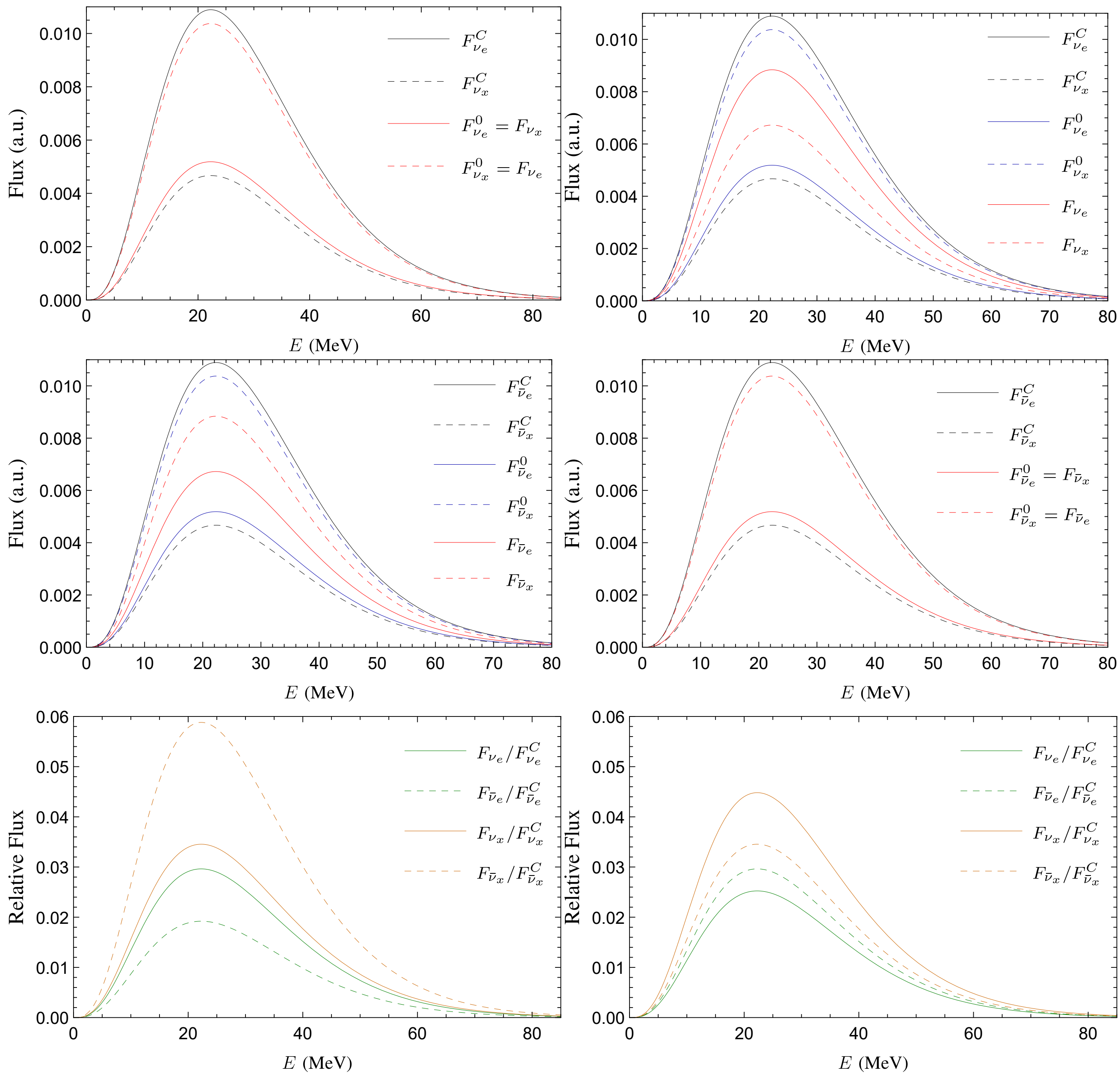

FIG. 7.— Several neutrino and antineutrino number fluxes for different neutrino flavors are presented for $\dot{M} = 10^{-2} M_\odot/\mathrm{s}$. Each column corresponds to a neutrino mass hierarchy: normal hierarchy on the left and inverted hierarchy on the right. The first two rows show the number fluxes after each process studied. F^C_ν, F^0_ν and F_ν are the creation flux at the bottom accretion zone due to e^+e^- pair annihilation, the flux after the region with dominant neutrino-neutrino potential and the final emission flux after the region with dominant neutrino-matter potential, respectively. The last row shows the relative fluxes F_ν/F^C_ν between the creation and emission fluxes.

are transparent, taking away most of the energy from the accretion. We are currently working on the relaxation of some of the above assumptions, e.g. the assumption of spherical symmetry to introduce a disk-like accretion picture, and the results will be presented elsewhere. In this line it is worth mentioning that some works have been done in this direction (see, e.g., Zhang & Dai 2008; Zhang & Dai 2009), although in a Newtonian framework, for complete dissociated matter, and within the thin-disk approximation. In these models, disk heights H are found to obey the relation $H/r \sim 0.1$ near the neutron star surface which suggests that the results might be similar to the ones of a spherical accretion as the ones we have adopted. We are currently working on a generalization including general relativistic effects in axial symmetry to account for the fast rotation that the NS acquires during the accretion process. This was already implemented for the computation of the accretion rates at the Bondi-Hoyle radius position in Becerra et al. (2016), but it still needs to be implemented in the computation of the matter and neutrino density-temperature structure near the NS surface. In addition, the description of the equation of state of the infalling matter can be further improved by taking into account beta and nuclear statistical equilibrium.

In forthcoming works we will relax the assumptions made not only on the binary system parameters but also make more detailed calculations on the neutrino oscillations including general relativistic and multi-angle effects. This paper, besides presenting a comprehensive non-relativistic account of flavor transformations in spherical accretion, serves as a primer that has allowed us to identify key theoretical and numerical features involved in the study of neutrino oscillations in the IGC scenario of GRBs. From this understanding, we can infer that neutrino oscillations might be markedly different in a disk-like accretion process. First, depending on the value of the neutron-star mass, the inner disk radius may be located at an $r_{\rm inner} > R_{\rm NS}$ beyond the NS surface (see e.g. Ruffini et al. 2016b; Cipolletta et al. 2017), hence the neutrino emission must be located at a distance $r \geq r_{\rm inner}$. On the other hand, depending on the accretion rate, the density near the inner radius can be higher than in the present case and move the condition for neutrino cooling farther from the inner disk radius, at $r > r_{\rm inner}$. Both of these conditions would change the geometric set up of the neutrino emission. Furthermore, possible larger values of T and ρ may change the mechanisms involved in neutrino production. For example, electron-positron pair capture, namely $p + e^- \to n + \nu_e$, $n + e^+ \to p + \bar{\nu}_e$ and $n \to p + e^- + \bar{\nu}_e$, may become as efficient as the electron-positron pair annihilation. This, besides changing the intensity of the neutrino emission, would change the initial neutrino-flavor configuration.

2. Having obtained the flux as well as the total number of neutrinos and antineutrinos of each flavor that leave the binary system during the hypercritical accretion process in XRFs and BdHNe, it raises naturally the question of the possibility for such neutrinos to be detected in current neutrino observatories. For instance, detectors such as Hyper-Kamiokande are more sensitive to the inverse beta decay events produced in the detector, i.e. $\bar{\nu}_e + p \to e^+ + n$ (see Abe et al. 2011, for more details), consequently, the $\bar{\nu}_e$ are the most plausible neutrinos to be detected. Liu et al. (2016) have pointed out that for a total energy in $\bar{\nu}_e$ of 10^{52} erg and $\langle E_{\bar{\nu}_e} \rangle \sim 20$ MeV, the Hyper-Kamiokande neutrino-horizon is of the order of 1 Mpc. In the more energetic case of BdHNe we have typically $\langle E_{\nu,\bar{\nu}} \rangle \sim 20$ MeV (see table 1) and a total energy carried out $\bar{\nu}_e$ of the order of the gravitational energy gain by accretion, i.e. $E_g \sim 10^{52}$–10^{53} erg. Therefore we expect the BdHN neutrino-horizon distance to be also of the order of 1 Mpc. These order-of-magnitude estimates need to be confirmed by detailed calculations, including the vacuum oscillations experienced by the neutrinos during their travel to the detector, which we are going to present elsewhere.

3. If we adopt the local BdHNe rate ~ 1 Gpc^{-3} yr^{-1} (Ruffini et al. 2016b) and the data reported above at face value, it seems that the direct detection of this neutrino signal is very unlikely. However, the physics of neutrino oscillations may have consequences on the powering mechanisms of GRBs such as the electron-positron pair production by neutrino-pair annihilation. The energy deposition rate of this process depends on the local energy-momentum distribution of (anti)neutrinos which, as we have discussed, is affected by the flavor oscillation dynamics. This phenomenon may lead to measurable effects on the GRB emission.

4. An IGC binary leading either to an XRF or to a BdHN is a unique neutrino-physics laboratory in which there are at least three neutrino emission channels at the early stages of the GRB-emission process: i) the neutrinos emitted in the explosion of the $CO_{\rm core}$ as SN; ii) the neutrinos studied in this work created in the hypercritical accretion process triggered by the above SN onto the NS companion, and iii) the neutrinos from fallback accretion onto the νNS created at the center of the SN explosion. It remains to establish the precise neutrino time sequence as well as the precise relative neutrino emissivities from all these events. This is relevant to establish both the time delays in the neutrino signals as well as their fluxes which will become a unique signature of GRB neutrinos following the IGC paradigm.

5. As discussed in Ruffini et al. (2016b), there are two cases in which there is the possibility to have hypercritical accretion onto a BH. First, in BdHNe there could be still some SN material around the newly-born BH which can create a new hypercritical accretion process (Becerra et al. 2016). Second, a $\sim 10\ M_\odot$ BH could be already formed before the SN explosion, namely the GRB could be produced in a $CO_{\rm core}$-BH binary progenitor. The conditions of temperature and density in the vicinity of these BHs might be very different to the ones analyzed here and, therefore, the neutrino emission and its associated phenomenology. We have recalled in the introduction that such an accretion process onto the BH can explain the observed 0.1–100 GeV emission in BdHNe (Ruffini et al. 2015a,b, 2016a,b; Aimuratov et al. 2017; see also Aimuratov et al. in preparation). The interaction of such an ultra-relativistic expanding emitter with the interstellar medium could be a possible source of high-energy (e.g. TeV-PeV) neutrinos, following a mechanisms similar to the one introduced in the traditional collapsar-fireball model of long GRBs (see e.g. Agostini et al. 2017; Kumar & Zhang 2015, and references therein).

6. Although the symmetry between the neutrino and antineutrino number densities has allowed us to generalize the results obtained within the single-angle and monochromatic spectrum approximations, to successfully answer the question of detectability, full-scale numerical solutions will be considered in the future to obtain a precise picture of the neutrino-emission spectrum. In particular, it would be possible to obtain an r-dependent neutrino spectrum without the restrictions discussed in Sec. 5.

7. For low accretion rates ($\dot{M} \lesssim 5 \times 10^{-5}\ M_\odot$ s^{-1}) the matter and self-interaction potentials in Eqs. (39) decrease and the general picture described in Fig. 3 changes. The resonance region could be located around closer to the NS surface, anticipating the MSW condition $\lambda_r \sim \omega_r$ and interfering with the kinematic decoherence. This changes the neutrino flavor evolution and, of course, the emission spectrum. Hence, the signature neutrino-emission spectrum associated with the least luminous XRFs might be different from the ones reported here.

We thank the Referee for the comments and suggestions which helped to make more clear the presentation of our results. M.M.G. thanks FAPESP (contract number 2016/00799–7) for the financial support and ICRANet in Pescara and Rome for the hospitality during the realization of this article. R.R. acknowledges the collaboration ICRANet-INFN. J.D.U. thanks COLCIENCIAS for the financial support. J.A.R acknowledges the partial support of the project N. 3101/GF4 IPC-11, and the target program F.0679 of the Ministry of Education and Science of the Republic of Kazakhstan.

REFERENCES

Aartsen, M. G., Abbasi, R., Abdou, Y., et al. 2013, Physical Review Letters, 111, 021103
Abe, K., Abe, T., Aihara, H., et al. 2011, ArXiv e-prints
Agostini, M., Altenmüller, K., Appel, S., et al. 2017, Astroparticle Physics, 86, 11
Aimuratov, Y., Ruffini, R., Muccino, M., et al. 2017, ApJ, 844, 83
Bayless, A. J., Even, W., Frey, L. H., et al. 2015, ApJ, 805, 98
Becerra, L., Bianco, C. L., Fryer, C. L., Rueda, J. A., & Ruffini, R. 2016, ApJ, 833, 107
Becerra, L., Cipolletta, F., Fryer, C. L., Rueda, J. A., & Ruffini, R. 2015, ApJ, 812, 100
Cardall, C. Y. 2008, Phys. Rev., D78, 085017
Chakraborty, S., Choubey, S., Dasgupta, B., & Kar, K. 2008, JCAP, 0809, 013
Cipolletta, F., Cherubini, C., Filippi, S., Rueda, J. A., & Ruffini, R. 2017, Phys. Rev. D, 96, 024046
Dasgupta, B., & Dighe, A. 2008, Phys. Rev., D77, 113002
Dasgupta, B., Dighe, A., & Mirizzi, A. 2008a, Phys. Rev. Lett., 101, 171801
Dasgupta, B., Dighe, A., Mirizzi, A., & Raffelt, G. G. 2008b, Phys. Rev., D78, 033014
Dicus, D. A. 1972, Phys. Rev., D6, 941
Dolgov, A. D. 1981, Sov. J. Nucl. Phys., 33, 700, [Yad. Fiz.33,1309(1981)]
Duan, H., Fuller, G. M., & Carlson, J. 2008a, Comput. Sci. Dis., 1, 015007
Duan, H., Fuller, G. M., Carlson, J., & Qian, Y.-Z. 2006a, Phys. Rev., D74, 105014
—. 2008b, Phys. Rev. Lett., 100, 021101
Duan, H., Fuller, G. M., & Qian, Y.-Z. 2006b, Phys. Rev., D74, 123004
—. 2007, Phys. Rev., D76, 085013
—. 2010, Ann. Rev. Nucl. Part. Sci., 60, 569
Eichler, D., Livio, M., Piran, T., & Schramm, D. N. 1989, Nature, 340, 126
Esteban-Pretel, A., Pastor, S., Tomas, R., Raffelt, G. G., & Sigl, G. 2007, Phys. Rev., D76, 125018
—. 2008, Phys. Rev., D77, 065024
Fogli, G. L., Lisi, E., Marrone, A., & Mirizzi, A. 2007, JCAP, 0712, 010
Fogli, G. L., Lisi, E., Mirizzi, A., & Montanino, D. 2005, JCAP, 0504, 002
Fogli, G. L., Lisi, E., Montanino, D., & Mirizzi, A. 2003, Phys. Rev., D68, 033005
Fryer, C. L., Oliveira, F. G., Rueda, J. A., & Ruffini, R. 2015, Physical Review Letters, 115, 231102
Fryer, C. L., Rueda, J. A., & Ruffini, R. 2014, Astrophys. J., 793, L36
Fuller, G. M., & Qian, Y.-Z. 2006, Phys. Rev., D73, 023004
Goodman, J. 1986, ApJ, 308, L47
Hannestad, S., Raffelt, G. G., Sigl, G., & Wong, Y. Y. Y. 2006, Phys. Rev., D74, 105010, [Erratum: Phys. Rev.D76,029901(2007)]
Izzo, L., Rueda, J. A., & Ruffini, R. 2012, A&A, 548, L5
Janka, H.-T., & Hillebrandt, W. 1989a, A&AS, 78, 375
—. 1989b, A&A, 224, 49
Keil, M. T., Raffelt, G. G., & Janka, H.-T. 2003, Astrophys. J., 590, 971
Kneller, J. P., & McLaughlin, G. C. 2006, Phys. Rev., D73, 056003
Kumar, P., & Zhang, B. 2015, Phys. Rep., 561, 1
Liu, T., Zhang, B., Li, Y., Ma, R.-Y., & Xue, L. 2016, Phys. Rev. D, 93, 123004
MacFadyen, A. I., & Woosley, S. E. 1999, ApJ, 524, 262
Malkus, A., McLaughlin, G. C., & Surman, R. 2016, Phys. Rev. D, 93, 045021
Mao, S., & Yi, I. 1994, ApJ, 424, L131
Meszaros, P., Laguna, P., & Rees, M. J. 1993, ApJ, 415, 181
Mikheev, S. P., & Smirnov, A. Yu. 1986, Nuovo Cim., C9, 17
Misiaszek, M., Odrzywołek, A., & Kutschera, M. 2006, Phys. Rev. D, 74, 043006
Narayan, R., Paczynski, B., & Piran, T. 1992, ApJ, 395, L83
Narayan, R., Piran, T., & Shemi, A. 1991, ApJ, 379, L17
Notzold, D., & Raffelt, G. 1988, Nucl. Phys., B307, 924
Paczynski, B. 1986, ApJ, 308, L43
Paczyński, B. 1998, The Astrophysical Journal Letters, 494, L45
Pantaleone, J. 1992, Physics Letters B, 287, 128
Pastor, S., & Raffelt, G. 2002, Phys. Rev. Lett., 89, 191101
Patrignani, C., et al. 2016, Chin. Phys., C40, 100001
Petcov, S. T. 1987, Phys. Lett., B191, 299, [,427(1987)]
Piran, T. 2004, Reviews of Modern Physics, 76, 1143
Piran, T., Shemi, A., & Narayan, R. 1993, MNRAS, 263, 861
Pontecorvo, B. 1957, Sov. Phys. JETP, 6, 429, [Zh. Eksp. Teor. Fiz.33,549(1957)]
—. 1968, Sov. Phys. JETP, 26, 984, [Zh. Eksp. Teor. Fiz.53,1717(1967)]
Qian, Y. Z., & Fuller, G. M. 1995, Phys. Rev., D51, 1479
Raffelt, G. G. 1996, Stars as laboratories for fundamental physics
Raffelt, G. G., & Sigl, G. 2007, Phys. Rev., D75, 083002
Raffelt, G. G., & Smirnov, A. Yu. 2007a, Phys. Rev., D76, 125008
—. 2007b, Phys. Rev., D76, 081301, [Erratum: Phys. Rev.D77,029903(2008)]
Rees, M. J., & Meszaros, P. 1992, MNRAS, 258, 41P
—. 1994, ApJ, 430, L93
Rueda, J. A., & Ruffini, R. 2012, ApJ, 758, L7
Ruffini, R., Bernardini, M. G., Bianco, C. L., et al. 2006, in The Tenth Marcel Grossmann Meeting. Proceedings of the MG10 Meeting held at Brazilian Center for Research in Physics (CBPF), Rio de Janeiro, Brazil, 20-26 July 2003, Eds.: Mário Novello; Santiago Perez Bergliaffa; Remo Ruffini. Singapore: World Scientific Publishing, in 3 volumes, ISBN 981-256-667-8 (set), ISBN 981-256-980-4 (Part A), ISBN 981-256-979-0 (Part B), ISBN 981-256-978-2 (Part C), 2006, XLVIII + 2492 pp.: 2006, p.369, ed. M. Novello, S. Perez Bergliaffa, & R. Ruffini, 369
Ruffini, R., Bernardini, M. G., Bianco, C. L., et al. 2008, in The Eleventh Marcel Grossmann Meeting On Recent Developments in Theoretical and Experimental General Relativity, Gravitation and Relativistic Field Theories, ed. H. Kleinert, R. T. Jantzen, & R. Ruffini, 368–505
Ruffini, R., Wang, Y., Enderli, M., et al. 2015a, ApJ, 798, 10
Ruffini, R., Muccino, M., Kovacevic, M., et al. 2015b, ApJ, 808, 190
Ruffini, R., Muccino, M., Aimuratov, Y., et al. 2016a, ApJ, 831, 178
Ruffini, R., Rueda, J. A., Muccino, M., et al. 2016b, ApJ, 832, 136
Ruffini, R., Wang, Y., Aimuratov, Y., et al. 2017, ArXiv e-prints
Salmonson, J. D., & Wilson, J. R. 2002, ApJ, 578, 310
Sawyer, R. F. 2005, Phys. Rev., D72, 045003
—. 2009, Phys. Rev., D79, 105003
Shemi, A., & Piran, T. 1990, ApJ, 365, L55
Sigl, G., & Raffelt, G. 1993, Nucl. Phys., B406, 423
Strack, P., & Burrows, A. 2005, Phys. Rev., D71, 093004
Wolfenstein, L. 1978, Phys. Rev., D17, 2369
Woosley, S. E. 1993, ApJ, 405, 273
Wu, M.-R., & Qian, Y.-Z. 2011, Phys. Rev., D84, 045009
Xing, Z.-z. 2013, Phys. Rev., D87, 053019
Yakovlev, D. G., Kaminker, A. D., Gnedin, O. Y., & Haensel, P. 2001, Phys. Rep., 354, 1
Zhang, D., & Dai, Z. G. 2008, Astrophys. J., 683, 329
Zhang, D., & Dai, Z. G. 2009, ApJ, 703, 461
Zhu, Y.-L., Perego, A., & McLaughlin, G. C. 2016, ArXiv e-prints

PHYSICAL REVIEW D **96,** 063001 (2017)

Dark matter dynamical friction versus gravitational wave emission in the evolution of compact-star binaries

L. Gabriel Gómez[1,2,3] and J. A. Rueda[1,3,4]

[1]*Dipartimento di Fisica and ICRA, Sapienza Università di Roma, P.le Aldo Moro 5, I–00185 Rome, Italy*
[2]*University of Nice-Sophia Antipolis, 28 Av. de Valrose, 06103 Nice Cedex 2, France*
[3]*ICRANet, Piazza della Repubblica 10, I–65122 Pescara, Italy*
[4]*ICRANet-Rio, CBPF, Rua Dr. Xavier Sigaud 150, Rio de Janeiro, RJ, 22290–180, Brazil*

(Received 16 June 2017; revised manuscript received 10 August 2017; published 6 September 2017)

The measured orbital period decay of relativistic compact-star binaries, with characteristic orbital periods ~0.1 days, is explained with very high precision by the gravitational wave (GW) emission of an inspiraling binary in a vacuum predicted by general relativity. However, the binary gravitational binding energy is also affected by an usually neglected phenomenon, namely the dark matter dynamical friction (DMDF) produced by the interaction of the binary components with their respective DM gravitational wakes. Therefore, the inclusion of the DMDF might lead to a binary evolution which is different from a purely GW-driven one. The entity of this effect depends on the orbital period and on the local value of the DM density, hence on the position of the binary in the Galaxy. We evaluate the DMDF produced by three different DM profiles: the Navarro-Frenk-White (NFW) profile, the nonsingular-isothermal-sphere (NSIS) and the Ruffini-Argüelles-Rueda (RAR) DM profile based on self-gravitating keV fermions. We first show that indeed, due to their Galactic position, the GW emission dominates over the DMDF in the Neutron star (NS)-NS, NS-(White Dwarf) WD and WD-WD binaries for which measurements of the orbital decay exist. Then, we evaluate the conditions (i.e. orbital period and Galactic location) under which the effect of DMDF on the binary evolution becomes comparable to, or overcomes, the one of the GW emission. We find that, for instance for 1.3–0.2 $M_\odot$ NS-WD, 1.3–1.3 $M_\odot$ NS-NS, and 0.25–0.50 $M_\odot$ WD-WD, located at 0.1 kpc, this occurs at orbital periods around 20–30 days in a NFW profile while, in a RAR profile, it occurs at about 100 days. For closer distances to the Galactic center, the DMDF effect increases and the above critical orbital periods become interestingly shorter. Finally, we also analyze the system parameters (for all the DM profiles) for which DMDF leads to an orbital widening instead of orbital decay. All the above imply that a direct/indirect observational verification of this effect in compact-star binaries might put strong constraints on the nature of DM and its Galactic distribution.

DOI: 10.1103/PhysRevD.96.063001

I. INTRODUCTION

Compact-star binaries composed of neutron stars (NSs) and/or white dwarfs (WDs) have turned out to be rich laboratories of physics and astrophysics that allow us to test fundamental theoretical predictions. In particular, NS-NS binaries have served to prove the existence of gravitational waves (GWs) [1] and the motion of matter and photons in strong gravitational fields [2], as well as other phenomena [3]. These latter aspects are of special interest in tests of general relativity and alternative theories of gravity [2,4].

The orbital motion of such systems also offers the possibility of analyzing further effects. An interesting physical situation arises when the orbiting object moves through an extended medium which is formed, for instance, from the mass loss of the binary companion. This interaction can be thought of as a drag force exerted by the circumbinary medium on the object in question, perturbing thereby its Keplerian orbital motion [5]. This dynamical friction produced by the gravitational drag force has been also studied in the context of different astrophysical phenomena such as mergers of star clusters, galaxies, and even galaxy clusters, to the inspiral of dwarf galaxies within dark matter halos and the orbital evolution of massive black hole (BH) binaries in a stellar medium [6]. Thus, dynamical friction plays an important role in the orbital evolution of many astrophysical systems. In a pioneering work, S. Chandrasekhar [7] calculated the dynamical friction force on a massive object traversing an infinite homogeneous collisionless background (representing the surrounding star neighbors).

It is thus natural to expect that a binary system moving through the galaxy can also experience a dynamical friction caused by collisionless DM particles, namely DM dynamical friction (hereafter DMDF), particularly in DM-dominated regions, as at the outer part of the Galactic halo and near the Galactic center [8]. The perturbed orbital motion may lead thus to interesting observable effects in the secular evolution of the orbital period. An interesting proposal was advanced in Ref. [9] on the possibility of inferring constraints to the DM density by determining the above DM effect on the orbital motion of binaries (see also the pioneering work by Bekenstein & Zamir [10], for a general discussion of collisionless background types as well as in the context of DM). They showed that the change in the orbital period could be due to the dynamical friction force exerted by the DM background on the binary. In that work, this effect was used to put an upper bound on the DM density in a given location of the Galaxy, independently of the density profile or the nature of the DM particles. It can be shown, however, that this upper limit is indeed fulfilled by any DM density profile consistent with the outer halo properties of the Milky Way. Thus, we explore in this work the dependence of the orbital period decay by DMDF on the different binary parameters and also on the DM density profile, in order to identify all possible physical situations suitable for an observational verification of the DMDF effect. For doing this we obtain DM profiles fulfilling definite Galactic-halo observables such as the escape velocity, the velocity dispersion and the one-halo scale length parameters. The velocity distribution function and the DM density profile are, as we shall show below, crucial elements in the dynamical friction force estimation.

It is known that the DM in the outer part of our Galaxy is well described by a classical Maxwell-Boltzmann distribution, e.g. by a nonsingular isothermal (hereafter NSIS) profile [6]. However, depending on the DM nature (e.g. particle type), the DM density distribution can deviate from the classical Maxwell-Boltzmann behavior towards the inner regions of the Galaxy. This implies that the DMDF effect will depend according to the phase-space density consistent with the DM particle nature. We shall consider, for the sake of comparison, three DM models: 1) the NSIS profile, 2) the Navarro-Frenk-White (NFW) profile [11], and 3) the recently introduced Ruffini-Argüelles-Rueda (RAR) model [12,13].

The RAR model is based on a self-gravitating system of massive (keV) fermions in thermodynamic equilibrium. The density profile of the RAR model exhibits a core-halo structure which allows to explain the DM distribution in galactic halos from dwarfs to big spirals, and predicts at the same time the presence of a DM high density core [12]. Under this approach and following the more realistic distribution function including violent relaxation processes [14] and the escape velocity of particles, the Fermi-Dirac distribution function was subsequently introduced to describe the finite size of halos. In the case of the Milky Way, such a DM core can explain the observed dynamics near the Galactic center Sgr A* without invoking a central supermassive black hole for fermion masses in the range 48 keV $\lesssim mc^2 \lesssim$ 345 keV [13].[1]

Having established the DM density profiles we shall analyze, we now describe the structure of this work. We start by discussing in Sec. II the effects which are commonly assumed to produce a change of the orbital period of binaries, putting special attention evidently to the one produced by GW emission. We analyze in Sec. III the dynamical friction force and its main ingredients for the case when it is produced by DM and when it acts on binary systems. We analyze in Sec. IV the perturbation effect of DMDF on the orbital motion of the pulsar and reproduce some general results presented in [9]. Furthermore, we introduce Galactic-halo observables in order to generalize the prescription presented in [9] and present thus a more realistic estimation of dynamical friction effects. Finally, we present in Sec. V the numerical results of $\dot{P}_b$ as a function of the radial position, the DM wind velocity and the orbital period. This latter computation leads us to compare directly the $\dot{P}_b$ due to GW emission to that given by DMDF. In Sec. V we summarize our results and present a general discussion.

II. BINARY SYSTEMS AND ORBITAL PERIOD DECAY BY GRAVITATIONAL WAVES

The precise pulsar timing measurements allow us to detect, with a high accuracy, tiny orbital effects which thus require a precise theoretical description of the orbital motion [1]. In the weak field regime (Newtonian approach), the binary motion of pulsar is simply described by the Kepler laws. However, relativistic and strong-field effects in the orbital motion should be taken into account in the vicinity of a close-orbit binary pulsar [2]. These relativistic effects can be described, for the known binaries, with sufficient accuracy in terms of the called *post-Keplerian* parameters that account for departures from Newtonian Keplerian dynamics owing e.g. to the GW emission, time delay caused by the curvature of space-time near the pulsar (Shapiro delay), and relativistic time dilation [16]. There exist a variety of effects that affect the orbital period stability and they can be, roughly speaking, classified in two large groups: kinematic and intrinsic to the system. The former include the effects of a secular increase due to the Galactic gravitational potential, secular acceleration resulting from the pulsars transverse velocity (proper motion of the pulsar) and the clusters gravitational field; while the latter is related to "local" effects in the system as mass loss either from the pulsar or its companion and the GW emission among others.[2] After subtracting kinematic effects from the observed change of the orbital period, the remaining intrinsic period decay has been shown to be explained by the GW emission predicted by general relativity of an inspiraling binary in vacuum.

The orbital period decay owing to the GW emission of a binary spiraling in circular orbits is given by

[1]See also Ref. [15] for the gravitational lensing properties of the RAR profile.

[2]For a more detail description of possible effects on the observed period decay see Refs. [3,17].

TABLE I. Intrinsic orbital decays for several binary systems in the Galaxy as well as the ones predicted by GR and DM dynamical friction. There, it is also shown the values of mass binaries, orbital periods and distances measured from the Galactic center. This information is taken completely from Table I in Ref. [18] and references therein. For updated values of masses of neutron stars see [19]. We have simply added the last row for the WD-WD binary and the last two columns to show the orbital decay predicted by DMDF for the NFW profile and the RAR model.

Name	Type	m_p $[M_\odot]$	m_c $[M_\odot]$	P_b [days]	d [kpc]	$\dot{P}_b^{\rm int}$ $[10^{-12}]$	$\dot{P}_b^{\rm GW}$ $[10^{-12}]$	$\dot{P}_{b,{\rm NFW}}^{\rm DF}$ $[10^{-21}]$	$\dot{P}_{b,{\rm RAR}}^{\rm DF}$ $[10^{-21}]$
J0737-3039	NS-NS	1.3381(7)	1.2489(7)	0.104	1.15(22)	−1.252(17)	−1.24787(13)	−10.498	−7.860
B1534 + 12	NS-NS	1.3330(4)	1.3455(4)	0.421	0.7	−0.19244(5)	−0.1366(3)	−244.166	−27.827
J1756-2251	NS-NS	1.312(17)	1.258(17)	0.321	2.5	−0.21(3)	−0.22(1)	−0.271	−20.695
J1906 + 0746	NS-NS	1.323(11)	1.290(11)	0.166	5.4	−0.565(6)	−0.52(2)	−2.655	−11.176
B1913 + 16	NS-NS	1.4398(2)	1.3886(2)	0.325	9.9	−2.396(5)	−2.402531(14)	−7.942	−17.747
B2127 + 11C[a]	NS-NS	1.358(10)	1.354(10)	0.333	10.3(4)	−3.961(2)	−3.95(13)	−8.083	−17.0154
J0348 + 0432	NS-WD	2.01(4)	0.172(3)	0.104	2.1(2)	−0.273(45)	−0.258(11)	−0.399	−1.514
J0751 + 1807	NS-WD	1.26(14)	0.13(2)	0.263	2.0	−0.031(14)	…	−1.022	−2.587
J1012 + 5307	NS-WD	1.64(22)	0.16(2)	0.60	0.836(80)	−0.15(15)	−0.11(2)	−3.404	−7.343
J1141-6545	NS-WD	1.27(1)	1.02(1)	0.20	3.7	−0.401(25)	−0.403(25)	−3.578	−11.469
J1738 + 0333	NS-WD	1.46(6)	0.181(7)	0.354	1.47(10)	−0.0259(32)	−0.028(2)	−2.120	−4.379
WDJ0651 + 2844	WD-WD	0.26(4)	0.50(4)	0.008	1	−9.8(28)	−8.2(17)	−0.014	−0.207

[a]This binary is located in the globular cluster M15 [20]. However we have made here a simple estimation of the DMDF effect assuming that the DM local density in its location does not change abruptly within the globular cluster, which may not be the case. This point is better discussed in footnote 9. For a comprehensive list of all known binaries in globular clusters see http://www.naic.edu/pfreire/GCpsr.html and references therein.

$$\dot{P}_b^{\rm GW} = -\frac{192\pi}{5}\left(\frac{2\pi G\mathcal{M}}{c^3 P_b}\right)^{5/3}, \qquad (1)$$

where G is the gravitational constant, P_b is the orbital period, $\mathcal{M} = (m_p m_c)^{3/5} M^{-1/5}$ is the so-called chirp mass and $M = m_p + m_c$ is the total mass, with the subscripts p and c denoting the primary component and its companion, respectively.

The theoretical prediction of general relativity given by Eq. (1) was first verified with the observed intrinsic orbital period decay of the famous Hulse-Taylor binary pulsar PSR B1913 + 16 [1], which is explained with an accuracy of 99,8%. Later on, additional successful verifications in other relativistic NS-NS and NS-WD binaries have been made and with even higher accuracy. We refer the reader to Ref. [18] for a review on this subject and also Table I.

As we have mentioned, the above orbital period decay by GW emission is calculated under the assumption of binary motion in empty space. We shall explore below the effect of the presence of DM background on the orbital motion via dynamical friction, i.e. by DM gravitational drag. We shall infer the predicted orbital period time derivative by this phenomenon to then compare it with the one produced by the GW emission.

III. DYNAMICAL FRICTION FORCE AND ITS MAIN INGREDIENTS

Dynamical friction has been widely used to account for the drag force when an object is moving through a collisionless medium of field particles. This drag induces a wake of medium particles on the object with a characteristic overdensity proportional to its mass [6]. In his seminal work, Chandrasekhar [7] computed the dynamical friction force onto an object that moved in an infinite homogeneous stellar medium obeying a Maxwell-Boltzmann velocity distribution, taking into account only the contribution of the field particle velocities smaller with respect to the object's velocity. However, the dynamical evolution of many astrophysical systems is driven by dynamical friction in a more realistic way [6]. We consider the drag force, $\mathbf{f}_{fr,i}$, experienced by a test body of mass $m_i \gg m$, being m the DM particle mass, and with orbital velocity v_i moving through the DM background with velocity distribution function $f(u)$ [6,7]:

$$\mathbf{f}_{fr,i} = -4\pi G^2 m_i^2 m \left(\int_0^{\tilde{v}_i} d^3u f(u) \ln\left[\frac{b_{\rm max}}{G m_i}(\tilde{v}_i^2 - u^2)\right] + \int_{\tilde{v}_i}^{v_{\rm esc}} d^3u f(u) \left[\ln\left(\frac{u+\tilde{v}_i}{u-\tilde{v}_i}\right) - 2\frac{\tilde{v}_i}{u}\right]\right)\frac{\tilde{\mathbf{v}}_i}{\tilde{v}_i^3}, \qquad (2)$$

where the integral in the first term accounts for low velocity contributions (fraction of particles moving slower than the object), while the integral in the second term refers to the faster particles, limited by the escape velocity $v_{\rm esc}$ according to the Galactic gravitational potential.[3] $b_{\rm max}$ is the maximum impact parameter defined below in Eq. (4). The above equation takes into account the orbital velocity of each object with respect to the DM wind relative to the

[3]It has been recently shown that the incorporation of the tidal radius into the background system can produce interesting features in infalling satellites in large cored galaxies [21].

center of mass of the binary system: $\tilde{\mathbf{v}}_i = \mathbf{v}_i + \mathbf{v}_w$, with $\mathbf{v}_w = v_w(\cos\alpha\sin\beta, \sin\alpha\sin\beta, \cos\beta)$ and β and α being the angles between the wind velocity vector and the perpendicular axis of the binary orbital plane and the projection of the wind velocity vector with an axes lying in the orbital plane, respectively. There are at least two different cases of wind velocities: bound and unbound binaries to the galaxy potential. In the former the DM wind velocity can be assumed as the negative of the binary circular velocity with respect to the galactic center $\mathbf{v}_w = -\mathbf{v}_{\rm rot}$. The latter case occurs often in binaries with NS components in which the system received a high kick velocity from the supernova event [22]. For high kick velocities the binary circular velocity with respect to the galactic center can be neglected [23] and we can assume $\mathbf{v}_w = -\mathbf{v}_T$, where $\mathbf{v}_T$ is the transversal velocity of the system. For intermediate kicks, the system can remain bound and we can consider, in a more general case, $\mathbf{v}_w = \mathbf{v}_{\rm rot} + \mathbf{v}_T$. Thus, we shall consider the value of v_w as a free parameter that can assume values ranging from $10\ {\rm km\,s^{-1}}$ all the way to $1000\ {\rm km\,s^{-1}}$ following the above discussion. There is the additional possibility for the binary components to experience an intrinsic DM wind. However, up to the best of our knowledge, there is no observational evidence of an intrinsic rotation of the DM with respect to the Galactic center and thus we do not consider it in our estimates.

It is important also to mention that the condition $L/a \ll 1$, where L is the size of the component's wake and a the orbital separation, must be fulfilled in order that Eq. (2) becomes linearly applicable to each binary component [6,10]. Since L is of the order of the radius of the sphere of gravitational influence of each component—see Eq. (5) below—this means that we are limited to binary systems with orbital velocities smaller than the velocity dispersion of the DM background. Namely, we deal with binary systems with sufficiently large orbital periods (small orbital compactness) so that each binary component does not interact with its respective companion's wake. Furthermore, we treat the binary system as composed of point masses no matter their internal structure. Thus, we can apply this approach under the above conditions to binary systems such as NS-NS/NS-WD [18] and WD-WD [24], or any other possible binary system of astrophysical interest.

We proceed now to introduce the most relevant ingredients entering into the computation of the dynamical friction force on the binary system. This analysis allows us to establish our system more accurately in terms of Milky Way galactic observables and to more realistically characterize the DM density properties.

A. The Coulomb logarithm

The Coulomb logarithm in the Chandrasekhar's dynamical friction formula accounts for the finite size of the system and is defined as the ratio of the maximum and minimum impact parameters for encounters, respectively $b_{\rm max}$ and $b_{\rm min}$, i.e.

$$\log\Lambda \equiv \log\left(\frac{b_{\rm max}}{b_{\rm min}}\right). \tag{3}$$

It is assumed typically that $b_{\rm max}$ is of the order of the size of the system, and $b_{\rm min}$ is defined as the impact parameter for a 90° deflection [6]

$$b_{\rm max} \approx a,\, b_{\rm min} = \max(r_h, R_A), \tag{4}$$

where $b_{\rm max}$ can be taken as the effective size of the system (the binary orbital separation) and r_h is the half-mass radius of the subject system. This is the radius that contains the body's half-mass and should be taken as $b_{\rm min}$ in the case it be an extended body. However it does not correspond to the present case. We instead adopt $b_{\rm min} = R_A$, where R_A is the radius at which a particle of the surrounding medium is affected by the sphere of gravitational influence of the test body, namely:

$$R_{A,i} = \frac{Gm_i}{\tilde{v}_i^2}, \tag{5}$$

being $\tilde{v}_i$ the relative velocity of the object with respect to the DM wind velocity as we defined above.

We can see from here that dynamical friction force is determined by the local distribution of matter producing the wake around each object. This also establishes the characteristic size of the wake. It is here assumed that $b_{\rm max} \gg b_{\rm min}$ and $b_{\rm max}$ is set to be the length scale over which the density can be assumed to be constant for a given system at fixed radial position. It is important to note that the choices of the impact parameters are somewhat arbitrary. However, we guarantee that the condition $\Lambda \gg 1$ is satisfied.

As an example we plot in Fig. 1 the Coulomb logarithm as a function of the wind velocity for a $1.3 + 0.2\ M_\odot$

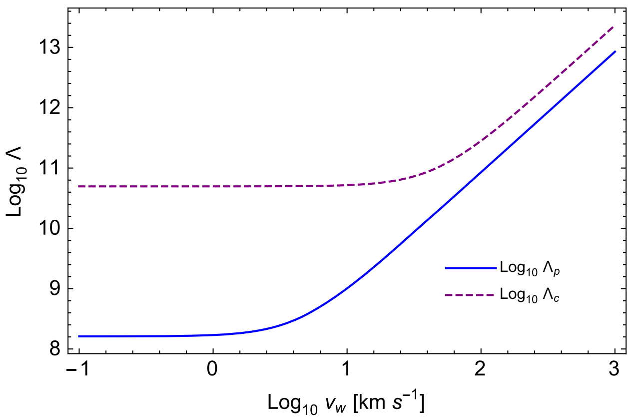

FIG. 1. Coulomb logarithm for the primary, $\log_{10}\Lambda_p$ (blue line), and for the secondary, $\log_{10}\Lambda_c$ (red line), as a function of the DM wind velocity. The primary is a NS of $1.3\ M_\odot$ and the companion secondary is a WD of $0.2\ M_\odot$. The NS-WD binary has an orbital period $P_b = 100$ days and $\beta = \pi/2$. The differences between the Coulomb logarithms lead every component of the system to experience distinct gravitational interactions with its respective wake.

NS-WD binary with orbital period $P_b = 100$ days. We stress that the Coulomb logarithm does not change with β, we choose however $\beta \neq 0$ to perform, in a more general way, a study of the orbital period decay. We also note that, for $v_w \geq 80\ \mathrm{km\,s^{-1}}$ there are not large differences between the Coulomb logarithm for each object. However, we will take into account these small differences for accuracy even though we consider, in some cases, large values for the wind velocity.

B. Velocity distribution function

The evolution of a collisionless self-gravitating system is determined by the Vlasov-Poisson equation that sets the conservation of the phase-space density [6]. This distribution function fully specifies the dynamic of a collisionless system. For instance, for spherical systems, the mass density is proportional to $\int d^3 v f$. It is also possible to derive the distribution function of a collisionless system for a given self-consistent density profile ρ following Eddington's formula [25]

$$f(\mathcal{E}) = \frac{1}{\sqrt{8}\pi^2}\left[\int_0^{\mathcal{E}} \frac{d^2\rho}{d\Psi^2}\frac{d\Psi}{\sqrt{\mathcal{E}-\Psi}} + \frac{1}{\sqrt{\mathcal{E}}}\left(\frac{d\rho}{d\Psi}\right)_{\Psi=0}\right], \quad (6)$$

where we have introduced the relative potential and binding energy (per unit mass) defined respectively as: $\Psi = -\Phi + \Phi_0$ and $\mathcal{E} = -E + \Phi_0 = \Psi - \frac{1}{2}v^2$. For a spherical system with an isotropic velocity dispersion, the phase space distribution function of dark halos depends only on the energy and not on the angular momentum. The above formula is particularly useful when we seek for a distribution function to associate with a density profile obtained from other methods. We shall apply this procedure in the appendix, to the NSIS and to the phenomenological NFW profile to validate the approximation of considering, within our estimations, the Maxwell-Boltzmann distribution for these both profiles. Significant but very small differences appear between the Maxwell-Boltzmann distribution and the distribution functions associated to the NFW and NSIS profile at nearby unbound energies, as can be seen in Fig. 7. In addition, the unbound energy ($\mathcal{E} = 0$) permits, in fact, to define the escape velocity $v_{\mathrm{esc}} = \sqrt{2|\Psi|}$. We shall see that the contribution of particles moving faster than the object and limited by the escape velocity, do not contribute substantially to the dynamical friction force. This consequence supports the fact of considering the Maxwell-Boltzmann distribution to describe the velocity distribution for the aforementioned profiles. The main motivation of this approach is then, due to the numerical facilities that the simple Maxwell-Boltzmann distribution provides in the computation of the dynamical friction force.

Accordingly, for the sake of comparison, let us assume then that the virialized NFW and NSIS halos, follow the Maxwell-Boltzmann distribution function

$$f^{\mathrm{MB}}(u) = \frac{n_0}{(2\pi\sigma^2)^{3/2}}\exp\left(-\frac{u^2}{2\sigma^2}\right), \quad (7)$$

where n_0 is the particle number such that $\rho = n_0 m$ and σ is the velocity dispersion which is defined in terms of the DM gravitational potential through the Jeans Eq. (14).

For the RAR model, we consider self-consistently a Fermi-Dirac distribution function with energy cutoff ϵ_c to describe the velocity distribution of self-gravitating halos in thermodynamic equilibrium [12][4]

$$f_c(p) = \frac{gm^3}{h^3}\begin{cases} \frac{1-e^{(\epsilon-\epsilon_c)/kT}}{e^{(\epsilon-\mu)/kT}+1} & \epsilon \leq \epsilon_c, \\ 0 & \epsilon > \epsilon_c. \end{cases} \quad (8)$$

Here $\epsilon = \sqrt{c^2p^2 + m^2c^4} - mc^2$ is the particle kinetic energy, m is the particle mass, μ is the chemical potential (with the particle rest mass subtracted off), T is the temperature, k is the Boltzmann constant. The quantity g denotes as usual the particle spin degeneracy ($g = 2$ in our case) and h is the Planck constant. It is important to stress that, the parameter ϵ_c serves to account for the finite size of galaxies. Note also that for $\epsilon_c \to +\infty$, we recover the Fermi-Dirac distribution. In the nondegenerate limit $\mu \to -\infty$, we recover on the other hand the classical King model [26], which reduces to the Boltzmann distribution in the limit $\epsilon_c \to +\infty$.

As we have mentioned, we are going to explore in this work the dynamical friction force effects on binary systems produced by DM profiles. However, it is important to note that, the dynamical friction force depends actually on the velocity distribution function whereby the introduction of the DM density profile, is somehow artificial; but in any case, it should be self-consistent for a given velocity distribution function according to the previous discussion.

C. The escape velocity

The escape velocity is defined in terms of the gravitational potential $\phi(r)$ of the background[5] as $v_{\mathrm{esc}} = \sqrt{-2\phi}$. The latter can be determined completely at any radius scale for a given density profile as follows

$$\phi(r) = 4\pi G\left[\frac{1}{r}\int_0^r dr' r'^2\rho(r') + \int_r^\infty dr' r'\rho(r')\right]. \quad (9)$$

The observed escape velocity of the Milky Way (considering the Galactic components, disk, bulge and halo) was found to be in the range $498\ \mathrm{km\,s^{-1}} \lesssim v_{\mathrm{esc}} \lesssim 608\ \mathrm{km\,s^{-1}}$ at the solar position, at 90% confidence interval and median

[4]See also Ref. [14] for a general discussion about the conditions under which statistical equilibrium state is reached.

[5]Note that we are ignoring the gravitational potential produced by the binary system as well as other possible contributions, such as those produced by the baryonic component.

likelihood of 544 $\mathrm{km\,s^{-1}}$ [27]. The RAVE survey has recently found the local escape speed to be $v_{\rm esc} = 533^{+54}_{-41}$ $\mathrm{km\,s^{-1}}$ [28]. These values depend significantly on the mass exterior to the solar circle within a certain halo radius r_h. For example, the halo mass $M_{\rm DM}(r_h = 40\ \mathrm{kpc}) \sim 2\times10^{11}\ M_\odot$ is consistent with the dynamics of the outer DM halo as was recently indicated in [29]. We note therefore that the Galactic escape velocity is either lower or closely equal to the orbital velocity of the binary pulsar for periods around $P_b \approx 0.1$ days. For large orbital periods $P_b \approx 100$ days, the orbital velocity is always well below the escape velocity. These two facts imply therefore that the contribution of the second integral (fast particles) to the dynamical friction force could be very small in most cases but not negligible in general. We will keep this term for a general study since, as we will see, it also leads to a change of sign in the orbital period time derivative (i.e. from decay to widening) for some values of the period as well as for the DM wind velocity.

D. The density profile

1. The NFW profile

We first recall the widely used phenomenological DM density profile arising within the ΛCDM cosmological paradigm, i.e. the NFW profile [11]

$$\rho(r) = \frac{\rho_c}{(r/r_s)(1+r/r_s)^2}, \tag{10}$$

where ρ_c is the characteristic density and r_s is the scale radius. This density profile exhibits a sharp cusp in the inner region $\rho \propto r^{-1}$ while in the halo part the density scales as $\rho \propto r^{-3}$.

It is worth to mention that there is an active debate in the literature on which is the best representation of the DM density profile that originates from the ΛCDM paradigm. For instance, some simulations have pointed out that the density profile of DM halos might be actually shallower than the one given by the NFW profile and found a cored structure represented more accurately by an Einasto profile (see Ref. [30] for details). It is out of the scope of this work to make an assessment on this issue and thus, for the sake of example, we adopt the NFW profile as the DM profile associated with the ΛCDM scenario. As we shall see, since the NSIS and the RAR profiles show also a shallower, cored inner halo,[6] they are useful to analyze the differences that arise in the DMDF effect between cuspy and cored density profiles.

[6] The similarity between the Einasto profile and the RAR profile in the inner halo region has been shown in Ref. [31].

2. The NSIS profile

Another often adopted DM density profile which also yields the asymptotic flatness of the rotation curves is represented by the NSIS profile [32]:

$$\rho(r) = \frac{\rho_0}{1+(r/r_0)^2}, \tag{11}$$

where ρ_0 is the central density and r_0 is the core radius.

3. The RAR profile

We will also examine the DMDF in the case of the RAR model [12,13]. This model describes the DM distribution along the entire galaxy in a continuous way, i.e. from the halo part to the Galactic center and without spoiling the baryonic component which dominates at intermediate scales. Likewise, the density ρ and pressure P for the Fermi-Dirac distribution function are defined respectively by

$$\rho = \frac{g}{h^3} m \int_0^{\epsilon_c} f_c(p)\left(1+\frac{\epsilon(p)}{mc^2}\right) d^3p, \tag{12}$$

$$P = \frac{2}{3}\frac{g}{h^3}\int_0^{\epsilon_c} f_c(p)\frac{1+\epsilon(p)/2mc^2}{1+\epsilon(p)/mc^2} d^3p. \tag{13}$$

Assuming a self-gravitating system of massive fermions (within the standard Fermi-Dirac phase-space distribution) in thermodynamic equilibrium, the DM density profile was computed in [12]. By imposing fixed boundary conditions at the halo and including the fulfillment of the rotation curves data, the parameters of the system have been constrained. This procedure was applied for different types of galaxies from dwarfs to big spirals exhibiting a universal *compact core-diluted halo* density profile. An extended version of the RAR model was recently presented [13], by introducing a fermion energy cutoff ϵ_c in the fermion distribution. Importantly, this generalization in the statistics naturally arises by studying the stationary solution of a generalized Kramer statistics which includes the effects of escape of particles and violent relaxation [14]. The new emerging density profile serves to account for the finite galaxy sizes due to the more realistic boundary conditions, while it opens the possibility to achieve a more compact solution for the quantum core working as a good alternative to the BH scenario in Sgr A* (see, Ref. [13], for details). The narrow particle mass range provides several solutions to satisfy either the rotation curve data in the halo part or both sets of data, namely including additionally the orbits of the S-cluster stars such as the S2 star, necessary to establish the compactness of the DM central core. A comparison between the RAR model, NFW profile and NSIS for MW-like spiral galaxies is also shown in Fig. 2, describing the outstanding inner structure below parsec scale for the RAR profile.

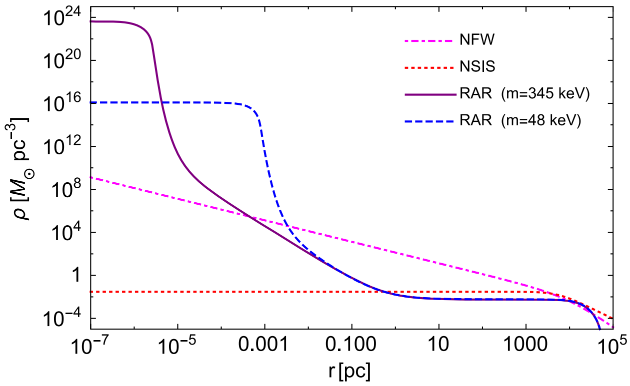

FIG. 2. Distribution of DM in MW-type galaxies predicted by the RAR model. The solid line in the legend, refers to the most compact solution for $m = 345$ keV. For comparison we show, with the dashed blue line, the solution for $m = 48$ keV. There are also shown the NFW and NSIS profiles given by Eqs. (10) and (11), respectively. The free parameters in these profiles were taken from [33,34], respectively, satisfying the same (total) rotation curve data as in the RAR case, with the corresponding considerations of bulge and disk counterparts.

It is important to clarify that the above DM density profiles are obtained without considering a DM-baryonic matter feedback nor DM self-annihilations. As shown in Ref. [35], these effects might produce changes in the DM density profile. We expect, however, the former to be important only locally in massive clusters and the latter stands on the largely model-dependent unknown DM nature. Thus, for the sake of generality, we shall not consider these effects in this work.

E. The velocity dispersion

According to observations of stars in outer part of halos and numerical simulation, the stellar velocity dispersion of the Milky Way halo σ_r, shows an almost constant value around 120 km s^{-1} at scales of 20 kpc where DM is supposed to dominate and the circular velocity V_c exhibits a flat behavior. Assuming that the galactic halo is stationary and spherically symmetric, it is possible to derive the DM radial velocity dispersion from the Jeans equation[7]

$$\frac{1}{\rho(r)}\frac{d(\rho(r)\sigma_r^2)}{dr} + 2\frac{\beta\sigma_r^2}{r} = -\frac{d\phi(r)}{dr} = -V_c^2, \tag{14}$$

where $\beta = 1 - \sigma_\theta^2/\sigma_r^2$ is the velocity anisotropic parameter, that in the isotropic case, takes evidently the value $\beta = 0$.

The circular velocity v_c is defined by the local radial gradient of the potential while the radial velocity dispersion $\sigma(r)$ depends on the shape of the potential at exterior radii. For a nonrotating spherical system the relation between these quantities is given by

$$v_c^2 = -\sigma_r^2\left(\frac{d\ln\rho}{d\ln r} + \frac{d\ln\sigma_r^2}{d\ln r} + 2\beta\right), \tag{15}$$

where the first term in parenthesis is (minus) the logarithmic slope γ of the density profile. For the singular isothermal sphere with a Maxwell Boltzmann distribution, the simple relation $v_c^2 = 2\sigma_r^2$ is satisfied for all radii. We note that, instead, for the NFW profile one obtains $1 \le \gamma \le 3$ and hence, this simple relation between the circular velocity and the velocity dispersion is not fulfilled at all radii (except at the virial radius where $\gamma = 2$, see e.g. Ref. [36]). Therefore, in order to find the right velocity dispersion profile for a given density profile, with associated gravitational potential, we solve hence the Jean equation for the isotropic case along the entire the Galaxy.

IV. ORBITAL PERIOD EVOLUTION

In this section we study the DMDF effect as an intrinsic effect on the binary system motion. Hence, in order to analyze the perturbed Keplerian orbit of binary systems, we use the osculating formalism that permits us to obtain the sequence of perturbed orbits [16]. We follow particularly both the formulation and the derived analysis presented in [9] to compute the orbital period decay due to DMDF. We start by defining the relative acceleration between two bodies as

$$\dot{\mathbf{v}} = -\frac{GM}{r^3}\mathbf{r} + \mathbf{f}, \tag{16}$$

with $\mathbf{f} = a_1\eta\mathbf{v} + a_2\mathbf{v}_w$ for the case in which the perturbing force is taking to be the drag force measured on the center of mass. To the zeroth order, the orbital velocity obeys a Keplerian motion, $v = \Omega_0 r_0$, with Ω_0 and r_0 being the angular velocity and orbital separation, respectively. We have also introduced the definitions: $\eta = \mu/M$, $\mu = m_p m_c/M$ and $M = m_p + m_c$. From here, the perturbed orbital elements can be then written as follows

$$\dot{a} = 2\sqrt{\frac{r_0^3}{GM}}S(t), \tag{17}$$

$$\dot{e} = 2\sqrt{\frac{r_0}{GM}}[R(t)\sin(\Omega_0 t) + 2S(t)\cos(\Omega_0 t)], \tag{18}$$

$$\dot{i} = 2\sqrt{\frac{r_0}{GM}}W(t)\cos(\Omega_0 t + \omega), \tag{19}$$

$$\dot{\Omega} = \frac{1}{\sin i}\sqrt{\frac{r_0}{GM}}W(t)\sin(\Omega_0 t + \omega), \tag{20}$$

where the orbital parameters a, e, ω, i and Ω are the semiaxis major, the eccentricity, the longitude of the pericenter, the

[7] Note that it is not the (observed) line of sight velocity dispersion of tracers.

inclination and longitude of the ascending node, respectively. In the right side of Eqs. (17)–(20), the source terms $S(t)$, $R(t)$ and $W(t)$ have been defined as a functions of the dynamical friction force as well as the wind velocity vector according to [9]

$$S(t) = a_1 \eta v - a_2 v_w \sin\beta \sin(\Omega_0 t - \alpha), \tag{21}$$

$$R(t) = a_2 v_w \sin\beta \cos(\Omega_0 t - \alpha), \tag{22}$$

$$W(t) = a_2 v_w \cos\beta. \tag{23}$$

The rate of change of the separation with time leads consequently to a change of the orbital period $P_b = 2\pi/\Omega_0$ given by [37]

$$\frac{\dot{P}_b}{P_b} = \frac{3}{2}\frac{\dot{a}}{r_0}. \tag{24}$$

This relation along with Eq. (17) provide the time derivative of the orbital period[8]

$$\dot{P}_b(t) = 3P_b[a_1\eta - a_2\Gamma \sin\beta \sin(\Omega_0 t - \alpha)]. \tag{25}$$

The resulting secular change in the orbital period is obtained by averaging over one period P_b, namely (see e.g. Ref. [9]):

$$\langle \dot{P}_b \rangle = \frac{1}{P_b}\int_0^{P_b} \dot{P}_b(t)dt. \tag{26}$$

In the above formulation we have introduced the same definitions as in [9] for an easier comparison of the results: $\Gamma = v_w/v$, $\Delta_\pm = \Delta \pm 1$, $\Delta = \sqrt{1-4\eta}$. The coefficients a_i can be written in terms of the integral velocity contribution function

$$b_i = \frac{1}{\rho(r)\log\Lambda_i}\frac{I_i}{\tilde{v}_i^3}, \tag{27}$$

as

$$a_1 = -(A_1 b_1 + A_2 b_2), a_2 = \frac{1}{2}(A_1 b_1 \Delta_+ + A_2 b_2 \Delta_-), \tag{28}$$

with $A_i = 4\pi\rho(r)\log\Lambda_i G^2 M$. The definition of b_i in the more general form given by Eq. (27) allows the use of any velocity distribution function, or equivalently any density profile through the integral term I_i [term in parenthesis in Eq. (2)]. This feature is contrary to the analyzed case in [9] where the Maxwell-Boltzmann distribution function was only considered there.

[8]We note there is a typo in Eq. (18) of Ref. [9], namely when compared with Eq. (25) of our present work it shows an extra factor $v/2$ which leads the equation to be dimensionally incorrect.

It is clear that the initial phase α can be set to any value without loss of generality, hence we set $\alpha = 0$ for simplicity. In the next section, we compute the secular change of $\dot{P}_b$ for different density profiles with the velocity dispersion profile determined by Eq. (14) and the associated velocity distribution function described by Eqs. (7) and (8). The incorporation of the radial scale dependence of these quantities, leads to reduce the number of free parameters presented in early calculations [9], as already pointed out previously.

There may be other contributions to a secular change of the orbital period in addition to the DMDF and the gravitational wave emission. A common effect in binaries with ordinary star components is the mass loss by star winds or accretion. A change of mass in the system would produce a change in the orbital period of the type $\dot{P}_b/P_b = -\dot{M}/M$, thus mass loss increases the orbital period (orbital widening) and mass accretion decreases it (orbital decay). In our case of binaries composed of compact stars the mass loss by winds is unlikely and accretion of matter from one component into the other could occur only via Roche lobe overflow for extremely short binary periods near the merging process. It remains the possibility of accretion of DM particles onto the binary components leading to a shrink of the orbit. The assessment of the importance of this effect, however, relies on the unknown cross section between DM and baryonic matter inside the stars (see, e.g., Ref. [38]). Thus, for the sake of generality of our conclusions, we shall not include this effect in our estimates.

V. NUMERICAL RESULTS

We present now the dependence of $\dot{P}_b$ according to Eq. (25) on the free parameters: the orbital period, the DM wind velocity and the radial position of the binary measured from the Galactic center.

Once the density profile has been chosen, and the binary position has been fixed, the velocity distribution function, the velocity dispersion, as well as the escape velocity that constrains the maximum velocity in phase space, [upper limit in the second integral Eq. (2)] can be determined uniquely. Thus, for an observed binary at a known galactic position, the above quantities acquire values that can not be treated as uncorrelated and fully free parameters.

In the following analysis we adopt for the RAR model the solution for the Milky Way with a particle mass $m = 345$ keV, which has the density profile with the most compact quantum core (see Fig. 2). We consider for the sake of example the following binary systems: NS-WD with masses $m_p = 1.3\ M_\odot$ and $m_c = 0.2\ M_\odot$, NS-NS with masses $m_p = m_c = 1.3\ M_\odot$ and WD-WD with masses $m_p = 0.5\ M_\odot$ and $m_c = 0.25\ M_\odot$. According to our above discussion of the DM wind, and considering the observed orbital period range and binary positions, we perform our analysis varying the parameters in the following ranges: $10\ \mathrm{km\,s^{-1}} \lesssim v_w \lesssim 1000\ \mathrm{km\,s^{-1}}$, 0.1 days $\lesssim P_b \lesssim$ 100 days and a scale radius 0.1 kpc $\lesssim r \lesssim$ 10 kpc. It is important to note that we will also consider binary systems near the Galactic center (at parsec scales) since it is of interest to check the DMDF in regions along the Galaxy where DM is supposed to dominate.

A. DMDF in observed binaries

We first apply the approach to the Galactic binaries with measured intrinsic orbital periods and which are remarkably well explained by GW emission. In the last three columns of Table I we compare $\dot{P}_b^{\rm GW}$ with $\dot{P}_b^{\rm DF}$. In this calculation we use the NFW profile and the RAR model for illustrative purposes and the following free parameters: $\beta = 0$ and $v_w = 100\ \mathrm{km\,s^{-1}}$. For other values of β, $\dot{P}_b^{\rm DF}$ does not change significantly, however a change of v_w by one order of magnitude may be more important in the computation of $\dot{P}_b^{\rm DF}$ as we shall see below. At this point we should discuss whether the binaries of Table I are bound or unbound to the Galactic gravitational potential to determine a more precise value for the DM velocity wind.[9] However, for the binaries of Table I which are characterized by short orbital periods, we checked that this is not relevant since for any DM wind in the range $10\ \mathrm{km\,s^{-1}} \lesssim v_w \lesssim 1000\ \mathrm{km\,s^{-1}}$ the value of $\dot{P}_b^{\rm DF}$ is still very small compared with the $\dot{P}_b^{\rm GW}$ and with the measured intrinsic orbital period decay.

As we can see the DMDF effect is very small for all the above binaries because of the short orbital periods (compact orbits) that lead them to experience a small drag force.

We can thus first conclude that, for the binary systems listed in Table I, the DMDF effect is indeed negligible and their secular evolution is fully dominated by GW emission.

B. DMDF as a function of the orbital period

A natural question that arises is whether DMDF effects can be comparable with the orbital period decay predicted by GW emission. To answer this question we explore the physical conditions (and hence the values for the model parameters) under which such equality may be attained. We thus consider the possibility to have binary systems with large periods, e.g. $P_b = 100$ days, since DMDF is enhanced in systems with small binary compactness. We also consider regions along the Galaxy where the DM is supposed to dominate as those near the Galactic center.

[9]It is important to clarify that the pulsar B2127 + 11C is located within the Galactic globular cluster M15 whereby it is subjected dominantly to the gravitational potential of its host globular cluster. As in the case of bulge globular clusters accelerating (possibly) pulsars through their stellar components [39], DM can also contribute to the total acceleration by the studied effect in this paper. This latter claim is motivated by recent observational analysis that point out favorably the importance of the DM component in the dynamical of globular clusters [40,41].

We start our analysis by plotting the secular change of P_b as a function of the orbital period for different density profiles in Fig. 3 with values for the free parameters $v_w = 100\ \mathrm{km\,s^{-1}}$ and $r = 0.1$ kpc in this analysis. We also show

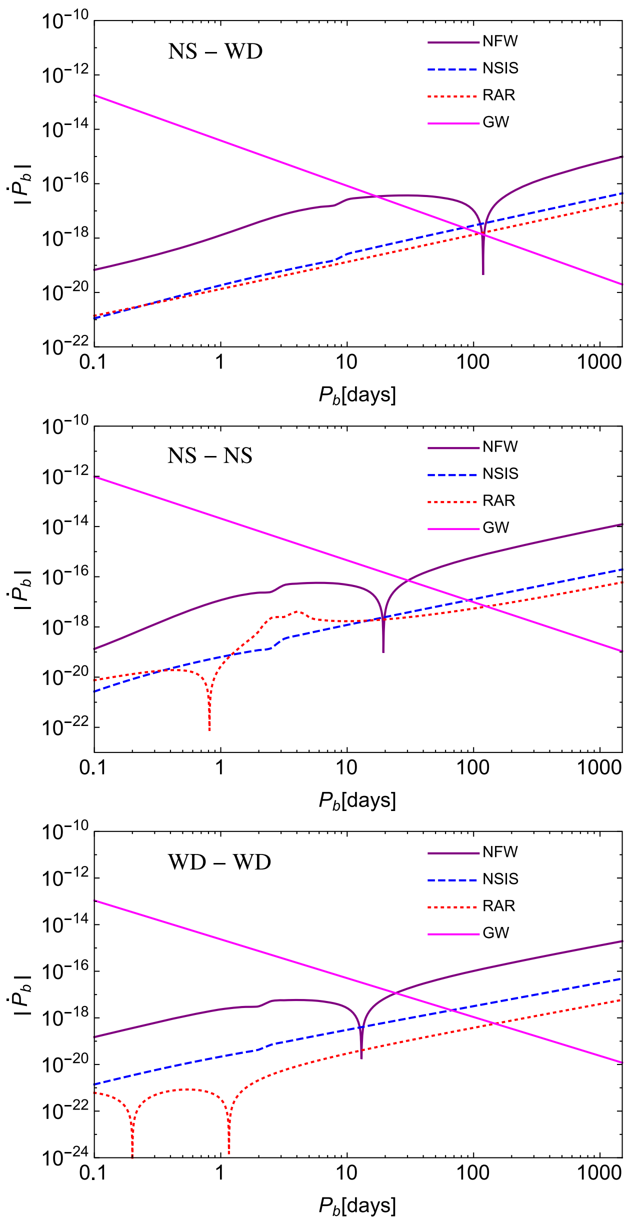

FIG. 3. Secular change of the orbital period as a function of the orbital period. The red dotted curve refers to the most compact solution of the RAR profile for the Milky Way, namely for a DM particle mass $m = 345$ keV. The blue dashed curve shows the results for the NSIS profile and the purple solid curve the ones for the NFW profile. The pink solid line shows the prediction of the orbital decay due to GW emission. We have here adopted the values $r = 0.1$ kpc, $v_w = 100\ \mathrm{km\,s^{-1}}$ and $\beta = \pi/2$. Top panel: NS-WD with $m_p = 1.3\ M_\odot$ and $m_c = 0.2\ M_\odot$. Middle panel: NS-NS with $m_p = m_c = 1.3\ M_\odot$. Bottom panel: WD-WD with $m_p = 0.5\ M_\odot$ and $m_c = 0.25\ M_\odot$.

TABLE II. This table displays theoretical predictions of orbital periods in days at which $\dot{P}_b^{\rm DF}$, computed by the indicated DM density profiles, equates $\dot{P}_b^{\rm GW}$ predicted by general relativity for different binary systems.

DM Profile	NS-WD	NS-NS	WD-WD
NFW	18	30	25
RAR	120	130	150
NSIS	80	90	70

in the same plot the orbital decay due to GW emission $\dot{P}_b^{\rm GW}$, according to Eq. (1).

We can see that for a NS-WD system (top panel in Fig. 3), the orbital period decay starts to be dominated by the DMDF effect shortly after than $P_b = 18$ days, for the NFW profile, i.e it is now larger that the one predicted by the GW emission. For the same system, The NSIS predicts a $\dot{P}_b^{DF}$ that matches $\dot{P}_b^{\rm GW}$ around $P_b = 80$ days while for the RAR model, it occurs around 120 days. For a NS-NS system (middle panel in Fig. 3), the NFW provides the match around 30 days and around 90 days and 130 days for the NSIS and RAR model respectively. For a WD-WD system (bottom panel in Fig. 3), the NFW provides the match around 25 days and around 70 days and 150 days for the NSIS and RAR model respectively. These results are also summarized in Table II for clarity. However, for such large periods, DMDF provides small orbital decays between 10^{-16} (for the NFW profile) and around 10^{-18} (for the other profiles) as can be seen in Fig. 3. It is evident from here that, the larger the orbital period, the larger the $\dot{P}_b$ reached. For instance for $P_b = 1000$ days, $\dot{P}_b \sim 10^{-14}$ for the NFW profile and NS-NS binaries (middle panel in Fig. 3). These values are however very small, with respect, for instance, to the measured intrinsic orbital decays shown in Table I for some binary systems. However, possible measurements of the intrinsic period decays for binary systems with characteristic large periods is a challenge of unprecedented precision for astronomical observations. If such measurements might be successfully attained, it could also lead to discriminate between different DM density profiles due to the outstanding precision which is a characteristic property in such systems.

C. DMDF as a function of the DM wind

In order to analyze the effect of the wind velocity, we choose the radial position of the binary system fixed (measured from the Galactic center) at $r = 1.5$ kpc and the orbital period $P_b = 100$ days. Figure 4 shows that, for the aforementioned parameters and for the NFW and the NSIS profile, $\dot{P}_b^{\rm DF}$ lies in the range 10^{-20}–10^{-16}. We can see from here that the smaller the DM wind velocity the larger the $\dot{P}_b^{\rm DF}$. However the latter statement does not apply for the RAR model which exhibits a constant value of $\dot{P}_b^{DF} \sim 5 \times 10^{-18}$ for NS-WD and WD-WD and around 10^{-17} for NS-NS, for $v_w \gtrsim 200$ km s^{-1}. this analysis leads to conclude that binaries into a DM background with small DM wind velocities (than the orbital velocity), experience a more effective drag force and hence a larger $\dot{P}_b$. We shall be then

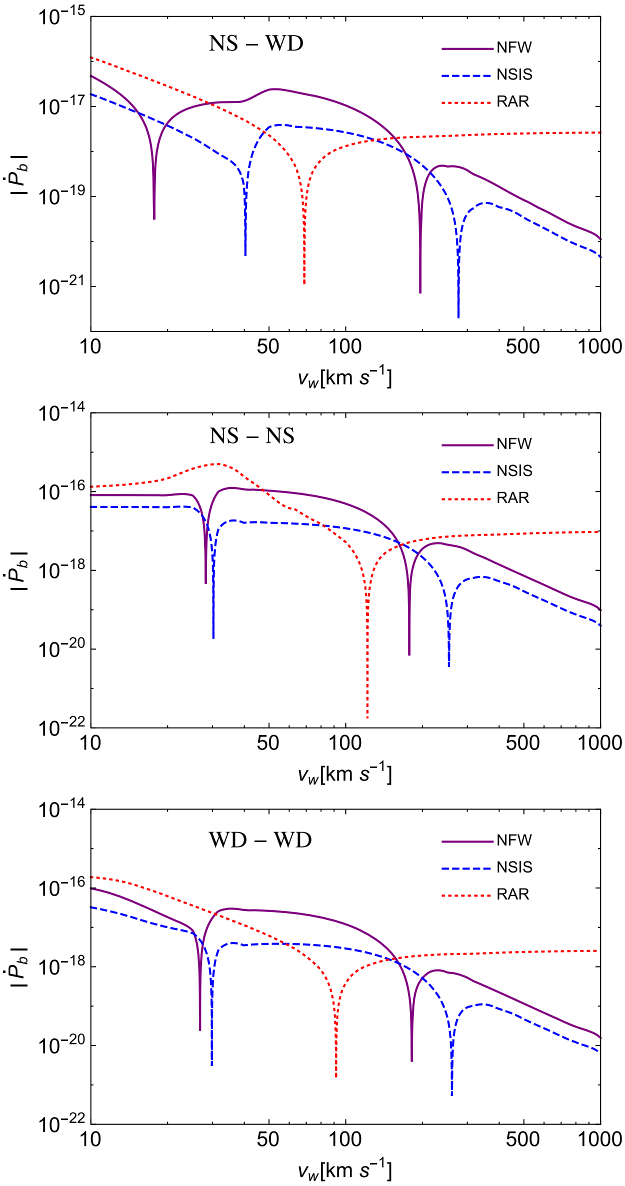

FIG. 4. Secular change of the orbital period as a function of the DM velocity wind. The red dotted curve refers to the most compact solution of the RAR profile for the Milky Way, namely for a DM particle mass $m = 345$ keV. The blue dashed curve shows the results for the NSIS profile and the purple solid curve the ones for the NFW profile. The pink solid line shows the prediction of the orbital decay due to GW emission. We have here adopted the values $r = 1.5$ kpc, $P_b = 100$ days and $\beta = \pi/2$. Top panel: NS-WD with $m_p = 1.3\ M_\odot$ and $m_c = 0.2\ M_\odot$. Middle panel: NS-NS with $m_p = m_c = 1.3\ M_\odot$. Bottom panel: WD-WD with $m_p = 0.5\ M_\odot$ and $m_c = 0.25\ M_\odot$.

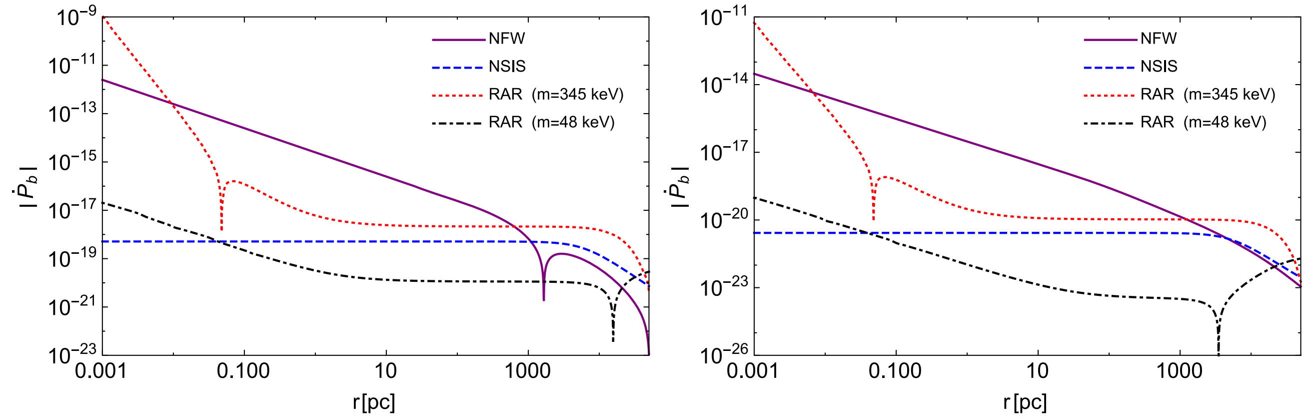

FIG. 5. Secular change of the orbital period of a NS-WD as a function of the radial position, for all the density profiles analyzed in this work. The red dotted curve refers to the most compact solution of the RAR profile for the Milky Way, namely for a DM particle mass $m = 345$ keV. The black dot-dashed curve shows the RAR profile for $m = 48$ keV. The blue dashed curve shows the results for the NSIS profile and the purple solid curve the ones for the NFW profile. We have here adopted the values $v_w = 200\ \mathrm{km\,s^{-1}}$ and $\beta = \pi/2$. Left panel: numerical results for the case $P_b = 100$ days. Right panel: numerical results for the case $P_b = 0.5$ days.

more interested in binary systems with small wind velocities, however we do not exclude at all binaries with (at least) one NS companion which may posses high kick velocities and then large wind velocities.

D. DMDF as a function of the binary position

We turn now to plot in Fig. 5 the value of $\dot{P}_b$ as a function of the radial position. We here adopt for the DM wind $v_w = 200\ \mathrm{km\,s^{-1}}$ and for the binary period $P_b = 100$ days (left panel) and $P_b = 0.5$ days (right panel). We can see that, differences between the solution provided by $m = 48$ keV and the one provided by $m = 345$ keV for the RAR model is $\approx 3 \times 10^3$. Interestingly, towards the Galactic center, for the two chosen cases of orbital periods ($P_b = 0.5$, 100 days), the NFW profile and the RAR model (for the most compact solution $m = 345$ keV) can reach a value of $\dot{P}_b$ that may be comparable with the one provided by Eq. (1) due to GW emissions. The prediction of $\dot{P}_b$ due to DMDF, for binaries with short orbital periods, can also be seen in Table I for the NFW profile and the RAR model, respectively. For large periods however (left panel in Fig. 5), DMDF effect is highly enhanced for all the binary systems as can be seen in Fig. 3. In particular, the RAR model predicts large orbital period decay very near the Galactic center (around 10^{-3} pc) due to the high DM density at such distances (see also Fig. 2). The most promising situation arises then for binary positions near the Galactic center either for long or short orbital periods. We expect hence that observational measurements reach a technological improvement that permit us to measure such short orbital periods decays with outstanding precision in the future. In addition, it would be interesting to observe binary systems near the Galactic center to put constraints on the Galactic center environment, particularly on the DM density profile and importantly, to check the GR predictions in the strong field regime.

E. From orbital shrinking to widening

We turn now to analyze the model parameters under which a change of sign in the orbital period first time-derivative occurs. Namely, the conditions under which DMDF produces an orbital widening instead of an orbital shrinking or vice-versa. For given binary parameters and β, there are values of the wind velocity for which occurs a change of sign of $\dot{P}_b$. This is clearly seen in Fig. 4 for each density profile, for binaries with known values of the orbital period and distance and setting $\beta = \pi/2$. Figure 6 shows, instead, how sensitive is this feature to the value of the β parameter and to the Galactic DM distribution, i.e on the DM density profile. We describe now, for the sake of example and without loss of generality, the case of the NS-WD binary of Fig. 6. In this analysis we have adopted $P_b = 100$ days and $r = 1.5$ kpc as known quantities. The two changes of signs occur at: $\beta = 68.75°$ and 114.6° for the RAR model with $v_w = 70\ \mathrm{km\,s^{-1}}$; $\beta = 80.21°$ and 97.40° for the NFW profile with $v_w = 200\ \mathrm{km\,s^{-1}}$; and $\beta = 74.49°$ and 103.13° for the NSIS profile with $v_w = 300\ \mathrm{km\,s^{-1}}$ (see Fig. 6). These results are in general agreement with the ones found in Ref. [9] within the approximation of large v_w. The contribution of fast moving particles with respect to the binary-components, along with particular choices of v_w, β and even P_b, might lead (although it is not a necessary condition) to multiple changes of sign of $\dot{P}_b$. This analysis supports the necessity of taking into account this contribution to check the conditions under which $\dot{P}_b$ may change sign. If one were interested in providing only negative values of $\dot{P}_b$, the particular choice $\beta = 0$ (or more generally a value of it out

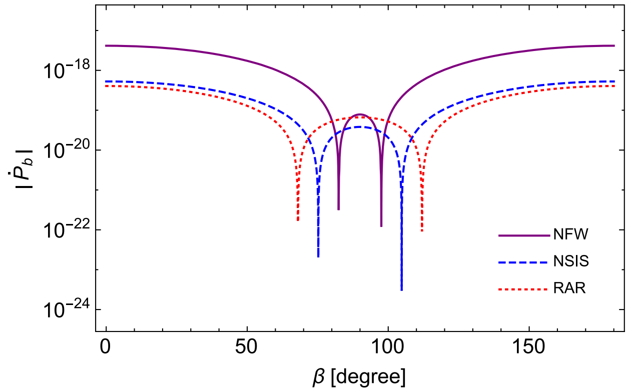

FIG. 6. Secular change of the orbital period for a NS-WD as a function of the angle β. The red-dotted curve refers to the most compact solution of the RAR profile for the Milky Way, namely for a DM particle mass $m = 345$ keV. The blue-dashed curve shows the results for the NSIS profile and the purple-solid curve the one for the NFW profile. We have here adopted the values $P_b = 100$ days and $r = 1.5$ kpc for all the profiles. Here we adopt values of the wind velocities that can lead to change of sing in the orbital period time-derivative. For the RAR model $v_w = 70\ \mathrm{km\,s^{-1}}$, for NFW profile $v_w = 200\ \mathrm{km\,s^{-1}}$ and for the NSIS profile $v_w = 300\ \mathrm{km\,s^{-1}}$.

the above ranges) would fulfill such requirement. We set then henceforth on the contrary $\beta = \pi/2$ in order to introduce a possible change of sign in $\dot{P}_b$ as a general case.

Let us turn back to Fig. 3. We note that the change of sign can occur for shorter or longer periods depending on the density profile and the DM wind velocity. For instance, for the NFW profile and $v_w = 200\ \mathrm{km\,s^{-1}}$, the change of sign occurs at $P_b \approx 2$ days contrary to the case $v_w = 100\ \mathrm{km\,s^{-1}}$ where the change is around 100 days for NS-WD as can be seen in the top panel of Fig. 3. The change of sign of $\dot{P}_b$ may occur at short period values for the RAR model, around 1 day for NS-NS and WD-WD (see middle and bottom panel in Fig. 3), while for the NFW profile, it may occur around 20 days for NS-NS, around 12 days for WD-WD and around 100 days for NS-WD. The NSIS profile always provides negatives values in all the binary systems shown in Fig. 3. Before the first peak and after the second one, $\dot{P}_b$ is always negative while between the two peaks $\dot{P}_b$ is positive. We recall that, however, negatives values can be obtained for all the orbital period range in the case in which β takes a value different from the aforementioned ranges, independently of the binary system and the other parameters as was inferred from Fig. 6.

It can be seen that negative values of $\dot{P}_b$ correspond to those binaries between the two peaks contrary to the curve given by the RAR model in the bottom panel in Fig 3. We also note that the position of those peaks does not change significantly when the orbital period varies, but rather the order of magnitude of $\dot{P}_b$. In some cases it can vary up to one order of magnitude. It is also important to note that this feature may change depending on the radial position and the density profile. As we can see from the same plot, the RAR model shows negative values of $\dot{P}_b$ below the first peak.

We can analyze the behavior as a function of the binary position in Fig. 5. For the case of NFW profile and left panel ($P_b = 100$ days), negatives values of $\dot{P}_b$ can still be found after the peak as pointed out previously; therefore, positives values are located below 1.5 kpc for the NFW profile, while for both the NSIS profile and the RAR model, $\dot{P}_b$ is always negative. In the right panel of the same figure (for $P_b = 0.5$ days), all the DM density profiles provide negatives values of $\dot{P}_b$ except the RAR model, before the peak, for $m = 48$ keV (also for $P_b = 100$ days). It is important to stress that this analysis is valid for $\beta = \pi/2$ since, for other values of it, as $\beta = 0$, $\dot{P}_b$ is always negative being independent of the DM density profile as can be inferred from Fig. 6.

VI. DISCUSSION AND CONCLUSIONS

It is by now well-known that the high-precision measurements of the orbital parameters of compact-star binaries (e.g. NS-NS, NS-WD and WD-WD) with short orbital periods ($P_b \lesssim 0.1$ days) have allowed a remarkable verification of the of the orbital decay predicted by general relativity due to GW emission (see Table II and references therein). However, the binary gravitational binding energy can be also affected by an usually neglected phenomenon, namely the DMDF (i.e. DM gravitational drag) induced by the DM on the binary owing to the interaction of the binary components with their DM gravitational wakes. We have qualified and quantified in this work this effect in the evolution of compact-star binaries and assessed the conditions under which it can become comparable to the one of the GW emission. We can draw the following conclusions from such an analysis:

(1) A first interesting situation may occur for binaries with long orbital periods above 20 days: the orbital decay produced by DMDF becomes comparable to the one produced by the emission of GWs. Clearly, the precise orbital period at which the two effects are quantitatively equal depends on the DM density profile and on the binary parameters (see Fig. 3).
(2) We have presented here, for the NFW, the NSIS and the RAR DM profiles, the orbital period for NS-NS, NS-WD and WD-WD binaries at which the DMDF effects, start to dominate over the produced by GW emission. These results are summarized in Table II (see also Fig. 3).
(3) The NFW profile and the RAR model provide a more significant effect in the drag force than the one given by the NSIS profile, as can be seen in Figs. 3–5. It is important to note that the RAR and the NSIS profile predictions are similar above $P_b = 100$ days, for all

the binary systems analyzed in this work (with $v_w = 100\ \mathrm{km\,s^{-1}}$ and located at 0.1 kpc), while also for those values of P_b the NFW profile predicts a much larger DMDF effect.

(4) Another promising situation arises for binary systems located very near the Galactic center. In this case, the $\dot{P}_b$ due to DMDF is increased even for short orbital periods ($P_b = 0.5$ days) as is shown in the right panel of Fig. 5. For long orbital periods the DMDF is notoriously strengthened, particularly for the NFW profile and the most compact solution for the RAR model ($m = 345$ keV). This latter situation corresponds to the most ideal case for testing the DMDF (left panel of Fig. 5).

(5) For the most ideal scenario of the DMDF effects in binary systems, kinematic effects, which are proportional to the orbital period, must be considered and respectively compared to the one studied in this work.

(6) It is known that positive values of $\dot{P}_b$ can be caused for example by binary mass-loss or mass-exchange. However, we have seen that $\dot{P}_b$ might change sign from negative to positive due to DMDF. This is shown in Fig. 6 for different DM density profiles. Thus, this effect could be study in binary systems dominated by kinematic effects.

To summarize, The DMDF is very sensitive to the DM properties: density profile, velocity distribution function and velocity dispersion profile; whereby it would permit to put stringent constraints on the DM properties (and presumably on the nature) at the binary position and thus to discriminate between different DM models. Following this idea, the determination of the orbital secular changes of compact-star binaries with long/short orbital periods located in the outer halo/center of the Galaxy, might constrain the DM density distribution in these locations. It would also be interesting to study such an effect in binaries with measured orbital decays within globular clusters (as in the case of B2127 + 11C) in order to put constraints on the DM distribution in these systems. Therefore, the possible identification of this effect establishes a topic for future high-precision astrophysical data for the analysis of the secular evolution of compact-star binaries.

ACKNOWLEDGMENTS

L. G. G. is supported by the Erasmus Mundus Joint Doctorate Program by Grant No. 2013–1471 from the EACEA of the European Commission. J. A. R. acknowledges the partial support of the project N 3101/GF4 IPC-11, and the target program F.0679 of the Ministry of Education and Science of the Republic of Kazakhstan. It is a pleasure to thank C. R. Arguëlles for interesting comments and discussions on the subject of this work. We thank the anonymous referee for all the insightful questions which helped to improve this manuscript.

APPENDIX: DISTRIBUTION FUNCTIONS FROM EDDINGTON'S FORMULA

For a given density profile, the gravitational potential can be obtained by solving the Poisson's equation $\nabla\Psi = -4\pi\rho(r)$. Now, in order to solve Eddington's formula Eq. (6), we express the integral there in terms of r instead of Ψ, and choose the appropriate limits of integrations by inverting numerically the equation $\Psi(r) = g(r)$, with $g(r)$ being a defined function of the radial position for a given density profile. In addition, the condition that the distribution function be positive for any positive energy, i.e, $f(\mathcal{E}) \geq 0$ for $\mathcal{E} \geq 0$, should be guaranteed. This condition is fulfilled when $\Phi(r)$ goes to zero at infinity along with the appropriated value of the central potential $\Phi_0 = \Phi(r = 0)$. We then set $\mathcal{E} = -E$ and do for convenience the simple change

$$\frac{d^2\bar{\rho}}{d\bar{\Psi}^2} = \frac{d}{d\bar{r}}\left(\frac{\bar{\rho}\prime(\bar{r})}{\bar{\Psi}\prime(\bar{r})}\right)\frac{d\bar{r}}{d\bar{\Psi}}. \tag{A1}$$

All quantities with bar are dimensionless by making use of the model parameters of the respective density profile. With all of this, we can perform numerically the integral in Eq. (6). In order to compare the distribution functions associated with the NFW and the NSIS profiles, with the Maxwell-Boltzmann one, we have to normalize f to common units. For this we follow the usual normalization $\sqrt{8}M/(RV)^3$, where M is the mass enclosed at a position R where the circular velocity V becomes flat, and E is given in units of square velocity V^2; hence we introduce the dimensionless quantity $\bar{E} = E/V^2$. For the NFW profile (Eq. (10) such a radius is given by the virial radius, $r_\mathrm{v} = cr_\mathrm{s}$, where c is the so-called concentration parameter c and r_s is the scale radius. For this profile, we measure then f in units of $\sqrt{8}M_\mathrm{v}/(R_\mathrm{v}V_\mathrm{v})^3$ and $\bar{E} = E/V_\mathrm{v}^2$. For the NSIS profile (Eq. (11), we adopt the core radius r_0 and thus all the quantities derived from it such that f is given in units of $\sqrt{8}M_0/(r_0V_0)^3$ and $\bar{E} = E/V_0^2$. Furthermore, we express the Maxwell-Boltzmann distribution as follows [6]

$$f(\mathcal{E}) = \frac{\bar{\rho}_0}{(2\pi\sigma^2)^{3/2}}\exp\left[\mathcal{E}/\sigma^2\right], \tag{A2}$$

with $\bar{E} = -\mathcal{E}/2\sigma^2$.

To check the consistency of our calculation we also apply the above method to the singular isothermal sphere (SIS)

$$\rho(r) = \frac{\sigma^2}{2\pi G\bar{r}_0^2}\left(\frac{\bar{r}_0}{r}\right)^2, \tag{A3}$$

which must follow the Maxwell-Boltzmann distribution function (see, e.g., [6]). We define the central density $\bar{\rho}_0 = \sigma^2/2\pi G\bar{r}_0^2$ and compute its associated distribution function also from Eddington's formula. This solution is represented

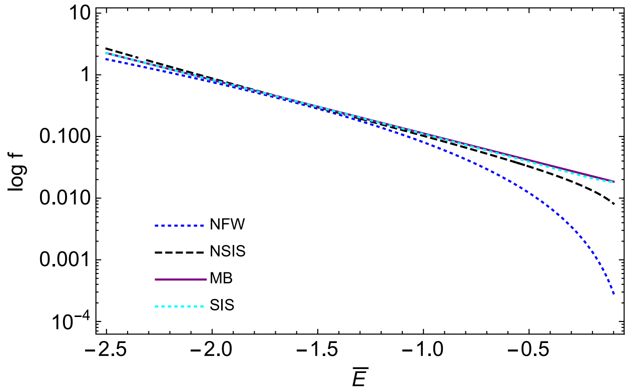

FIG. 7. Distribution functions for all the density profiles listed in the legend. These self-consistent distributions correspond to the solution of Eddington's formula Eq. (6).

by the cyan-dotted line in Fig. 7 which can be seen overlaps with the Maxwell-Boltzmann distribution. For this profile, we measure f in units of $\sqrt{8}\bar{M}_0/(\bar{r}_0\sqrt{2}\sigma)^3$. Thus, all the distribution functions and the dimensionless energy $\bar{E}$ are given in terms of theirs model parameters. Therefore, once we set the units of f and $\bar{E}$, we can infer quantitatively the scale factor that lead to compare our results. However, it is important to mention that such a scale factor may be somewhat arbitrary when one does not consider a finite size for the halo which forces us to introduce a cutoff at some radius scale. The relation between the relative energy $\mathcal{E} = -E$ and the particle velocity v is determined by $E = \frac{1}{2}(v^2 - v_{\rm esc}^2)$. For $v < v_{\rm esc}$ particles are of course bounded. Finally, we present numerical results of the distribution functions associated to the NFW and the NSIS profiles and the comparison with the Maxwell-Boltzmann distribution function in Fig. 7. Our goal in this computation is to validate the approximation of taking the Maxwell-Boltzmann distribution to describe the velocity distribution for the aforementioned profiles. We can see that the largest differences occur close to unbound energies, precisely where the contribution of particle velocities near the escape velocity do not contribute significantly to the dynamical friction force. These results then lead us to approximate, within our estimations, the velocity distributions function for the aforementioned profiles to follow the Maxwell-Boltzmann distribution. Such approximation permits us to notoriously facilitate all the numerical computations regarding the orbital period decay. However, if we had at disposition observational timing pulsar data to test robustly our predictions, we would have to use the exact velocity distribution function for every density profile according to Eddington's formula.

[1] R. A. Hulse and J. H. Taylor, Astrophys. J. **195**, L51 (1975).
[2] M. Kramer, I. H. Stairs, R. N. Manchester, M. A. McLaughlin, A. G. Lyne, R. D. Ferdman, M. Burgay, D. R. Lorimer, A. Possenti, N. D'Amico, J. M. Sarkissian, G. B. Hobbs, J. E. Reynolds, P. C. C. Freire, and F. Camilo, Science **314**, 97 (2006).
[3] D. R. Lorimer and M. Kramer, *Handbook of Pulsar Astronomy* (Cambridge University Press, Cambridge, 2012).
[4] J. Antoniadis *et al.*, Science **340**, 448 (2013).
[5] M. E. Alexander, W. Y. Chau, and R. N. Henriksen, Astrophys. J. **204**, 879 (1976).
[6] J. Binney and S. Tremaine, *Galactic Dynamics* (Princeton University Press, Princeton, 2008), ISBN 978-0-691-13026-2 (HB); Second Edition.
[7] S. Chandrasekhar, Astrophys. J. **97**, 255 (1943).
[8] L. E. Strigari, Phys. Rep. **531**, 1 (2013).
[9] P. Pani, Phys. Rev. D **92**, 123530 (2015).
[10] J. D. Bekenstein and R. Zamir, Astrophys. J. **359**, 427 (1990).
[11] J. F. Navarro, C. S. Frenk, and S. D. M. White, Astrophys. J. **462**, 563 (1996).
[12] R. Ruffini, C. R. Argüelles, and J. A. Rueda, Mon. Not. R. Astron. Soc. **451**, 622 (2015).
[13] C. R. Argüelles, J. A. Rueda, and R. Ruffini, arXiv: 1606.07040.
[14] P.-H. Chavanis, Physica (Amsterdam) **332A**, 89 (2004).
[15] L. G. Gómez, C. R. Argüelles, V. Perlick, J. A. Rueda, and R. Ruffini, Phys. Rev. D **94**, 123004 (2016).
[16] E. Poisson and C. M. Will, *Gravity*, (Cambridge University Press, Cambridge, 2014).
[17] T. Damour and J. H. Taylor, Astrophys. J. **366**, 501 (1991).
[18] J. Antoniadis, in *Gravitational Wave Astrophysics*, edited by C. F. Sopuerta [*Astrophysics and Space Science Proceedings* 40, 1 (2015)].
[19] F. Özel and P. Freire, Annu. Rev. Astron. Astrophys. **54**, 401 (2016).
[20] S. B. Anderson, P. W. Gorham, S. R. Kulkarni, T. A. Prince, and A. Wolszczan, Nature (London) **346**, 42 (1990).
[21] J. A. Petts, J. I. Read, and A. Gualandris, Mon. Not. R. Astron. Soc. **463**, 858 (2016).
[22] A. G. Lyne and D. R. Lorimer, Nature (London) **369**, 127 (1994).
[23] K. A. Postnov and L. R. Yungelson, Living Rev. Relativ. **9**, 6 (2006).
[24] J. J. Hermes, M. Kilic, W. R. Brown, D. E. Winget, C. Allende Prieto, A. Gianninas, A. S. Mukadam, A. Cabrera-Lavers, and S. J. Kenyon, Astrophys. J. **757**, L21 (2012).
[25] A. S. Eddington, Mon. Not. R. Astron. Soc. **76**, 572 (1916).
[26] I. R. King, Astron. J. **70**, 376 (1965).

[27] M. C. Smith, G. R. Ruchti, A. Helmi, R. F. G. Wyse, J. P. Fulbright, K. C. Freeman, J. F. Navarro, G. M. Seabroke, M. Steinmetz, M. Williams, O. Bienaymé, J. Binney, J. Bland-Hawthorn, W. Dehnen, B. K. Gibson, G. Gilmore, E. K. Grebel, U. Munari, Q. A. Parker, R.-D. Scholz, A. Siebert, F. G. Watson, and T. Zwitter, Mon. Not. R. Astron. Soc. **379**, 755 (2007).

[28] T. Piffl, C. Scannapieco, J. Binney, M. Steinmetz, R.-D. Scholz, M. E. K. Williams, R. S. de Jong, G. Kordopatis, G. Matijevič, O. Bienaymé, J. Bland-Hawthorn, C. Boeche, K. Freeman, B. Gibson, G. Gilmore, E. K. Grebel, A. Helmi, U. Munari, J. F. Navarro, Q. Parker, W. A. Reid, G. Seabroke, F. Watson, R. F. G. Wyse, and T. Zwitter, Astron. Astrophys. **562**, A91 (2014).

[29] S. L. J. Gibbons, V. Belokurov, and N. W. Evans, Mon. Not. R. Astron. Soc. **445**, 3788 (2014).

[30] D. Merritt, A. W. Graham, B. Moore, J. Diemand, and B. Terzić, Astron. J. **132**, 2685 (2006).

[31] I. Siutsou, C. R. Argüelles, and R. Ruffini, Astronomy Reports **59**, 656 (2015).

[32] P. R. Shapiro, I. T. Iliev, and A. C. Raga, Mon. Not. R. Astron. Soc. **307**, 203 (1999).

[33] Y. Sofue, Publ. Astron. Soc. Jpn. **65**, 118 (2013).

[34] Y. Sofue, M. Honma, and T. Omodaka, Publ. Astron. Soc. Jpn. **61**, 227 (2009).

[35] G. Bertone and D. Merritt, Phys. Rev. D **72**, 103502 (2005).

[36] J. F. Navarro, A. Ludlow, V. Springel, J. Wang, M. Vogelsberger, S. D. M. White, A. Jenkins, C. S. Frenk, and A. Helmi, Mon. Not. R. Astron. Soc. **402**, 21 (2010).

[37] L. D. Landau and E. M. Lifshitz, *Course of theoretical physics, Pergamon International Library of Science, Technology, Engineering and Social Studies* (Pergamon Press, Oxford, 1980) 3rd rev. and enlarged ed.

[38] C. F. B. Macedo, P. Pani, V. Cardoso, and L. C. B. Crispino, Astrophys. J. **774**, 48 (2013).

[39] B. Prager, S. Ransom, P. Freire, J. Hessels, I. Stairs, P. Arras, and M. Cadelano, arXiv:1612.04395.

[40] R. Ibata, C. Nipoti, A. Sollima, M. Bellazzini, S. C. Chapman, and E. Dalessandro, Mon. Not. R. Astron. Soc. **428**, 3648 (2013).

[41] A. Sollima, F. R. Ferraro, L. Lovisi, F. Contenta, E. Vesperini, L. Origlia, E. Lapenna, B. Lanzoni, A. Mucciarelli, E. Dalessandro, and C. Pallanca, Mon. Not. R. Astron. Soc. **462**, 1937 (2016).

Commun. Comput. Phys.
doi: 10.4208/cicp.OA-2017-0007

Vol. **22**, No. 3, pp. 863-888
September 2017

Equilibrium Configurations of Classical Polytropic Stars with a Multi-Parametric Differential Rotation Law: A Numerical Analysis

Federico Cipolletta[1,2], Christian Cherubini[3,4,*], Simonetta Filippi[3,4], Jorge A. Rueda[1,2,5] and Remo Ruffini[1,2,5]

[1] *Dipartimento di Fisica and ICRA, Sapienza Università di Roma, P.le Aldo Moro 5, I–00185 Rome, Italy.*
[2] *ICRANet, Piazza della Repubblica 10, I–65122 Pescara, Italy.*
[3] *Unit of Nonlinear Physics and Mathematical Modeling, University Campus Bio-Medico of Rome, Via A. del Portillo 21, I–00128 Rome, Italy.*
[4] *International Center for Relativistic Astrophysics-ICRA, University Campus Bio-Medico of Rome, Via A. del Portillo 21, I–00128 Rome, Italy.*
[5] *ICRANet-Rio, Centro Brasileiro de Pesquisas Físicas, Rua Dr. Xavier Sigaud 150, Rio de Janeiro, RJ, 22290–180, Brazil.*

Received 13 January 2017; Accepted (in revised version) 27 February 2017

Abstract. In this paper we analyze in detail the equilibrium configurations of classical polytropic stars with a multi-parametric differential rotation law of the literature using the standard numerical method introduced by Eriguchi and Mueller. Specifically we numerically investigate the parameters' space associated with the velocity field characterizing both equilibrium and non-equilibrium configurations for which the stability condition is violated or the mass-shedding criterion is verified.

PACS: 04.40.-b, 02.30.Jr, 02.60.-x

Key words: Free boundary problems, self-gravitating systems, numerical methods for partial differential equations.

1 Introduction

The problem of equilibrium of rotating self-gravitating systems, dating back to Newton's Principia Mathematica studies on the Earth's shape, still represents a very actual topic in

*Corresponding author. *Email addresses:* `cipo87@gmail.com` (F. Cipolletta), `c.cherubini@unicampus.it` (C. Cherubini), `s.filippi@unicampus.it` (F. Filippi), `jorge.rueda@icra.it` (J. A. Rueda), `ruffini@icra.it` (R. Ruffini)

the field of astrophysics. Its main target is to reconstruct the structure of rotating stars considered to be, in a first approximation, in hydrostatic equilibrium although more complicated hydrodynamical effects can be taken into account by using modern tools of numerical analysis. Historically the studies on spherical non rotating self-gravitating bodies (well summarized in the classical Chandrasekhar's monograph on stellar structure [1]) and on uniformly rotating ones in the case of incompressible fluids (deeply analysed too in the companion Chandrasekhar's monograph on ellipsoidal figures of equilibrium [2], as well as, for instance, in [4–12]) preceded the study of compressible uniformly rotating polytropic stars [3]. All of these studies were completed by a series of refined numerical integrations of the complicated field equations governing the problem, performed by the Japanese school, which specifically investigated the problem of self-gravitating fluid's shape bifurcations [13–20]. The next step then has been the inclusion of differential rotation laws in the treatment, for instance in [21, 22], where rotation profiles were considered admitting an exact integral relation leading to an analytical expression of the centrifugal potential term in the hydrostatic equilibrium equation. In the literature it is known that differential rotation plays an important role in modelling the rotating stars' structure, in particular for both initial and ending phases of the stars' life. Most of the aforementioned works dealt with barotropic stars, i.e. configurations in which isopycnic (constant density) and isobaric (constant pressure) surfaces coincide, although it has been recently stressed the importance to consider also more general situations, like the baroclinic one (in which isopycnic surfaces are inclined over isobaric ones) in order to obtain more realistic configurations [23]. We have to point out also that although many recent papers dealt with relativistic figures of equilibrium (see for instance e.g. [24] and references therein) in relation to the problem of modelling possible sources of gravitational waves, the initial step to investigate the effects of pure rotation is to consider the problem of classical figures of equilibrium first. In the present paper, we will analyse in detail i) a polytropic classical self-gravitating fluid, ii) with axial and equatorial symmetry and with iii) a multi-parametric differential rotation law, which was proposed in [25] without a systematic analysis of the possible configurations belonging to such a velocity profile. The main feature of this rotation profile is that, with respect to the study in [21], this one can be considered as a generalization because it does not admit an analytical expression for the integral for centrifugal potential term. In addition, the presence of different free-parameters allows a more detailed study of the way in which the star rotates. By using the general method given in [21] in order to perform an analysis of the free-parameters' space, we identify the presence of possible bifurcation points in the configurations' sequences. The article is organized as follows. In Section 2, the numerical method by Eriguchi and Mueller [21] is briefly reviewed, the multi-parametric differential rotation profile taken by [25] is discussed and an analysis of possible instabilities which may be reached is performed. In Section 3, we show results locating stable configurations within the free-parameters' space and focusing on how different values of parameters in the rotation law could lead to different shaped configurations. The correctness of results is checked and already known results of [21] are recovered. In Section 4 we summarize and discuss the results obtained. Finally, details on the numerical implementation and on the definitions of physical quantities adopted in the analysis are given in Appendix A.

2 Theoretical framework

2.1 The problem of equilibrium

In this section we review the general method for analyzing rotating and self-gravitating fluids as presented in [21]. In this method the attention is focused on a configuration of rotating and self-gravitating gas for which the equation of hydrostationary equilibrium, in its differential form, reads

$$-(\vec{v}\cdot\vec{\nabla})\vec{v}=\frac{\vec{\nabla}P}{\rho}+\vec{\nabla}\Phi_g, \tag{2.1}$$

being $\vec{v}$, ρ, P and Φ_g respectively the fluid's velocity, density, pressure and gravitational potential. The latter quantity must satisfy the Poisson's equation, which for a general configuration reads

$$\Delta\Phi_g=\begin{cases} 4\pi G\rho, & \text{inside},\\ 0, & \text{outside},\end{cases} \tag{2.2}$$

being G the constant of gravitation. Note that left-hand side of Eq. (2.1) can be written as

$$-(\vec{v}\cdot\vec{\nabla})\vec{v}=-\frac{1}{2}\vec{\nabla}(\vec{v}\cdot\vec{v})-(\vec{\nabla}\times\vec{v})\times\vec{v}, \tag{2.3}$$

so that using Eq. (2.1) we get

$$\frac{\vec{\nabla}P}{\rho}+(\vec{\nabla}\times\vec{v})\times\vec{v}=-\left(\vec{\nabla}\Phi_g+\frac{1}{2}\vec{\nabla}(\vec{v}\cdot\vec{v})\right), \tag{2.4}$$

and as the right-hand side has null curl, one obtains the following integrability condition for Eq. (2.1)

$$\vec{\nabla}\times\left\{\frac{\vec{\nabla}P}{\rho}+(\vec{\nabla}\times\vec{v})\times\vec{v}\right\}=0. \tag{2.5}$$

Writing explicitly the fluid's velocity of a rotating gas in hydrostationary equilibrium in cylindrical coordinates (ϖ,z,ϕ) as

$$\vec{v}=\varpi\Omega(\varpi,z)\hat{e}_\phi, \tag{2.6}$$

one obtains that Eqs. (2.1) and (2.5) are respectively equivalent to

$$\frac{\vec{\nabla}P}{\rho}=-\nabla\Phi_g+\varpi\Omega^2(\varpi,z)\hat{e}_\varpi, \tag{2.7}$$

$$2\varpi\Omega(\varpi,z)\frac{\partial\Omega(\varpi,z)}{\partial z}\hat{e}_\phi=\vec{\nabla}\frac{1}{\rho}\times\vec{\nabla}P. \tag{2.8}$$

From Eq. (2.8), by assuming a barotropic Equation of State (EOS), $P=P(\rho)$, we get

$$\frac{\partial\Omega}{\partial z}=0, \tag{2.9}$$

which is a well known sufficient condition (see [26]) for isopycnic (constant density) and isobaric (constant pressure) surfaces to be coincident. In addition, we also obtain that the centrifugal term in Eq. (2.7) comes out from a potential which can be defined as

$$\Phi_c=-\int_0^{\varpi}\varpi'\Omega^2(\varpi')d\varpi'. \tag{2.10}$$

One can in principle investigate Eqs. (2.2) and (2.7) in their differential form, but this gives rise to problems in treating the boundary conditions to impose, which are the finiteness of Φ_g and P at the center of the star, the vanishing of Φ_g at infinity and the definition of the surface where P vanishes. On the other hand, by treating the integral form of these equations, one can incorporate the boundary condition in an easier way. To do so, we have to note that Φ_g at a point $\vec{x}$, due to the presence of mass in the volume V, can be written as (see e.g. [27])

$$\Phi_g(\vec{x})=-G\int_V\frac{\rho(\vec{x}')}{|\vec{x}-\vec{x}'|}dV', \tag{2.11}$$

which using spherical coordinates (r,θ,ϕ) together with axial and equatorial symmetries, is equal to

$$\begin{aligned}\Phi_g(r,\theta)=&-4\pi G\int_0^{\frac{\pi}{2}}\sin(\theta')d\theta'\int_0^{r_{\text{surf}}(\theta)}r'^2dr'\\ &\cdot\sum_{n=0}^{\infty}f_{2n}(r,r')P_{2n}(\cos(\theta))P_{2n}(\cos(\theta'))\rho(r',\theta').\end{aligned} \tag{2.12}$$

Here we indicate with $P_{2n}(\cos(\theta))$ the Legendre's polynomial of order $2n$ computed in $\cos(\theta)$ and f_{2n} are the Green's functions (of even order), defined by

$$f_{2n}(r,r')=\begin{cases}\frac{r'^{2n}}{r^{2n+1}} & \text{for } r\geq r',\\ \frac{r^{2n}}{r'^{2n+1}} & \text{for } r<r'.\end{cases} \tag{2.13}$$

It is possible now to have Eq. (2.1) in its integral form, which can be written as

$$\int\frac{1}{\rho}dP+\Phi_g+\Phi_c=C\ (\text{const.})\ . \tag{2.14}$$

The system to be solved is defined via Eq. (2.14) coupled to Eq. (2.12). But one still has to insert the EOS and the boundary conditions to define the surface (a free boundary problem) of the figure of equilibrium, namely

$$\rho(r_{\text{surf}})=0 \tag{2.15}$$

and a rotation law, that is a relation to express Ω as a function of the adopted coordinates, which will be used in the centrifugal potential term, Φ_c. The choice of the EOS relation is one the most delicate points in approaching the problem of equilibrium of rotating gases from the physical point of view. In fact, different EOSs can result in very different configurations of equilibrium of rotating stars. For the sake of simplicity we suppose that the gas we are modelling is perfect, in the sense that it is composed of non-interacting particles (i.e. the effects of interacting particles is negligible, thus we can neglect viscosity implicated by energy dissipation during motion due to the interaction between particles) and it is non-degenerate (see e.g. [27]). An EOS which in a first approximation is able to model this kind of physical properties is the polytropic one

$$P = K\rho^{1+\frac{1}{n}}, \tag{2.16}$$

where K is the polytropic constant and n is the polytropic index. At this point, the only missing ingredient to numerically solve the system of equations (which we report in Appendix A) is a rotation profile.

2.2 Multi-parametric differential rotation law

When integrating hydrostationary equilibrium equation together with Poisson's equation on a discretized numerical grid (see Appendix A for details) one should also supply a rotation law, i.e. a relation to express the angular velocity on each grid-point as a function of the spatial variables. In particular, actually we are interested in the study of the axisymmetric case, in which equatorial symmetry is also prescribed, thus a natural choice of coordinates' set will be the spherical one (r,θ,ϕ). In literature many cases have already been studied, taking into account both uniform rotation, i.e. $\Omega = \text{const.}$ (see e.g. [3]), and differential rotation, i.e. $\Omega = \Omega(\varpi)$, being $\varpi = r\sin(\theta)$ the cylindrical radius (see e.g. [22] and [21]). More precisely, in papers dealing with differential rotation, a single-free-parameter differential rotation law is chosen, i.e. where $\Omega(\varpi)$ depends also on one single free parameter which allows to control how much differential is the rotation, in the sense that for a defined value the uniformly rotating case is recovered. We consider here a differential rotation law of the following kind (see Ref. [25]):

$$\Omega(\varpi) = \Omega_0 \frac{e^{-B\varpi^2}}{1+\left(\frac{\varpi}{A}\right)^2}, \tag{2.17}$$

being Ω_0 the central angular velocity and A and B parameters which control the rotation law and that in a limiting case can reproduce uniform rotation. It is worth noting that the if $A \to \infty$, the rotation law tends to the one of [22], while if $B = 0$, it is the so-called j-const. rotation law of [21]. Although it may seem that Ω_0, A and B are all free-parameters, the reader will see that Ω_0 is treated as an unknown by the method adopted, thus the actual free-parameters' number is two as the value of Ω_0 is obtained from the choice of the axis ratio. We then require $A,B \geq 0$. It is useful to introduce dimensionless variables within the method, adopting the following relation:

$$F = k_F \tilde{F}, \tag{2.18}$$

where F is the physical quantity in real dimension, k_F is the constant for non-dimensionalization and $\tilde{F}$ is the quantity in dimensionless form. In particular, as in [21] we adopt non-dimensional constants as reported in Table 1, where n is the polytropic index, K is the polytropic constant and G is the gravitational constant. Looking at Eq. (2.17) is evident that parameters A and B have dimensions of length and length^{-2} respectively, thus it is also useful to impose

$$A = a r_s, \tag{2.19}$$

$$B = \frac{b}{{r_{eq}}^2}, \tag{2.20}$$

with r_s being the radius of the spherical configuration and r_{eq} the equatorial spherical coordinate radius, just like in [21] (for parameter A) and [22] (for parameter B). The main problem in choosing differential rotation given by Eq. (2.17), is that the integral to compute the centrifugal potential term in the hydrostationary equilibrium equation (see Section 2) cannot be performed analytically. For this reason we have decided to

Table 1: Constants adopted to obtain dimensionless quantities from Eq. (2.18).

F	k_F	$\tilde{F}$	Physical Meaning
ρ	ρ_c	σ^n	Density
P	$K{\rho_c}^{1+\frac{1}{n}}$	σ^{n+1}	Pressure
Ω^2	$[4\pi G\rho_c]$	ν	Squared Angular Velocity
Φ_g	$K(n+1)\rho_c^{\frac{1}{n}}$	Ψ	Gravitational Potential
r	$\left[\frac{K(n+1)}{4\pi G}\rho_c^{\frac{1}{n}-1}\right]^{\frac{1}{2}}$	ξ	Spherical Radius
M	$4\pi\left[\frac{K(n+1)}{4\pi G}\right]^{\frac{3}{2}}{\rho_c}^{\frac{3-n}{2n}}$	$\tilde{M}$	Mass
J	$\frac{[K(n+1)]^{\frac{5}{2}}}{4\pi G^2}{\rho_c}^{\frac{5-2n}{2n}}$	j	Angular Momentum
I_Ω	$\frac{[K(n+1)]^{\frac{5}{2}}}{[4\pi]^{\frac{3}{2}}G^{\frac{5}{2}}}{\rho_c}^{\frac{5-3n}{2n}}$	$\tilde{I}$	Moment of Intertia
T	$\frac{[K(n+1)]^{\frac{5}{2}}}{[4\pi]^{\frac{1}{2}}G^{\frac{3}{2}}}{\rho_c}^{\frac{5-n}{2n}}$	$\tilde{T}$	Kinetic Energy
W	$\frac{[K(n+1)]^{\frac{5}{2}}}{[4\pi]^{\frac{1}{2}}G^{\frac{3}{2}}}{\rho_c}^{\frac{5-n}{2n}}$	$\tilde{W}$	Gravitational Potential Energy
U	$\frac{[K(n+1)]^{\frac{5}{2}}}{[4\pi]^{\frac{1}{2}}G^{\frac{3}{2}}}{\rho_c}^{\frac{5-n}{2n}}$	$\tilde{U}$	Thermal Energy

perform a numerical integration (via trapezoidal method) on an artificial numerical grid for each axis distance from the particular grid-point in which to compute the value of centrifugal potential, considering a very large set of $N_{\rm cyl}$ points (namely $N_{\rm cyl}=1000$ for each grid-point and $N_{\rm cyl}=10000$ to find the integration constant). With such numerical grid in the cylindrical radial coordinate, the aforementioned numerical integration for the centrifugal potential is able to properly reproduce already known results [21] (see Section 4). This allows us to study in a general numerical way every kind of differential rotation law, without requiring an analytical form for centrifugal potential.

2.3 Stability

As already pointed out in [22], an important condition which the chosen rotation law should satisfy is the stability condition against axisymmetric perturbation, provided by the Solberg-Høiland criterion,

$$\frac{d\left[\varpi^2\Omega(\varpi)\right]}{d\varpi}>0, \tag{2.21}$$

which states that the angular momentum per unit mass $\varpi^2\Omega$ must increase outwards (c.f. [22], [26] and [27]), i. e. going from the pole to the equator (for a complete derivation of this criterion we refer to [28]). Thus, when choosing a rotation law, one must always verify that Eq. (2.21) is satisfied in order to guarantee stability. Using Eq. (2.17) in Eq. (2.21), it is easy to check that this condition is equivalent to

$$B\varpi^2A^2+B\varpi^4-A^2<0, \tag{2.22}$$

which, using definitions given in Eqs. (2.19), (2.20) and in Table 1 for r and simplifying for a factor ${K_r}^2$, in dimensionless form reads as:

$$\frac{b}{{\xi_{\rm eq}}^2}\widetilde{\varpi}^2a^2{\xi_{\rm s}}^2+\frac{b}{{\xi_{\rm eq}}^2}\widetilde{\varpi}^4-a^2{\xi_{\rm s}}^2<0, \tag{2.23}$$

where $\widetilde{\varpi}=\xi\sin(\theta)$ is the dimensionless cylindrical radius, $\xi_{\rm eq}$ is the dimensionless spherical equatorial radius of the configuration and $\xi_{\rm s}$ is the dimensionless radius of the initial spherical configuration. It is now evident that the stability condition may be violated for particular choices of the two free-parameters. It could be interesting to have a sample of what violation of criterion of Eq. (2.21) would imply. Anticipating some results, in Fig. 1 the angular momentum per unit mass distribution along the distance from rotation axis direction is plotted for three configurations, obtained with same differential rotation exponential parameter $b=0.128$ and axis ratio $\frac{r_{\rm eq}}{r_{\rm pol}}=1.05$ but with different choices of parameter a (namely 0.02,1.12,2.00). It can be noted that for sequences represented by dashed and dash-dotted curves (respectively with $a=1.12$ and $a=2.00$) the condition of Eq. (2.21) is obviously satisfied, leading to stable configurations and allowing the entire sequence to be constructed (as the reader will see in figures of next section), while for sequence represented by solid the curve, obtained with $a=0.02$, the angular momentum

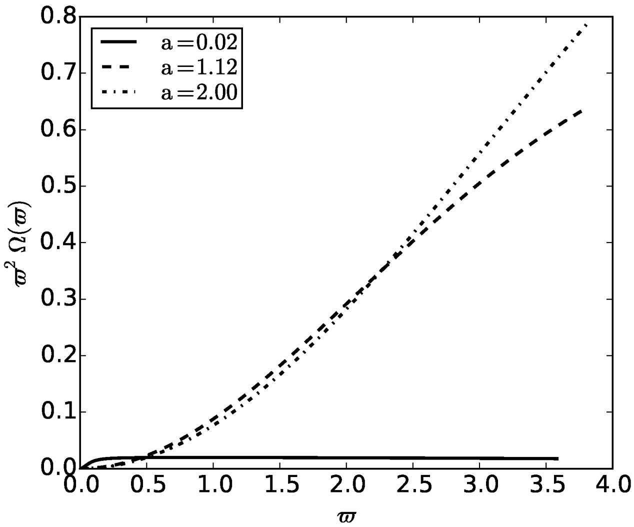

Figure 1: Angular momentum per unit mass distribution along distance from rotation axis for three sample sequences obtained with same choice of parameter $b=0.128$ and axis ratio $\frac{r_{\rm eq}}{r_{\rm pol}}=1.05$, but different choices of parameter $a=0.02,\ 1.12,\ 2.00$.

per unit mass distribution is slowly decreasing. The stability condition given by Eq. (2.21) is not the only one to be controlled. In fact, another physical limit for the rotation which is worth to take into account is the mass-shedding limit, namely the point in which the rotation becomes too fast to allow stability. As already presented in [3] or [26] the aforementioned limit for equilibrium configurations in the axisymmetric case occurs when the effective gravity of the surface at the equator becomes zero, which means that the gravitational force is perfectly balanced by the centrifugal one (and vice-versa). Actually, if the angular velocity would increase further after this condition is reached, a portion of the total mass should begin to shed from the star, because the centrifugal force would become greater than the gravitational one (the so-called "mass-shedding"). Using a polytropic EOS and the constants for dimensionless form given by Table 1, one gets the following criterion for dimensionless effective gravity

$$\tilde{g}_{\rm eq\;eff}=\frac{\partial\sigma}{\partial\tilde{\xi}}\left(\tilde{\xi}_{\rm surf\;eq},\frac{\pi}{2}\right)\leq 0, \tag{2.24}$$

necessary to avoid mass-shedding.

3 Results

3.1 Differentially rotating polytropes

In the following analyses, we have specifically adopted for the polytropic relation of Eq. (2.16) the value $n=1.5$. Adopting a multi-parametric differential rotation law, such the one given in Eq. (2.17), it is possible to have a very detailed control on the way the star rotates. It is interesting to understand the different figures of equilibrium which could result from different choices of these control parameters. Summarizing, to perform such an analysis, one can use the method given in [21] to build several equilibrium sequences, each obtained by a fixed change in the axis ratio from one configuration to another (see Section 2), taking into account the Solberg-Høiland criterion in Eq. (2.21) and the mass-shedding condition given in Eq. (2.24). Thus, we decided to fix initial extrema for parameters value, namely $a_{\min}$, $a_{\max}$, $b_{\min}$ and $b_{\max}$ and to compute respectively N_a and N_b linearly equally spaced parameter's values between these extremes. Explicitly, the parameters value are given by the following equation:

$$p_k = p_{\min} + \left((p_{\max} - p_{\min}) \times \frac{(k-1)}{(N_p - 1)} \right) \quad \text{for } k = 1, \cdots, N_p, \tag{3.1}$$

where with letter p the parameter's name is intended, namely a or b. After having fixed the set of values for free-parameters, several sequences can be computed starting from the spherical configuration until some kind of instability is reached. However we notice that it is possible that none of the two instability condition could be reached, thus we decided to stop the computations when 101 configurations have been built (this in order to limit the computation time). Precisely, the maximum axis ratio of equilibrium configurations which is reached in this way is $(1.05)^{101} \sim 138.07$.

In Fig. 2 the kind of instability reached (after the entire sequence is computed) for each choice of the two rotational parameters is represented, with color convention given in the

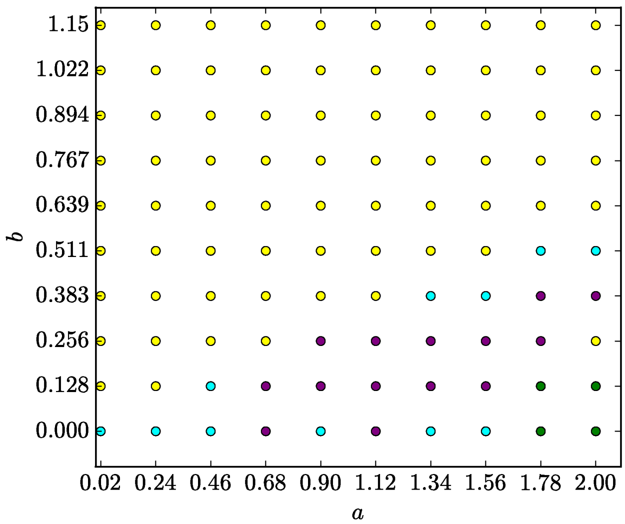

Figure 2: Resulting equilibrium configurations for different choices of rotational parameters b and a of Eq. (2.17), obtained with 15-angular times 40-radial points in the numerical grid. Colour convention is: green is for mass-shedding criterion violation, yellow is for Solberg-Høiland criterion violation, blue is for concave hamburger configurations, which after 101 configurations did not violate any stability criterion and purple is for concave hamburger configuration which reach mass-shedding at equator.

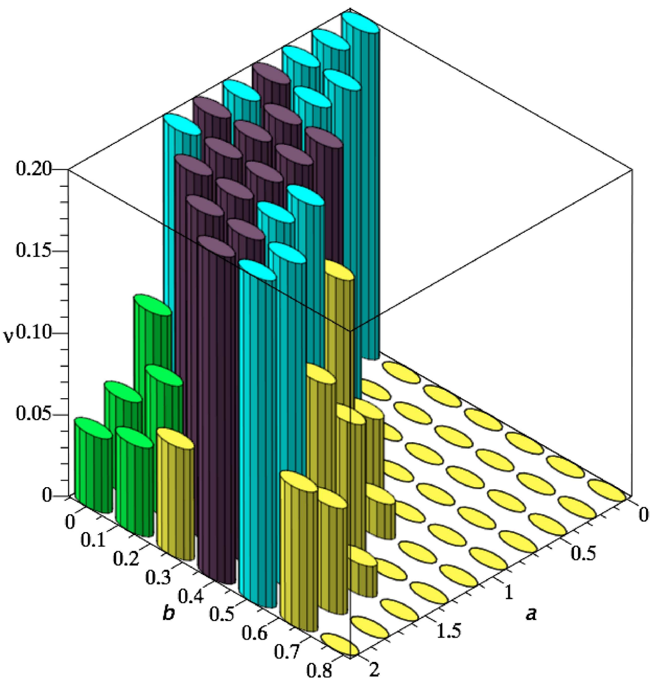

Figure 3: Same as Fig. 2, but with a 8×22 points numerical grid, where in vertical axes is indicated the maximum value of dimensionless central angular velocity of the last stable configuration for each sequence of configurations computed (squeezing for visual purposes).

caption. Here, computations where performed with a 15×40 points numerical grid. From this figure, it is clear that, depending on the choice of rotational parameters, different kinds of configurations can result. It is interesting to study the parameters' space in three dimensions, e.g. taking into account the maximum value of central dimensionless angular velocity reached in each sequence.

In Fig. 3 a three-dimensional plot of the aforementioned kind is presented. It has been obtained considering in x-y plane the same as Fig. 2 and in the vertical axes the maximum dimensionless central angular velocity reached by configurations in each sequence of configurations just before the different kinds of instability occur, but considering a 8×22 points numerical grid. In particular, it is worth noting that the value of central angular velocity goes well beyond the value of 0.2 for each sequence in which a concave hamburger structure appears (this nomenclature follows [17]). This is due to the fact that effective gravity slightly increases along these sequences, although in some cases mass-shedding occurs before the limit of 101 configurations is reached. In addition, some evident differences in color of points of Fig. 2 and Fig. 3 must be underlined manifesting the strong grid-dependence of the model implemented. In Figs. 4, 5, 6 and 7 density distributions of some configurations are plotted, revealing also the shape of configuration. In particular, Fig. 4 is obtained through the solution of Lane-Emden equation (see Appendix A) for the construction of the spherical configuration. From this configuration,

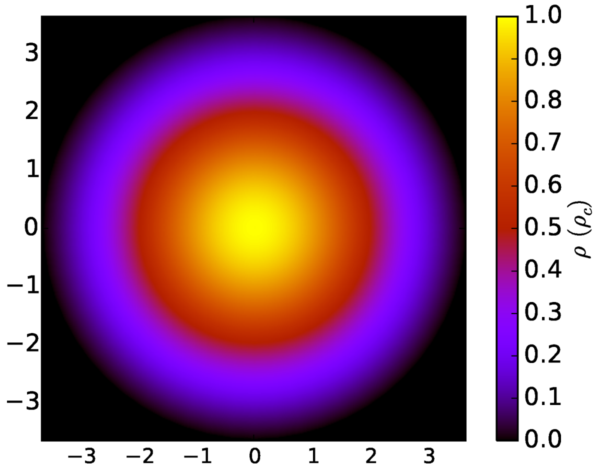

Figure 4: Density distribution for spherical configuration obtained via solution of Lane-Emden equation (see Appendix A).

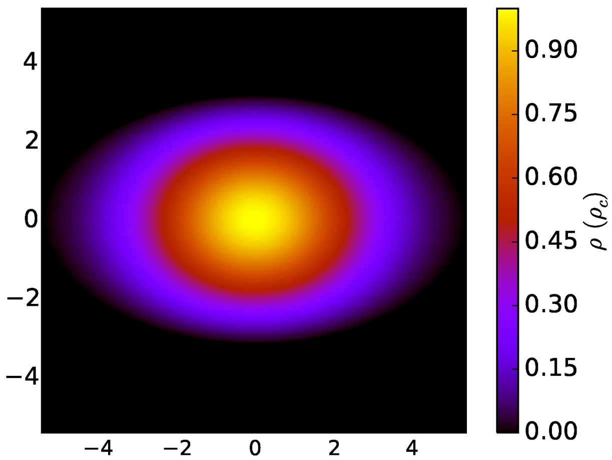

Figure 5: Density distribution for an oblate configuration, obtained fixing $b=0.0$ and $a=2.0$ in Eqs. (2.17), (2.19) and (2.20). The axis ratio value here is $\frac{r_{\rm eq}}{r_{\rm pol}}=1.71$, thus the oblateness is evident. This kind of configuration will undergo to mass-shedding instability, according to Fig. 2.

all the other configurations are obtained by increasing the axis ratio with the method described in Section 2, fixing several values for differential rotation parameters. In Fig. 5, fixing $b=0$ and $a=2.0$ in Eqs. (2.19) and (2.20) and increasing the axis ratio value up to $\frac{r_{\rm eq}}{r_{\rm pol}}=1.71$, produces an evident oblate structure, in which the equatorial centrifugal force will increase until a mass-shedding instability is reached (see Fig. 2). Finally, Figs. 6 and 7 belong to the same sequence of configurations, obtained fixing $b=0.128$ and $a=0.46$ in Eqs. (2.19) and (2.20), respectively with $\frac{r_{\rm eq}}{r_{\rm pol}}=1.22$ and 7.04. In these two figures the forma-

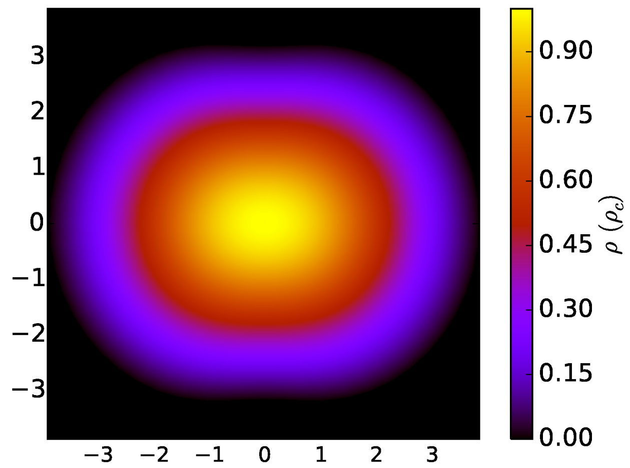

Figure 6: Density distribution for a configuration which is starting to be a concave hamburger one, obtained fixing $b = 0.128$ and $a = 0.46$ in Eqs. (2.17), (2.19) and (2.20). The axis ratio value here is $\frac{r_{\rm eq}}{r_{\rm pol}} = 1.22$ and although it is nearly spherical an accurate observation shows that the differential rotation parameters' value begin to create a oblate hamburger structure.

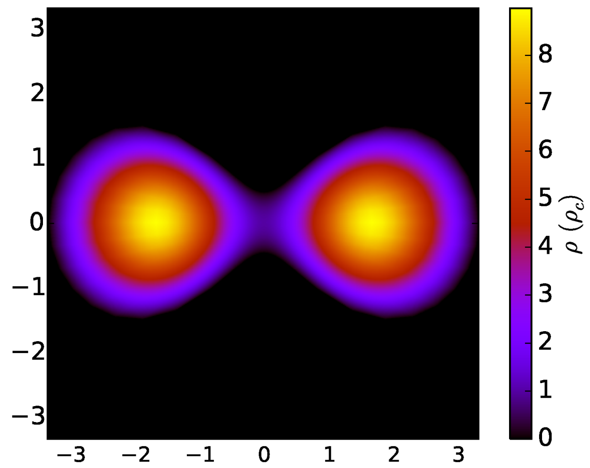

Figure 7: Same as Fig. 6, but with axis ratio value here fixed as $\frac{r_{\rm eq}}{r_{\rm pol}} = 7.04$.

tion of a ring-like structure is evident: as the axis ratio increases, mass density maximum transfers from the center of configuration to a certain grid point and this process, with further increasing in axis ratio, would produce a torus (although in present calculation this result can not be seen, as the method is not appropriate for the study of ring-like structures, see [21] for details; in particular, the present method does not allow to see the hole formation leading to a toroidal configuration).

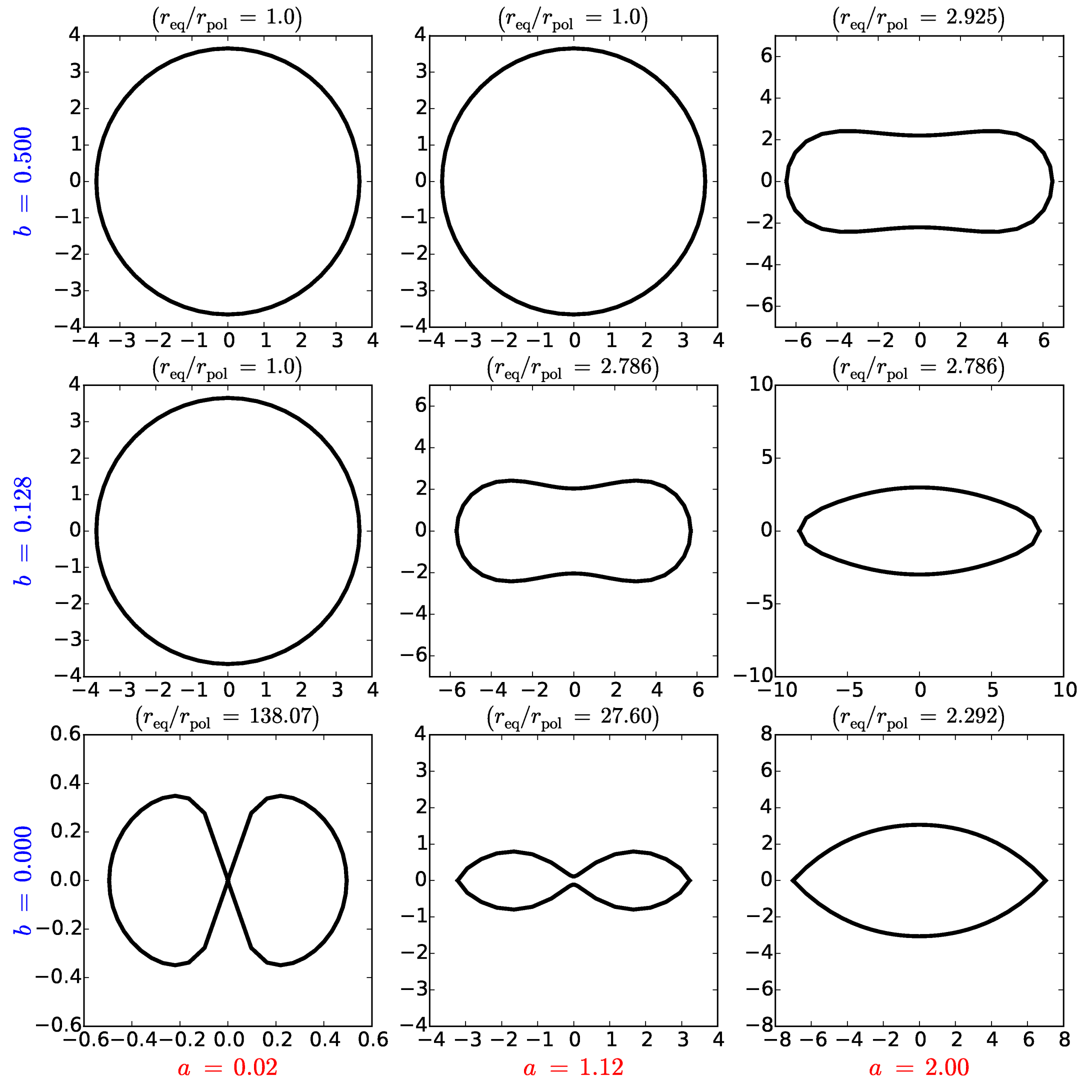

Figure 8: Sample of configurations surfaces for different choices of parameters of differential rotation. Figures show the last stable configurations just before computation is stopped because of aforementioned conditions (namely mass-shedding, violation of Solberg-Høiland criterion or error in N-R method's implementation). For each row and column of figures, values of parameters a and b of Eqs. (2.19) and (2.20) are indicated respectively with red and blue colors. Cusps are an artifact due to the absence of the graphical interpolation between two grid points.

In Fig. 8 we show some samples of possible figures of equilibrium which can be obtained using the differential rotation law of Eqs. (2.17), (2.19) and (2.20), with different choices of free parameters a and b. In particular, each plot corresponds to the last stable configuration which our code produced just before the computation has been stopped due to aforementioned possible reasons (namely mass-shedding, violation of stability criterion, exceeding in the number of configurations). The axis ratio r_{eq}/r_{pol} of each configuration is reported in parentheses above each plot. A spherical figure means that the particular choice of rotational parameter leads immediately to some kind of instability (the reader should refer specifically to Fig. 2). Before concluding this section, an important consideration must be done. Our code adopts the Newton-Raphson (N-R) method as discussed in Ref. [29] in order to compute the solution of a set of non-linear equations. The code uses the LU decomposition method in order to invert the Jacobian matrix but we found in some cases instabilities. In fact, the Newton-Raphson method implemented could lead to local minima of the system, instead to an absolute one. For this reason and because of the strong grid-dependence of Eriguchi and Mueller method, in some cases, the computation could be interrupted for some particular choices of rotational parameters before one of the stopping conditions occurs. How can be possible to recover these missing result? In these cases the grid-dependence study helps us. In fact, one could perform some cross-checks between results obtained using several grids and this guarantees the accuracy of results presented. In particular, for results presented in this section, we compared results obtained with 8×22 and 15×40 grids. We also report in Tables 2-4, the physically relevant values of some of the sequences computed, exemplifying the different configurations of equilibrium obtained. It is worth noting that, although usually convergence may be recovered changing the initial guess, this is not possible for the present situation, because the computation is always starting from the spherically symmetric configuration, obtained by the solution of Eq. (A.9). We also tried to reduce the step of axis ratio from one configuration to another (e.g. 1.01), but neither this could give any benefit to the convergence.

Table 2: Results of our numerical computations for an almost uniformly rotating sequence of equilibrium configurations obtained fixing $b=0$ and $a=2.0$. This sequence will end in mass-shedding.

$\frac{\xi_{eq}}{\xi_{pol}}$	j^2	$\frac{\widetilde{T}}{\lvert\widetilde{W}\rvert}$	$\frac{\widetilde{U}}{\lvert\widetilde{W}\rvert}$	$\widetilde{M}$	V.T.
1.000	0.000000	0.000000	0.500	2.710	9.55e−4
1.158	0.972e−3	0.2861e−1	0.472	2.994	4.87e−4
1.276	0.165e−2	0.4607e−1	0.454	3.156	4.24e−4
1.407	0.234e−2	0.6242e−1	0.438	3.323	3.93e−4
1.551	0.304e−2	0.7720e−1	0.423	3.488	3.71e−4
1.710	0.369e−2	0.9003e−1	0.410	3.643	3.59e−4
1.886	0.425e−2	0.1002000	0.400	3.774	3.48e−4
2.078	0.465e−2	0.1069000	0.393	3.867	3.23e−4
2.292	0.487e−2	0.1102000	0.390	3.934	3.28e−4

3.2 Numerical tests

To test our results with ones from literature, we will refer to tables presented in [21], for the so-called *j-const* rotation law, for choices of parameter $A=2.0r_s$, $0.2r_s$ and $0.02r_s$

Table 3: Results of our numerical computations for an almost uniformly rotating sequence of equilibrium configurations obtained fixing $b=0.0$ and $a=1.12$. This sequence will end in mass-shedding although it will also tend to have a concave hamburger structure.

$\frac{\xi_{eq}}{\xi_{pol}}$	j^2	$\frac{T}{\vert W\vert}$	$\frac{U}{\vert W\vert}$	$\widetilde{M}$	V.T.
1.000	0.000000	0.000000	0.500	2.710	$9.55e-4$
1.477	$0.307e-2$	$0.8168e-1$	0.419	3.565	$4.23e-4$
2.407	$0.853e-2$	0.1873000	0.313	6.146	$5.43e-4$
3.920	$0.133e-1$	0.2583000	0.242	17.172	$6.54e-4$
6.385	$0.166e-1$	0.2763000	0.224	47.965	$9.09e-4$
10.401	$0.187e-1$	0.2867000	0.214	114.025	$7.76e-4$
16.943	$0.201e-1$	0.2949000	0.206	246.237	$7.34e-4$
27.598	$0.212e-1$	0.3016000	0.199	467.418	$8.63e-4$

Table 4: Results of our numerical computations for an almost uniformly rotating sequence of equilibrium configurations obtained fixing $b=0.383$ and $a=1.34$. This sequence will have a concave hamburger structure and it will not reach an instability although 101 configurations are computed.

$\frac{\xi_{eq}}{\xi_{pol}}$	j^2	$\frac{T}{\vert W\vert}$	$\frac{U}{\vert W\vert}$	$\widetilde{M}$	V.T.
1.000	0.000000	0.000000	0.500	2.710	$9.55e-4$
2.079	$0.698e-2$	0.1620000	0.338	5.299	$5.23e-4$
3.733	$0.128e-1$	0.2527000	0.248	16.536	$7.49e-4$
6.705	$0.162e-1$	0.2714000	0.229	54.776	$7.77e-4$
12.041	$0.182e-1$	0.2813000	0.219	150.250	$1.083e-3$
21.623	$0.193e-1$	0.2884000	0.212	378.059	$9.17e-4$
38.833	$0.201e-1$	0.2936000	0.207	915.252	$6.78e-4$
69.739	$0.207e-1$	0.2977000	0.207	2165.079	$7.81e-4$

which are reported in the following Tables 5, 6 and 7. Precisely the definition of quantities reported in each table is the same given in Table 1, with the exception of j^2, the squared dimensionless angular momentum, which in paper [21] is defined as

$$j^2 = \frac{\widetilde{J}^2}{(4\pi)^{\frac{4}{3}}\widetilde{M}^{\frac{10}{3}}\sigma_{\max}^{\frac{n}{3}}}, \tag{3.2}$$

where dimensionless quantities are again defined in Table 1 and $\sigma_{\max}$ is the maximum value of the dimensionless density of configuration. It is worth noting that with rotation law given in Eq. (2.17), keeping parameter $B=0$, one obtains exactly the same aforementioned j-const rotation law. We will now turn to compare results of our computations with values given in Tables 5, 6 and 7, plotting each quantity as a function of axis ratio in the subsequent figures. Calculations have been performed using several numerical grids,

Table 5: Results for numerical computations taken from [21] $A=2.0r_s$.

$\frac{\xi_{eq}}{\xi_{pol}}$	j^2	$\frac{T}{\|W\|}$	$\frac{U}{\|W\|}$	V.T.
1.050	2.966e−4	9.183e−3	0.4911	5.7e−4
1.276	1.622e−3	4.530e−2	0.4549	4.8e−4
1.551	3.0228e−3	7.689e−2	0.4233	4.1e−4
1.886	4.244e−3	9.991e−2	0.4003	4.3e−4
2.292	4.766e−3	1.086e−1	0.3916	4.3e−4

Table 6: Results for numerical computations taken from [21] $A=0.2r_s$.

$\frac{\xi_{eq}}{\xi_{pol}}$	j^2	$\frac{T}{\|W\|}$	$\frac{U}{\|W\|}$	V.T.
1.050	1.521e−4	7.236e−3	0.4931	5.7e−4
1.340	9.305e−4	4.323e−2	0.4570	5.3e−4
1.710	1.789e−3	7.514e−2	0.4251	4.9e−4
2.183	2.616e−3	1.022e−1	0.3991	5.0e−4
2.786	3.446e−3	1.220e−1	0.3783	5.1e−4
3.386	4.089e−3	1.356e−1	0.3647	5.0e−4
4.538	5.037e−3	1.528e−1	0.3475	4.6e−4
5.792	5.840e−3	1.651e−1	0.3352	4.6e−4
7.392	6.639e−3	1.762e−1	0.3240	4.7e−4
9.434	7.446e−3	1.864e−1	0.3138	4.8e−4
12.04	8.290e−3	1.961e−1	0.3042	4.6e−4

Table 7: Results for numerical computations taken from [21] $A=0.02r_s$.

$\frac{\xi_{eq}}{\xi_{pol}}$	j^2	$\frac{T}{\|W\|}$	$\frac{U}{\|W\|}$	V.T.
1.050	3.393e−6	4.472e−4	0.4998	5.8e−4
1.710	5.310e−5	6.282e−3	0.4940	5.6e−4
2.786	1.253e−4	1.302e−2	0.4872	5.5e−4
3.920	1.896e−4	1.808e−2	0.4822	5.5e−4
6.385	3.098e−4	2.596e−2	0.4743	5.5e−4
9.434	4.392e−4	3.331e−2	0.4670	5.5e−4
14.64	6.332e−4	4.305e−2	0.4572	5.4e−4
25.03	9.597e−4	5.705e−2	0.4432	5.4e−4
38.83	1.315e−3	6.996e−2	0.4303	5.2e−4
60.24	1.771e−3	8.428e−2	0.4160	5.1e−4
89.01	2.277e−3	9.806e−2	0.4022	5.0e−4

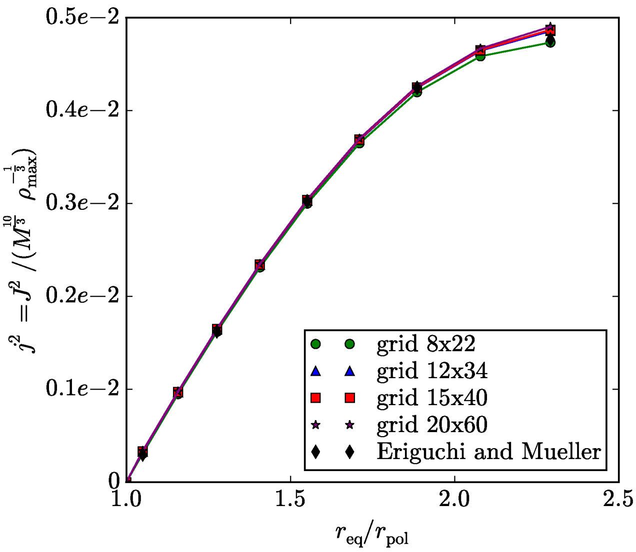

Figure 9: Comparison of results obtained with our own implementation of method by Eriguchi and Mueller and results from Table 5 (thus taking $A = 2.0r_s$), where dimensionless squared angular momentum j^2 is plotted as a function of axis ratio $\frac{r_{\rm eq}}{r_{\rm pol}}$.

to obtain different resolution in configurations. Namely, we considered $N_T \times N_R = 8\times 22$ (green dots in figures), 12×34 (blue triangles), 15×40 (red squares) and 20×60 (purple stars) and in each plot results by Eriguchi and Mueller are represented by black diamonds. In addition, three different values of the rotational parameter have been considered, analogously to results presented in Tables 5, 6 and 7. The step factor for axis ratio change has been taken as 1.05 for the construction of each sequence.

From Figs. 2, 3, 9, 10, 11, 12, 13, 14, 15, 16 and 17 a grid dependent behavior arises from computation: in effect we could not obtain the entire sequences of configurations for all grids considered. For example, if one takes a grid of 10×30 points, the code reaches an error in the Newton-Raphson method. This instability of the code can occur due to the method's implementation. In addition, considering again a step factor "too" small for axis ratio from one configuration to the subsequent, some numerical oscillations occur, most of all in the first sequence of configurations, that is the one in which $A = 2.0r_s$ (or in other words the most rigid one). On the other hand, from these figures the reader can easily notice that deviations from results of paper [21] are negligible thus we may conclude that our code is well calibrated. Moreover, deviations between results obtained with grid 15×40 (red squares) and 20×60 (purple stars) could not be observed, thus, the suggestion given in [21] to use a 15×40 grid to obtain accurate results is confirmed.

In conclusion, it is worth to remember the softening condition taken in [33], where variables are updated from one iteration to another with a softening parameter, usually between 0.5 and 1.0, which often reduce numerical oscillations increasing the rate of convergence. Further studies in this direction would be useful in the present framework.

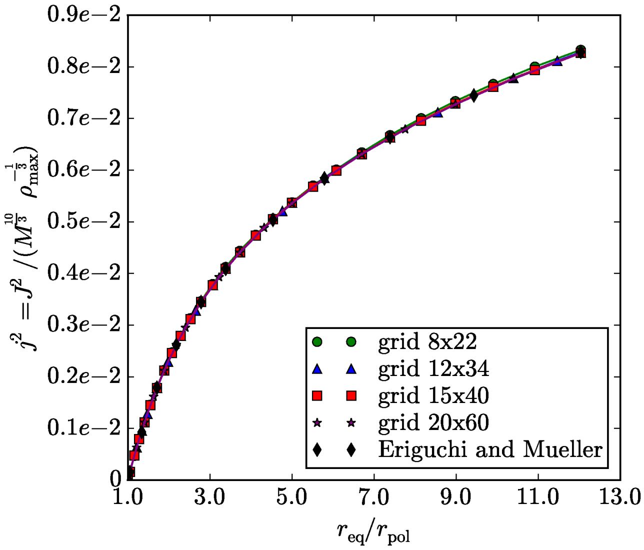

Figure 10: Same as Fig. 9 but in comparison with results from Table 6 (thus taking $A=0.2r_s$).

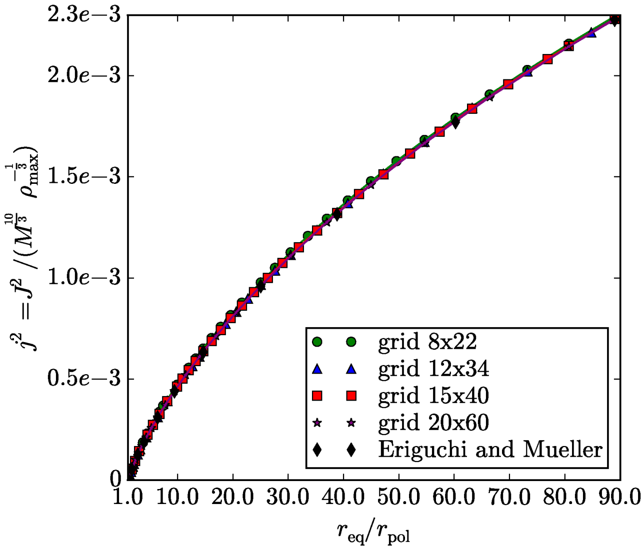

Figure 11: Same as Fig. 9 but in comparison with results from Table 7 (thus taking $A=0.02r_s$).

4 Summary and discussion

In this paper we have implemented a multi-parametric rotation law proposed in [25] with the method introduced by Eriguchi and Mueller in [21] and studied in detail the corresponding configurations. We had treated the stability of differentially rotating polytropic stars against violations of Solberg-Høiland criterion and mass-shedding, analysing the

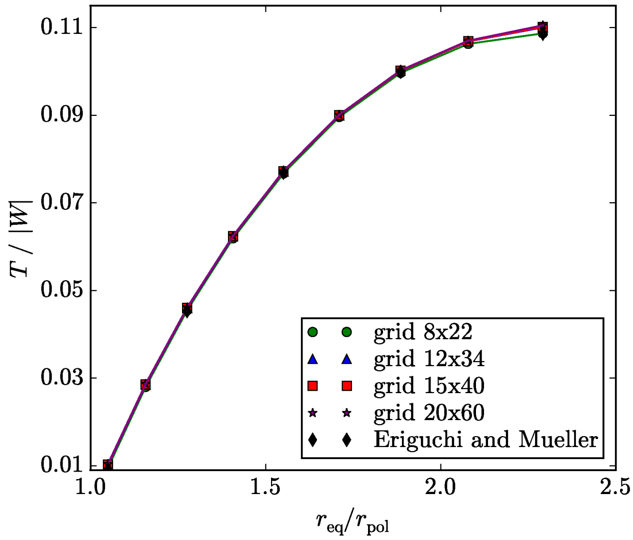

Figure 12: Comparison of results obtained with our own implementation of method by Eriguchi and Mueller and results form Table 5 (thus taking $A=2.0r_s$), where ratio between rotational kinetic energy and gravitational potential energy is plotted as a function of axis ratio $\frac{r_{eq}}{r_{pol}}$.

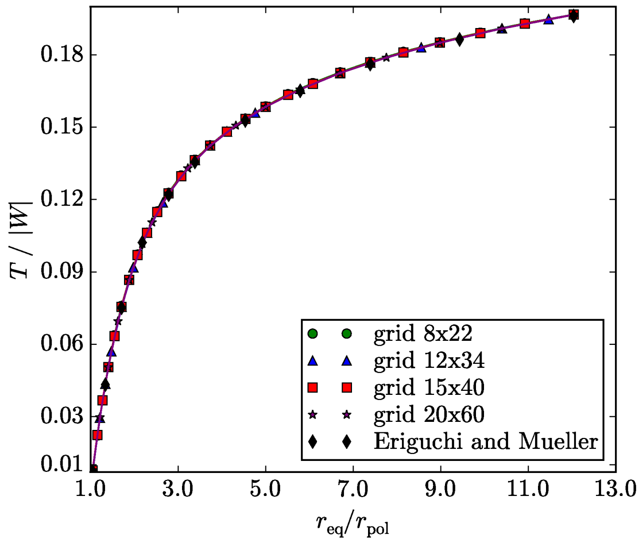

Figure 13: Same as Fig. 12 but in comparison with results from Table 6 (thus taking $A=0.2r_s$).

free-parameters' space in search of sort of catastrophic points at which small changes in free-parameters can lead to relevant changes in the equilibrium configuration (e.g. from a concave hamburger to an ellipsoidal one) or to instabilities. It is worth noting that the rotation law as a function of the distance from the axis of rotation (namely the cylindrical

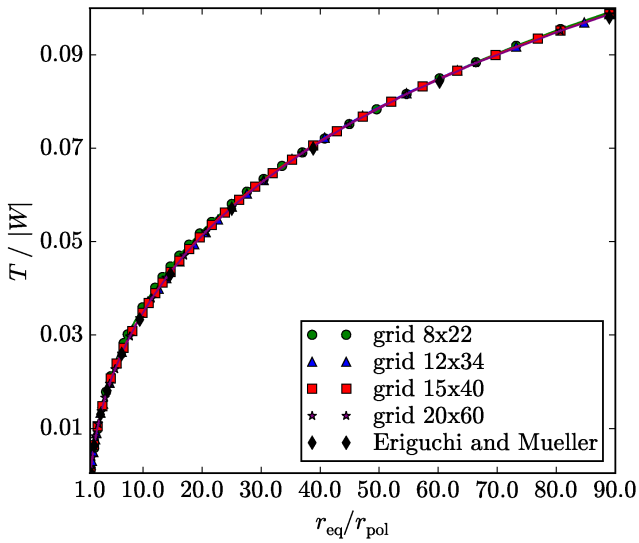

Figure 14: Same as Fig. 12 but in comparison with results from Table 7 (thus taking $A=0.02r_s$).

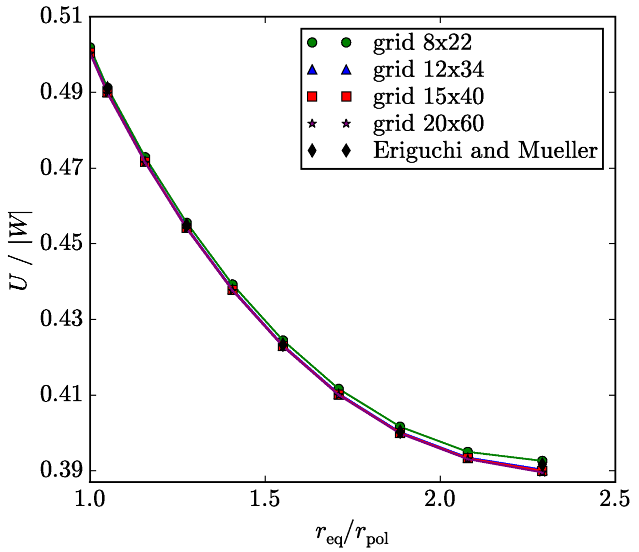

Figure 15: Comparison of results obtained with our own implementation of method by Eriguchi and Mueller and results form Table 5 (thus taking $A=2.0r_s$), where ratio between thermal energy and gravitational potential energy is plotted as a function of axis ratio $\frac{r_{eq}}{r_{pol}}$.

radius) introduced in Eq. (2.17) in a strictly decreasing one. For future studies, we would like to stress the necessity to focus on achievement of an improved convergence, as already mentioned in Section 3, possibly obtained by introducing a softening condition as the one presented in [33]. In addition, it would be interesting also to implement a non-

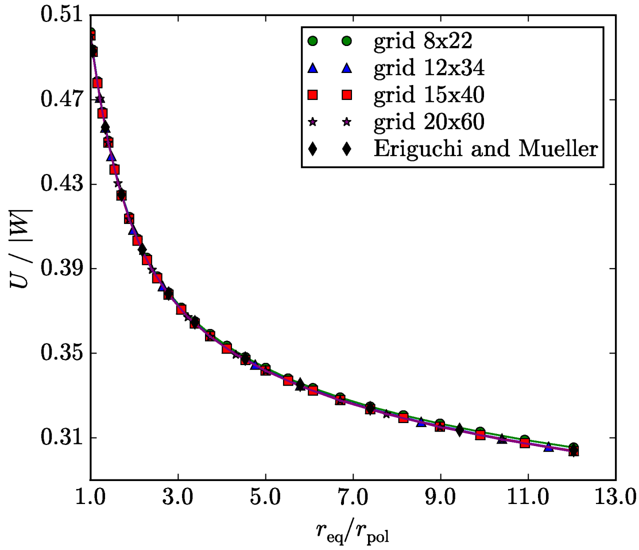

Figure 16: Same as Fig. 15 but in comparison with results from Table 6 (thus taking $A=0.2r_s$).

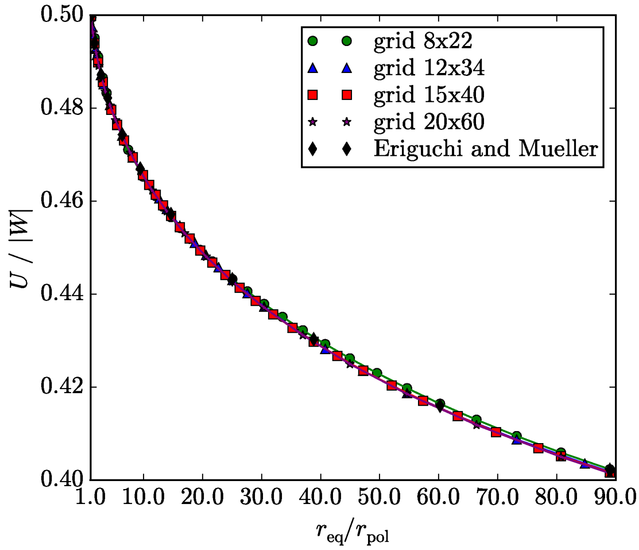

Figure 17: Same as Fig. 15 but in comparison with results from Table 7 (thus taking $A=0.02r_s$).

completely decreasing rotation law, where angular velocity may also increase in small portion of the configuration, e.g. one interesting case could be, for instance, the one in which the angular velocity in not a strictly decreasing function of the cylindrical radius as in the case of the coalescence of the two component of a binary system (for example of white dwarfs), during merging. In effect the idea to perform numerical integration in order to obtain the centrifugal potential allows one to study every kind of rotation law, and studying the free-parameters space as in the way we propose, should in general allow to locate instability points. We would also focus the attention to the fact that the method presented in [21] is in principle a general one, thus it should allow to consider different kinds of EOS. In the present case, all previously presented results were obtained with a $n=1.5$ polytropic EOS, but it could also be interesting to treat the case of a numerical EOS, in which no analytical relation is known.

Appendix

A Numerical implementation and physical properties

A.1 Numerical method

Once an EOS and a rotation law are supplied, to solve the system of equations defined by Eqs. (2.14), (2.15) and (2.12), in [21] a numerical method has been presented in which the interior of the star is discretized in a mesh of points. Considering spherical coordinates, a grid is built dividing the domain into N_T points along the θ-direction, and in N_R points along each r-direction. Grid points are defined as follows:

$$\theta_i = \frac{\pi}{2}\frac{i-1}{N_T-1}, \quad i=1,\cdots,N_T, \tag{A.1}$$

$$r_{ij} = r_j(\theta_i) = r_{\mathrm{surf}}(\theta_i)\frac{j}{N_R}, \quad i=1,\cdots,N_T, \; j=1,\cdots,N_R. \tag{A.2}$$

In particular, this grid does not consider the center of configuration because it has to be treated separately from other points. Note in addition that the angular values vary between 0 and $\frac{\pi}{2}$, as equatorial symmetry is taken into account, while there is no dependence on the φ coordinate as expected by axial symmetry. Then, with the use of dimensionless variables as given in Table 1 it is possible to discretize the equations. Explicitly writing the system for the fixed EOS and the rotation law, one can note that a model is completely determined by the prescription of polytropic constant K, central density ρ_c and angular velocity Ω (this last condition holds in the case of uniform rotation; in case of differential rotation one should instead fix the central value of angular velocity only, knowing that the values in all other points are given by the chosen rotation law). In the method by Eriguchi and Mueller [21], it is stressed that fixing the angular velocity is not the best way to solve the system of equation. Instead a better choice for numerical calculation is to fix the axis ratio, namely $\frac{r_{\mathrm{eq}}}{r_{\mathrm{pol}}} = \frac{r_{N_R}(\frac{\pi}{2})}{r_{N_R}(0)} = \frac{\xi_{\mathrm{eq}}}{\xi_{\mathrm{pol}}}$, the last equality obtained by the introduction of the dimensionless radial coordinate. This condition gives one last equation which will make the system solvable (see discussion on the number of equations and variables at the end of the present section). Now we can write the discretized system of equations, which will read as follows:

(i) at the centre of configuration:

$$1+\Psi_{\text{centre}}=C, \tag{A.3}$$

$$\Psi_{\text{centre}}=-\sum_{p=1}^{N_T}\sin(\theta_p)\Theta_p\sum_{q=1}^{N_R}\xi_{pq}R_{pq}\sigma_{pq}^n; \tag{A.4}$$

(ii) at all the grid points:

$$\sigma_{ij}+\Psi_{ij}-\frac{1}{2}\nu\xi_{ij}^2\sin(\theta_i)^2=C, \tag{A.5}$$

$$\begin{aligned}\Psi_{ij}=&-\sum_{p=1}^{N_T}\sin(\theta_p)\Theta_p\sum_{q=1}^{N_R}\xi_{pq}^2R_{pq}\sigma_{pq}^n\\ &\cdot\sum_{m=0}^{\infty}f_{2m}(\xi_{ij},\xi_{pq})P_{2n}(\cos(\theta_i))P_{2n}(\cos(\theta_p))\sigma_{pq}^n;\end{aligned} \tag{A.6}$$

(iii) boundary conditions to define the surface:

$$\sigma_{i,N_R}=0, \quad \text{for } \ i=1,\cdots,N_T; \tag{A.7}$$

(iv) a last equation for the axis ratio:

$$\frac{\xi_{N_T,N_R}}{\xi_{1,N_R}}=\lambda. \tag{A.8}$$

To note that in Eqs. (A.4) and (A.6), the integral over the volume is discretized. In particular, the terms Θ_p and R_{pq} denote respectively angular and radial grid spacings multiplied by weight factors which depend on the numerical integration scheme which in radial direction is the Simpson rule while in angular direction is the trapezoidal rule. The system of $N_T\times(N_R+1)+2$ equations for the same number of unknowns (namely N_T surface radii, $N_T\times N_R$ densities in each grid-point, the central value of angular velocity and the integration constant which turns out to be the gravitational potential at the pole) can be solved using an iterative numerical method, such the one called the Newton-Raphson's. The Newton-Raphson's method in [21] starts from a spherical (non-rotating) configuration and gradually increases the axis ratio of the configuration by a constant factor near 1 (for example 1.05 or less) to obtain a new configuration and then repeats the procedure until a certain stopping condition is reached. The computation of a spherically symmetric model (meant as the density distribution and the surface radius) of a polytropic star of index n is a well-known problem in astrophysics and it was studied by many authors in the past (see e.g. [30]). The equation to solve, namely the Lane-Emden equation, reads

$$\frac{1}{\xi^2}\frac{\partial}{\partial\xi}\left(\xi^2\frac{\partial\sigma(\xi)}{\partial\xi}\right)+\sigma(\xi)^n=0, \tag{A.9}$$

where we have adopted the same notation for dimensionless variables as in the Section 1. One can solve Eq. (A.9) numerically, finding $\sigma(\xi)$, imposing as initial conditions

$$\sigma(0)=1, \tag{A.10a}$$
$$\sigma'(0)=0. \tag{A.10b}$$

Through a Newton-Raphson iteration scheme, one can also find the zero of function $\sigma(\xi)$, which represents the surface radius of the spherical solution. Finally, one can put $\nu=\nu_0=0$ and find $C\equiv C_0$ with expression given by Eq. (A.5) in which Eq. (A.6) can be used.

A.2 Definition of relevant physical quantities

Once the density distribution and surface radii of a configuration are computed, one could also evaluate its physical properties (cf. [27] and [31]). Firstly, the rotational kinetic energy of a rotating configuration can be found with the following expression

$$T=\frac{1}{2}\int_V \rho\varpi^2\Omega^2 dV, \tag{A.11}$$

where V is the volume, ϖ is the cylindrical radius (distance from the axis of rotation, thus $\varpi=r\sin(\theta)$ when spherical coordinates are considered) and ρ represents as usual the density. The gravitational potential energy, on the other hand, can be computed as

$$W=-\frac{1}{2}G\int_V \rho\Phi_g dV, \tag{A.12}$$

being G the constant of gravitation and Φ_g the gravitational potential, which can be computed with Eq. (2.11). The internal energy of the system reads as

$$U=\frac{1}{\gamma-1}\int_V \rho dV, \tag{A.13}$$

where γ is the polytropic adiabatic exponent defined as $\gamma=1+\frac{1}{n}$. Obviously the total mass of the configuration is simply

$$M=\int_V \rho dV, \tag{A.14}$$

while the total angular momentum is given by

$$J=\int_V \rho\Omega\varpi^2 dV. \tag{A.15}$$

Finally another quantity which is worth computing is the value of virial test, which in [21] (just as in [32]) is expressed in the following form

$$V.T.=\left|\frac{(2T+W+3(\gamma-1)U)}{W}\right|, \tag{A.16}$$

and it should be zero in order to have an accurate model.

Acknowledgments

C.C. and S.F. acknowledge INdAM-GNFM and ICRANet for support. J.A.R. acknowledges partial support of the project No. 3101/GF4 IPC-11/2015 and the target program of the Ministry of Education and Science of the Republic of Kazakhstan.

References

[1] Chandrasekhar, S., 1967: An Introduction to the Study of Stellar Structure, Dover.

[2] Chandrasekhar, S., 1987: Ellipsoidal Figures of Equilibrium, Dover.

[3] James R. A., 1964: The Structure and Stability of Rotating Gas Masses, Astrophys. J., 140, 552-582.

[4] Busarello, G., Filippi, S. and Ruffini R., 1988: Anisotropic tensor virial models for elliptical galaxies with rotation or vorticity, Astron. Astrophys., 197, 91-104.

[5] Busarello G., Filippi S. and Ruffini R., 1989: Anisotropic and inhomogeneous tensor virial models for elliptical galaxies with figure rotation and internal streaming, Astron. Astrophys., 213, 80-88.

[6] Busarello G., Filippi S. and Ruffini R., 1990: 'b-type' spheroids, Astron. Astrophys., 227, 30-32.

[7] Filippi S., Ruffini R. and Sepulveda A., 1990: Generalized Riemann configurations and Dedekind's theorem - The case of non-linear internal velocities, Astron. Astrophys., 231, 30-40.

[8] Filippi, S.; Ruffini, R.; Sepulveda, A. 1990: On the generalization of Dedekind-Riemann sequences to nonlinear velocities., Europhys. Lett., 12, 735-740.

[9] Filippi, S.; Ruffini, R.; Sepulveda, A., 1990: Nonlinear velocities in generalized Riemann ellipsoids., Nuovo Cim. B, 105, 1047-1054.

[10] Filippi S., Ruffini R. and Sepulveda A., 1991: Generalized Riemann ellipsoids - Equilibrium and stability, Astron. Astrophys., 246, 59-70.

[11] Filippi S., Ruffini R. and Sepulveda A., 1996: On the Implications of the nth-Order Virial Equations for Heterogeneous and Concentric Jacobi, Dedekind, and Riemann Ellipsoids, Astrophys. J., 460, 762

[12] Filippi S., Ruffini R. and Sepulveda A., 2002: Functional approach to the problem of self-gravitating systems: Conditions of integrability, Phys. Rev. D, 65, 044019.

[13] Eriguchi Y. and Sugimoto D. 1981: Another Equilibrium Sequences of Self-Gravitating and Rotating Incompressible Fluid, Prog. Theor. Phys., 65, 1870-1875.

[14] Sugimoto D., Nomoto K. and Eriguchi Y. 1981: Stable Numerical Method in Computing of Stellar Evolution, Prog. Theor. Phys. Supp., 70, 115-131.

[15] Eriguchi Y. and Hachisu I., 1982: New Equilibrium Sequences Bifurcating from Maclaurin Sequence, Prog. Theor. Phys., 67, 844-851.

[16] Eriguchi Y., Hachisu I. and Sugimoto D., 1982: Dumb-Bell Shape Equilibrium and Mass Shedding Pear-Shape of Self-Gravitating Incompressible Fluid, Prog. Theor. Phys., 67, 1068-1075.

[17] Hachisu I., Eriguchi Y., and Sugimoto D. 1982: Rapidly Rotating Polytropes and Concave Hamburger Equilibrium, Prog. Theor. Phys., 68, 191-205.

[18] Hachisu I. and Eriguchi Y., 1982: Bifurcation and Fission of Three Dimensional, Rigidly Rotating and Self-Gravitating Polytropes, Prog. Theor. Phys., 68, 206-221.

[19] Eriguchi Y. and Hachisu I., 1983: Two Kinds of Axially Symmetric Equilibrium Sequences of Self-Gravitating and Rotating Incompressible Fluid, Prog. Theor. Phys., 69, 1131-1136.
[20] Hachisu I. and Eriguchi Y., 1983: Bifurcation and Phase Transitions of Self-Gravitating and Uniformly Rotating Fluid, Mon. Not. R. Astron. Soc., 204, 583-589.
[21] Eriguchi Y. and & Mueller E.: 1985, A general computational method for obtaining equilibria of self-gravitating and rotating gases, Astron. Astrophys., 146, 260-268.
[22] Stoeckly R., 1965: Polytropic Models with Fast, Non-Uniform Rotation, Astrophys. J., 142, 208-228.
[23] Fujisawa K., 2015: A versatile numerical method for obtaining structures of rapidly rotating baroclinic stars: self-consistent and systematic solutions with shellular-type rotation, Mon. Not. R. Astron. Soc., 454, 3060-3072.
[24] Galeazzi F., Yoshida S. and Eriguchi Y., 2012: Differentially-rotating neutron star models with a parametrized rotation profile, Astron. Astrophys., 541, A156.
[25] Cherubini C., Filippi S., Ruffini R., Sepulveda A. and Zuluaga J. I., 2008: Non-Homogeneous Axisymmetric Models of Self-Gravitating Systems. The Eleventh Marcel Grossmann Meeting On Recent Developments in Theoretical and Experimental General Relativity, Gravitation and Relativistic Field Theories, 2340-2342.
[26] Tassoul, J.-L., 1978: Theory of rotating stars. Princeton Series in Astrophysics, Princeton University Press.
[27] Horedt, G. P., 2004: Polytropes - Applications in Astrophysics and Related Fields. Kluwer Academic Publishers.
[28] Maeder, A., 2009: Physics, Formation and Evolution of Rotating Stars. Astronomy and Astrophysics, Springer, Berlin.
[29] Press, W. H., Teukolsky, S. A., Vetterling, W. T. and Flannery, B. P., 1992: Numerical recipes in C. The art of scientific computing. Cambridge University Press, 2nd ed.
[30] Chandrasekhar S., 1933: The equilibrium of distorted polytropes. I. The rotational problem, Mon. Not. R. Astron. Soc., 93, 390-406.
[31] Chandrasekhar S., 1961: Hydrodynamic and hydromagnetic stability. Dover Publications.
[32] Ostriker J. P. and Bodenheimer P., 1968: Rapidly Rotating Stars. II. Massive White Dwarfs, Astrophys. J., 151, 1089-1098.
[33] Uryū K., Limousin F., Friedman J.L., Gourgoulhon E. and Shibata, M., 2009: Nonconformally flat initial data for binary compact objects, Phys. Rev. D, 80, 124004.

PHYSICAL REVIEW D **96,** 024046 (2017)

Last stable orbit around rapidly rotating neutron stars

F. Cipolletta,[1,*] C. Cherubini,[2,3,†] S. Filippi,[2,3,‡] J. A. Rueda,[1,4,5,§] and R. Ruffini[1,4,5,‖]

[1] *Dipartimento di Fisica and ICRA, Sapienza Università di Roma, P.le Aldo Moro 5, I–00185 Rome, Italy*
[2] *Unit of Nonlinear Physics and Mathematical Modeling, University Campus Bio-Medico of Rome, Via A. del Portillo 21, I–00128 Rome, Italy*
[3] *International Center for Relativistic Astrophysics-ICRA, University Campus Bio-Medico of Rome, Via A. del Portillo 21, I–00128 Rome, Italy*
[4] *ICRANet, Piazza della Repubblica 10, I–65122 Pescara, Italy*
[5] *ICRANet-Rio, Centro Brasileiro de Pesquisas Físicas, Rua Dr. Xavier Sigaud 150, Rio de Janeiro, Rio de Janeiro 22290–180, Brazil*
(Received 7 December 2016; published 25 July 2017)

We compute the binding energy and angular momentum of a test particle at the last stable circular orbit (LSO) on the equatorial plane around a general relativistic, rotating neutron star (NS). We present simple, analytic, but accurate formulas for these quantities that fit the numerical results and which can be used in several astrophysical applications. We demonstrate the accuracy of these formulas for three different equations of state (EOS) based on nuclear relativistic mean-field theory models and argue that they should remain still valid for any NS EOS that satisfy current astrophysical constraints. We compare and contrast our numerical results with the corresponding ones for the Kerr metric characterized by the same mass and angular momentum.

DOI: 10.1103/PhysRevD.96.024046

I. INTRODUCTION

It is well known that the knowledge of the properties of the circular orbits of test particles, e.g., energy and angular momentum around compact objects such as neutron stars (NSs) and black holes (BHs) are of paramount importance for the understanding of several astrophysical scenarios such as the accretion processes in binary x-ray sources [1].

The precise knowledge of NS properties is essential for the correct description of the NS structure evolution during the accretion process. This is particulary relevant in the evolution of accreting NSs in x-ray binaries leading to the NS spin-up and final formation of the millisecond *recycled* pulsars [2]. It is by now clear that the inclusion in the accretion process of subtle effects such as the NS binding energy [3], and the precise energy and angular momentum trasnferred to the NS including general relativistic effects and the NS interior compression [4,5], can have an impact in the determination of the correct evolutionary scenario and therefore in the determination of the binary progenitors of millisecond pulsars (see, e.g., Refs. [6–8]).

On the other hand, it has been shown that such an information becomes also relevant within the induced gravitational paradigm of gamma-ray bursts (GRBs), where a hypercritical accretion process is triggered onto a NS by the supernova explosion of a binary companion carbon-oxygen core [9–13]. In contrast to binary x-ray sources in which the NS accretes matter from a companion at sub-Eddington rates $\dot{M} \equiv dM/dt \lesssim 10^{-8}\, M_\odot\, \mathrm{y}^{-1}$, hence evolving quietly on very long time scales $t_{\rm acc} \equiv M/\dot{M} \gtrsim 10^8$ y, the aforementioned hypercritical accretion process in GRBs leads to a NS which evolves in time scales as short as $t_{\rm acc} = M/\dot{M} \sim 10^2$ s. In such a short time interval, the NS can reach either the mass-shedding or the secular axisymmetric instability with consequent gravitational collapse to a BH (see, e.g., Refs. [10,11,13]).

It is clear that the description of processes similar to the above one needs the knowledge of the properties of the NS interior, of its exterior spacetime, and of the circular orbits around it. The aim of this article is to provide these ingredients.

Uniformly rotating NS equilibrium configurations form a two-parameter family of solutions characterized by baryonic mass M_b and angular momentum J. We can write the evolution of a uniformly rotating NS gravitational mass M as:

$$\dot{M} = \left(\frac{\partial M}{\partial M_b}\right)_J \dot{M}_b + \left(\frac{\partial M}{\partial J}\right)_{M_b} \dot{J}, \tag{1}$$

where $\dot{M}_b$ and $\dot{J}$ are the amount of baryonic mass and angular momentum being transferred to the NS per-unit-time, namely the mass accretion rate and torque acting onto the NS. The two above partial derivatives have to be obtained from the relation $M(M_b, J)$ which is obtained numerically. We have recently found in Ref. [14] that,

*cipo87@gmail.com
†c.cherubini@unicampus.it
‡s.filippi@unicampus.it
§jorge.rueda@icra.it
‖ruffini@icra.it

independent on the nuclear equation of state (EOS), such a relation for uniformly rotating NSs is well fitted by

$$\frac{M_b}{M_\odot} = \frac{M}{M_\odot} + \frac{13}{200}\left(\frac{M}{M_\odot}\right)^2\left(1 - \frac{1}{130}j^{1.7}\right), \tag{2}$$

where $j \equiv cJ/(GM_\odot^2)$. This relation has been shown to be very accurate also in the description of the binding energy of other nuclear EOS models including hyperonic and hybrid ones [15].

The total energy released in an accretion process is given by the amount of gravitational energy gained by the material in its way to the NS surface and that is not spent in increasing the gravitational binding energy of the NS, namely (see, e.g., [11,16]):

$$\begin{aligned} L_{\rm acc} &= (\dot{M}_b - \dot{M})c^2 \\ &= \dot{M}_b c^2\left[1 - \left(\frac{\partial M}{\partial J}\right)_{M_b}\frac{\dot{J}}{\dot{M}_b} - \left(\frac{\partial M}{\partial M_b}\right)_J\right], \end{aligned} \tag{3}$$

where we have used Eq. (1).

If the accretion of matter comes from a disk-like structure, *such a total radiated energy* $L_{\rm acc}$ *is given by the sum of the energy radiated in the disk*, $L_{\rm disk}$, *and the energy radiated at the NS surface when the material is incorporated to the star*, L_s, *i.e.*

$$L_{\rm acc} = L_s + L_{\rm disk}. \tag{4}$$

In the case when the magnetic field effects can be neglected, the inner boundary of an accretion disk around a compact object is assumed to be given by the radius of the last stable circular orbit (hereafter LSO) of a test particle of mass $\mu \ll M$. Thus, the knowledge of the energy and angular momentum of a test particle at the LSO is essential for the determination of the evolution of the NS during the accretion process. We denote hereafter by $\tilde{E} \equiv E/\mu$ and $\tilde{L} \equiv L/(G\mu M/c)$ the energy per-unit-mass and dimensionless angular momentum of a particle at the LSO.

From energy and angular momentum conservation we have that the mass-energy and angular momentum transferred to the NS from a particle infalling from the LSO are (see, e.g., Ref. [16]):

$$\dot{M}c^2 = \tilde{E}\dot{M}_b c^2 - L_s \tag{5}$$

$$\dot{J} = \dot{M}_b \tilde{L}\frac{GM}{c}. \tag{6}$$

Equations (1)–(6) lead, therefore, to the surface luminosity,

$$L_s = \dot{M}_b c^2\left[\tilde{E} - \left(\frac{\partial M}{\partial J}\right)_{M_b}\tilde{L}\frac{GM}{c} - \left(\frac{\partial M}{\partial M_b}\right)_J\right], \tag{7}$$

and to the disk luminosity

$$L_{\rm disk} \equiv L_{\rm acc} - L_s = \dot{M}_b c^2(1 - \tilde{E}). \tag{8}$$

From Eqs. (1)–(6), one can compute the time evolution of the mass and angular momentum of the NS in an accretion process, providing we know how $\tilde{E}$ and $\tilde{L}$ depend on the gravitational (or on the baryonic mass) and angular momentum of the NS. At the same time, Eqs. (7) and (8) give us, respectively, the surface and disk luminosities which are important from the observational point of view. It is worth to mention that the contribution of L_s and $L_{\rm disk}$ to the total radiated energy can be comparable depending on the angular momentum [16].

In this article we present simple but accurate fitting formulas of $\tilde{E}(M,J)$ and $\tilde{L}(M,J)$ both for corotating and counter-rotating orbits around rotating NS and are valid for any rotation rate within the NS region of stability bounded by mass-shedding and secular axisymmetric instability limits.

We show below that the aforementioned formulas for $\tilde{E}(M,J)$ and $\tilde{L}(M,J)$ are shown to be the same for three different nuclear EOS based on relativistic mean-field theory, suggesting a possible *universal* character. We elaborate on this concept and show that current astrophysical constraints imply that, indeed, our formulas should remain valid for other astrophysically relevant set of EOS and for the relevant NS masses leading to an LSO located outside the NS surface.

Despite the complexity of NSs and the still debated EOS governing their interior physics, there have been discovered features which seem to be EOS-independent such as the relation between the moment of inertia, Love number and quadrupole moment, i.e. the I-Love-Q relation [17,18], and the NS binding energy shown in Eq. (2) [14]. We show in this work that indeed also the energy and angular momentum of the LSO around rotating NSs are very weakly EOS-dependent properties in the limits established by current astrophysical constraints. All the above allow the construction of a set of analytic and/or semianalytic set of NS properties that can be used in a variety of NS astrophysical scenarios as the accretion process exemplified above.

The article is organized as follows. In Sec. II, we compute the interior and exterior spacetime geometry of uniformly rotating NSs. The general formulation of the problem of circular orbits is recalled in Sec. III. Then, in Sec. IV, we compute the configurations for which there exists a LSO outside the NS surface. In Sec. V, we focus on those configurations and compute the binding energy and angular momentum of the LSO. Finally, we shall present simple but very accurate fitting formulas for these quantities.

II. NEUTRON STAR STRUCTURE AND SPACETIME GEOMETRY

We first compute the interior and exterior spacetime of uniformly rotating NSs in order to derive the equations of motion for the test particle. Following [14], we consider the stationary axisymmetric spacetime metric in quasi-isotropic coordinates and in geometric units $c = G = 1$ [19],

$$ds^2 = -e^{\gamma+\rho}dt^2 + e^{\gamma-\rho}r^2\sin^2\theta(d\phi - \omega dt)^2 + e^{2\lambda}(dr^2 + r^2 d\theta^2), \tag{9}$$

where γ, ρ, ω and λ depend only on variables r and θ.

It is useful to introduce the variable $e^{\psi} = r\sin(\theta)Be^{-\nu}$, being again $B = B(r,\theta)$. The energy-momentum tensor of the NS interior is given by

$$T^{\alpha\beta} = (\varepsilon + P)u^\alpha u^\beta + Pg^{\alpha\beta}, \tag{10}$$

where ε and P denote the energy density and pressure of the fluid, and u^α is the fluid 4-velocity. Thus, with the metric given by equation (9) and the above energy-momentum tensor, one can write the field equations as (setting $\zeta = \lambda + \nu$):

$$\nabla\cdot(B\nabla\nu) = \frac{1}{2}r^2\sin^2\theta B^3 e^{-4\nu}\nabla\omega\cdot\nabla\omega + 4\pi B e^{2\zeta-2\nu}\left[\frac{(\varepsilon+P)(1+v^2)}{1-v^2} + 2P\right], \tag{11a}$$

$$\nabla\cdot(r^2\sin^2\theta B^3 e^{-4\nu}\nabla\omega) = -16\pi r\sin\theta B^2 e^{2\zeta-4\nu}\frac{(\varepsilon+P)v}{1-v^2}, \tag{11b}$$

$$\nabla\cdot(r\sin(\theta)\nabla B) = 16\pi r\sin\theta B e^{2\zeta-2\nu}P, \tag{11c}$$

$$\begin{aligned}
\zeta_{,\mu} = -&\left\{(1-\mu^2)\left(1 + r\frac{B_{,r}}{B}\right)^2 + \left[\mu - (1-\mu^2)\frac{B_{,r}}{B}\right]^2\right\}^{-1}\left[\frac{1}{2}B^{-1}\{r^2 B_{,rr} - [(1-\mu^2)B_{,\mu}]_{,\mu} - 2\mu B_{,\mu}\}\right.\\
&\times\left\{-\mu + (1-\mu^2)\frac{B_{,\mu}}{B}\right\} + r\frac{B_{,r}}{B}\left[\frac{1}{2}\mu + \mu r\frac{B_{,r}}{B} + \frac{1}{2}(1-\mu^2)\frac{B_{,\mu}}{B}\right] + \frac{3}{2}\frac{B_{,\mu}}{B}\left[-\mu^2 + \mu(1-\mu^2)\frac{B_{,\mu}}{B}\right]\\
&-(1-\mu^2)r\frac{B_{,\mu r}}{B}\left(1 + r\frac{B_{,r}}{B}\right) - \mu r^2(\nu_{,r})^2 - 2(1-\mu^2)r\nu_{,\mu}\nu_{,r} + \mu(1-\mu^2)(\nu_{,\mu})^2 - 2(1-\mu^2)r^2B^{-1}B_{,r}\nu_{,\mu}\nu_{,r}\\
&+(1-\mu^2)B^{-1}B_{,\mu}[r^2(\nu_{,r})^2 - (1-\mu^2)(\nu_{,\mu})^2] + (1-\mu^2)B^2e^{-4\nu}\left\{\frac{1}{4}\mu r^4(\omega_{,r})^2 + \frac{1}{2}(1-\mu^2)r^3\omega_{,\mu}\omega_{,r}\right.\\
&\left.\left.-\frac{1}{4}\mu(1-\mu^2)r^2(\omega_{,\mu})^2 + \frac{1}{2}(1-\mu^2)r^4B^{-1}B_{,r}\omega_{,\mu}\omega_{,r} - \frac{1}{4}(1-\mu^2)r^2B^{-1}B_{,\mu}[r^2(\omega_{,r})^2 - (-\mu^2)(\omega_{,\mu})^2]\right\}\right],
\end{aligned} \tag{11d}$$

where, in the equation for $\zeta_{,\mu}$, we introduced $\mu \equiv \cos(\theta)$.

The NS interior is made of a core and a crust. The core of the star has densities higher than the nuclear value, $\rho_{\rm nuc} \approx 3\times 10^{14}$ g cm^{-3}, and it is composed by a degenerate gas of baryons (e.g. neutrons, protons, hyperons) and leptons (e.g. electrons and muons). The crust, in its outer region ($\rho \le \rho_{\rm drip} \approx 4.3\times 10^{11}$ g cm^{-3}), is composed of ions and electrons, and in the so-called inner crust ($\rho_{\rm drip} < \rho < \rho_{\rm nuc}$), there are also free neutrons that drip out from the nuclei. For the crust, we adopt the Baym-Pethick-Sutherland (BPS) EOS [20]. For the core, we adopt instead the relativistic mean-field (RMF) theory models within the extension of the formulation of Boguta and Bodmer [21] with massive scalar and vector meson mediators (σ, ω, and ρ mesons). In this work, we present results for NSs constructed using the NL3 [22], TM1 [23] and GM1 [24,25] EOS.

Our preference for EOS based on RMF models is because they satisfy important properties such as Lorentz covariance, they are self-consistent relativistic models and therefore they do not violate causality, and they are successful in providing an intrinsic inclusion of spin as well as a simple mechanism of saturation of nuclear matter. We refer to Refs. [26,27] for recent extensive studies of RMF models both from the nuclear experiments point of view and from the astrophysical one. The above three representative models that we use in this work satisfy the astrophysical constraint of producing nonrotating, stable NSs up to masses larger than the most massive NS observed, PSR J0348+0432, with $M = 2.01 \pm 0.04\, M_\odot$ [28]. The mass-radius relation for nonrotating models obtained with these three EOS is shown in Fig. 1.

With the knowledge of the EOS we can compute equilibrium configurations integrating the above Einstein equations for suitable initial conditions, e.g. central density and angular momentum (or angular velocity) of the star. Then the properties of the NS such as the total gravitational mass, the total baryon mass, polar and equatorial radii,

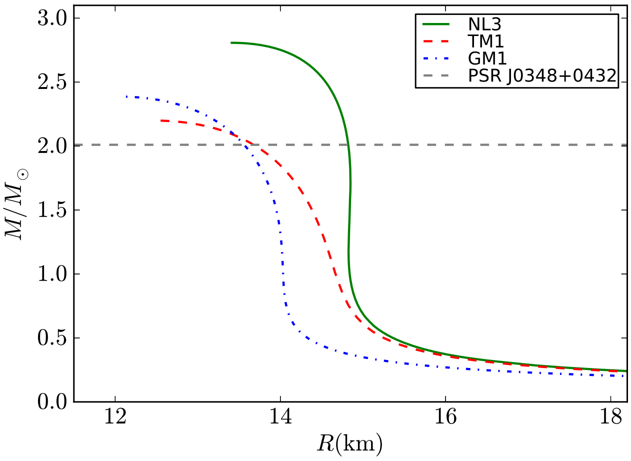

FIG. 1. Mass-radius relation for nonrotating NSs for the three EOS NL3 (green solid curve), TM1 (red dashed curve) and GM1 (blue dotted-dashed curve) used in this work. The gray dashed horizontal line shows the mass of the heaviest NS observed, PSR J0348 + 0432, $M = 2.01 \pm 0.04\ M_\odot$ [28].

moment of inertia, quadrupole moment, etc, can be obtained as a function of the central density and angular momentum.

The equilibrium configurations are limited by the Keplerian, mass-shedding, or maximally rotating sequence, and by the secular axisymmetric instability. At the Keplerian sequence the dimensionless angular momentum $a/M \equiv cJ/(GM^2)$, where $a = J/M$ is the angular momentum per-unit-mass, reaches a maximum value of $a_{\rm max}/M \approx 0.7$, independently on the EOS [14]. This value is lower than the maximum dimensionless angular momentum parameter of a rotating BH given by the extreme Kerr solution, i.e. $a_{\rm max,BH}/M_{\rm BH} = 1$.

The secular axisymmetric instability sequence separates stable from unstable stars against axisymmetric perturbations. The turning-point method [29] gives a sufficient condition for the onset of this instability. Such a sequence, for the present EOS, is well fitted by

$$M_{\rm NS}^{\rm crit} = M_{\rm crit}^{J=0}(1 + k j_{\rm NS}^{p}), \tag{12}$$

with a maximum error of 0.45% [14]. The parameters k and p and $M_{\rm crit}^{J=0}$ depend of the nuclear EOS (see Table I). The latter, the critical NS mass in the nonrotating case, is as expeceted below the upper bound to the critical mass by Rhoades and Ruffini, 3.2 $M_\odot$ [30].

TABLE I. Parameters needed to compute the secular axisymmetric instability sequence as given by Eq. (12).

EOS	$M_{\rm crit}^{J=0}$ ($M_\odot$)	p	k
NL3	2.81	1.68	0.006
GM1	2.39	1.69	0.011
TM1	2.20	1.61	0.017

III. LAST STABLE CIRCULAR ORBIT

We are interested in circular orbits of particles on the equatorial plane of the NS, that is to fix $\theta = \frac{\pi}{2}$ (see [31]). It is well known that a practical way to analyze the problem of the circular orbits is through the effective potential $V(r, \tilde{E}, \tilde{L})$ (see, e.g., Ruffini and Wheeler 1969 in Sec. 104 in [32]; see also Refs. [33,34]), whose turning points give us the radii of the circular orbits. For the metric given by Eq. (9), one can express the effective potential $V(r, \tilde{E}, \tilde{L})$ as follows [19]:

$$\begin{aligned} V(r, \tilde{E}, \tilde{L}) &= e^{2\lambda+\gamma}\left(\frac{dr}{d\tau}\right)^2 \\ &= e^{-\rho}(\tilde{E} - \omega\tilde{L})^2 - e^{\gamma} - \frac{e^{\rho}}{r^2}\tilde{L}^2, \end{aligned} \tag{13}$$

where τ is the proper time of the free particle. In order to obtain a circular orbit, one should impose the conditions

$$V = V_{,r} = 0, \tag{14}$$

and from equations (13) and (14), one obtains

$$\tilde{E} = \frac{\tilde{v}e^{\frac{\gamma+\rho}{2}}}{(1 - \tilde{v}^2)^{\frac{1}{2}}} + \omega\tilde{L}, \tag{15}$$

$$\tilde{L} = \frac{\tilde{v}re^{\frac{\gamma-\rho}{2}}}{(1 - \tilde{v}^2)^{\frac{1}{2}}}, \tag{16}$$

with $\tilde{v}$ the velocity as measured by the zero angular momentum observer (ZAMO):

$$\begin{aligned} \tilde{v} = \frac{1}{2 + r(\gamma_{,r} - \rho_{,r})}\{&e^{-\rho}r^2\omega_{,r} \pm [e^{-2\rho}r^4\omega_{,r}{}^2 + \\ &+ 2r(\gamma_{,r} + \rho_{,r}) + r^2(\gamma_{,r}{}^2 - \rho_{,r}{}^2)]^{\frac{1}{2}}\}, \end{aligned} \tag{17}$$

where the upper (plus) sign is for corotating particles and the lower (minus) sign is for counter-rotating particles.

Stable orbits are those for which the above equations are satisfied and, in addition, $V_{,rr} \geq 0$, where the equality corresponds to the LSO. We shall denote the radius of the LSO to as $r_{\rm lso}$. Depending upon the mass and angular momentum of the NS, we have situations in which $r_{\rm lso} > r_{\rm eq}$, being $r_{\rm eq}$ the coordinate equatorial radius of the star, and situations in which stable circular orbits exist down to the stellar surface, namely $r_{\rm lso} = r_{\rm eq}$.

A. Location of the last stable circular orbit

We now check the conditions under which the LSO actually resides outside the NS. It is then clear that the condition of the LSO to lie outside the NS, i.e. the condition $r_{\rm lso} \geq r_{\rm eq}$, establishes a minimum mass (for a given value of the angular momentum), or conversely, a maximum angular momentum (for a given mass), over which this condition is satisfied. In the case $J = 0$, namely for nonrotating stars, it is known that the LSO is located at $r_{\rm lso}^{J=0} = 6GM/c^2$, and therefore the minimum mass to have this orbit outside the star is obtained for the configuration with radius $R = r_{\rm lso}^{J=0}$. For the NL3, TM1 and GM1 EOS, in the case of corotating particles this minimum mass is $[1.68, 1.61, 1.57]\ M_\odot$, respectively. On the other hand, for counter-rotating particles, this minimum mass is given for the maximally rotating (Keplerian) configuration and for the NL3, TM1 and GM1 EOS is $[1.42, 1.41, 1.34]\ M_\odot$.

Fig. 2 shows the results in the rotating case for the GM1 EOS and for corotating and counter-rotating orbits. The stable NS models reside in the interior region bounded by the static (solid red curve), Keplerian (solid green curve), and secular instability (solid black curve) sequences. The configurations along the dashed curve have the radius of the LSO equal to the NS equatorial radius, i.e. $r_{\rm lso} = R_{\rm eq}$. Only the configurations on the right side of this curve have

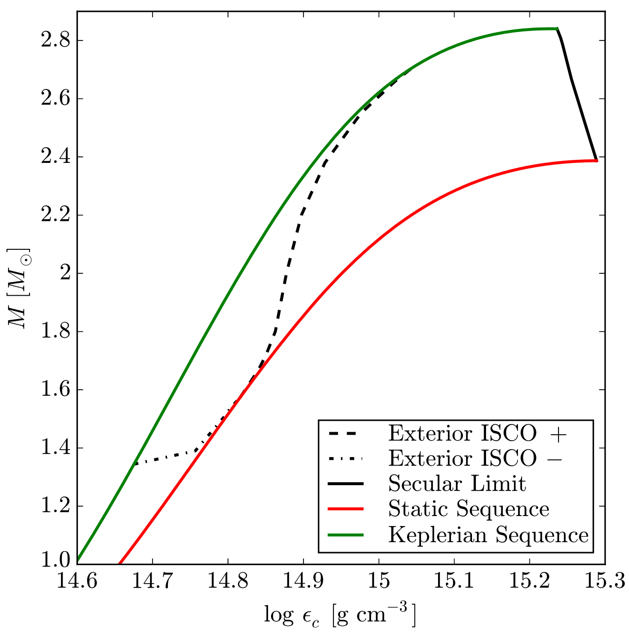

FIG. 2. Mass versus central density of uniformly rotating NSs with the GM1 EOS. The region of stability is bounded by the nonrotating sequence (solid red curve), the maximally rotating models (solid green curve), namely the mass-shedding limit or Keplerian sequence, and the secular axisymmetric stability limit (solid black curve). The dashed curve corresponds to configurations for which the LSO of corotating particles equals the NS equatorial radius: configurations on the right side of it possess an LSO exterior to their surface while configurations on the left side of the curve, have stable circular orbits down to the NS surface. Analogously, the dashed-dotted curve corresponds to configurations for which the LSO of counter-rotating particles equals the NS equatorial radius: configurations above it possess an LSO exterior to their surface while, configurations below it, have stable circular orbits down to the NS surface.

TABLE II. Parameters of the fitting formulas given by Eq. (18) for the three EOS used, together with maximum relative errors.

EOS	$M_{\rm min}^{j=0}\ [M_\odot]$	c_1	c_2	Max rel err(%)	$j_{\rm max}$
NL3	1.68	0.225	0.94	1.71	6.31
TM1	1.61	0.238	0.94	1.68	4.47
GM1	1.57	0.242	0.94	1.66	4.98

$r_{\rm lso} > R_{\rm eq}$. The configurations on the left side of the curve have stable circular orbits down to the NS surface. The dashed-dotted curve is the analogous limit for orbits of counter-rotating particles, thus the configurations under this curve have stable circular orbits down to the NS surface, while the configurations above it have $r_{\rm lso} > R_{\rm eq}$.

For the corotating case we can obtain a fitting function of the minimum NS mass, $M_{\rm min}$, for which given a value of the angular momentum one has $r_{\rm LSO} \geq R_{\rm eq}$. For the selected EOS such a function is:

$$\frac{M_{\rm min}}{M_\odot} = \frac{M_{\rm min}^{j=0}}{M_\odot} + c_1 j^{c_2}, \tag{18}$$

where $M_{\rm min}^{j=0}$, c_1 and c_2 are dimensionless constants that depend on the EOS. We report the values of these fitting parameters in Table II together the maximum relative error and the values of NS mass for which this maximum error is obtained. Clearly, the above fitting formula is valid up to the configuration that intersects the Keplerian sequence, namely where the dashed black curve intersects the solid green curve in Fig. 2. The value of the dimensionless angular momentum of that configuration, which we denote here to as $j_{\rm max}$, is reported in Table II. It can be easily checked that introducing the value of $j_{\rm max}$ given in Table II into the Eq. (18), one obtains the correct value of the mass of this precise configuration on the Keplerian sequence.

It is important to stress that Eq. (18) is not EOS-independent and it is here presented with the only purpose of providing the reader a complete set of analytic formulas that simplify the analysis of several astrophysical scenarios. The information provided by Eq. (18) is therefore complementary to the one recalled in Sec. I on the NS binding energy and accretion luminosity, and the one on the LSO energy and angular momentum that is obtained in the next Sec. V.

B. Orbital binding energy and angular momentum

We now focus on the properties of the LSO, therefore we deal with NS configurations with $r_{\rm LSO} \geq R_{\rm eq}$. We here present the numerical results obtained through integrations performed with RNS public code (http://www.gravity.phys.uwm.edu/rns/) for NSs considering mass-constant sequences within the region of stability bounded by the spherical symmetric case (nonrotating), by the Keplerian sequence

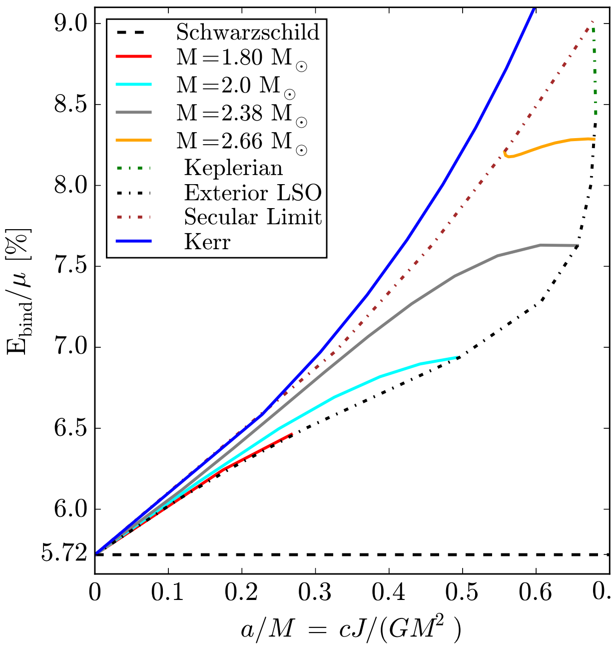

FIG. 3. Binding energy ($E_{\rm bind}/\mu \equiv 1 - \tilde{E}$) of corotating test particles in the LSO for constant mass sequences of NS configurations versus the dimensionless angular momentum $a/M = cJ/(GM^2)$. We compare and contrast our results with the values given by the Schwarzschild and Kerr solutions. In this example the NSs obey the GM1 EOS.

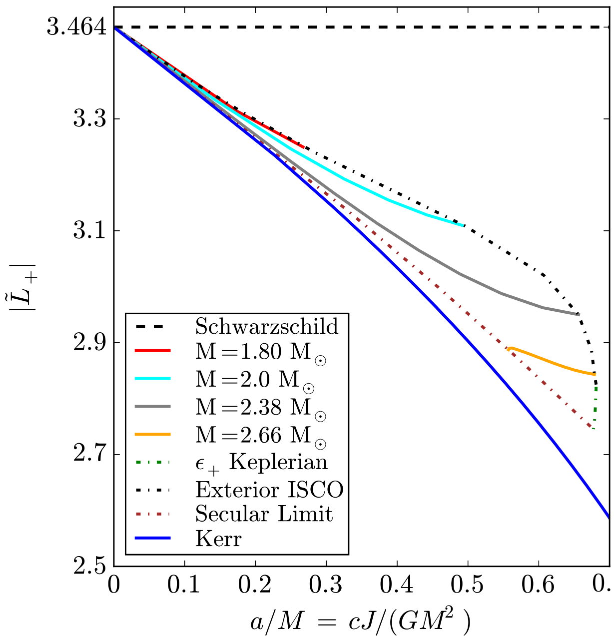

FIG. 4. Dimensionless angular momentum ($|L|/(\mu M)$) of corotating test particles in the LSO for constant mass sequences of NS configurations versus the dimensionless angular momentum $a/M = cJ/(GM^2)$. We compare and contrast our results with the values given by the Schwarzschild and Kerr solutions. In this example the NSs obey the GM1 EOS.

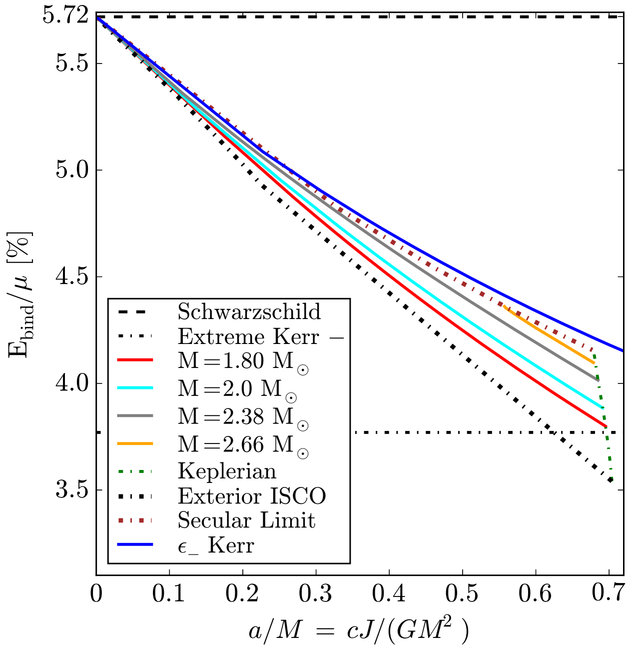

FIG. 5. Same as Fig. 3 but for counter-rotating orbits.

(mass-shedding) and by the secular axisymmetric instability limit. We shall refer to as supramassive NSs those with a mass larger than the critical mass of nonrotating NSs, i.e. configurations without a stable nonrotating counterpart.

We show in Figs. 3–6 the results of our computations for corotating and counter-rotating orbits around NSs obeying the GM1 EOS. The results for the other EOS

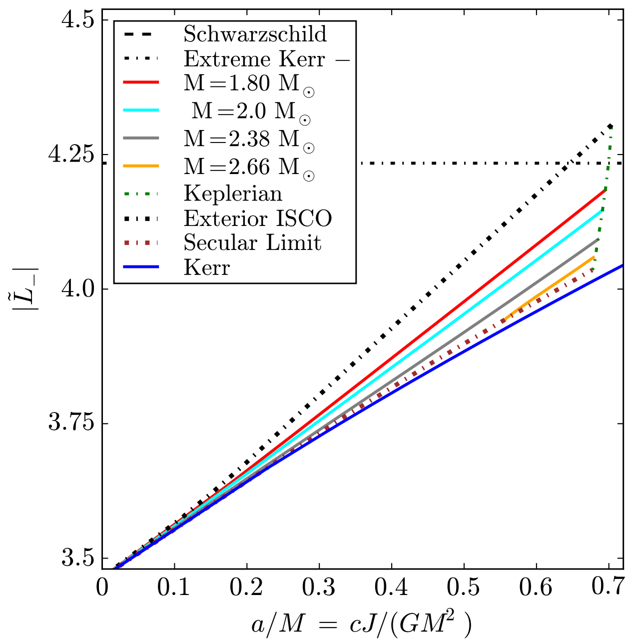

FIG. 6. Same as Fig. 6 but for counter-rotating orbits.

are analogous. Fig. 3 shows the binding energy per-unit-mass, $E_{\rm bind}/\mu = 1 - \tilde{E}$, as a function of the dimensionless angular momentum parameter, $a/M = cJ/(GM^2)$, for selected constant mass-sequences in case of corotating particles. Fig. 5 shows the results for counter-rotating particles. Fig. 4 shows the modulus of the dimensionless angular momentum of particles in the LSO, $|L|/(G\mu M/c)$, as a function of $a/M = cJ/(GM^2)$ for the same constant mass sequences in case of corotating particles. Fig. 6 shows the results for counter-rotating particles.

It can be seen that the sequences are bounded by the Keplerian (mass-shedding) sequence, i.e. $a/M \approx 0.7$, by the limit $r_{\rm LSO} = R_{\rm eq}$, by the secular axisymmetric instability and by the nonrotating limit at $a/M = 0$ (except the supramassive sequences which have no static counterpart), for which the LSO properties have the well-known results of the Schwarzschild exterior solution. We recall that $j = cJ/(GM_\odot^2) = (a/M)(M/M_\odot)^2$. We compare and contrast our results with the corresponding values given by the Kerr metric [34]. Deviations from the behavior given by

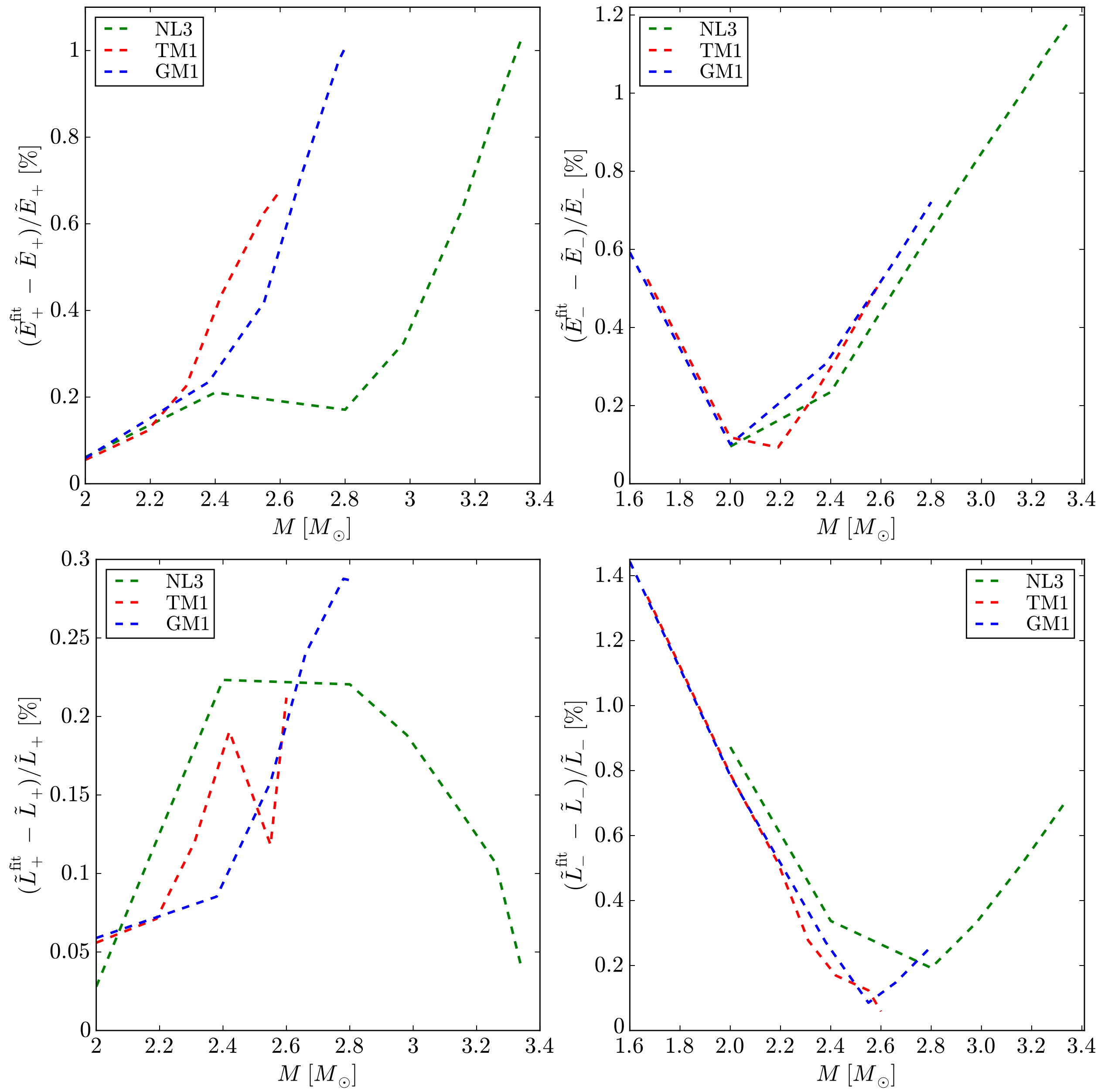

FIG. 7. Maximum error (in percentage) of Eqs. (19) and (20) with respect to the numerical value of $\tilde{E}$ and $\tilde{L}$ for the sequences of constant gravitational mass in the range 2–3.4 $M_\odot$. The results for corotating orbits are shown in the left upper and lower panels and for counter-rotating ones in the right upper and lower ones.

the Kerr solution are evident at almost any value of the dimensionless angular momentum, except for the region of very slow rotation $a/M \ll 1$.

As one can note from Figs. 3, 4, 5 and 6, the binding energy and the angular momentum of particles orbiting rotating NSs seem to be power-law functions of the mass and the dimensionless angular momentum. Indeed, we find that the following relations

$$\tilde{E} - \tilde{E}_0 = \mp 0.0132 \left(\frac{j}{M/M_\odot} \right)^{0.85}, \tag{19}$$

$$|\tilde{L}| - \tilde{L}_0 = \mp 0.37 \left(\frac{j}{M/M_\odot} \right)^{0.85}, \tag{20}$$

where the upper(lower) sign corresponds to co(counter)-rotating orbits, hold for the three studied EOS. This leads to the conjecture that these relations might be universal. The values $\tilde{E}_0 = \sqrt{8/9}$ and $\tilde{L}_0 = 2\sqrt{3}$ are the well-known values of the Schwarzschild solution, hence our formulas recover the correct values in the nonrotating case. We note that in the slow rotation regime, $a/M \ll 1$, the Kerr solution seems to approach this behavior (see Figs. 3 and 4, for the corotating case). The above fitting formula for $\tilde{E}$ is accurate with a maximum error of 1% and the one for $\tilde{L}$ has a maximum error of 0.3%. It is interesting to note that we obtain that the same fitting formulas apply to both co- and counter-rotating orbits.

We have shown in Figs. 3–6 the results for the GM1 EOS. For the other EOS similar plots are obtained. Indeed, the formulas (19) and (20) perform with similar accuracy in the case of the TM1 and NL3 EOS. In Fig. 7 we show the details of the performance of formulas (19) and (20) as a function of the NS mass for the three EOS. Specifically, for each sequence of fixed gravitational mass we compute the maximum error (in percentage) of Eqs. (19) and (20) with respect to the values of $\tilde{E}$ and $\tilde{L}$ obtained from the numerical integration. Fig. 7 shows the results for the range of mass 2–3.4 $M_\odot$ for co- and counter-rotating orbits.

IV. DISCUSSION

We have shown that expressions for $\tilde{E}$ and $\tilde{L}$ remain rather accurate for the three EOS used in this work. One is therefore brought to conjecture on the possible "universality" of such equations, namely that such simple relations would remain valid for a broader set of NS EOS. Below, through a set of logically connected statements, we shall conclude that this should be indeed the case.

1. There is a firm observational lower limit to the NS critical mass: it must be larger than the mass of the heaviest NS observed, $2.01 \pm 0.04\ M_\odot$, of PSR J0348 + 0432 [28].
2. The above point constraints the nuclear EOS to be stiff. These EOS with sound velocity approaching, but not exceeding, the speed of light (see, e.g., [35]), have a very narrow critical mass *domain of dependence* [30,36].
3. For such stiff EOS, the condition for the existence of an LSO, namely that the radius of the NS is smaller than the LSO radius, is satisfied only for heavy NSs. In the specific cases studied in this work we have shown that this condition implies $M \gtrsim 1.7\ M_\odot$. For details we refer to Sec. III A, specifically to Eq. (18) with the aid of Table II.
4. In Ref. [37], it was presented a general expansion of the LSO energy $\tilde{E}$ and angular momentum $\tilde{L}$ in terms of $\alpha \equiv a/M = J/M^2$, the NS dimensionless angular momentum parameter, and in terms of the dimensionless quadrupole moment $q \equiv Q/M^3$. Such an expansion shows that the dependence of $\tilde{E}$ and $\tilde{L}$ on the EOS occurs first at linear order in q.
5. On the other hand, it has been shown that the dimensionless quadrupole moment of NSs can be written as $q = k(\mathrm{EOS}, M)\alpha^2$, where the coefficient $k(\mathrm{EOS}, M)$ depends on the NS mass and the EOS (see, e.g., Ref. [38]). The dependence $q \propto \alpha^2$ is satisfied by both slow and fast rotating NSs. Typically $k > 1$ but the larger the NS mass, the more k approaches unity, namely the quadrupole moment of massive NSs approaches the one of the Kerr solution (see Refs. [14,39] for more details).
6. The above points 4 and 5 imply that the dependence $\tilde{E}$ and $\tilde{L}$ on the EOS occurs only at order α^2 through the k and, since for NSs $\alpha < 0.7$ [14], such EOS dependence is expected to be weak.
7. Following Ref. [37], we can write up to second order in α (and first order in q):

$$\tilde{E} - \tilde{E}_0 = -0.032\alpha + \delta E(k)\alpha^2 + \mathcal{O}(\alpha^3) \tag{21}$$

$$\tilde{L} - \tilde{L}_0 = -0.943\alpha + \delta J(k)\alpha^2 + \mathcal{O}(\alpha^3) \tag{22}$$

where $\delta E(k) = 0.008k - 0.022$ and $\delta J(k) = 0.189k - 0.258$. For values of k of the order of unity as the ones expected for the aforementioned massive NSs of points 1–3, both $\delta E(k)$ and $\delta J(k)$ imply a very small deviation of the $\tilde{E}$ and $\tilde{L}$ from a linear dependence α^1. To be more precise, the values of k are such that $\delta E(k)$ and $\delta J(k)$ are slightly positive and therefore the contribution at second order has opposite sign with respect to the one at first order and thus when trying a fit with a sole power of α we should expect a power smaller than unity. Indeed, our results summarized by Eqs. (19) and (20) show $\tilde{E} - \tilde{E}_0 \propto \alpha^{0.85}$ and $\tilde{L} - \tilde{L}_0 \propto \alpha^{0.85}$.
8. At such linear order in α, the LSO energy and angular momentum are indeed "universal" since they have no EOS dependence up to this order. The dependence on the EOS should be evident only when the contributions of $\delta E(k)$ and $\delta J(k)$ are non-negligible. This

happens for instance when $k \sim 10$ which is the case of NSs with $M \lesssim 1.4\ M_\odot$. However, such NSs do not satisfy condition imposed by point 3 unless the EOS is very soft, but in the latter case from the points 1 and 2 such EOS are not of astrophysical relevance.

It is important to stress that, in general, the energy and angular momentum of the LSO depend on the details of the EOS, however, the above points 1–8 imply that our Eqs. (19) and (20) should remain valid for a wide set of EOS, providing they are of astrophysical relevance in the sense of the points 1 and 2. It is only under these conditions that we can consider these formulas as *universal*.

Although the knowledge of the quadrupole moment appear to be relevant for the determination of several NS properties such as the angular velocity and the LSO radius (see, e.g., Ref. [40]), our results show that its role in the determination of the energy and angular momentum of the LSO can be much less important. The main reason for this is that, besides being the contribution of order α^2 naturally small by itself (because $\alpha < 0.7$) with respect to the leading order, the contribution of the quadrupole moment via the coefficients $\delta E(k)$ and $\delta J(k)$, is of opposite sign with respect to the one given by the centrifugal potential, almost canceling each other for the relevant NS masses. This effect confirms for the LSO the results of Ref. [41] on the circular orbits around rotating NSs where this feature had been already noticed.

In Sec. III B, we have compared and contrasted our results for $\tilde{E}$ and $\tilde{L}$ with the ones of the LSO in the Kerr background characterized with the same mass and angular momentum. We have seen how the properties of the LSO given by the Kerr metric deviate from the ones of NSs except in the slow rotation regime $\alpha = a/M \gg 1$. This is indeed in agreement with the above discussion on the almost linear dependence in α obtained for $\tilde{E}$ and $\tilde{L}$. Indeed, the expansion of these quantities for small α for the Kerr metric coincide at the linear level (see, e.g, Eqs. (B3) and (B4) in Ref. [40]) with the above expansion (21). Thus, $\tilde{E}$ and $\tilde{L}$ for rotating NSs are relatively well represented by the corresponding values of the Kerr metric kept only at linear order in α. However, if more terms of the expansion in the Kerr metric (or the full solution) are taken into account, the predictions of the Kerr solution deviate considerably from the realistic NS values as it is shown in Figs. 3–6.

V. CONCLUDING REMARKS

We have computed the binding energy and angular momentum of test particles orbiting on the equatorial plane of uniformly rotating NSs. The NS equilibrium configurations were constructed for up-to-date nuclear EOS by integrating the Einstein equations in the axially symmetric case. Our study was limited to stable NSs with respect to the mass-shedding (Keplerian) limit and the secular axisymmetric instability. Our conclusions are as follows.

(i) There is a limiting configuration for which the radius of the LSO equals the equatorial radius of the NS (see, e.g., Fig. 2). As an example, we have obtained the fitting function (18) that connects the mass and angular momentum of such a limiting configuration in the case of corotating orbits, for the three EOS used in this work. Thus, given a NS mass (angular momentum), Eq. (18) gives the maximum (minimum) angular momentum(mass) for which $r_{\rm lso} > R_{\rm eq}$. It is important to recall that Eq. (18) is not a universal, i.e. EOS-independent equation, and thus it must be computed for every EOS. For more details see Sec. III A.

(ii) We obtained simple formulas for the energy and angular momentum of the LSO of co- and counter-rotating test particles as a function of the NS mass and angular momentum [see, respectively, Eqs. (19) and (20)]. We have obtained these formulas for the three EOS studied in this work (NL3, TM1 and GM1) and are valid for any rotation rate within the established stability limits.

(iii) We have argued that such formulas will remain valid for other nuclear EOS which satisfy the astrophysical request of having a critical NS mass larger than 2 $M_\odot$ [28]. The EOS-dependent contributions to $\tilde{E}$ and $\tilde{L}$ appear at higher powers of the dimensionless angular momentum parameter $\alpha = a/M$ and are due to the NS mass quadrupole moment. However, such a contribution becomes negligible for massive NSs which are the ones that possess an LSO exterior to their surface. See Sec. IV for details on this discussion.

(iv) The simplicity and high accuracy of these formulas, which show a maximum error of 1% and 0.3% respectively for the energy and angular momentum of corotating orbits (see Fig. 7), makes them particularly suitable for astrophysical applications where taking into due account general relativistic effects of rotating NSs are important, e.g. the accretion processes in x-ray binaries (see, e.g., Refs. [3–5]) or hypercritical accretion in GRBs (see, e.g., Refs. [11,13]).

(v) Our results are qualitatively and quantitatively different from the corresponding ones obtained in the Kerr geometry, except in the slow rotation regime $a/M \ll 1$.

ACKNOWLEDGMENTS

We would like to thank the referee for the detailed report which has helped us to improve the presentation of our results. It is a pleasure to thank D. Bini for discussions on the subject of this work. C. C. and S. F. would like to acknowledge GNFM INdAM and ICRANet for partial support. J. A. R. acknowledges partial support of the project No. 3101/GF4 IPC-11 and the target program F.0679 of the Ministry of Education and Science of the Republic of Kazakhstan.

[1] *Neutron Stars, Black Holes and Binary X-ray Sources*, Astrophysics and Space Science Library, Vol. 48, edited by H. Gursky and R. Ruffini (Springer, New York, 1975).
[2] M. A. Alpar, A. F. Cheng, M. A. Ruderman, and J. Shaham, Nature (London) **300**, 728 (1982).
[3] M. Bagchi, Mon. Not. R. Astron. Soc. **413**, L47 (2011).
[4] M. Bejger, M. Fortin, P. Haensel, and J. L. Zdunik, Astron. Astrophys. **536**, A87 (2011).
[5] M. Bejger, J. L. Zdunik, P. Haensel, and M. Fortin, Astron. Astrophys. **536**, A92 (2011).
[6] T. M. Tauris, N. Langer, and M. Kramer, Mon. Not. R. Astron. Soc. **416**, 2130 (2011).
[7] T. M. Tauris, N. Langer, and M. Kramer, Mon. Not. R. Astron. Soc. **425**, 1601 (2012).
[8] M. Fortin, M. Bejger, P. Haensel, and J. L. Zdunik, Astron. Astrohys. **586**, A109 (2016).
[9] J. A. Rueda and R. Ruffini, Astrophys. J. **758**, L7 (2012).
[10] C. L. Fryer, J. A. Rueda, and R. Ruffini, Astrophys. J. **793**, L36 (2014).
[11] L. Becerra, F. Cipolletta, C. L. Fryer, J. A. Rueda, and R. Ruffini, Astrophys. J. **812**, 100 (2015).
[12] C. L. Fryer, F. G. Oliveira, J. A. Rueda, and R. Ruffini, Phys. Rev. Lett. **115**, 231102 (2015).
[13] L. Becerra, C. L. Bianco, C. L. Fryer, J. A. Rueda, and R. Ruffini, Astrophys. J. **833**, 107 (2016).
[14] F. Cipolletta, C. Cherubini, S. Filippi, J. A. Rueda, and R. Ruffini, Phys. Rev. D **92**, 023007 (2015).
[15] S. Bhattacharyya, I. Bombaci, D. Bandyopadhyay, A. V. Thampan, and D. Logoteta, New Astron. **54**, 61 (2017).
[16] N. R. Sibgatullin and R. A. Sunyaev, Astron. Lett. **26**, 772 (2000).
[17] K. Yagi and N. Yunes, Science **341**, 365 (2013).
[18] K. Yagi and N. Yunes, Phys. Rev. D **88**, 023009 (2013).
[19] G. B. Cook, S. L. Shapiro, and S. A. Teukolsky, Astrophys. J. **424**, 823 (1994).
[20] G. Baym, C. Pethick, and P. Sutherland, Astrophys. J. **170**, 299 (1971).
[21] J. Boguta and A. R. Bodmer, Nucl. Phys. **A292**, 413 (1977).
[22] G. A. Lalazissis, J. König, and P. Ring, Phys. Rev. C **55**, 540 (1997).
[23] Y. Sugahara and H. Toki, Nucl. Phys. A **579**, 557 (1994).
[24] N. K. Glendenning and S. A. Moszkowski, Phys. Rev. Lett. **67**, 2414 (1991).
[25] S. Pal, D. Bandyopadhyay, and W. Greiner, Nucl. Phys. **A674**, 553 (2000).
[26] M. Dutra, O. Lourenço, S. S. Avancini, B. V. Carlson, A. Delfino, D. P. Menezes, C. Providência, S. Typel, and J. R. Stone, Phys. Rev. C **90**, 055203 (2014).
[27] M. Dutra, O. Lourenço, and D. P. Menezes, Phys. Rev. C **93**, 025806 (2016).
[28] J. Antoniadis, P. C. C. Freire, N. Wex, T. M. Tauris, R. S. Lynch, M. H. van Kerkwijk, M. Kramer, C. Bassa, V. S. Dhillon, T. Driebe, J. W. T. Hessels, V. M. Kaspi, V. I. Kondratiev, N. Langer, T. R. Marsh, M. A. McLaughlin, T. T. Pennucci, S. M. Ransom, I. H. Stairs, J. van Leeuwen, J. P. W. Verbiest, and D. G. Whelan, Science **340**, 1233232 (2013).
[29] J. L. Friedman, J. R. Ipser, and R. D. Sorkin, Astrophys. J. **325**, 722 (1988).
[30] C. E. Rhoades and R. Ruffini, Phys. Rev. Lett. **32**, 324 (1974).
[31] J. M. Bardeen, Astrophys. J. **161**, 103 (1970).
[32] L. D. Landau and E. M. Lifshitz, *Course of Theoretical physics—Pergamon International Library of Science, Technology, Engineering and Social Studies*, 4th ed. (Pergamon Press, Oxford, 1975).
[33] M. Rees, R. Ruffini, and J. Wheeler, *Black holes, Gravitational Waves and Cosmology* (Gordon and Breach, London, 1972).
[34] J. M. Bardeen, in *Black Holes (Les Astres Occlus)*, edited by C. Dewitt and B. S. Dewitt (World Scientific, Singapore, 1973), p. 215.
[35] J. A. Rueda, R. Ruffini, Y.-B. Wu, and S.-S. Xue, Phys. Rev. C **89**, 035804 (2014).
[36] R. Ruffini, in *Black Holes (Les Astres Occlus)*, edited by C. Dewitt and B. S. Dewitt (1973), pp. 451–546.
[37] N. R. Sibgatullin and R. A. Sunyaev, Astron. Lett. **26**, 699 (2000).
[38] W. G. Laarakkers and E. Poisson, Astrophys. J. **512**, 282 (1999).
[39] M. Urbanec, J. C. Miller, and Z. Stuchlík, Mon. Not. R. Astron. Soc. **433**, 1903 (2013).
[40] M. Shibata and M. Sasaki, Phys. Rev. D **58**, 104011 (1998).
[41] M. Bejger, J. L. Zdunik, and P. Haensel, Astron. Astrophys. **520**, A16 (2010).

A&A 599, A87 (2017)
DOI: 10.1051/0004-6361/201629521

Astronomy & Astrophysics

The rotation-powered nature of some soft gamma-ray repeaters and anomalous X-ray pulsars

Jaziel G. Coelho[1,2], D. L. Cáceres[2], R. C. R. de Lima[3,4], M. Malheiro[5], J. A. Rueda[2,3,6], and R. Ruffini[2,3,6]

[1] Div. Astrofísica, Instituto Nacional de Pesquisas Espaciais, Av. dos Astronautas 1758, 12227–010 São José dos Campos, Brazil
e-mail: jaziel.coelho@inpe.br
[2] Dipartimento di Fisica and ICRA, Sapienza Università di Roma, Piazzale Aldo Moro 5, 00185 Rome, Italy
[3] ICRANet, Piazza della Repubblica 10, 65122 Pescara, Italy
[4] Universidade do Estado de Santa Catarina, Av. Madre Benvenuta, 2007 Itacorubi, 88.035–901 Florianópolis, Brazil
[5] Instituto Tecnológico de Aeronáutica, Praça Marechal Eduardo Gomes, 50 Vila das Acácias, 12228–900 São José dos Campos, Brazil
[6] ICRANet-Rio, Centro Brasileiro de Pesquisas Físicas, Rua Dr. Xavier Sigaud 150, 2290–180 Rio de Janeiro, Brazil

Received 12 August 2016 / Accepted 6 December 2016

ABSTRACT

Context. Soft gamma-ray repeaters (SGRs) and anomalous X-ray pulsars (AXPs) are slow rotating isolated pulsars whose energy reservoir is still matter of debate. Adopting neutron star (NS) fiducial parameters; mass $M = 1.4\,M_\odot$, radius $R = 10$ km, and moment of inertia, $I = 10^{45}$ g cm^2, the rotational energy loss, $\dot{E}_{\rm rot}$, is lower than the observed luminosity (dominated by the X-rays) $L_{\rm X}$ for many of the sources.

Aims. We investigate the possibility that some members of this family could be canonical rotation-powered pulsars using realistic NS structure parameters instead of fiducial values.

Methods. We compute the NS mass, radius, moment of inertia and angular momentum from numerical integration of the axisymmetric general relativistic equations of equilibrium. We then compute the entire range of allowed values of the rotational energy loss, $\dot{E}_{\rm rot}$, for the observed values of rotation period P and spin-down rate $\dot{P}$. We also estimate the surface magnetic field using a general relativistic model of a rotating magnetic dipole.

Results. We show that realistic NS parameters lowers the estimated value of the magnetic field and radiation efficiency, $L_{\rm X}/\dot{E}_{\rm rot}$, with respect to estimates based on fiducial NS parameters. We show that nine SGRs/AXPs can be described as canonical pulsars driven by the NS rotational energy, for $L_{\rm X}$ computed in the soft (2–10 keV) X-ray band. We compute the range of NS masses for which $L_{\rm X}/\dot{E}_{\rm rot} < 1$. We discuss the observed hard X-ray emission in three sources of the group of nine potentially rotation-powered NSs. This additional hard X-ray component dominates over the soft one leading to $L_{\rm X}/\dot{E}_{\rm rot} > 1$ in two of them.

Conclusions. We show that 9 SGRs/AXPs can be rotation-powered NSs if we analyze their X-ray luminosity in the soft 2–10 keV band. Interestingly, four of them show radio emission and six have been associated with supernova remnants (including *Swift* J1834.9-0846 the first SGR observed with a surrounding wind nebula). These observations give additional support to our results of a natural explanation of these sources in terms of ordinary pulsars. Including the hard X-ray emission observed in three sources of the group of potential rotation-powered NSs, this number of sources with $L_{\rm X}/\dot{E}_{\rm rot} < 1$ becomes seven. It remains open to verification 1) the accuracy of the estimated distances and 2) the possible contribution of the associated supernova remnants to the hard X-ray emission.

Key words. pulsars: general – stars: rotation – stars: neutron – stars: magnetic field

1. Introduction

Soft gamma-ray repeaters (SGRs) and anomalous X-ray pulsars (AXPs) constitute a class of pulsars with the following main properties (Mereghetti 2008): rotation periods $P \sim$ (2–12) s, slowing down rates $\dot{P} \sim (10^{-15}–10^{-10})$ s/s, persistent X-ray luminosity as large as 10^{35} erg s^{-1} and transient activity in the form of outbursts of energies around $(10^{41}–10^{43})$ erg. Giant flares of even larger energies, $(10^{44}–10^{47})$ erg, up to now only observed in SGRs.

A spinning down neutron star (NS) loses rotational energy at a rate given by

$$\dot{E}_{\rm rot} = -4\pi^2 I \frac{\dot{P}}{P^3} \quad (1)$$

which, adopting fiducial moment of inertia $I = 10^{45}$ g cm^2, becomes

$$\dot{E}^{\rm fid}_{\rm rot} = -3.95 \times 10^{46} \frac{\dot{P}}{P^3} \quad {\rm erg\ s^{-1}}. \quad (2)$$

Correspondingly to the fiducial moment of inertia, usual fiducial values for the mass and radius of a NS adopted in the literature are, respectively, $M = 1.4\,M_\odot$ and radius $R = 10$ km. For the observed values of P and $\dot{P}$, Eq. (2) leads to values lower than the observed X-ray luminosity from SGR/AXPs (i.e. $\dot{E}^{\rm fid}_{\rm rot} < L_{\rm X}$). This is in contrast with traditional rotation-powered pulsars which show $\dot{E}_{\rm rot} > L^{\rm obs}_{\rm X}$.

The apparent failure of the traditional energy reservoir of pulsars in SGR/AXPs has led to different scenarios for the explanation of SGRs and AXPs, e.g.: magnetars (Duncan & Thompson 1992; Thompson & Duncan 1995); drift waves near the light-cylinder of NSs (see Malov 2010, and references therein); fallback accretion onto NSs (Trümper et al. 2013); accretion onto exotic compact stars such as quark stars (Xu et al. 2006); the quark-nova remnant model (Ouyed et al. 2011); and massive, fast rotating, highly magnetized white dwarfs (WDs; Malheiro et al. 2012; Boshkayev et al. 2013; Rueda et al. 2013; Coelho & Malheiro 2014).

None of the above scenarios appears to be ruled out by the current observational data, thus further scrutiny of the nature and the possible energy reservoir of SGRs and AXPs deserves still attention.

Following the above reasoning, we aim to revisit in this work the possibility that some SGR/AXPs could be rotation-powered NSs, but now exploring the entire range of NS parameters allowed by the conditions of stability of the star, and not only on the use of fiducial parameters. We have already examined this possibility in Malheiro et al. (2012), Coelho & Malheiro (2013, 2014, 2015), Lobato et al. (2016) and have found at the time four sources (1E 1547.0−5408, SGR 1627−41, PSR J1622−4950, and XTE J1810−197) of the SGR/AXPs catalog explainable as rotation-powered NSs (see, also, Rea et al. 2012). We show in this article that this conclusion can be indeed extended to other seven sources. For the total eleven objects we report the range of masses where the rotation-power condition $\dot{E}_{\rm rot} > L_X$ is satisfied.

Once identified as rotation-powered NSs, one is led to the theoretical prediction that some of the phenomena observed in ordinary pulsars could also be observed in SGRs and AXPs. Indeed, we found that for the above 11 SGRs/AXPs describable as rotation-powered NSs:

- The energetics of their observed outbursts can be explained from the gain of rotational energy during an accompanied glitch. Such a glitch-outburst connection is not expected in a source not driven by rotational energy.
- The radio emission, a property common in pulsars but generally absent in SGRs and AXPs, is observed in four of these objects (see, e.g., Halpern et al. 2005; Camilo et al. 2006, 2007a,b; Helfand et al. 2006; Levin et al. 2010, 2012; Eatough et al. 2013).
- Six sources have possible associations with supernova remnants (SNRs), including *Swift* J1834.9-0846 the first SGR for which a pulsar wind nebula has been observed (Younes et al. 2016).

We also analyze the observed hard X-ray emission in the 20−150 keV band in 5 of the above 11 sources. As we shall discuss, this emission dominates over the soft X-rays leading to $L_X/\dot{E}_{\rm rot} > 1$ in 4 of them. With this, the number of potential rotation-powered sources becomes seven. However, this conclusion remains open for further verification since it critically depends 1) on the accuracy of the estimated distances to the sources and 2) on the possible contribution of the supernova remnants present in the hard X-ray component.

This article is organized as follows. We first compute in Sect. 2 the structure properties of NSs, and then Sect. 3 we estimate the surface magnetic field using both realistic structure parameters and a general relativistic model of a rotating magnetic dipole. We compute in Sect. 4 the ratio $L_X/\dot{E}_{\rm rot}$ for all the SGRs/AXPs for the entire range of possible NS masses. We also show in Sect. 5 an analysis of the glitch/outburst connection in the nine aforementioned sources. Finally, in Sect. 6, we summarize the main conclusions and remarks.

2. Neutron star structure

In order to compute the rotational energy loss of a NS as a function of its structure parameters, e.g. mass and radius, we need to construct the equilibrium configurations of a uniformly rotating NS in the range of the observed periods. We have shown in Rotondo et al. (2011), Rueda et al. (2011), Belvedere et al. (2012, 2014) that, in the case of both static and rotating NSs, the Tolman-Oppenheimer-Volkoff (TOV) system of equations (Oppenheimer & Volkoff 1939; Tolman 1939) is superseded by the Einstein-Maxwell system of equations coupled to the general relativistic Thomas-Fermi equations of equilibrium, giving rise to what we have called the Einstein-Maxwell-Thomas-Fermi (EMTF) equations. In the TOV-like approach, the condition of local charge neutrality is applied to each point of the configuration, while in the EMTF equations the condition of global charge neutrality is imposed. The EMTF equations account for the weak, strong, gravitational and electromagnetic interactions within the framework of general relativity and relativistic nuclear mean field theory. In this work we shall use both global (EMTF) and local (TOV) charge neutrality to compare and contrast their results.

Table 1. Meson masses and coupling constants in the parameterizations NL3, TM1, and GM1.

	NL3	TM1	GM1
M(MeV)	939.00	938.00	938.93
m_σ(MeV)	508.194	511.198	512.000
m_ω(MeV)	782.501	783.000	783.000
m_ρ(MeV)	763.000	770.000	770.000
g_σ	10.2170	10.0289	8.9073
g_ω	12.8680	12.6139	10.6089
g_ρ	4.4740	7.2325	4.0972

2.1. Nuclear equation of state (EOS)

The NS interior is made up of a core and a crust. The core of the star has densities higher than the nuclear one, $\rho_{\rm nuc} \approx 3 \times 10^{14}$ g cm^{-3}, and it is composed of a degenerate gas of baryons (e.g. neutrons, protons, hyperons) and leptons (e.g. electrons and muons). The crust, in its outer region ($\rho \leq \rho_{\rm drip} \approx 4.3 \times 10^{11}$ g cm^{-3}), is composed of ions and electrons, and in the inner crust ($\rho_{\rm drip} < \rho < \rho_{\rm nuc}$), there are also free neutrons that drip out from the nuclei. For the crust, we adopt the Baym-Pethick-Sutherland (BPS) EOS (Baym et al. 1971b), which is based on the Baym et al. (1971a) work. For the core, we adopt relativistic mean-field (RMF) theory models. We use an extension of the Boguta & Bodmer (1977) formulation with a massive scalar meson (σ) and two vector mesons (ω and ρ) mediators, and possible interactions amongst them. We adopt in this work three sets of parameterizations of these models (see Table 1 and Fig. 1): the NL3 (Lalazissis et al. 1997), TM1 (Sugahara & Toki 1994), and GM1 (Glendenning & Moszkowski 1991) EOS.

2.2. Mass-radius relation and moment of inertia

For the rotational periods as the ones observed in SGR/AXPs ($P \sim$ 2–12 s), the structure of the rotating NS can be accurately described by small rotation perturbations from the spherically symmetric configuration (see, e.g., Belvedere et al. 2014, 2015), using the Hartle's formalism (Hartle 1967). Following this method we compute rotating configurations, accurate up to second-order in Ω, with the same central density as the seed static non-rotating configurations. The mass-radius relation for non-rotating configurations in the cases of global and local charge neutrality are shown in Fig. 2. For the rotation periods of interest here, the mass-equatorial radius relation of the uniformly rotating NSs practically overlaps the one given by the static se-

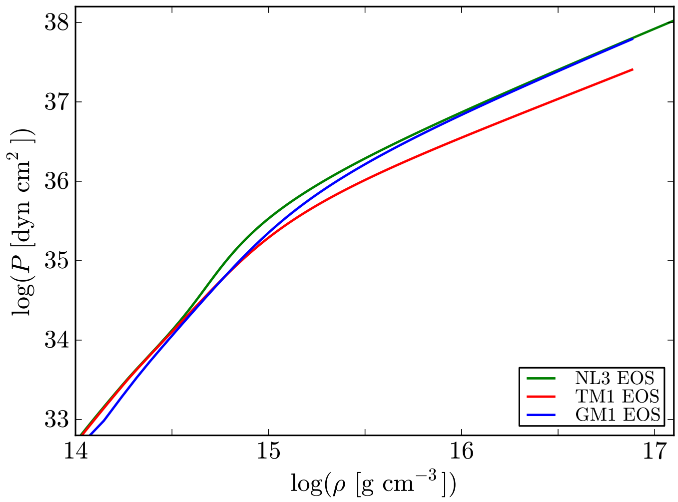

Fig. 1. NL3, TM1, and GM1 EOS behavior at sub and supranuclear densities.

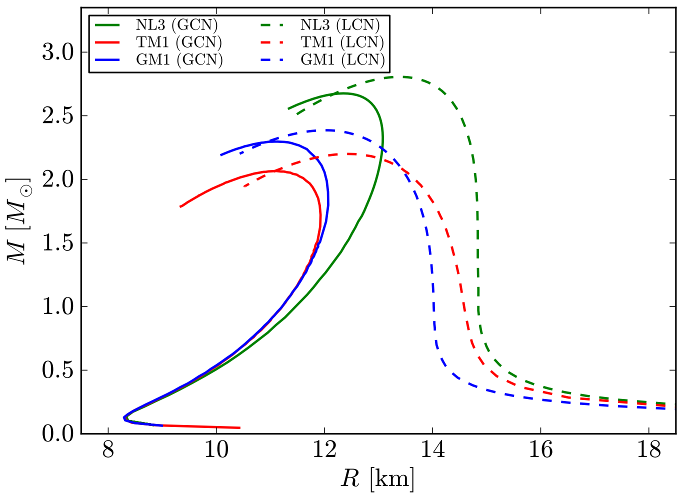

Fig. 2. Mass-radius relation for the NL3, TM1, and GM1 EOS in the cases of global (solid curves) and local (dashed curves) charge neutrality.

quence (see Fig. 1 in Belvedere et al. 2015). Thus, we take here advantage of this result and consider hereafter, as masses and corresponding radii, the values of the non-rotating NSs.

The moment of inertia is given by

$$I = \frac{J}{\Omega}, \tag{3}$$

where Ω is the angular velocity and J is the angular momentum given by

$$J = \frac{1}{6} R^4 \left(\frac{\mathrm{d}\bar{\omega}}{\mathrm{d}r} \right)_{r=R} \cdot \tag{4}$$

Here R is the radius of the non-rotating star with the same central density as the rotating one, $\bar{\omega} = \Omega - \omega(r)$ is the angular velocity of the fluid relative to the local inertial frame, and ω is the angular velocity of the local frame. The angular velocity Ω is related the angular momentum J by

$$\Omega = \bar{\omega}(R) + \frac{2J}{R^3} \cdot \tag{5}$$

Figure 3 shows the behavior of the moment of inertia as a function of the mass of the NS for the three EOS NL3, TM1 and GM1 and both in the case of global and local charge neutrality. Although in general there is a dependence of all the structure parameters on the nuclear EOS, we use below, without loss of generality and for the sake of exemplification, only the GM1 EOS. Similar qualitatively and quantitatively results are obtained for the other EOSs. It is worth mentioning that the chosen EOS lead to a maximum stable mass larger than $2\,M_\odot$, the heaviest NS mass measured (Demorest et al. 2010; Antoniadis et al. 2013).

3. Surface magnetic field

Since the range of P for SGRs and AXPs is similar to the one concerning the high-magnetic field pulsar class, we can directly apply the results of Belvedere et al. (2015), applying only the most relevant correction for this range of periods to estimate the surface magnetic field, namely the finite-size correction. The exact solution of the radiation power of a (slowly) rotating, magnetic dipole, which duly generalizes the classic solution by Deutsch (1955), is given by (see Rezzolla & Ahmedov 2004, and references therein)

$$P_{\rm dip}^{\rm GR} = -\frac{2}{3} \frac{\mu_\perp^2 \Omega^4}{c^3} \left(\frac{f}{N^2} \right)^2, \tag{6}$$

where $\mu_\perp = \mu \sin\chi$, is the component of the magnetic dipole moment perpendicular to the rotation axis, $\mu = BR^3$ with B the surface magnetic field at the star's equator, χ is the inclination angle between the magnetic dipole and rotation axis, and f and N are the general relativistic corrections

$$f = -\frac{3}{8} \left(\frac{R}{M} \right)^3 \left[\ln(N^2) + \frac{2M}{R} \left(1 + \frac{M}{R} \right) \right], \tag{7}$$

$$N = \sqrt{1 - \frac{2M}{R}}, \tag{8}$$

with M the mass of the non-rotating configuration. Now, equating the rotational energy loss, Eq. (1) to the above electromagnetic radiation power, Eq. (6), one obtains the formula to infer the surface magnetic field, given the rotation period and the spin-down rate:

$$B_{\rm GR} = \frac{N^2}{f} \left(\frac{3c^3}{8\pi^2} \frac{I}{R^6} P\dot{P} \right)^{1/2}, \tag{9}$$

where we have introduced the subscript "GR" to indicate explicitly the magnetic field inferred from the above general relativistic expression, and we have adopted for simplicity an inclination angle $\chi = \pi/2$.

Figures 4 and 5 show our theoretical prediction for the surface magnetic fields of the SGR/AXPs as a function of the NS mass, using Eq. (9), for the GM1 EOS and for the global and local charge neutrality cases, respectively. We find that in both cases some of the sources have inferred magnetic fields lower than the critical value, B_c, for some range of NS masses. Clearly this set of sources includes SGR 0418+5729, *Swift* J1822.3-1606 and 3XMM J185246.6+003317, which are already known to show this feature even using fiducial NS parameters and the classic magnetic dipole model (see e.g., Olausen & Kaspi 2014). It is worth to note that Eq. (9) is derived for a rotating magnetic dipole in electrovacuum, thus neglecting the extra torque from the presence of magnetospheric plasma. The addition of this torque certainly leads to values of the magnetic field still lower than the ones shown here. However, the inclusion of the torques from the magnetosphere is beyond the scope of this work and will be taken into account in future works.

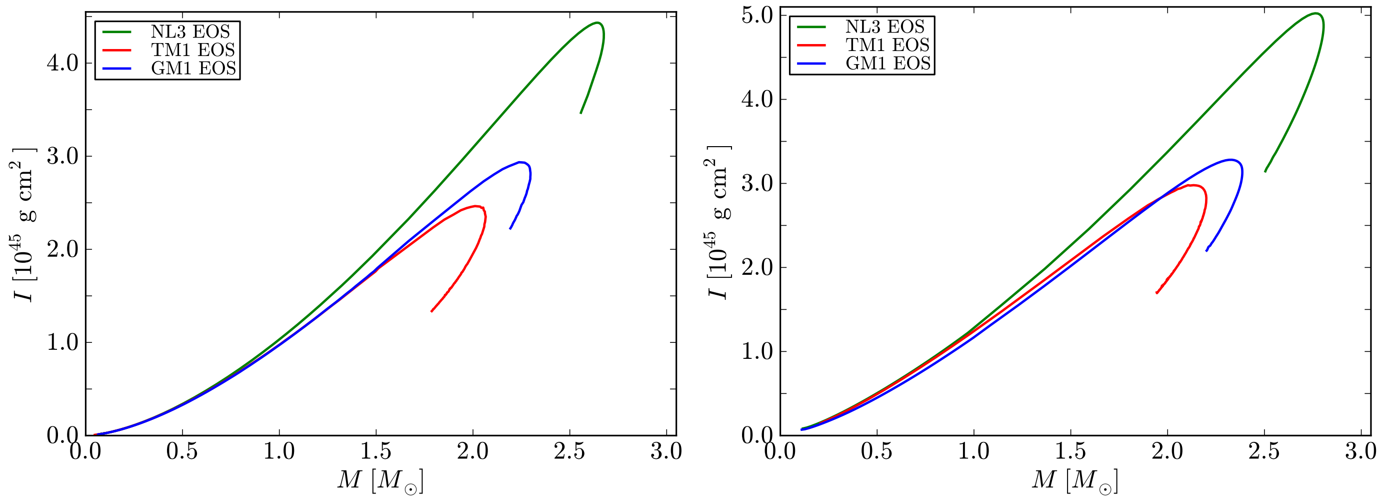

Fig. 3. Moment of inertia as a function of the NS mass for the NL3, TM1, and GM1 EOS in the cases of global (*left panel*) and local (*right panel*) charge neutrality.

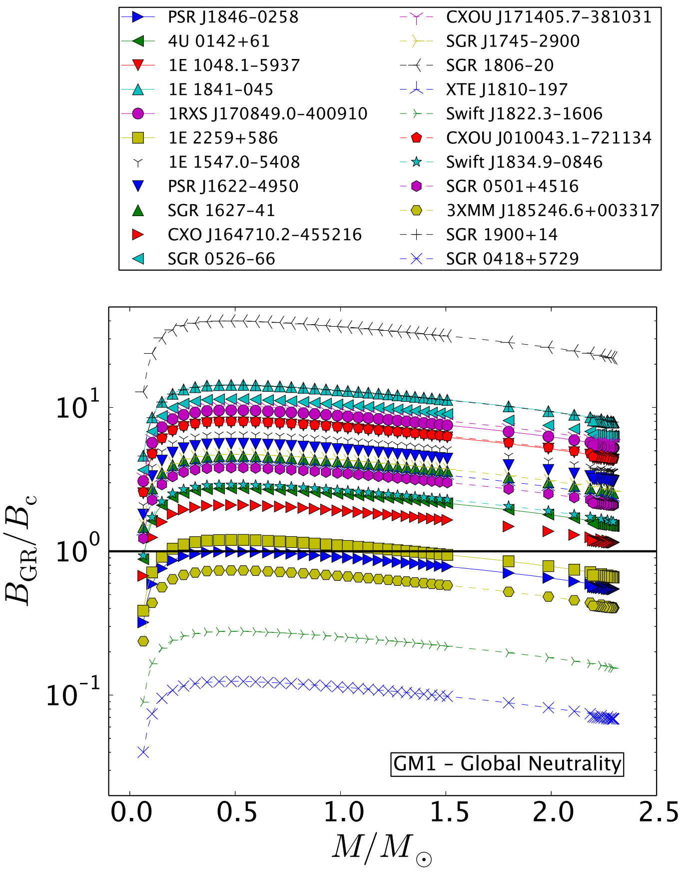

Fig. 4. Magnetic field $B_{\rm GR}$ given by Eq. (9), in units of $B_{\rm c} = m_{\rm e}^2c^3/(e\hbar) = 4.4 \times 10^{13}$ G, as function of the mass (in solar masses) in the global charge neutrality case.

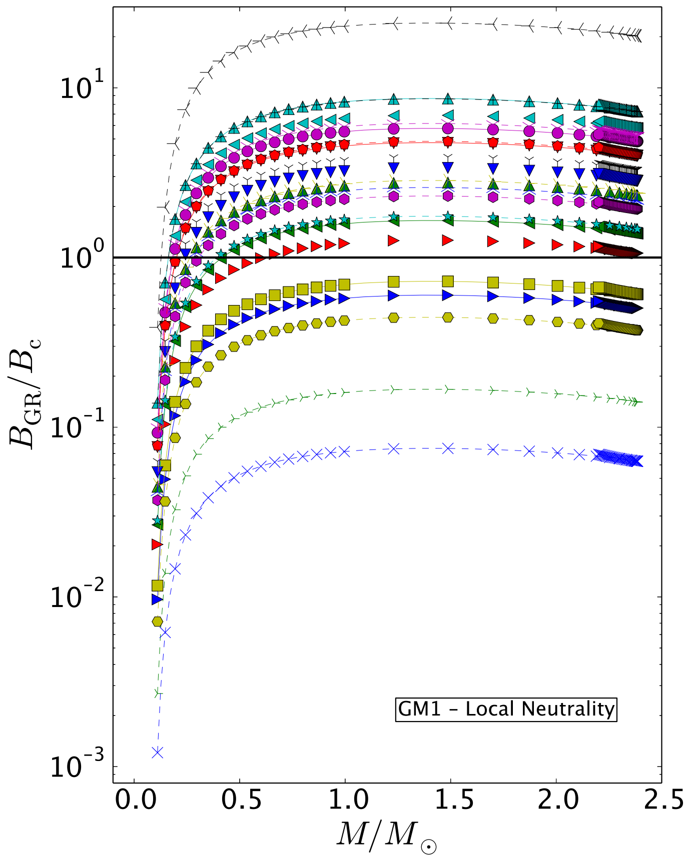

Fig. 5. Magnetic field $B_{\rm GR}$ given by Eq. (9), in units of $B_{\rm c} = 4.4 \times 10^{13}$ G, as function of the mass (in solar masses) in the local charge neutrality case.

4. SGRs and AXPs efficiency

Another important quantity for the identification of the nature of the sources is the radiation efficiency, namely the ratio between the observed luminosity and the rotational energy loss (1). It is clear from Fig. 3 that such a ratio is a function of the NS mass, via the moment of inertia. For SGR/AXPs the dominant emission is in X-rays, thus we analyze all the possible values of the ratio $L_{\rm X}/\dot{E}_{\rm rot}$ in the entire parameter space of NSs. As we show below, some SGRs and AXPs allow a wide range of masses for which $L_{\rm X}/\dot{E}_{\rm rot} \lesssim 1$, implying a possible rotation-powered nature for those sources.

Figure 6 shows the X-ray luminosity to rotational energy loss ratio as a function of the NS mass, for both global and local charge neutrality configurations. We can see from these figures that nine out of the twenty three SGR/AXPs could have masses in which $L_{\rm X} < \dot{E}_{\rm rot}$, and therefore they could be

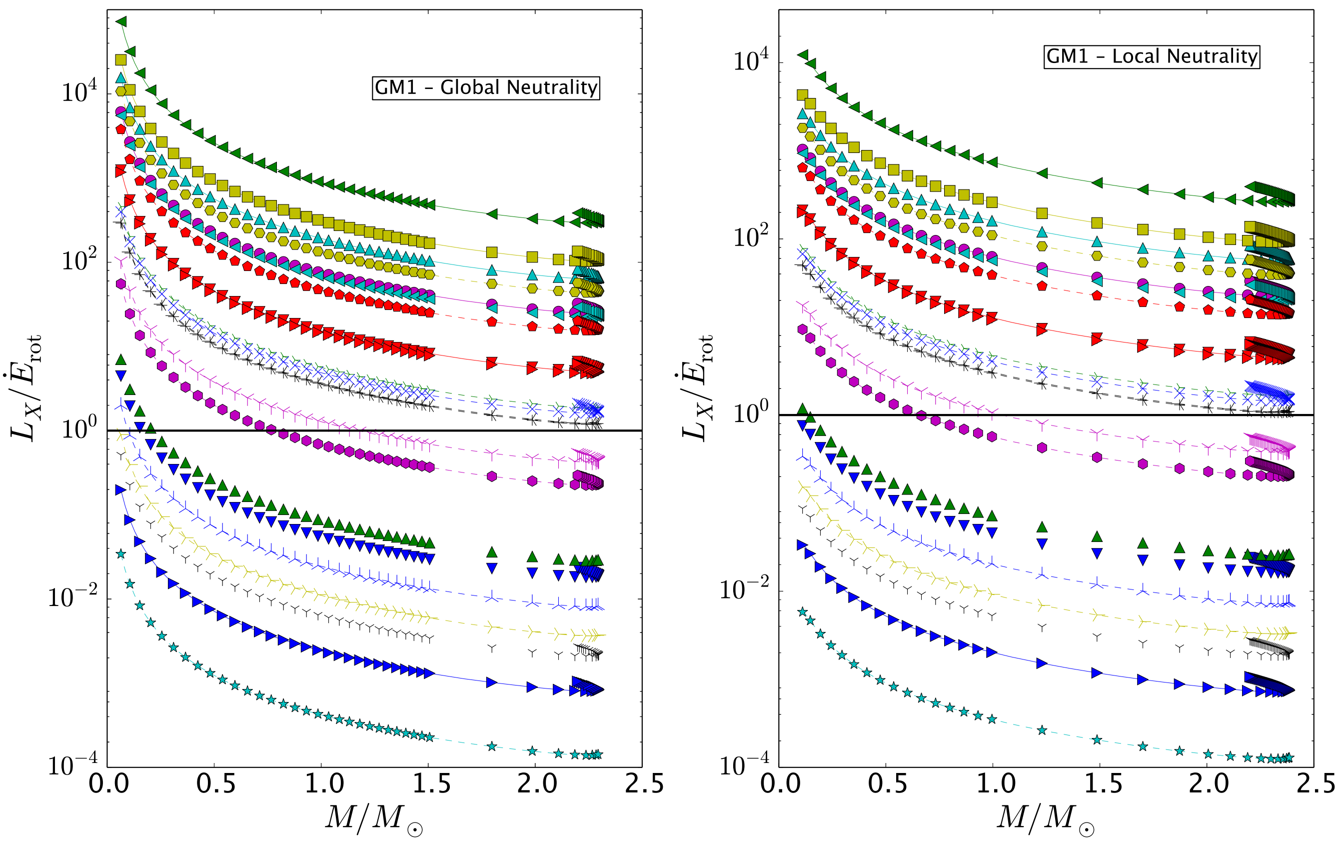

Fig. 6. Radiation efficiency $L_X/\dot{E}_{rot}$ as a function of the NS mass (in solar masses), for the global (*left panel*) and local (*right panel*) neutrality cases.

Table 2. Some properties of nine SGRs/AXPs potential rotation-powered NSs.

Source	P (s)	$\dot{P}$	d (kpc)	L_X (10^{33} erg s^{-1})	L_X^{hard} (10^{33} erg s^{-1})	L_{radio} (10^{28} sr^{-1} erg s^{-1})	SNR assoc.	Obs. glitches	Burst	Transient
SGR 0501+4516	5.8	0.59	2	0.81	40.2	–	HB 9 (?)	No	Yes	Yes
1E 1547.0–5408	2.07	4.77	4.5	1.3	193.9	1.19	G327.24-0.13	Yes	Yes	Yes
PSR J1622-4950	4.33	1.7	9	0.44	–	5.18	G333.9+0.0	No	No	Yes
SGR 1627-41	2.59	1.9	11	3.6	–	–	G337.0-0.1	No	Yes	Yes
CXOU J171405.7-381031	3.8	6.4	13.2	56	–	–	CTB 37B	No	No	No
SGR J1745-2900	3.76	1.38	8.5	0.11	57.9	84.6	–	No	Yes	Yes
XTE J1810-197	5.54	0.77	3.5	0.043	–	0.98	–	No	Yes	Yes
Swift J1834.9-0846	2.48	0.79	4.2	0.0084	–	–	W41	No	Yes	Yes
PSR J1846-0258	0.33	0.71	6	19	–	–	Kes 75	Yes	Yes	No

Notes. Column 1: source name. Column 2: rotation period P in units of seconds. Column 3: spin-down rate $\dot{P}$ in units of 10^{-11}. Column 4: source distance in units of kpc. Column 5: X-ray luminosity in the 2–10 keV band in units of 10^{33} erg s^{-1}. Column 6: hard X-ray luminosity in the 20–150 keV band in units of 10^{33} erg s^{-1}. Column 7: radio luminosity per solid angle at the frequency $f_0 = 1.4$ GHz, i.e. $L_{radio} = S_{1.4}d^2$ in units of 10^{28} sr^{-1} erg s^{-1} where $S_{1.4}$ is the measured flux density at f_0. In the case of SGR J1745-2900 we report the luminosity per beam at the frequency 41 GHz according to Yusef-Zadeh et al. (2015). In Cols. 8–11 we report respectively if the source has reported association with SNR, observed glitches, outbursts, and if it is considered as a transient X-ray lumminosity (in the sense explained in Sect. 6). Data have been taken from the McGill catalog (Olausen & Kaspi 2014; see `http://www.physics.mcgill.ca/~pulsar/magnetar/main.html`).

explained as ordinary rotation-powered NSs. Such sources are: *Swift* J1834.9–0846, PSR J1846–0258, 1E 1547.0–5408, SGR J1745-2900, XTE J1810–197, PSR J1622–4950, SGR 1627–41, SGR 0501+4516, CXOU J171405.7381031 (see Table 2). In view of the proximity of some of the sources to the line $L_X/\dot{E}_{rot} = 1$ (e.g., SGR 1900+14, SGR 0418+5729, and *Swift* J1822.3–1606), and the currently poorly constrained determination of the distance to the sources, there is still the possibility of having additional sources as rotation powered NSs.

In this line, two sources are particularly interesting, namely SGR 1900+14 and SGR 1806-20, which appear very close (but above) to the limit of becoming rotation-powered NSs. The soft X-rays spectra of SGRs and AXPs are usually well fitted by a blackbody + power-law spectral model (see e.g., Mereghetti 2008). The blackbody temperature is usually of the order $k_B T \sim 0.5$ keV and surface radii of the emitting region are ∼1 km. In the case of a NS, one could interpret such a thermal component as due to the surface temperature of the NS, namely associated with the thermal reservoir of the star. The power-law component has instead a non-thermal nature and must be due to magnetospheric processes which are connected with the rotational energy reservoir in a rotation-powered star. Within this interpretation,

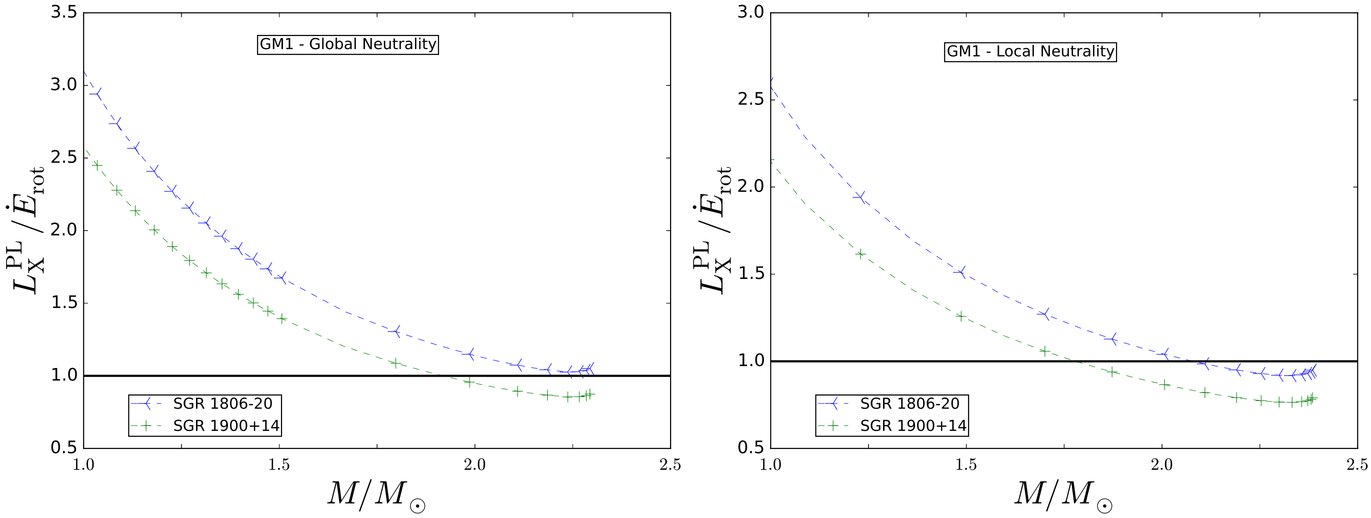

Fig. 7. Radiation efficiency $L_X/\dot{E}_{rot}$ as a function of the NS mass (in solar masses), for the global (*left panel*) and local (*right panel*) neutrality cases.

the request that the rotational energy loss pays also for the contribution of the thermal component of the luminosity is unnecessarily rigorous. Thus, the above ratio $L_X/\dot{E}_{rot}$ becomes an upper limit to the actual efficiency for the conversion of rotational into electromagnetic energy. We can now apply this interpretation, for the sake of example, to the above two sources.

SGR 1900+14: the blackbody component of the spectrum is characterized by $k_BT_{BB} = 0.47$ keV, and a surface radius of $R_{BB} = 4.0$ km, assuming a distance of 15 kpc (Mereghetti et al. 2006). The total (blackbody + power-law) flux in the 2–10 keV energy band is $F_X = 4.8 \times 10^{-12}$ erg cm^{-2} s^{-1}. With the above data, we infer that the blackbody and the power-law components contribute respectively 28% and 72% to the total flux. Namely, we have $F_X^{BB} = 0.28F_X$ and $F_X^{PL} = 0.72F_X$. This leads to $L_X^{PL} = 9.3 \times 10^{34}$ erg s^{-1}.

SGR 1806–20: in this case we have $k_BT_{BB} = 0.55$ keV and $R_{BB} = 3.7$ km, assuming a distance of 15 kpc (Esposito et al. 2007). For this source $F_X = 1.8 \times 10^{-11}$ erg cm^{-2} s^{-1}, and we infer $F_X^{BB} = 0.16F_X$ and $F_X^{PL} = 0.84F_X$. This leads to $L_X^{PL} = 4.1 \times 10^{35}$ erg s^{-1}. If we use instead the revised distance of 8.7 kpc (Bibby et al. 2008), we have $L_X^{PL} = 1.4 \times 10^{35}$ erg s^{-1}.

Figure 7 shows the ratio $L_X^{PL}/\dot{E}_{rot}$ as a function of the NS mass in the case of SGR 1900+14 and SGR 1806–20, adopting the GM1 EOS and assuming a distance of 15 kpc for both sources. It is clear from this analysis the importance of identifying the different contributions to the emission of the object. There is no doubt that the subtraction of the contribution from the thermal reservoir to the total flux in soft X-rays can be important for the correct identification of the nature of these sources: now there is a range of masses for which the luminosity to rotational energy loss ratio becomes lower than unity. Again, it is worth to recall that there are still additional effects which could improve the above analysis: (i) the distance to the sources are not known accurately; (ii) the spectrum could be equally well-fitted by a different spectral model such as a double blackbody which would have a different interpretation; (iii) the NS EOS is still unknown and so the moment of inertia and radius for a given mass might be different. These effects might lead to a different value of the luminosity, and of the contributions of thermal and rotational energy reservoirs to it. Clearly, the above analysis can be extended to all the other SGRs and AXPs, and in the case of the nine sources already identified with $L_X/\dot{E}_{rot} < 1$, it will further diminish their radiation efficiency.

It is now appropriate to discuss the non-thermal hard X-ray emission (above 10 keV) in SGRs/AXPs which has been observed by some missions like RXTE, INTEGRAL, *Suzaku* and *NuSTAR*. First we discuss the observations of the above two sources which could in principle join the possibly rotation-powered group. Adopting a distance of 15 kpc, SGR 1900+14 has an observed 20–100 keV band luminosity of $L_X^{hard} = 4 \times 10^{35}$ erg s^{-1} (Götz et al. 2006). This implies $L_X^{hard} \approx 4.3L_X^{PL}$, so a total X-ray luminosity (hard + soft) $L_x = 5.3L_X^{PL} \approx 4.9 \times 10^{35}$ erg s^{-1}. SGR 1806–20 has a 20–100 keV band flux three times higher than the one of SGR 1900+14 (Götz et al. 2006), thus assuming also a distance of 15 kpc for this source we obtain $L_X^{hard} \approx 2.9L_X^{PL}$, so a total X-ray luminosity (hard + soft) $L_x = 3.9L_X^{PL} \approx 1.6 \times 10^{36}$ erg s^{-1}. This means that the points in Fig. 7 would shift 5 and 4 times up respectively and therefore there will be no solution for these sources as rotation-powered, unless their distances are poorly constrained. In this line it is worth mentioning that the distance to these sources has been established via their possible association with star clusters (see Vrba et al. 2000; Corbel & Eikenberry 2004, for details).

From the set of nine potential rotation-powered sources, only three ones have persistent hard X-ray emission (see Table 2): SGR 0501+4516, 1E 1547.0–5408 and SGR J1745–2900. For these sources we can see the hard X-ray luminosity in the 20–150 keV band overcomes the soft X-ray contribution to the luminosity respectively by a factor 50, 149 and 527. Figure 8 shows the ratio $L_X^{Hard}/\dot{E}_{rot}$ as a function of the NS mass in the case of SGR 0501+4516, 1E 1547.0–5408 and SGR J1745–2900. We can see that, after including the hard X-ray component in these three sources, 1 E1547.0–5408 stands still below the line $L_X/\dot{E}_{rot} = 1$, while the other two sources appear above it.

The existence of persistent hard X-ray emission provides new constraints on the emission models for SGRs/AXPs since, as in ordinary pulsars, the higher the energy band the higher the luminosity, namely their luminosities can be dominated by hard X-rays and/or gamma-rays. At the present, the mechanisms responsible for the hard energy emission is still poorly understood, what causes the hard X-ray tails is still an open issue. In this respect it is worth mentioning that, since these sources are also associated with supernova remnants (see Table 2 and Sect. 6), the

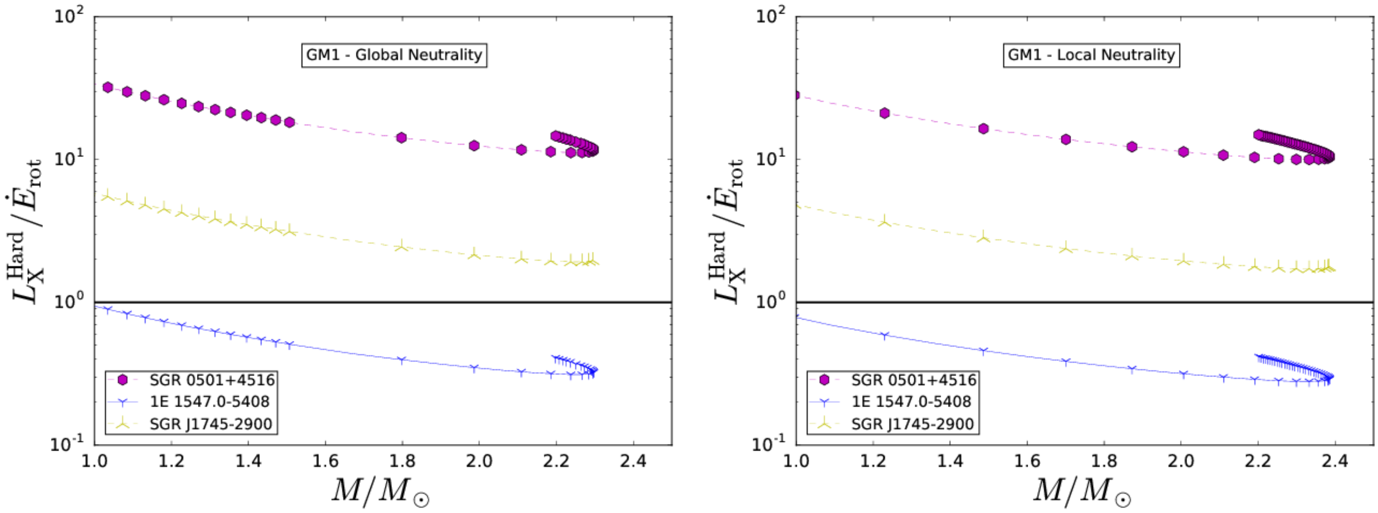

Fig. 8. Radiation efficiency $L_X^{\rm Hard}/\dot{E}_{\rm rot}$ as a function of the NS mass (in solar masses), for the global (*left panel*) and local (*right panel*) neutrality cases.

emission in hard X and/or gamma-rays could be contaminated by the remnant emission. The disentanglement of the contributions of the remnant and the central pulsar to the total emission is an interesting issue to be explored, in addition to the confirmation of the estimated distances. If the above numbers will be confirmed, then the number of rotation-powered SGRs/AXPs becomes seven.

5. Glitches and bursts in SGRs/AXPs

We have shown in the last section that nine (and up to eleven) of the twenty three SGR/AXPs are potential rotation-powered NSs. Once the possible rotation-power nature of the source is established, one expects that also the transient phenomena observed in these sources could be powered by rotation. Based on that idea, we here discuss a possible glitch-outburst connection. Thus, it is interesting to scrutinize the outburst data of SGR/AXPs, to seek for associated glitches, and check if the energetics of its bursting activity could be explained by the gain of rotational energy during an associated (observed or unobserved) glitch.

In a glitch, the release of the accumulated stress leads to a sudden decrease of the moment of inertia and, via angular momentum conservation,

$$J = I\Omega = (I + \Delta I)(\Omega + \Delta\Omega) = \text{constant}, \tag{10}$$

to a decrease of both the rotational period (spin-up) and the radius, i.e.

$$\frac{\Delta I}{I} = 2\frac{\Delta R}{R} = \frac{\Delta P}{P} = -\frac{\Delta\Omega}{\Omega}. \tag{11}$$

The sudden spin-up leads to a gain of rotational energy

$$\Delta E_{\rm rot} = -\frac{2\pi^2 I}{P^2}\frac{\Delta P}{P}, \tag{12}$$

which is paid by the gravitational energy gain by the star's contraction (Malheiro et al. 2012).

It is important to start our analysis by recalling the case of PSR J1846–0258, which has $L_X < \dot{E}_{\rm rot}$ even when fiducial NS parameters are adopted. The importance of this source relies on the fact that, although it is recognized as rotation-powered NS, it has been classified as SGR/AXP (Olausen & Kaspi 2014) owing to its outburst event in June 2006 (Gavriil et al. 2008). In view of the possible NS rotation-power nature of PSR, Malheiro et al. (2012) explored the possibility that the outburst energetics $(3.8–4.8) \times 10^{41}$ erg (Kumar & Safi-Harb 2008) can be explained by the rotational energy gained by a NS glitch. It was there found that a glitch with fractional change of period $|\Delta P|/P \sim (1.73–2.2) \times 10^{-6}$ could explain the outburst of 2006. This theoretical result is in full agreement with the observational analysis by Kuiper & Hermsen (2009), who showed that indeed a major glitch with $|\Delta P|/P \sim (2–4.4) \times 10^{-6}$ is associated with the outburst. Very recently, Archibald et al. (2016) reported another example of an X-ray outburst from a radio pulsar, PSR J1119–6127, which also has $L_X < \dot{E}_{\rm rot}$. This source is similar to the rotation-powered pulsar PSR J1846–0258. The pulsar's spin period $P = 0.407$ s and spin-down rate $\dot{P} = 4.0 \times 10^{-12}$ imply a dipolar surface magnetic field $B = 4.1 \times 10^{13}$ G adopting fiducial values. It is clear from Figs. 4 and 5 that also in this case the magnetic field would become undercritical for realistic NS parameters.

We follow this reasoning and proceed to theoretically infer the fractional change of rotation period, $|\Delta P|/P$, which explains the energetics of the bursts of the family of SGR/AXPs with $L_X < \dot{E}_{\rm rot}$ presented in this work. We do this by assuming that $|\Delta E_{\rm rot}|$, given by Eq. (12), equals the observed energy of the burst event, $E_{\rm burst}$, namely

$$\frac{|\Delta P|}{P} = \frac{E_{\rm burst} P^2}{2\pi^2 I}. \tag{13}$$

From the set of nine potential rotation-powered sources, only two ones have glitches detected: PSR J1846–0258 which has been discussed above and 1E 1547.0–5408 with $|\Delta P|/P \approx 1.9 \times 10^{-6}$ (Kuiper et al. 2012). In particular, figure 9 shows the value of $|\Delta P|/P$ obtained from Eq. (13) as a function of the NS mass for PSR J1846–0258 (a similar analysis can be applied to the radio pulsar PSR J1119–6127, whose timing analysis presented in Archibald et al. 2016 suggests the pulsar had a similar-sized spin-up glitch with $|\Delta P|/P \sim 5.8 \times 10^{-6}$). Indeed a minimum mass for the NS can be established for the sources by requesting that: (1) the entire moment of inertia is involved in the glitch and (2) the theoretical value of $|\Delta P|/P$ coincides with the observed value. We obtain a minimum mass for PSR J1846–0258, $M_{\rm min} = 0.72\ M_\odot$ and $M_{\rm min} = 0.61\ M_\odot$, for the global and local charge neutrality cases, respectively. On the other hand, if we substitute the moment of inertia I in Eq. (13) by $I_{\rm glitch} = \eta I$

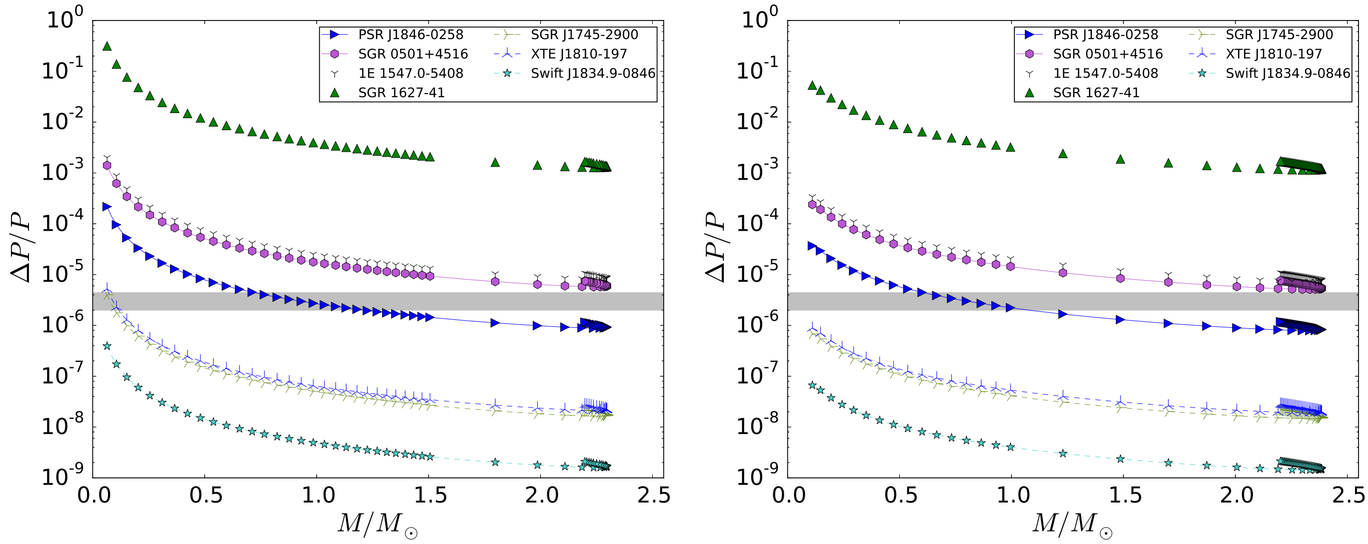

Fig. 9. Inferred fractional change of rotation period during the glitch, $\Delta P/P$, obtained by equating the rotational energy gained during the glitch, $\Delta E_{\rm rot}$, to the energy of the burst, for globally neutral (*left panel*) and locally neutral (*right panel*) NSs. In this example the NS obeys the GM1 EOS. The gray-shaded area corresponds to the value of $|\Delta P|/P$ in the observed glitch of PSR J1846–0258 in June 2006 (Kuiper & Hermsen 2009).

Table 3. Predicted values of $|\Delta P|/P$ assuming rotation-powered NSs – Global charge neutrality case.

Source name	Year of burst	Total isotropic burst energy (erg)	Predicted $\lvert\Delta P\rvert/P$ for $M > 1\,M_\odot$
PSR J1846–0258	2006	4.8×10^{41}	8.8×10^{-7}–2.6×10^{-6}
1E 1547.0–5408	2009	1.1×10^{41}	8.1×10^{-6}–2.4×10^{-5}
XTE J1810–197	2004	4.0×10^{37}	2.1×10^{-8}–6.3×10^{-8}
SGR 1627–41	1998	1.0×10^{41}	1.0×10^{-5}–3.8×10^{-5}
SGR 0501+4516	2008	1.0×10^{40}	5.7×10^{-6}–1.7×10^{-5}
Swift J1834.9–0846	2011	1.5×10^{37}	1.6×10^{-9}–4.8×10^{-9}
SGR 1745–2900	2013	6.7×10^{37}	1.61×10^{-8}–4.9×10^{-8}

Table 4. Predicted values of $|\Delta P|/P$ assuming rotation-powered NSs – Local charge neutrality case.

Source name	Year of burst	Total isotropic burst energy (erg)	Predicted $\lvert\Delta P\rvert/P$ for $M > 1\,M_\odot$
PSR J1846–0258	2006	4.8×10^{41}	7.9×10^{-7}–2.2×10^{-6}
1E 1547.0–5408	2009	1.1×10^{41}	7.2×10^{-6}–2.0×10^{-5}
XTE J1810–197	2004	4.0×10^{37}	1.9×10^{-8}–5.3×10^{-8}
SGR 1627–41	1998	1.0×10^{41}	1.1×10^{-5}–3.2×10^{-5}
SGR 0501+4516	2008	1.0×10^{40}	5.0×10^{-6}–1.4×10^{-5}
Swift J1834.9–0846	2011	1.5×10^{37}	1.4×10^{-9}–3.9×10^{-9}
SGR 1745–2900	2013	6.7×10^{37}	1.4×10^{-8}–4.1×10^{-8}

where $\eta \leq 1$, being $I_{\rm glitch}$ the moment of inertia powering the glitch, then we can obtain a lower limit for the parameter η: we obtain $\eta = 0.20$ and $\eta = 0.18$ for the global and local charge neutrality cases, respectively. Tables 3 and 4 show the theoretically predicted value of $|\Delta P|/P$ for the seven sources with known bursts energy, assuming the mass of the NS is larger than 1 $M_\odot$ and $\eta = 1$, in the cases of global and local charge neutrality, respectively.

Table 4 shows that from the nine potentially rotation-powered sources, two have a firmly established glitch-outburst connection. For the other sources there are two possibilities. (1) The glitch could be missed because absence of timing monitoring of the source prior to the burst, as it is certainly the case of the SGRs/AXPs discovered from an outburst. (2) The source timing was monitored and indeed there is no glitch associated with the outburst. In this case, it remains open the possibility that the outburst could be of magnetospheric origin. (3) There are also observed glitches without associated outburst activity (see, e.g., Pons & Rea 2012). It is worth mentioning that a recent systematic analysis of the glitch-outburst connection in five AXPs by Dib & Kaspi (2014) concluded (amongst other important results): 1) glitches associated and not associated with outbursts or radiative changes show similar timing properties, namely outburst activity is not necessarily associated with large glitches; and 2) all glitches observed point to have their origin in the stellar interior. The second conclusion gives observational support to our theoretical interpretation of glitches as a phenomenon associated to cracking occurring in the NS interior. Whether a glitch can or not lead to observable radiative changes depends on specific properties of the phenomenon such as the energy budget and the localization of the event in the star's interior (Dib & Kaspi 2014), as well as on the efficiency in converting mechanical energy into radiation. The first two features have been here analyzed through $\Delta E_{\rm rot}$ and the parameter η, the latter which defines $I_{\rm glitch}$, the amount of moment of inertia involved in the glitch.

Thus, the glitch-outburst connection remains one of the most interesting problems of SGR/AXP physics and astrophysics. There are still several issues which need to be addressed both from systematic observational analyses and from theoretical point of view of NS physics.

6. Possible additional evidence

We have shown above for the nine potential rotation-powered SGRs/AXPs that, when timing observations allowed for the glitch/outburst connection identification, the rotational energy gain in the glitch can explain the outburst energetics. This characteristic is expected from a rotation-powered object.

We discuss now three additional pieces of astrophysical evidence pointing to a rotation-power nature of these sources. First, we note that four of the above nine sources, namely 1E 1547.0−5408, SGR J1745−2900, XTE J1810−197, and PSR J1622−4950, are the only SGR/AXPs with detected radio emission (see, e.g., Halpern et al. 2005; Camilo et al. 2006, 2007a,b, 2008; Helfand et al. 2006; Kramer et al. 2007; Levin et al. 2010, 2012; Eatough et al. 2013; Olausen & Kaspi 2014; Lobato et al. 2015; Yusef-Zadeh et al. 2015). This property, expected in ordinary rotation-powered pulsars, is generally absent in SGR/AXPs. As discussed in Kramer et al. (2007), the radio emission of SGRs/AXPs and normal radio pulsars shows differences but also similarities, e.g. the case of XTE J1810-197. We show in Table 2 the observed radio luminosity per solid angle at the 1.4 GHz frequency. For all of them we have $L_{\rm radio} \ll L_{\rm X}$, a feature also observed in ordinary pulsars. The continuous observation, as well as theoretical analysis and comparison of the radio emission of rotating radio transients (RRATS), high-B pulsars, SGRs/AXPs, and ordinary radio pulsars will allow us to understand the NS properties leading to the differences and similarities of the radio emission of these sources. New observational capabilities such as the ones of the Square Kilometer Array (SKA) expect to give also important contributions in this direction (Tauris et al. 2015).

In order to understand better the nature of these nine SGRs/AXPs it is worth to seek for additional emission features which could distinguish them from the rest of the sources. In this line we would like to point out that, at present, eleven SGRs/AXPs have been identified as *transient* sources, i.e. sources which show flux variations by a factor ∼(10−1000) over the quiescent level (see, e.g., Turolla et al. 2015), in timescales from days to months. Such a variations are usually accompanied by an enhancement of the bursting activity. Seven of the nine potentially rotation-powered sources shown in Table 2 are transient sources. Therefore it is possible to identify common features in these sources, although more observational and theoretical investigation is needed. For instance, the above shows that all radio SGR/AXPs are rotation-powered sources and have a transient nature in the X-ray flux. The theoretical analysis of the evolution of the X-ray flux can constrain the properties of the NS and the emission geometry, for instance the angles between the rotation axis, the line of sight and the magnetic field (see, e.g., Albano et al. 2010). Such constraints can help in constraining, at the same time, the properties of the radio emission. Such an analysis is however out of the scope of the present work and opens a window of new research which we plan to present elsewhere.

There is an additional observational property which support to a NS nature for the nine sources of Table 2, namely six of them have possible associations with supernova remnants (SNRs). As it is summarized in Table 2, *Swift* J1834.9–0846 has been associated with SNR W41 (see, Younes et al. 2016, for the detection of a wind nebula around this source); PSR J1846−0258 with SNR Kes75; 1E 1547.0−5408 with SNR G327.24−0.13; PSR J1622−4950 with SNR G333.9+0.0; SGR 1627−41 with NR G337.0-0; and CXOU J171405.7–381031 with SNR CTB37B (Olausen & Kaspi 2014). If these associations will be fully confirmed, then it is clear that the NS was born from the core-collapse of a massive star which triggered the SN explosion. Further analysis of the supernova remnant and/or pulsar wind nebulae energetics and emission properties is needed to check their consistency with the rotation-powered nature of the object at the center.

7. Conclusions

We consider here the possibility that some SGRs and AXPs could be rotation-powered NSs by exploring the allowed range of realistic NS structure parameters for the observed rotation periods of SGRs/AXPs, instead of using only fiducial parameters $M = 1.4\ M_\odot$, $R = 10$ km, and $I = 10^{45}$ g cm^2. We obtained the NS properties from the numerical integration of the general relativistic axisymmetric equations of equilibrium for EOS based on relativistic nuclear mean-field models both in the case of local and global charge neutrality. We thus calculated the rotational energy loss, $\dot{E}_{\rm rot}$, (hence a radiation efficiency $L_{\rm X}/\dot{E}_{\rm rot}$) as a function of the NS mass. In addition, we estimated the surface magnetic field from a general relativistic model of a rotating magnetic dipole in vacuum.

Based on the above, we have shown that fiducial parameters overestimate both the radiation efficiency and the surface magnetic field of pulsars. Moreover, the X-ray luminosity of nine sources shown in Table 2, that is *Swift* J1834.9–0846, PSR J1846–0258, 1E 1547.0–5408, SGR J1745–2900, XTE J1810−197, PSR J1622–4950, SGR 1627–41, SGR 0501+4516, and CXOU J171405.7381031 can be explained via the loss of rotational energy of NSs (see Fig. 6). Thus, they fit into the family of ordinary rotation-powered pulsars. For the above nine sources, we obtained lower mass limits from the request $\dot{E}_{\rm rot} \geq L_{\rm X}$.

We also show that, if the thermal reservoir of the NS is responsible for the blackbody component observed in soft X-rays, both SGR 1900+14 and SGR 1806-20 join the above family of rotation-powered NSs, since the rotational energy loss is enough to cover their non-thermal X-ray luminosity. This implies that up to 11 SGR/AXPs could be rotation-powered pulsars. This argument could also be, in principle, applied to the other sources, further lowering their radiation efficiency $L_{\rm X}/\dot{E}_{\rm rot}$. Thus, we argue that the observational uncertainties in the determination of the distances and/or luminosities, as well as the uncertainties in the NS nuclear EOS, as well as the different interpretations of the observed spectrum still leave room for a possible explanation in terms of spin-down power for additional sources. It is worth mentioning that the distance for some sources has been established via their association with SNRs, as pointed out in Table 2.

Furthermore, we then proceeded to discuss the observed emission in hard X-rays (in the 20–150 keV band) in both SGR 1900+14 and SGR 1806-20. Including this contribution, the luminosity increases up to a factor of five and four, respectively, for each source, making it impossible to interpret them as rotation-powered sources unless their estimated distances are poorly constrained. We then examined the three sources of the group of nine potential rotation-powered sources for which hard X-ray emission has been observed: SGR J1745–2900, 1E 1547.0–5408 and SGR 0501+4516. Fig. 8 shows that 1E 1547.0–5408 still remains within the rotation-powered group while the other two sources do not. Thus, for these sources, it becomes critical to verify the accuracy of the estimated distances and to explore the possible contribution of their associated supernova remnants to the hard X-ray emission. If these sources are powered by rotation, then other phenomena observed in known rotation-powered NSs could also have been observed in these objects. Thus, for the nine sources with $L_X < \dot{E}_{rot}$, we explored the possibility that the energetics of their bursting activity, E_{burst}, could be explained from the rotational energy gained in an associated glitch, ΔE_{rot}. We thus computed lower limits to the fractional change of rotation period of NSs caused by glitches, $|\Delta P|/P$, by requesting $\Delta E_{rot} = E_{burst}$. The fact that there exist physically plausible solutions for $|\Delta P|/P$ reinforces the possibility that these sources are indeed rotation-powered (e.g., the cases of PSR J1846–0258 and PSR J1119–6127).

Finally, we discuss in Sect. 6 possible additional evidence pointing to the rotation-power nature of these nine sources: the radio emission is observed in four SGRs/AXPs and all of them are part of these nine sources. Radio emission characterizes ordinary pulsars but it is generally absent/unobserved in SGRs/AXPs. We also draw attention to a peculiar emission property of the majority of these nine sources: seven of them belong to the group of the so-called transient sources (which are eleven in total). Within these seven transient rotation-powered objects, we find four showing radio emission. We argue that the analysis of the varying X-ray flux can provide information on the NS properties and magnetospheric geometry, improving our understanding of the properties of the radio emission. It is worth mentioning that six of the nine sources have potential associations with supernova remnants, supporting a NS nature (see Table 2 for details).

Although we have shown the possibility that some SGRs and AXPs are rotation-powered pulsars, we are far from getting a final answer to the question of the nature of SGRs/AXPs. It is not yet clear whether or not all the current members of the SGR/AXP family actually form a separate class of objects, with respect to traditional pulsars, for example, or if their current classification leads to misleading theoretical interpretations. Therefore, we encourage further theoretical predictions and observations in additional bands of the electromagnetic spectrum such as the optical, high, and ultra-high gamma-rays and cosmic-rays to discriminate amongst the different models and make it possible to elucidate the nature of SGRs and AXPs.

Acknowledgements. It is a great pleasure to thank Sergio Campana for the comments and suggestions on the presentation of our results. Likewise, we would like to thank the anonymous referee for valuable comments. J.G.C., R.C.R. de Lima, and J.A.R., acknowledges the support by the International Cooperation Program CAPES-ICRANet financed by CAPES – Brazilian Federal Agency for Support and Evaluation of Graduate Education within the Ministry of Education of Brazil. M.M. and J.G.C. acknowledge the support of FAPESP through the projects 2013/15088–0 and 2013/26258–4. J.A.R. acknowledges partial support of the project No. 3101/GF4 IPC-11, and the target program F.0679 of the Ministry of Education and Science of the Republic of Kazakhstan.

References

Albano, A., Turolla, R., Israel, G. L., et al. 2010, ApJ, 722, 788
Antoniadis, J., Freire, P. C. C., Wex, N., et al. 2013, Science, 340, 448
Archibald, R. F., Kaspi, V. M., Tendulkar, S. P., & Scholz, P. 2016, ApJ, 829, L21
Baym, G., Bethe, H. A., & Pethick, C. J. 1971a, A&ARv, 175, 225
Baym, G., Pethick, C., & Sutherland, P. 1971b, ApJ, 170, 299
Belvedere, R., Pugliese, D., Rueda, J. A., Ruffini, R., & Xue, S.-S. 2012, Nucl. Phys. A, 883, 1
Belvedere, R., Boshkayev, K., Rueda, J. A., & Ruffini, R. 2014, Nucl. Phys. A, 921, 33
Belvedere, R., Rueda, J. A., & Ruffini, R. 2015, ApJ, 799, 23
Bibby, J. L., Crowther, P. A., Furness, J. P., & Clark, J. S. 2008, MNRAS, 386, L23
Boguta, J., & Bodmer, A. R. 1977, Nucl. Phys. A, 292, 413
Boshkayev, K., Izzo, L., Rueda Hernandez, J. A., & Ruffini, R. 2013, A&A, 555, A151
Camilo, F., Ransom, S. M., Halpern, J. P., et al. 2006, Nature, 442, 892
Camilo, F., Cognard, I., Ransom, S. M., et al. 2007a, ApJ, 663, 497
Camilo, F., Ransom, S. M., Halpern, J. P., & Reynolds, J. 2007b, ApJ, 666, L93
Camilo, F., Reynolds, J., Johnston, S., Halpern, J. P., & Ransom, S. M. 2008, ApJ, 679, 681
Coelho, J. G., & Malheiro, M. 2013, ArXiv e-print [arXiv:1307.8158]
Coelho, J. G., & Malheiro, M. 2014, PASJ, 66, 14
Coelho, J. G., & Malheiro, M. 2015, in Thirteenth Marcel Grossmann Meeting: On Recent Developments in Theoretical and Experimental General Relativity, Astrophysics and Relativistic Field Theories, ed. K. Rosquist (World Scientific Publ. Co), 2465
Corbel, S., & Eikenberry, S. S. 2004, A&A, 419, 191
Demorest, P. B., Pennucci, T., Ransom, S. M., Roberts, M. S. E., & Hessels, J. W. T. 2010, Nature, 467, 1081
Deutsch, A. J. 1955, Annales d'Astrophysique, 18, 1
Dib, R., & Kaspi, V. M. 2014, ApJ, 784, 37
Duncan, R. C., & Thompson, C. 1992, ApJ, 392, L9
Eatough, R. P., Falcke, H., Karuppusamy, R., et al. 2013, Nature, 501, 391
Esposito, P., Mereghetti, S., Tiengo, A., et al. 2007, A&A, 476, 321
Gavriil, F. P., Gonzalez, M. E., Gotthelf, E. V., et al. 2008, Science, 319, 1802
Glendenning, N. K., & Moszkowski, S. A. 1991, Phys. Rev. Lett., 67, 2414
Götz, D., Mereghetti, S., Tiengo, A., & Esposito, P. 2006, A&A, 449, L31
Halpern, J. P., Gotthelf, E. V., Becker, R. H., Helfand, D. J., & White, R. L. 2005, ApJ, 632, L29
Hartle, J. B. 1967, ApJ, 150, 1005
Helfand, D. J., Camilo, F., Ransom, S. M., et al. 2006, in AAS/High Energy Astrophysics Division #9, BAAS, 38, 349
Kramer, M., Stappers, B. W., Jessner, A., Lyne, A. G., & Jordan, C. A. 2007, MNRAS, 377, 107
Kuiper, L., & Hermsen, W. 2009, A&A, 501, 1031
Kuiper, L., Hermsen, W., den Hartog, P. R., & Urama, J. O. 2012, ApJ, 748, 133
Kumar, H. S., & Safi-Harb, S. 2008, ApJ, 678, L43
Lalazissis, G. A., König, J., & Ring, P. 1997, Phys. Rev. C, 55, 540
Levin, L., Bailes, M., Bates, S., et al. 2010, ApJ, 721, L33
Levin, L., Bailes, M., Bates, S. D., et al. 2012, MNRAS, 422, 2489
Lobato, R. V., Coelho, J., & Malheiro, M. 2015, J. Phys. Conf. Ser., 630, 012015
Lobato, R. V., Malheiro, M., & Coelho, J. G. 2016, Int. J. Mod. Phys. D, 25, 1641025
Malheiro, M., Rueda, J. A., & Ruffini, R. 2012, PASJ, 64, 56
Malov, I. F. 2010, Astron. Rep., 54, 925
Mereghetti, S. 2008, A&AR, 15, 225
Mereghetti, S., Esposito, P., Tiengo, A., et al. 2006, ApJ, 653, 1423
Olausen, S. A., & Kaspi, V. M. 2014, ApJS, 212, 6
Oppenheimer, J. R., & Volkoff, G. M. 1939, Phys. Rev., 55, 374
Ouyed, R., Leahy, D., & Niebergal, B. 2011, MNRAS, 415, 1590
Pons, J. A., & Rea, N. 2012, ApJ, 750, L6
Rea, N., Pons, J. A., Torres, D. F., & Turolla, R. 2012, ApJ, 748, L12
Rezzolla, L., & Ahmedov, B. J. 2004, MNRAS, 352, 1161
Rotondo, M., Rueda, J. A., Ruffini, R., & Xue, S.-S. 2011, Phys. Lett. B, 701, 667
Rueda, J. A., Ruffini, R., & Xue, S.-S. 2011, Nucl. Phys. A, 872, 286
Rueda, J. A., Boshkayev, K., Izzo, L., et al. 2013, ApJ, 772, L24
Sugahara, Y., & Toki, H. 1994, Nucl. Phys. A, 579, 557
Tauris, T. M., Kaspi, V. M., Breton, R. P., et al. 2015, Adv. Astrophys. with the Square Kilometre Array (AASKA14), 39
Thompson, C., & Duncan, R. C. 1995, MNRAS, 275, 255
Tolman, R. C. 1939, Phys. Rev., 55, 364
Trümper, J. E., Dennerl, K., Kylafis, N. D., Ertan, Ü., & Zezas, A. 2013, ApJ, 764, 49
Turolla, R., Zane, S., & Watts, A. L. 2015, Rep. Prog. Phys., 78, 116901
Vrba, F. J., Henden, A. A., Luginbuhl, C. B., et al. 2000, ApJ, 533, L17
Xu, R. X., Tao, D. J., & Yang, Y. 2006, MNRAS, 373, L85
Younes, G., Kouveliotou, C., Kargaltsev, O., et al. 2016, ApJ, 824, 138
Yusef-Zadeh, F., Diesing, R., Wardle, M., et al. 2015, ApJ, 811, L35

Monthly Notices
of the
ROYAL ASTRONOMICAL SOCIETY

MNRAS **465,** 4434–4440 (2017) doi:10.1093/mnras/stw3047
Advance Access publication 2016 November 23

Thermal X-ray emission from massive, fast rotating, highly magnetized white dwarfs

D. L. Cáceres,[1,2] S. M. de Carvalho,[3] J. G. Coelho,[4] R. C. R. de Lima[2,5] and Jorge A. Rueda[1,2,6★]

[1]*Dipartimento di Fisica and ICRA, Sapienza Università di Roma, P.le Aldo Moro 5, I-00185 Rome, Italy*
[2]*ICRANet, P.zza della Repubblica 10, I-65122 Pescara, Italy*
[3]*Universidade Federal do Tocantins, Campus Araguaína, Av. Paraguai 77814-970 Araguaína, TO, Brazil*
[4]*Div. Astrofísica, Instituto Nacional de Pesquisas Espaciais, Av. dos Astronautas 1758, 12227–010 São José dos Campos, SP, Brazil*
[5]*Universidade do Estado de Santa Catarina, Av. Madre Benvenuta, 2007 Itacorubi, 88.035–901 Florianópolis, Brazil*
[6]*ICRANet-Rio, Centro Brasileiro de Pesquisas Físicas, Rua Dr. Xavier Sigaud 150, 2290–180 Rio de Janeiro, Brazil*

Accepted 2016 November 22. Received 2016 November 21; in original form 2016 February 5

ABSTRACT

There is solid observational evidence on the existence of massive, $M \sim 1\,\mathrm{M}_{\odot}$, highly magnetized white dwarfs (WDs) with surface magnetic fields up to $B \sim 10^9$ G. We show that, if in addition to these features, the star is fast rotating, it can become a rotation-powered pulsar-like WD and emit detectable high-energy radiation. We infer the values of the structure parameters (mass, radius, moment of inertia), magnetic field, rotation period and spin-down rates of a WD pulsar death-line. We show that WDs above the death-line emit blackbody radiation in the soft X-ray band via the magnetic polar cap heating by back flowing pair-created particle bombardment and discuss as an example the X-ray emission of soft gamma-repeaters and anomalous X-ray pulsars within the WD model.

Key words: acceleration of particles – radiation mechanisms: thermal – stars: magnetic field – starspots – white dwarfs.

1 INTRODUCTION

The increasing data from observational campaigns leave no room for doubts on the existence of massive ($M \sim 1\,\mathrm{M}_{\odot}$) white dwarfs (WDs) with magnetic fields comprised in the range $B = 10^6$–10^9 G (Külebi et al. 2009; Kepler et al. 2013, 2015). It has been recently shown that massive, highly magnetized WDs could be formed by mergers of double WDs (García-Berro et al. 2012). The fact that WDs produced in mergers, besides being massive and highly magnetized, can be also fast rotators with periods $P \sim 10$ s was used in Rueda et al. (2013) to show that they could be the WDs postulated in Malheiro, Rueda & Ruffini (2012) to describe the observational properties of soft gamma-repeaters (SGRs) and anomalous X-ray pulsars (AXPs), in alternative to the 'magnetar' model (Duncan & Thompson 1992; Thompson & Duncan 1995). In the WD model, the observed X-ray luminosity of SGRs/AXPs is explained via the loss of rotational energy of the fast rotating WD.[1] The WD gravitational stability imposes a lower bound to the rotation period $P \approx 0.5$ s, in agreement with the minimum measured rotation period of SGRs/AXPs, $P \sim 2$ s (Boshkayev et al. 2013b). On the other hand, the surface area and temperature of the emitting region inferred from the available infrared, optical and ultraviolet data of SGR/AXPs (i.e. for SGR 0418+5729, J1822.3–1606, 1E 2259+586 and 4U 0142+61) were shown to be consistent with the values expected from WDs (Boshkayev et al. 2013a; Rueda et al. 2013). The similarities of these WDs with ordinary, rotation-powered pulsars imply that similar radiation mechanisms are expected to be at work in their magnetosphere. Indeed, the loss of rotational energy of the WD, owing to magnetic breaking, is sufficient to explain the X-ray luminosity observed in SGRs/AXPs, and the inferred magnetic field from the observed spindown rates, $B \sim 10^9$ G, agrees with the aforementioned observed values in Galactic WDs (Malheiro et al. 2012; Coelho & Malheiro 2014).

Following this line, it was advanced in Rueda et al. (2013) that the blackbody observed in the soft X-rays of SGRs/AXPs, with observationally inferred radii $R_{\rm bb} \sim 1$ km and temperatures $T_{\rm bb} \sim 10^6$ K, could be due to a known phenomenon expected to occur in pulsars, namely the magnetospheric currents flowing back towards the WD, heating up the magnetic polar caps creating surface hot spots (see e.g. Usov 1988, 1993). The aim of this work is to estimate this

★ E-mail: jorge.rueda@icra.it

[1] It remains open the case of 1E 161348–5055, the central compact object in the supernova remnant RCW 103, to be confirmed as a new SGR/AXP (see e.g. Rea et al. 2016; D'Aì et al. 2016). The observed luminosity and light-curve periodicity with $P = 6.67$ h, if confirmed to be due to the rotation period, together with the upper limit of to the possible spin-down rate $|\dot{P}| < 7 \times 10^{-10}$, rule out the rotational energy of either a neutron star or a WD as the possible source of energy.

magnetospheric process for massive, highly magnetized, fast rotating WDs, exploiting the full analogy with pulsars. This calculation is interesting by its own and becomes of observational relevance in view of the latest results by Marsh et al. (2016) which point to the observational evidence of pulsar behaviour of a magnetized WD. It is interesting that, as in the well-known case of AE Aquari, also this WD belongs to a binary system. Pulsar behaviour can be observed from WDs in binaries when they can be considered approximately as isolated objects as in the case of detached binaries or in binaries in a propeller phase. White dwarf pulsars have been also considered as possible sources of high-energy and cosmic rays (see e.g. Kashiyama, Ioka & Kawanaka 2011). Bearing this in mind, we focus in this work on the observable emission from isolated magnetized WDs in the X-rays. In order to exemplify the mechanism with appealing numbers, we apply it to the case of the WD model of SGRs and AXPs. Specifically, we evaluate the decay rate of curvature radiation photons in e^-e^+ pairs, and the subsequent backward flow of pair-produced particles that bombards and heats up the magnetosphere polar caps, producing the observable thermal radiation. We compute in Section 2 the condition for e^-e^+ pair creation within the inner gap model. In Section 3, we calculate the expected thermal luminosity and infer the values of mass, radius, magnetic field and potential drop that ensure that the polar cap thermal emission explains the observed blackbody in the soft X-ray spectrum of SGRs/AXPs. The cases of 1E 2259+586 and 4U 0142+61 are analysed as specific examples. In Section 4, we simulate the observed X-ray flux from this spotty emission and compute the expected pulsed fraction, which we compare with the observed values in SGRs and AXPs. We outline the conclusions in Section 5.

2 WD MAGNETOSPHERE

Rotating, highly magnetized WDs can develop a magnetosphere analog to the one of pulsars. A corotating magnetosphere (Davis 1947; Ferraro & Unthank 1949; Gold 1962; Ferraro & Bhatia 1967) is enforced up to a maximum distance given by the so-called light cylinder, $R_{\rm lc} = c/\Omega = cP/(2\pi)$, where c is the speed of light and Ω is the angular velocity of the star, since corotation at larger distances would imply superluminal velocities for the magnetospheric particles. For an axisymmetric star with aligned magnetic moment and rotation axes, the local density of charged plasma within the corotating magnetosphere is (Goldreich & Julian 1969)

$$\rho_{\rm GJ} = -\frac{\boldsymbol{\Omega}\cdot\boldsymbol{B}}{2\pi c}\frac{1}{1-(\Omega r_\perp/c)^2}, \tag{1}$$

where $r_\perp = r\sin\theta$ with θ the polar angle.

The last B-field line closing within the corotating magnetosphere can be easily located from the B-field lines equation for a magnetic dipole $r/\sin^2\theta$ = constant $=R_{\rm lc}$, and is located at an angle $\theta_{\rm pc} = \arcsin(\sqrt{R/R_{\rm lc}}) \approx \sqrt{R/R_{\rm lc}} = \sqrt{R\Omega/c} = \sqrt{2\pi R/(cP)}$ from the star's pole, with R the radius of the star. The B-field lines that originate in the region between $\theta = 0$ and $\theta = \theta_{\rm pc}$ (referred to as *magnetic polar caps*) cross the light cylinder, and are called 'open' field lines. The size of the cap is given by the polar cap radius $R_{\rm pc} = R\,\theta_{\rm pc} \approx R\sqrt{2\pi R/(cP)}$. Clearly, by symmetry, there are two (antipodal) polar caps on the stellar surface from which the charged particles leave the star moving along the open field lines and escaping from the magnetosphere passing through the light cylinder.

Particle acceleration is possible in regions called *vacuum gaps* where corotation cannot be enforced, i.e. where the density of charged particles is lower than the Goldreich–Julian value $\rho_{\rm GJ}$ given by equation (1). For aligned (anti-aligned) rotation and magnetic axes, we have $\rho_{\rm GJ} < 0$ ($\rho_{\rm GJ} > 0$), hence magnetosphere has to be supplied by electrons (ions) from the WD surface. This work is done by the existence of an electric field parallel to the magnetic field. Independently on whether $\boldsymbol{\Omega}\cdot\boldsymbol{B}$ is positive or negative, we assume that the condition of a particle injection density lower than $\rho_{\rm GJ}$ is fulfilled. In this *inner gap* model, the gaps are located just above the polar caps (Ruderman & Sutherland 1975) and the potential drop generated by the unipolar effect and that accelerates the electrons along the open B-field lines above the surface is

$$\Delta V = \frac{B_s\Omega h^2}{c}, \tag{2}$$

where h is the height of the vacuum gap and B_s is the surface magnetic field, which does not necessarily coincides with the dipole field B_p.

The electrons (or positrons) accelerated through this potential and following the B-field lines will emit curvature photons whose energy depends on the γ-factor, $\gamma = e\Delta V/(mc^2)$, where e and m are the electron charge and mass, and on the B-field line curvature radius r_c, i.e. $\omega_c = \gamma^3 c/r_c$. Following Chen & Ruderman (1993), we adopt the constraint on the potential ΔV for pair production via $\gamma + B \to e^- + e^+$,

$$\frac{1}{2}\left(\frac{e\Delta V}{mc^2}\right)^3\frac{\lambda}{r_c}\frac{h}{r_c}\frac{B_s}{B_q} \approx \frac{1}{15}, \tag{3}$$

or in terms of a condition on the value of the potential,

$$\Delta V \approx \left(\frac{2}{15}\right)^{2/7}\left(\frac{r_c}{\lambda}\right)^{4/7}\left(\frac{\lambda\Omega}{c}\right)^{1/7}\left(\frac{B_s}{B_q}\right)^{-1/7}\frac{mc^2}{e}, \tag{4}$$

where we have used equation (2), $\lambda = \hbar/(mc)$, $B_q \equiv m^2c^3/(e\hbar) = 4.4\times10^{13}$ G, is the quantum electrodynamic field, with $\hbar$ the reduced Planck's constant.

For a magnetic dipole geometry, i.e. $B_s = B_d$ and $r_c = \sqrt{Rc/\Omega}$, the potential drop ΔV cannot exceed the maximum potential (i.e. for $h = h_{\rm max} = R_{\rm pc}/\sqrt{2}$),

$$\Delta V_{\rm max} = \frac{B_d\Omega^2R^3}{2c^2}. \tag{5}$$

Here, we are interested in the possible magnetospheric mechanism of X-ray emission from magnetized WDs, thus we will consider the heating of the polar caps by the inward flux of pair-produced particles in the magnetosphere. These particles of opposite sign to the parallel electric field move inwards and deposit most of their kinetic energy on an area

$$A_{\rm spot} = f A_{\rm pc}, \tag{6}$$

i.e. a fraction $f \le 1$ of the polar cap area, $A_{\rm pc} = \pi R_{\rm pc}^2$. The temperature $T_{\rm spot}$ of this surface hotspot can be estimated from the condition that it re-radiates efficiently the deposit kinetic energy, as follows. The rate of particles flowing to the polar cap is $\dot{N} = JA_{\rm pc}/e$, where $J = \eta\rho_{\rm GJ}c$ is the current density in the gap and $\eta < 1$ a parameter that accounts for the reduction of the particle density in the gap with respect to the Goldreich–Julian value (Cheng & Ruderman 1977 used $\eta = 1$ for order-of-magnitude estimates). In this model, the filling factor f is not theoretically constrained, and it has been estimated from pulsar's observations in X-rays that its value can be much smaller than unity (Cheng & Ruderman 1977). The condition that the hotspot luminosity equals the deposited kinetic energy rate reads

$$A_{\rm spot}\sigma T_{\rm spot}^4 = e\Delta V\dot{N} = JA_{\rm pc}\Delta V = \eta\rho_{\rm GJ}(R)cA_{\rm pc}\Delta V, \tag{7}$$

where σ is the Stefan–Boltzmann constant. From equations (1), (6) and (7), we obtain the spot temperature

$$T_{\rm spot} = \left(\eta \frac{B_d \Delta V}{\sigma f P}\right)^{1/4}. \tag{8}$$

It is worth mentioning that in the above estimate, we have assumed a full efficiency in the conversion from the deposited kinetic energy to the hotspot emission. This assumption is accurate if the heating source, namely the energy deposition, occurs not too deep under the star's surface and it is not conducted away to larger regions being mainly re-radiated from the surface area filled by the penetrating particles (Cheng & Ruderman 1980). In Appendix, we estimate the cooling and heating characteristic times and the heating and re-radiation efficiency. For the densities and temperatures of interest here, we show that the polar cap surface re-radiates efficiently most of the kinetic energy deposited by the particle influx validating our assumption.

3 SPECIFIC EXAMPLES

As in our previous analyses (Malheiro et al. 2012; Boshkayev et al. 2013a; Rueda et al. 2013; Coelho & Malheiro 2014), we use the traditional dipole formula to get an estimate for the WD dipole magnetic field, i.e.:

$$B_d = \left(\frac{3c^3}{8\pi^2}\frac{I}{R^6} P \dot{P}\right)^{1/2}, \tag{9}$$

where I is the moment of inertia of the star, $\dot{P} \equiv {\rm d}P/{\rm d}t$ is the first time derivative of the rotation period (spin-down rate) and an inclination of $\pi/2$ between the magnetic dipole and the rotation axis has been adopted. It is worth recalling that the estimate of the B-field by equation (9) is not necessarily in contrast, from the quantitative point of view, with an estimate using an aligned field but introducing a breaking from the particles escaping from the magnetosphere, since also in this case a quantitatively and qualitatively similar energy loss is obtained.

For a given rotation period P, the WD structure parameters such as mass M, radius R and moment of inertia I are bounded from below and above if the stability of the WD is requested (Boshkayev et al. 2013a). From those bounds, we established their lower and upper bounds for the field B_d of the WD.

3.1 1E 2259+586

We apply the above theoretical framework to a specific source, AXP 1E 2259+586. This source, with a rotation period $P = 6.98$ s (Fahlman & Gregory 1981) and a spin-down rate $\dot{P} = 4.8 \times 10^{-13}$ (Davies, Coe & Wood 1990), has a historical importance since Paczynski (1990) first pointed out the possibility of this object being a WD. This object produced a major outburst in 2002 (Kaspi et al. 2003; Woods et al. 2004), in which the pulsed and persistent fluxes rose suddenly by a factor of $\geq$20 and decayed on a time-scale of months. Coincident with the X-ray brightening, the pulsar suffered a large glitch of rotation frequency fractional change 4×10^{-6} (Kaspi et al. 2003; Woods et al. 2004). It is worth recalling that the observed temporal coincidence of glitch/bursting activity, as first pointed out by Usov (1994) in the case of 1E 2259+586, and then extended in Malheiro et al. (2012) and Boshkayev et al. (2013a), can be explained as due to the release of the rotational energy, gained in a starquake occurring in a total or partially crystallized WD. Since we are interested in the quiescent behaviour, we will not consider this interesting topic here. Therefore, only X-ray data prior to this outburst event will be used in this work (Zhu et al. 2008).

The soft X-ray spectrum of 1E 2259+586 is well fitted by a blackbody plus a power-law model. The blackbody is characterized by a temperature $kT_{\rm bb} \approx 0.37$ keV ($T_{\rm bb} \approx 4.3 \times 10^6$ K) and emitting surface are $A_{\rm bb} \approx 1.3 \times 10^{12}$ cm^2 (Zhu et al. 2008). These values of temperature and radius are inconsistent (too high and too small, respectively) with an explanation based on the cooling of a hot WD, and therefore such a soft X-ray emission must be explained from a spotty surface due to magnetospheric processes, as the one explored in this work.

The stability of the WD for such a rotation period constrains the WD radius to the range $R \approx (1.04$–$4.76) \times 10^8$ cm. For example, in the case of a WD with radius $R \approx 10^8$ cm, the polar cap area is $A_{\rm pc} = 6.6 \times 10^{14}$ cm, hence using equation (6) we have $f \approx 0.002$. From equation (8) the spot temperature $kT_{\rm spot} \approx 0.37$ keV can be obtained using $B_d \approx 6 \times 10^9$ G from the dipole formula (9), a potential drop $\Delta V \approx 3.5 \times 10^{11}$ V (lower than $\Delta V_{\rm max} \approx 5.4 \times 10^{12}$ V), and using the typical value $\eta = 1/2$ of the reduced particle density in the gap adopted in the literature. These parameters suggest a height of the gap, obtained with equation (2), $h \approx 0.11 R_{\rm pc}$.

The smallness of the filling factor, which appears to be not attributable to the value of h, could be explained by a multipolar magnetic field near the surface. It is interesting that the existence of complex multipolar magnetic field close to the WD surface is observationally supported (see e.g. Ferrario, de Martino & Gänsicke 2015). It is important to clarify that the above defined filling factor has only a physical meaning when, besides a strong non-dipolar surface field, the physical parameters of the star (magnetic field and rotational velocity) fulfill the requirement for the creation of electron–positron pairs in such a way that an avalanche of particles hits the surface. This is given by the request that the potential drop (4) does not exceed the maximum value (5). For example, for the largest magnetic field measured in WDs, $B \sim 10^9$G, and WD radii 10^8–10^9 cm, the maximum period that allows the avalanche of electron–positron pairs gives the range $P \sim 4$–100 s, values much shorter than the value of typical rotation periods measured in most of magnetic WDs, $P \gtrsim 725$ s (see e.g. Ferrario et al. 2015). It is interesting to note that the condition of e^+e^- pair creation in the WD magnetosphere could explain the narrow range of observed rotation periods of SGRs/AXPs, $P \sim 2$–12 s. Such a local, strong non-dipolar field in the surface diminishes the area bombarded by the incoming particles and, via magnetic flux conservation, the filling factor establishes the intensity of the multipolar magnetic field component as (see e.g. Cheng & Zhang 1999; Gil & Sendyk 2000; Gil & Melikidze 2002, and references therein)

$$B_s = \frac{B_d}{f}, \tag{10}$$

which implies that, close to the surface, there could be small magnetic domains with magnetic field intensity as large as 10^{11}–10^{12} G (see Fig. 1).

3.2 4U 0142+61

We can repeat the above analysis for the case of 4U 0142+61. This source, with a rotation period $P \approx 8.69$ s, was first detected by *Uhuru* (Forman et al. 1978). The measured period derivative of this source is $\dot{P} = 2.03 \times 10^{-12}$ (Hulleman, van Kerkwijk & Kulkarni 2000). The time-integrated X-ray spectrum of 4U 0142+61 is also described by a blackbody plus a power-law model. The blackbody component shows a temperature

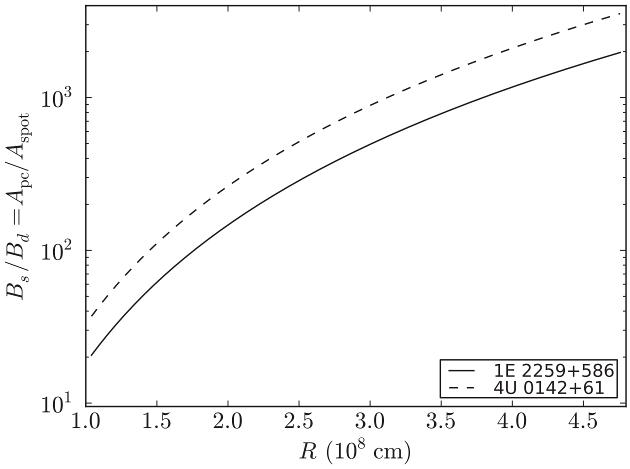

Figure 1. Surface to dipole magnetic field ratio given by magnetic flux conservation (10) for the AXPs 1E 2259+586 and 4U 0142+61.

$kT_{\rm bb} = 0.39$ keV ($T_{\rm bb} \approx 4.6 \times 10^6$ K) and a surface area $A_{\rm bb} \approx 5.75 \times 10^{11}$ cm^2 (Göhler, Wilms & Staubert 2005). As for the above case of 1E 2259+5726, such a blackbody cannot be explained from the cooling of a WD but instead from a magnetospheric hotspot created by the heating of the polar cap.

For a WD radius $R = 10^8$ cm and a magnetic field $B_d \approx 10^{10}$ G for a rotating dipole (9), we have a filling factor $f \approx 0.001$, a potential drop $\Delta V \approx 1.4 \times 10^{11}$ V (smaller than $\Delta V_{\rm max} \approx 5.8 \times 10^{12}$ Volts) and a gap height $h \approx 0.06 R_{\rm pc}$. Again the filling factor suggests the presence of a strong multipolar component as shown in Fig. 1.

We show in Fig. 2 the potential drop inferred from equation (8) using the X-ray blackbody data for the above two sources. We check that for all the possible stable WD configurations, the potential drop satisfies the self-consistence condition $\Delta V < \Delta V_{\rm max}$, where the latter is given by equation (5).

4 FLUX PROFILES AND PULSED FRACTION

We turn now to examine the properties of the flux emitted by such hot spots. Even if the gravitational field of a WD is not strong enough to cause appreciable general relativistic effects, for the sake of generality we compute the flux from the star taken into account the bending of light. We shall follow here the treatment in Turolla & Nobili (2013) to calculate the observed flux that allows us to treat circular spots of arbitrary finite size and arbitrarily located in the star surface. The mass and radius of the star are denoted by M and R and the outer space–time is described by the Schwarzschild metric, i.e. we shall neglect at first approximation the effects of rotation. Let (r, θ, ϕ) be the spherical coordinate system centred on the star and the line-of-sight (LOS) the polar axis.

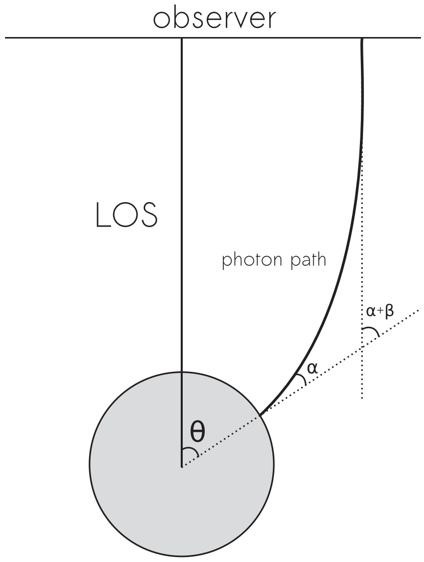

Figure 3. View of the photon trajectory and angles θ, α and β.

We consider an observer at $r \to \infty$ and a photon that arises from the star surface at $dS = R^2 \sin\theta d\theta d\phi$ making an angle α with the local surface normal, where $0 \le \alpha \le \pi/2$. The photon path is then bended by an additional angle β owing to the space–time curvature, reaching the observer with an angle $\psi = \alpha + \beta$. Since we have chosen the polar axis aligned with the LOS, it is easy to see that $\psi = \theta$ (see Fig. 3). Beloborodov (2002) showed that a simple approximate formula can be used to relate the emission angle α to the final angle θ:

$$1 - \cos\alpha = (1 - \cos\theta)\left(1 - \frac{R_s}{R}\right), \tag{11}$$

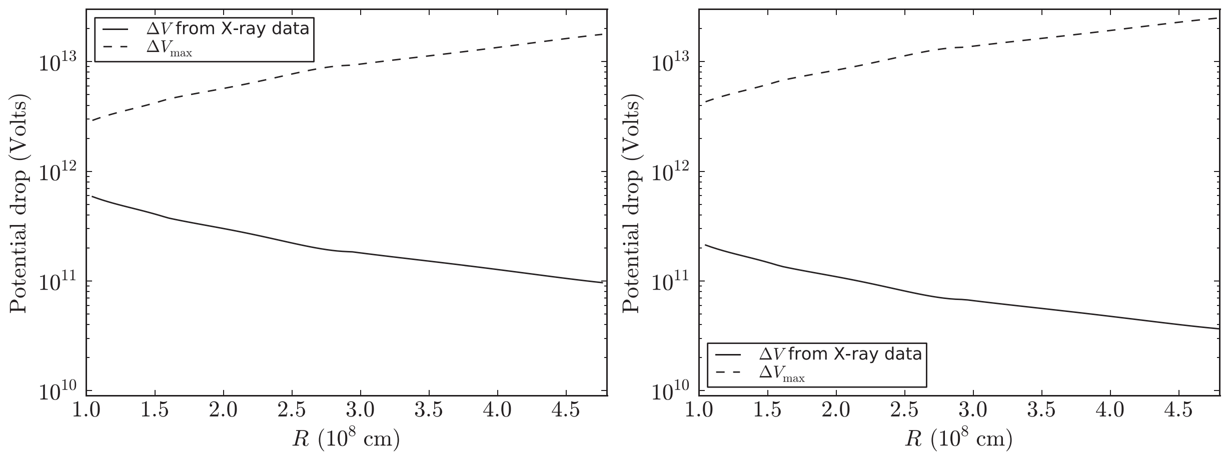

Figure 2. WD polar gap potential drop ΔV inferred via equation (8) using the blackbody observed in soft X-rays in 1E 2259+586 (left-hand panel) and 4U 0142+61 (right-hand panel). In this plot, we check the potential drop developed in the WD polar gap does not exceed the maximum potential reachable $\Delta V_{\rm max}$ given by equation (5).

where $R_s = 2GM/c^2$ is the Schwarzschild radius and, as usual, G denotes the gravitational constant.

For an emission with a local Planck spectrum, the intensity is given by a blackbody of temperature T, $B_\nu(T)$, where ν is the photon frequency. The flux is proportional to the visible area of the emitting region (S_V) plus a relativistic correction proportional to the surface, given by the equation

$$F_\nu = \left(1 - \frac{Rs}{R}\right) B\nu(T) \int_{S_V} \cos\alpha \frac{\mathrm{d}cos\alpha}{\mathrm{d}(\cos\theta)} \mathrm{d}s$$

$$= \left(1 - \frac{Rs}{R}\right)^2 B_\nu(T)(I_p + I_s), \tag{12}$$

where

$$I_p = \int_{S_V} \cos\theta \sin\theta \mathrm{d}\theta \mathrm{d}\phi, \quad I_s = \int_{S_V} \sin\theta \mathrm{d}\theta \mathrm{d}\phi. \tag{13}$$

In polar coordinates, the circular spot has its centre at θ_0 and a semi-aperture θ_c. The spot is bounded by the function $\phi_b(\theta)$, where $0 \le \phi_b \le \pi$, and since we must consider just the star visible part, the spot must be also limited by a constant θ_F. For a given bending angle β, the maximum θ_F is given by the maximum emission α, i.e. $\alpha = \pi/2$. One can see that in a Newtonian gravity, where $\beta = 0$, the maximum visible angle is $\theta_F = \pi/2$, which means half of the star is visible, while in a relativistic star, values $\theta_F > \pi/2$ are possible, as expected. Then

$$I_p = 2\int_{\theta_{\min}}^{\theta_{\max}} \cos\theta \sin\theta \phi_b(\theta) \mathrm{d}\theta,$$

$$I_s = 2\int_{\theta_{\min}}^{\theta_{\max}} \sin\theta \phi_b(\theta) \mathrm{d}\theta, \tag{14}$$

where $\theta_{\min}$, $\theta_{\max}$ are the limiting values to be determined for the spot considered. Turolla & Nobili (2013) showed how to solve these integrals and how to treat carefully the limiting angles. The I_p and I_s integrals can be then written as $I_{p,\,s} = I_{1,\,2}(\theta_{\max}) - I_{1,\,2}(\theta_{\min})$ and we refer the reader to that work for the precise expressions.

Finally, the flux (12) is written as

$$F_\nu = \left(1 - \frac{Rs}{R}\right)^2 B_\nu(T) A_{\rm eff}(\theta_c, \theta_0), \tag{15}$$

where $A_{\rm eff}$ is the effective area, given by

$$A_{\rm eff}(\theta_c, \theta_0) = R^2 \left[\frac{Rs}{R} I_s + \left(1 - \frac{Rs}{R}\right) I_p\right]. \tag{16}$$

The total flux produced by two antipodal spots, with semi-apertures $\theta_{c,i}$ and temperatures T_i (i = 1,2), can be calculated by adding each contribution, so we have

$$F_\nu^{\rm TOT} = \left(1 - \frac{Rs}{R}\right)^2 [B_\nu(T_1) A_{\rm eff}(\theta_{c,1}, \theta_0)$$

$$+ B_\nu(T_2) A_{\rm eff}(\theta_{c,2}, \theta_0 + \pi/2)]. \tag{17}$$

Besides, the pulse profile in a given energy band $[\nu_1, \nu_2]$ for one spot is given by

$$F(\nu_1, \nu_2) = \left(1 - \frac{Rs}{R}\right)^2 A_{\rm eff}(\theta_c, \theta_0) \int_{\nu_1}^{\nu_2} B_\nu(T) \mathrm{d}\nu. \tag{18}$$

The star rotates with a period P (angular velocity $\Omega = 2\pi/P$), so we consider $\hat{\boldsymbol{r}}$ the unit vector parallel to the rotating axis. It is useful to introduce the angles ξ, the angle between the LOS (unit vector $\hat{\boldsymbol{l}}$) and the rotation axis and the angle χ between the spot axis (unit vector $\hat{\boldsymbol{c}}$) and the rotation axis, i.e. $\cos\xi = \hat{\boldsymbol{r}} \cdot \hat{\boldsymbol{l}}$ and $\cos\chi = \hat{\boldsymbol{r}} \cdot \hat{\boldsymbol{c}}$.

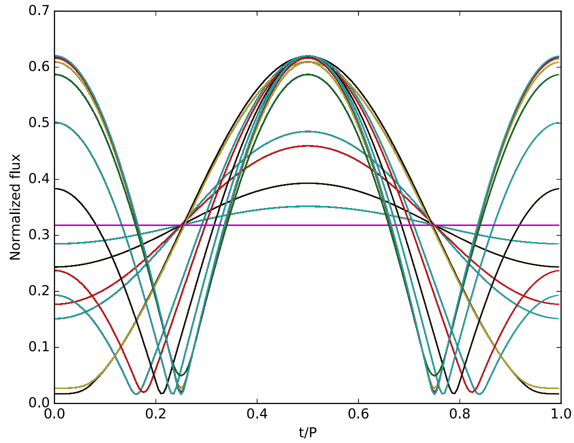

Figure 4. Flux profiles for different configurations of antipodal spots as a function of the phase. The semi-aperture for all the lines is $\theta_c = 3°$. The WD parameters correspond to the ones of the WD of minimum radius adopted for AXP 1E 2259+586.

As the star rotates, the spot's centre, θ_0, changes. Let $\gamma(t) = \Omega t$ be the rotational phase, thus by geometrical reasoning we have

$$\cos\theta_0(t) = \cos\xi \cos\chi - \sin\xi \sin\chi \cos\gamma(t), \tag{19}$$

where it is indicated that ξ and χ do not change in time. When the total flux (17) is calculated for a given configuration (ξ, χ) in the whole period of time, the typical result is a pulsed flux with a maximum ($F_{\max}$) and a minimum flux ($F_{\min}$). As an example, we show in Fig. 4 flux profiles for different configurations of antipodal spots as a function of the phase for the WD of minimum radius in the case of AXP 1E 2259+586 used in Section 3.1.

We can measure the amount of pulsed emission by defining the *pulsed fraction*

$$\mathrm{PF} = \frac{F_{\max} - F_{\min}}{F_{\max} + F_{\min}}, \tag{20}$$

which we show in Fig. 5, as a function of the angles ξ and χ, for AXP 1E 2259+586. In the left-hand panel of this figure, we consider only the flux given by the blackbody produced by the two antipodal hotspots on the WD. We can see that indeed pulsed fractions as small as the above values can be obtained from magnetized WDs, for appropriate values of the geometric angles ξ and χ. However, the soft X-ray spectrum shows a non-thermal power-law component, additional to the blackbody one. As we have shown, the blackbody itself can contribute to the PF if produced by surface hotspots and thus the observed total PF of a source in those cases includes both contributions, mixed. It is thus of interest to explore this problem from the theoretical point of view. To do this, we first recall that total intrinsic flux of this source in the 2–10 keV band is $F_{\rm tot} \approx 1.4 \times 10^{-11}$ erg cm^{-2} s^{-1} and the power-law flux is $F_{\rm PL} \approx 1.8 F_{\rm bb} \approx 8.5 \times 10^{-12}$ erg cm^{-2} s^{-1} (Zhu et al. 2008). The right-hand panel of Fig. 5 shows the PF map for this source taking into account both the blackbody and the power-law components. By comparing this PF map with the one in the left-hand panel which considers only the pulsed blackbody we can see that they are very similar each other. This means that in these cases where both pulsed components are in phase and have comparable fluxes, it is difficult (although still possible if good data are available) to disentangle the single contributions.

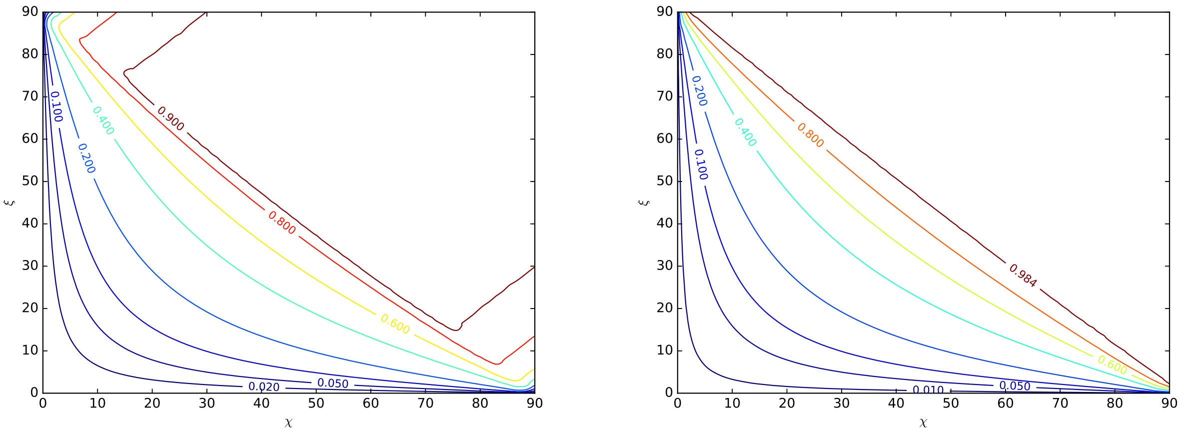

Figure 5. Theoretical PF as a function of the angles ξ and χ, computed in this work for the source 1E 2259+586 modelled as a WD of radius $R_{\rm min} \approx 1.04 \times 10^8$ cm. The left-hand panel shows the results of the PF produced by the blackbody given by the two antipodal hot spots. The right-hand panel shows the results for the total flux given by the blackbody plus the non-thermal power-law component, both pulsed. The observed total PF of this source in the 2–10 keV is about 20 per cent (Zhu et al. 2008).

5 CONCLUSIONS

We exploited the analogy with pulsars to investigate whether or not massive, highly magnetized, fast rotating WDs can behave as neutron star pulsars and emit observable high-energy radiation. We conclude the following:

(i) We showed that WDs can produce e^-e^+ pairs in their magnetosphere from the decay of curvature radiation photons, i.e. we infer the structure parameters for which they are located above the WD pulsar death-line. We evaluated the rate of such a process. Then, we calculated the thermal emission produced by the polar cap heating by the pair-created particles that flow back to the WD surface due to the action of the induction electric field.

(ii) In order to give a precise example of the process, we applied the theoretical results to the case of the WD model of SGRs and AXPs. We have shown that the inferred values of the WD parameters obtained from fitting with this magnetospheric emission, the blackbody spectrum observed in the soft X-rays of SGRs and AXPs, are in agreement with our previous estimates using the IR, optical, and UV data and fall within the constraints imposed by the gravitational stability of the WD.

(iii) We have related the size of the spot with the size of the surface under the polar cap filled by the inward particle bombardment. We have shown that the spot area is much smaller than the polar cap area pointing to the existence of strong non-dipolar magnetic fields close to the WD surface.

(iv) We have used the heat transport and energy balance equations to show that for the actual conditions of density and temperature under the polar cap, the hotspot re-radiates efficiently the heat proportioned by the inward particle bombardment.

(v) The spot, which is aligned with the magnetic dipole moment of the WD, produces a pulsed emission in phase with the rotation period of the object. We showed that the theoretically inferred pulsed fraction of the WD spans from very low values all the way to unity depending on the viewing angles. Therefore, it can also account for the observed pulsed fraction in SGRs and AXPs for appropriate choices of the viewing angles. In addition, the low-energy tail of the blackbody spectrum of the hotspot could produce a non-null pulsed fraction of the flux in the optical bands as well. However, this depends on the flux produced by the surface temperature of the WD which certainly dominates the light curve at low energies. From the quantitative point of view, the size of the surface area of the spots is crucial for the explanation of the observed pulsed fraction in soft X-rays.

(vi) We have also shown that the addition of a pulsed power-law component as the one observed in SGRs/AXPs does not modify appreciably the above result. The reason for this is that the non-thermal power-law component and the blackbody due to the surface hotspot have comparable fluxes and are in phase with each other. In those cases, it is difficult to disentangle the siingle contributions to the pulsed fraction.

We have shown that, as advanced in Rueda et al. (2013), indeed the blackbody observed in the optical wavelengths of SGRs and AXPs can be due to the surface temperature of the WD, while the one observed in the X-rays can be of magnetospheric origin. For the power-law component, also observed in the soft X-rays, a deeper analysis of processes, such as curvature radiation, inverse Compton scattering, as well as other emission mechanisms, is currently under study.

There is also room for application and extension of the results presented in this work to other astrophysical phenomena. WD mergers can lead to a system formed by a central massive, highly magnetized, fast rotating WD, surrounded by a Keplerian disc (see Rueda et al. 2013, and references therein). At the early stages, the WD and the disc are hot and there is ongoing accretion of the disc material on to the WD. In such a case, the WD surface shows hot regions that deviate from the spotty case, e.g. hot surface rings. That case is also of interest and will be presented elsewhere.

ACKNOWLEDGEMENTS

It is a great pleasure to thank M. Malheiro for thoughtful discussions and for the comments and suggestions on the presentation of our results. Likewise, we would like to thank N. Rea. We are grateful to L. Becerra for providing us tables of the heat capacity and thermal conductivity in the range of densities and temperatures of interest for this work. DLC acknowledges the financial support by the International Relativistic Astrophysics (IRAP) Ph. D. Program. JGC, RCRL, SMC and JAR acknowledge the support by the International Cooperation Program CAPES-ICRANet financed by CAPES – Brazilian Federal Agency for Support and

Evaluation of Graduate Education within the Ministry of Education of Brazil. JGC acknowledges the support of FAPESP through the project 2013/15088–0 and 2013/26258–4.

REFERENCES

Beloborodov A. M., 2002, ApJ, 566, L85
Boshkayev K., Izzo L., Rueda Hernandez J. A., Ruffini R., 2013a, A&A, 555, A151
Boshkayev K., Rueda J. A., Ruffini R., Siutsou I., 2013b, ApJ, 762, 117
Chabrier G., Potekhin A. Y., 1998, Phys. Rev. E, 58, 4941
Chen K., Ruderman M., 1993, ApJ, 402, 264
Cheng A. F., Ruderman M. A., 1977, ApJ, 214, 598
Cheng A. F., Ruderman M. A., 1980, ApJ, 235, 576
Cheng K. S., Zhang L., 1999, ApJ, 515, 337
Coelho J. G., Malheiro M., 2014, PASJ, 66, 14
D'Aì A. et al., 2016, MNRAS, 463, 2394
Davies S. R., Coe M. J., Wood K. S., 1990, MNRAS, 245, 268
Davis L., 1947, Phys. Rev., 72, 632
Duncan R. C., Thompson C., 1992, ApJ, 392, L9
Fahlman G. G., Gregory P. C., 1981, Nature, 293, 202
Ferrario L., de Martino D., Gänsicke B. T., 2015, Space Sci. Rev., 191, 111
Ferraro V. C. A., Bhatia V. B., 1967, ApJ, 147, 220
Ferraro V. C. A., Unthank H. W., 1949, MNRAS, 109, 462
Forman W., Jones C., Cominsky L., Julien P., Murray S., Peters G., Tananbaum H., Giacconi R., 1978, ApJS, 38, 357
García-Berro E. et al., 2012, ApJ, 749, 25
Gil J., Melikidze G. I., 2002, ApJ, 577, 909
Gil J. A., Sendyk M., 2000, ApJ, 541, 351
Gil J., Melikidze G. I., Geppert U., 2003, A&A, 407, 315
Göhler E., Wilms J., Staubert R., 2005, A&A, 433, 1079
Gold T., 1962, J. Phys. Soc. Japan Suppl., 17, A187
Goldreich P., Julian W. H., 1969, ApJ, 157, 869
Hulleman F., van Kerkwijk M. H., Kulkarni S. R., 2000, Nature, 408, 689
Itoh N., Hayashi H., Kohyama Y., 1993, ApJ, 418, 405
Kashiyama K., Ioka K., Kawanaka N., 2011, Phys. Rev. D, 83, 023002
Kaspi V. M., Gavriil F. P., Woods P. M., Jensen J. B., Roberts M. S. E., Chakrabarty D., 2003, ApJ, 588, L93
Kepler S. O. et al., 2013, MNRAS, 429, 2934
Kepler S. O. et al., 2015, MNRAS, 446, 4078
Külebi B., Jordan S., Euchner F., Gänsicke B. T., Hirsch H., 2009, A&A, 506, 1341
Malheiro M., Rueda J. A., Ruffini R., 2012, PASJ, 64, 56
Marsh T. R. et al., 2016, Nature, 537, 374
Paczynski B., 1990, ApJ, 365, L9
Potekhin A. Y., Chabrier G., 2000, Phys. Rev. E, 62, 8554
Rea N., Borghese A., Esposito P., Coti Zelati F., Bachetti M., Israel G. L., De Luca A., 2016, ApJ, 828, L13
Ruderman M. A., Sutherland P. G., 1975, ApJ, 196, 51
Rueda J. A., Boshkayev K., Izzo L., Ruffini R., Lorén-Aguilar P., Külebi B., Aznar-Siguán G., García-Berro E., 2013, ApJ, 772, L24
Thompson C., Duncan R. C., 1995, MNRAS, 275, 255
Tsai Y.-S., 1974, Rev. Mod. Phys., 46, 815
Turolla R., Nobili L., 2013, ApJ, 768, 147
Usov V. V., 1988, Sov. Astron. Lett., 14, 258
Usov V. V., 1993, ApJ, 410, 761
Usov V. V., 1994, ApJ, 427, 984
Woods P. M. et al., 2004, ApJ, 605, 378
Zhu W., Kaspi V. M., Dib R., Woods P. M., Gavriil F. P., Archibald A. M., 2008, ApJ, 686, 520

APPENDIX: HEATING AND COOLING OF PARTICLE INFLUX BOMBARDMENT

We estimate in this appendix the efficiency of the particle bombardment in heating (and re-rediating) the surface area they hit. We follow the discussion in Gil & Melikidze (2002), Gil, Melikidze & Geppert (2003) for the heat flow conditions in the polar cap surface of neutron stars, and extended it to the present case of magnetized WDs.

The particles arriving to the surface penetrate up to a depth that can be estimated using the concept of *radiation length* (Cheng & Ruderman 1980). For a carbon composition, the radiation length is $\Sigma \approx 43$ g cm^{-2} (Tsai 1974), so an electron would penetrate the WD surface up to a depth

$$\Delta z \approx \frac{\Sigma}{\rho} = 4.3 \times 10^{-3}\,\mathrm{cm} \left(\frac{10^4\,\mathrm{g\,cm^{-3}}}{\rho}\right). \tag{A1}$$

With the knowledge of the thickness of the layer under the surface where the energy deposition occurs, we can proceed to estimate the properties of the diffusion and re-radiation of the kinetic energy of the particle influx using the heat transport and energy balance equations on the star's surface corresponding to the polar cap. The typically small distances (see equation A1) allow us to introduce a plane-parallel approximation in the direction parallel to the magnetic field lines, say in the direction z orthogonal to the surface.

The energy balance can be simply written as

$$F_{\rm rad} = F_{\rm heat} + F_{\rm cond}, \tag{A2}$$

where $F_{\rm heat} = e\Delta V \eta \rho_{\rm GJ} c$, $F_{\rm cond} = -\kappa\, \partial T/\partial z$ and $F_{\rm rad} = \sigma T^4$, with κ the thermal conductivity (along the z-direction).

Let us first estimate the characteristic cooling time. To do this, we switch off energy losses and heating terms in the energy balance equation (A2), i.e. the radiation flux is only given by conduction:

$$\sigma T^4 = -\kappa \frac{\partial T}{\partial z}, \tag{A3}$$

which leads to the heat transport equation

$$c_v \frac{\partial T}{\partial t} = \frac{\partial}{\partial z}\left(\kappa \frac{\partial T}{\partial z}\right), \tag{A4}$$

where c_v is the heat capacity per unit volume. We can therefore obtain the characteristic (e-folding) cooling and heating time assuming the quantities are uniform within the penetration depth Δz, i.e.

$$\Delta t_{\rm cool} = \frac{\Delta z^2 c_v}{\kappa}, \qquad \Delta t_{\rm heat} = \frac{c_v \Delta z}{\sigma T^3}. \tag{A5}$$

We can now introduce the radiation to heating efficiency parameter

$$\epsilon \equiv \frac{F_{\rm rad}}{F_{\rm heat}} = \frac{1}{1 + \Delta t_{\rm heat}/\Delta t_{\rm cool}} = \frac{1}{1 + \kappa/(\sigma T^3 \Delta z)}, \tag{A6}$$

which shows that in equilibrium, $\Delta t_{\rm heat} = \Delta t_{\rm cool}$, we have $\epsilon = 1/2$.

In estimating the spot temperature (8), we have assumed in equation (7) full re-radiation of the influx, namely we assumed $\epsilon = 1$. We proceed now to estimate the realistic values of ϵ from equation (A6) to check our assumption. We compute the thermal conductivity from Itoh, Hayashi & Kohyama (1993) and the heat capacity from Chabrier & Potekhin (1998); Potekhin & Chabrier (2000). For example, at a density $\rho = 10^3$ g cm^{-3} and $T = 10^6$ K, we have $c_v = 2.7 \times 10^{10}$ erg cm^{-3} K^{-1} and $\kappa \approx 4 \times 10^{11}$ erg cm^{-1} s^{-1} K^{-1}, and equation (A6) gives $\epsilon \approx 0.86$. At $T = 10^7$ K, we have $c_v = 3.8 \times 10^{11}$ erg cm^{-3} K^{-1} and $\kappa \approx 3.4 \times 10^{13}$ erg cm^{-1} s^{-1} K^{-1} and $\epsilon \approx 1$.

This paper has been typeset from a TEX/LATEX file prepared by the author.

International Journal of Modern Physics D
Vol. 26, No. 9 (2017) 1730016 (19 pages)

DOI: 10.1142/S0218271817300166

The binary systems associated with short and long gamma-ray bursts and their detectability*

Jorge A. Rueda[†,‡,§,***], Y. Aimuratov[†,‡,¶], U. Barres de Almeida[‖], L. Becerra[†,‡], C. L. Bianco[†,‡], C. Cherubini[**,††], S. Filippi[**,††], M. Karlica[†,‡,¶], M. Kovacevic[†,‡,¶], J. D. Melon Fuksman[†,‡], R. Moradi[†,‡], M. Muccino[†,‡], A. V. Penacchioni[‡‡,§§], G. B. Pisani[†,‡], D. Primorac[†,‡], R. Ruffini[†,‡,§], N. Sahakyan[¶¶], S. Shakeri[†,‖‖] and Y. Wang[†,‡]

[†]*ICRANet, Piazza Della Repubblica 10, I-65122 Pescara, Italy*

[‡]*Dip. di Fisica and ICRA, Sapienza Università di Roma, P.le Aldo Moro 5, I-00185 Rome, Italy*

[§]*ICRANet-Rio, Centro Brasileiro de Pesquisas Físicas, Rua Dr. Xavier Sigaud 150, 22290–180 Rio de Janeiro, Brazil*

[¶]*Université de Nice Sophia Antipolis, CEDEX 2, Grand Château Parc Valrose, Nice, France*

[‖]*Centro Brasileiro de Pesquisas Físicas, Rua Dr. Xavier Sigaud 150, 22290–180 Rio de Janeiro, Brazil*

[**]*Unit of Nonlinear Physics and Mathematical Modeling, Università Campus Bio-Medico di Roma, Via A. del Portillo 21, I-00128 Rome, Italy*

[††]*ICRA, Università Campus Bio-Medico di Roma, Via A. del Portillo 21, I-00128 Rome, Italy*

[‡‡]*ASI Science Data Center, Via del Politecnico s.n.c., I-00133 Rome, Italy*

[§§]*Dept. of Physical Sciences, Earth and Environment, University of Siena, Via Roma 56, I-53100 Siena, Italy*

[¶¶]*ICRANet-Yerevan, Marshall Baghramian Avenue 24a, Yerevan 0019, Republic of Armenia*

[‖‖]*Department of Physics, Isfahan University of Technology, 84156–83111, Iran*

[***]*jorge.rueda@icra.it*

Received 2 March 2017
Accepted 3 March 2017
Published 13 April 2017

Short and long-duration gamma-ray bursts (GRBs) have been recently sub-classified into seven families according to the binary nature of their progenitors. For short GRBs, mergers of neutron star binaries (NS–NS) or neutron star-black hole binaries (NS-BH) are proposed. For long GRBs, the induced gravitational collapse (IGC) paradigm proposes

*Based on a talks presented at the Fourteenth Marcel Grossmann Meeting on General Relativity, Rome, July 2015.

a tight binary system composed of a carbon–oxygen core (CO_{core}) and a NS companion. The explosion of the CO_{core} as supernova (SN) triggers a hypercritical accretion process onto the NS companion which might reach the critical mass for the gravitational collapse to a BH. Thus, this process can lead either to a NS-BH or to NS–NS depending on whether or not the accretion is sufficient to induce the collapse of the NS into a BH. We shall discuss for the above compact object binaries: (1) the role of the NS structure and the equation-of-state on their final fate; (2) their occurrence rates as inferred from the X and gamma-ray observations; (3) the expected number of detections of their gravitational wave (GW) emission by the Advanced LIGO interferometer.

Keywords: Gamma-ray bursts; neutron stars; black holes.

PACS Number(s): 04.30.Tv, 04.40.Dg, 97.60.Bw, 97.60.Jd, 97.60.Lf, 98.62.Mw

1. Introduction

There has been a traditional phenomenological classification of GRBs based on the observed prompt duration, T_{90}: long GRBs for $T_{90} > 2\,\mathrm{s}$ and short GRBs for $T_{90} < 2\,\mathrm{s}$.[1–5] In this paper, we shall review the recent progress reached in the understanding of the nature of long and short GRBs that has led to a physical GRB classification, proposed in Refs. 6–8. Such a classification, as we will see below, is based on the possible outcomes in the final stages of the evolution of the progenitor systems.

1.1. *Long GRBs*

The induced gravitational collapse (IGC) scenario introduces, as the progenitor of the long GRBs associated with SNe Ib/c, binaries composed of a carbon–oxygen core (CO_{core}) on the verge of supernova with a NS companion.[9–15] The explosion of the CO_{core} as SN, forming at its center a newly-born NS called hereafter νNS, triggers an accretion process onto the NS binary companion. Depending on the parameters of the *in-state*, i.e. of CO_{core}-NS binary, two sub-classes of long GRBs with corresponding *out-states* are envisaged[6]:

- *X-ray flashes* (*XRFs*). Long bursts with $E_{\rm iso} \lesssim 10^{52}$ erg are produced by CO_{core}-NS binaries with relatively large binary separations ($a \gtrsim 10^{11}$ cm). The accretion rate of the SN ejecta onto the NS in these systems is not high enough to bring the NS mass to the critical value $M_{\rm crit}$, hence no BH is formed. The out-state of this GRB sub-class can be either a νNS–NS binary if the system keeps bound after the SN explosion, or two runaway NSs if the binary system is disrupted.
- *Binary driven hypernovae* (*BdHNe*). Long bursts with $E_{\rm iso} \gtrsim 10^{52}$ erg are instead produced by more compact CO_{core}-NS binaries ($a \lesssim 10^{11}$ cm, see e.g. Refs. 13 and 15). In this case, the SN triggers a larger accretion rate onto the NS companion, e.g. $\gtrsim 10^{-2}$–$10^{-1}\,M_\odot\,\mathrm{s}^{-1}$, bringing the NS to its critical mass $M_{\rm crit}$,[11–13] namely to the point of gravitational collapse with consequent formation of a BH. Remarkably, in Ref. 14, it was recently shown that the large majority of BdHNe leads naturally to NS-BH binaries owing to the high compactness of the binary that avoids the disruption of it even in cases of very high mass loss exceeding 50% of the total mass of the initial CO_{core}-NS binary.

In addition, it exists the possibility of BH-SNe.[6] Long burst with $E_{\rm iso} \gtrsim 10^{54}$ erg occurring in close $CO_{\rm core}$-BH binaries in which the hypercritical accretion produces, as *out-states*, a more massive BH and a νNS. These systems have been considered in Ref. 6 as a subset of the BdHNe but no specific example have been yet observationally identified.

1.2. *Short GRBs*

There is the consensus within the GRB community that the progenitors of short GRBs are mergers of NS–NS and/or NS-BH binaries (see, e.g. Refs. 16–20 for a recent review). Similarly to the case of long GRBs, in Ref. 6 short GRBs have been split into different sub-classes:

- *Short gamma-ray flashes* (*S-GRFs*). Short bursts with energies $E_{\rm iso} \lesssim 10^{52}$ erg, produced when the post-merger core do not surpass the NS critical mass $M_{\rm crit}$, hence there is no BH formation. Thus, these systems left as byproduct a massive NS and possibly, due to the energy and angular momentum conservation, orbiting material in a disk-like structure or a low-mass binary companion.
- *Authentic short gamma-ray bursts* (*S-GRBs*). Short bursts with $E_{\rm iso} \gtrsim 10^{52}$ erg, produced when the post-merger core reaches or overcome $M_{\rm crit}$, hence forming a Kerr or Kerr–Newman BH,[8] and also in this case possibly orbiting material.
- *Ultra-short GRBs* (*U-GRBs*). A new sub-class of short bursts originating from νNS-BH merging binaries. They can originate from BdHNe (see Ref. 14) or from BH-SNe.

In addition, it exists the possibility of *gamma-ray flashes* (*GRFs*). These are bursts with hybrid properties between short and long, they have $10^{51} \lesssim E_{\rm iso} \lesssim 10^{52}$ erg. This sub-class of sources originates in NS-WD mergers.[6]

Table 1 summarized some observational aspects of the GRB sub-classes including the occurrence rate calculated in Ref. 6.

Table 1. Some observational aspects of the GRB sub-classes. In the first three columns, we indicate the GRB sub-class and their corresponding *in-states* and the *out-states*. In column 4, we list the $E_{\rm iso}$ (rest-frame 1–10^4 keV), columns 5–6 list, for each GRB sub-class, the maximum observed redshift and the local occurrence rate computed in Ref. 6.

GRB sub-class	In-state	Out-state	$E_{\rm iso}$ (erg)	$z_{\rm max}$	$\rho_{\rm GRB}$ ($\rm Gpc^{-3}yr^{-1}$)
XRFs	$CO_{\rm core}$-NS	νNS-NS	10^{48}–10^{52}	1.096	100^{+45}_{-34}
BdHNe	$CO_{\rm core}$-NS	νNS-BH	10^{52}–10^{54}	9.3	$0.77^{+0.09}_{-0.08}$
BH-SN	$CO_{\rm core}$-BH	νNS-BH	$>10^{54}$	9.3	$\lesssim 0.77^{+0.09}_{-0.08}$
S-GRFs	NS-NS	MNS	10^{49}–10^{52}	2.609	$3.6^{+1.4}_{-1.0}$
S-GRBs	NS-NS	BH	10^{52}–10^{53}	5.52	$(1.9^{+1.8}_{-1.1}) \times 10^{-3}$
U-GRBs	νNS-BH	BH	$>10^{52}$	—	$\gtrsim 0.77^{+0.09}_{-0.08}$
GRFs	NS-WD	MNS	10^{51}–10^{52}	2.31	$1.02^{+0.71}_{-0.46}$

We focus here on the physical properties of the above progenitors, as well as on the main properties of NSs that play a relevant role in the dynamics of these systems and that lead to the above different GRB sub-classes. We shall discuss as well recent estimates of the rates of occurrence on all the above subclasses based on X and gamma-ray observations, and also elaborate on the possibility of detecting the gravitational wave (GW) emission originated in these systems.

2. IGC, Hypercritical Accretion, and Long GRBs

We turn now to the details of the accretion process within the IGC scenario. Realistic simulations of the IGC process were performed in Ref. 12, including: (1) detailed SN explosions of the $\mathrm{CO}_{\mathrm{core}}$; (2) the hydrodynamic details of the hypercritical accretion process; (3) the evolution of the SN ejecta material entering the Bondi–Hoyle region all the way up to its incorporation into the NS. Here, the concept of hypercritical accretion refers to the fact the accretion rates are highly super-Eddington. The accretion process in the IGC scenario is allowed to exceed the Eddington limit mainly for two reasons: (i) the photons are trapped within the infalling material impeding them to transfer momentum; (ii) the accreting material creates a very hot NS atmosphere ($T \sim 10^{10}\,\mathrm{K}$) that triggers a very efficient neutrino emission which become the main energy sink of these systems unlike photons.

The hypercritical accretion process in the above simulations was computed within a spherically symmetric approximation. A further step was given in Ref. 13 by estimating the angular momentum that the SN ejecta carries and transfer to the NS via accretion, and how it affects the evolution and fate of the system. The calculations are as follows: first the accretion rate onto the NS is computed adopting an homologous expansion of the SN ejecta and introducing the pre-SN density profile of the $\mathrm{CO}_{\mathrm{core}}$ envelope from numerical simulations. Then, it is estimated the angular momentum that the SN material might transfer to the NS: it comes out that the ejecta have enough angular momentum to circularize for a short time and form a disc around the NS. Finally, the evolution of the NS central density and rotation angular velocity (spin-up) is followed computing the equilibrium configurations from the numerical solution of the axisymmetric Einstein equations in full rotation, until the critical point of collapse of the NS to a BH taking into due account the equilibrium limits given by mass-shedding and the secular axisymmetric instability.

Now we enter into the details of each of the above steps. The accretion rate of the SN ejecta onto the NS can be estimated via the Bondi–Hoyle–Lyttleton accretion formula:

$$\dot{M}_B(t) = \pi \rho_{\mathrm{ej}} R_{\mathrm{cap}}^2 \sqrt{v_{\mathrm{rel}}^2 + c_{\mathrm{s,ej}}^2}, \quad R_{\mathrm{cap}}(t) = \frac{2GM_{\mathrm{NS}}(t)}{v_{\mathrm{rel}}^2 + c_{\mathrm{s,ej}}^2}, \tag{1}$$

where G is the gravitational constant, ρ_{ej} and $c_{\mathrm{s,ej}}$ are the density and sound speed of the SN ejecta, R_{cap} is the NS gravitational capture radius (Bondi–Hoyle radius), M_{NS}, the NS mass, and v_{rel} the ejecta velocity relative to the NS: $\mathbf{v}_{\mathrm{rel}} = \mathbf{v}_{\mathrm{orb}} - \mathbf{v}_{\mathrm{ej}}$,

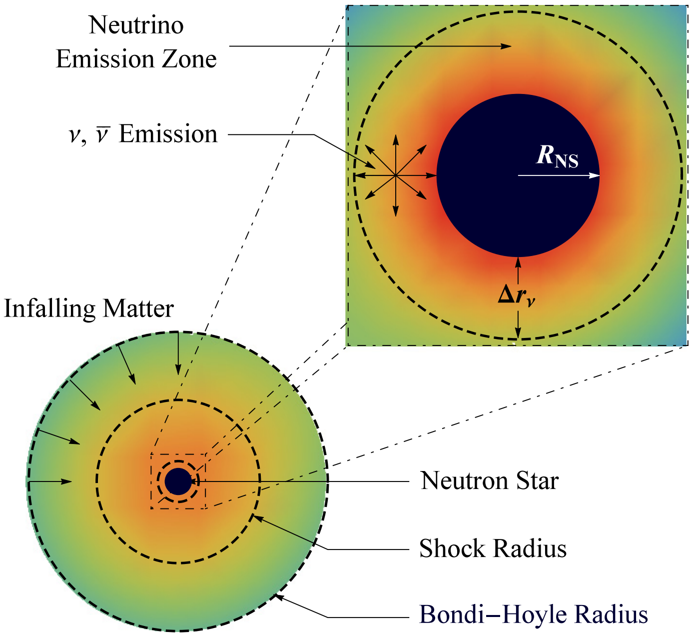

Fig. 1. Scheme of the IGC scenario: the CO_{core} undergoes SN explosion, the NS accretes part of the SN ejecta and then reaches the critical mass for gravitational collapse to a BH, with consequent emission of a GRB. The SN ejecta reach the NS Bondi–Hoyle radius and fall toward the NS surface. The material shocks and decelerates as it piles over the NS surface. At the neutrino emission zone, neutrinos take away most of the infalling matter gravitational energy gain. The neutrinos are emitted above the NS surface in a region of thickness Δr_ν about half the NS radius that allow the material to reduce its entropy to be finally incorporated to the NS. The image is not to scale. For further details and numerical simulations of the above process, see Refs. 12–15.

with $|\mathbf{v}_{\rm orb}| = \sqrt{G(M_{\rm core}+M_{\rm NS})/a}$, the module of the NS orbital velocity around the CO_{core}, and $\mathbf{v}_{\rm ej}$ the velocity of the supernova ejecta (see Fig. 1).

Extrapolating the results for the accretion process from stellar wind accretion in binary systems, the angular momentum per unit time that crosses the NS capture region can be approximated by: $\dot{L}_{\rm cap} = (\pi/2)(\epsilon_\rho/2 - 3\epsilon_\nu)\rho_{\rm ej}(a,t)v_{\rm rel}^2(a,t)R_{\rm cap}^4(a,t)$, where ϵ_ρ and ϵ_ν are parameters measuring the inhomogeneity of the flow (see Ref. 13 for details).

In order to simulate the hypercritical accretion, it is adopted an homologous expansion of the SN ejecta, i.e. the ejecta velocity evolves as $v_{\rm ej}(r,t) = nr/t$, where r is the position of every ejecta layer from the SN center and n is called expansion parameter. The ejecta density is given by $\rho_{\rm ej}(r,t) = \rho_{\rm ej}^0(r/R_{\rm star}(t), t_0)\frac{M_{\rm env}(t)}{M_{\rm env}(0)}(\frac{R_{\rm star}(0)}{R_{\rm star}(t)})^3$, where $M_{\rm env}(t)$ the mass of the CO_{core} envelope, namely the mass of the ejected material in the SN explosion and available to be accreted by the NS, $R_{\rm star}(t)$ is the position of the outermost layer of the ejected material, and $\rho_{\rm ej}^0$ is the pre-SN density profile. The latter can be approximated with a power law: $\rho_{\rm ej}(r,t_0) = \rho_{\rm core}(R_{\rm core}/r)^m$, where $\rho_{\rm core}$, $R_{\rm core}$ and m are the profile parameters which are fixed by fitting the pre-SN profiles obtained from numerical simulations.

For the typical parameters of pre-SN CO_{core} and assuming a velocity of the outermost SN layer $v_{\rm sn}(R_{\rm star}, t_0) \sim 10^9\,{\rm cm\,s^{-1}}$ and a free expansion $n = 1$ (for details of typical initial conditions of the binary system see Refs. 12 and 13), Eq. (1) gives accretion rates around the order of $10^{-4} - 10^{-2} M_\odot\,\mathrm{s}^{-1}$, and an angular momentum per unit time crossing the capture region $\dot{L}_{\rm cap} \sim 10^{46}$–$10^{49}\,\mathrm{g\,cm^2\,s^{-2}}$.

We consider the NS companion of the $\mathrm{CO_{core}}$ initially as nonrotating, thus at the beginning, the NS exterior spacetime is described by the Schwarzschild metric. The SN ejecta approach the NS with specific angular momentum, $l_{\rm acc} = \dot{L}_{\rm cap}/\dot{M}_B$, thus they will circularize at a radius $r_{\rm st}$ if they have enough angular momentum. What does the word "enough" means here? The last stable circular orbit (LSO) around a nonrotating NS is located at a distance $r_{\rm lso} = 6GM_{\rm NS}/c^2$ and has an angular momentum per unit mass $l_{\rm lso} = 2\sqrt{3}GM_{\rm NS}/c$. The radius $r_{\rm lso}$ is larger than the NS radius for masses larger than $1.67\,M_\odot$, $1.71\,M_\odot$, and $1.78\,M_\odot$ for the GM1, TM1, and NL3 nuclear equation-of-state (EOS).[13] If $l_{\rm acc} \geq l_{\rm lso}$, the material circularizes around the NS at locations $r_{\rm st} \geq r_{\rm lso}$. For the values of the IGC systems under discussion here, $r_{\rm st}/r_{\rm lso} \sim 10 - 10^3$, thus the SN ejecta have enough angular momentum to form a sort of disc around the NS. Even in this case, the viscous forces and other angular momentum losses that act on the disk will allow the matter in the disk to reach the inner boundary at $r_{\rm in} \sim r_{\rm lso}$, to then be accreted by the NS.

Within this picture, the NS accretes the material from $r_{\rm in}$ and the NS mass and angular momentum evolve as:

$$\dot{M}_{\rm NS} = \left(\frac{\partial M_{\rm NS}}{\partial M_b}\right)_{J_{\rm NS}} \dot{M}_b + \left(\frac{\partial M_{\rm NS}}{\partial J_{\rm NS}}\right)_{M_b} \dot{J}_{\rm NS}, \quad \dot{J}_{\rm NS} = \xi l(r_{\rm in})\dot{M}_{\rm B}, \tag{2}$$

where M_b is the NS baryonic mass, $l(r_{\rm in})$ is the specific angular momentum of the accreted material at $r_{\rm in}$, which corresponds to the angular momentum of the LSO, and $\xi \leq 1$ is a parameter that measures the efficiency of angular momentum transfer. We assume in our simulations $\dot{M}_b = \dot{M}_B$.

In order to integrate Eqs. (1) and (2), we have to supply the two above partial derivatives which are obtained from the relation of the NS gravitational mass with M_b and $J_{\rm NS}$, namely from the NS binding energy. The general relativistic calculations of rotating NSs in Ref. 21 show that, independent on the nuclear EOS, this relation is well approximated by the formula

$$\frac{M_b}{M_\odot} = \frac{M_{\rm NS}}{M_\odot} + \frac{13}{200}\left(\frac{M_{\rm NS}}{M_\odot}\right)^2 \left(1 - \frac{1}{137} j_{\rm NS}^{1.7}\right), \tag{3}$$

where $j_{\rm NS} \equiv cJ_{\rm NS}/(GM_\odot^2)$. In addition, since the NS will spin up with accretion, we need information of the dependence of the specific angular momentum of the LSO as a function of both the NS mass and angular momentum. For corotating orbits, the following relation is valid for all the aforementioned EOS[13]:

$$l_{\rm lso} = \frac{GM_{\rm NS}}{c}\left[2\sqrt{3} - 0.37\left(\frac{j_{\rm NS}}{\frac{M_{\rm NS}}{M_\odot}}\right)^{0.85}\right]. \tag{4}$$

The NS accretes mass until it reaches a region of instability. There are two main instability limits for rotating NSs: mass-shedding or Keplerian limit and the secular

Table 2. Critical NS mass in the nonrotating case and constants k and p needed to compute the NS critical mass in the nonrotating case given by Eq. (5). The values are given for the NL3, GM1 and TM1 EOS.

EOS	$M_{\rm crit}^{J=0}$ ($M_\odot$)	p	k
NL3	2.81	1.68	0.006
GM1	2.39	1.69	0.011
TM1	2.20	1.61	0.017

axisymmetric instability. The critical NS mass along the secular instability line is approximately given by[21]:

$$M_{\rm NS}^{\rm crit} = M_{\rm NS}^{J=0}(1 + k j_{\rm NS}^{p}), \tag{5}$$

where the parameters k and p depends of the nuclear EOS (see Table 2). These formulas fit the numerical results with a maximum error of 0.45%.

Along the mass-shedding sequence, the NS has the maximum possible angular momentum[21]: $J_{\rm NS,max} \approx 0.7 G M_{\rm NS}^2/c$. Figure 2 shows the evolution of the NS dimensionless angular momentum, $cJ_{\rm NS}/(GM_{\rm NS}^2)$, as a function of the NS mass for $\xi = 0.5$ and for selected values of the initial NS mass. The NS fate depends of the NS initial mass and the efficiency parameter ξ. The less massive initial configurations reach the mass-shedding limit with a maximum dimensionless angular momentum value while the initially more massive configurations reach the secular axisymmetric instability. It is interesting to note that the total angular momentum of the SN ejecta entering the Bondi–Hoyle region, $L_{\rm cap}$, is much larger than the

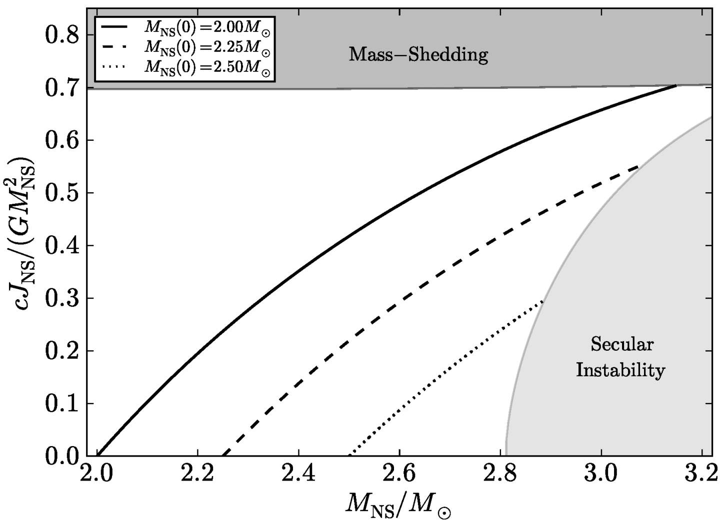

Fig. 2. Evolution of NSs of different initial masses $M_{\rm NS} = 2.0, 2.25$ and $2.5\,M_\odot$ during the hypercritical accretion in a BdHN.[13] It is shown the dimensionless angular momentum as a function of the NS mass. The binary parameters are: $\rm CO_{core}$ of a $M_{\rm ZAMS} = 30\,M_\odot$ progenitor star ($m = 2.801$, $M_{\rm env} = 7.94\,M_\odot$, $\rho_{\rm core} = 3.08 \times 10^8\,{\rm g\,cm^{-3}}$ and $R_{0_{\rm star}} = 7.65 \times 10^9$ cm), a free expansion ($n = 1$) and a SN outermost ejecta velocity $v_{0_{\rm star}} = 2 \times 10^9\,{\rm cm\,s^{-1}}$. The orbital period is of approximately 5 min.

maximum angular momentum that a uniformly rotating NS can support, $J_{\rm NS,max}$. The numerical simulations in Ref. 13 indicate $L_{\rm cap} \sim 10 J_{\rm NS,max}$. Thus, part of this angular momentum must be lost or redistributed before the material can reach the NS surface. This result leads to a clear prediction: the BHs produced through the IGC mechanism, namely those formed in BdHNe, have initial dimensionless spin ~0.7 and the excess of angular momentum could lead to a jetted emission with possible high-energy signatures and/or to the presence of a disk-like structure first around the NS as shown above and possibly also around the BH originated from the gravitational collapse of the NS.

2.1. *Most recent simulations of the IGC process*

Additional details and improvements of the hypercritical accretion process leading to XRFs and BdHNe have been recently presented in Ref. 15. In particular:

(1) It was there improved the accretion rate estimate including the density profile finite size/thickness and additional $\mathrm{CO_{core}}$ progenitors leading to different SN ejecta masses were also considered.
(2) It was shown in Ref. 13, the existence of a maximum orbital period, $P_{\rm max}$, over which the accretion onto NS companion is not high enough to bring it to the critical mass for gravitational collapse to a BH. Therefore, $\mathrm{CO_{core}}$-NS binaries with $P > P_{\rm max}$ lead to XRFs while the ones with $P \lesssim P_{\rm max}$ lead to BdHNe. In Ref. 15, the determination of $P_{\rm max}$ was extended to all the possible initial values of the mass of the NS companion and the angular momentum transfer efficiency parameter was also allowed to vary.
(3) It was computed the expected luminosity during the hypercritical accretion process for a wide range of binary periods covering XRFs and BdHNe.
(4) It was there shown that the presence of the NS companion originates large asymmetries (see, e.g. simulation in Fig. 3) in the SN ejecta leading to observable signatures in the X-rays.

Figure 3 shows a simulation of an IGC process presented in Ref. 15. We considered the effects of the gravitational field of the NS on the SN ejecta including the orbital motion as well as the changes in the NS gravitational mass owing to the accretion process via the Bondi formalism. The supernova matter was described as formed by point-like particles whose trajectory was computed by solving the Newtonian equation of motion. The initial conditions of the SN ejecta are computed assuming an homologous velocity distribution in free expansion. The initial power-law density profile of the CO envelope is simulated by populating the inner layers with more particles. For the $M_{\rm ZAMS} = 30\,M_\odot$ progenitor which gives a $\mathrm{CO_{core}}$ with envelope profile $\rho_{\rm ej}^0 \approx 3.1 \times 10^8 (8.3 \times 10^7/r)^{2.8}\,{\rm g\,cm^{-3}}$, we adopt for the simulation a total number of $N = 10^6$ particles. We assume that particles crossing the Bondi–Hoyle radius are captured and accreted by the NS so we removed them from the system as they reach that region. We removed these particles according to the

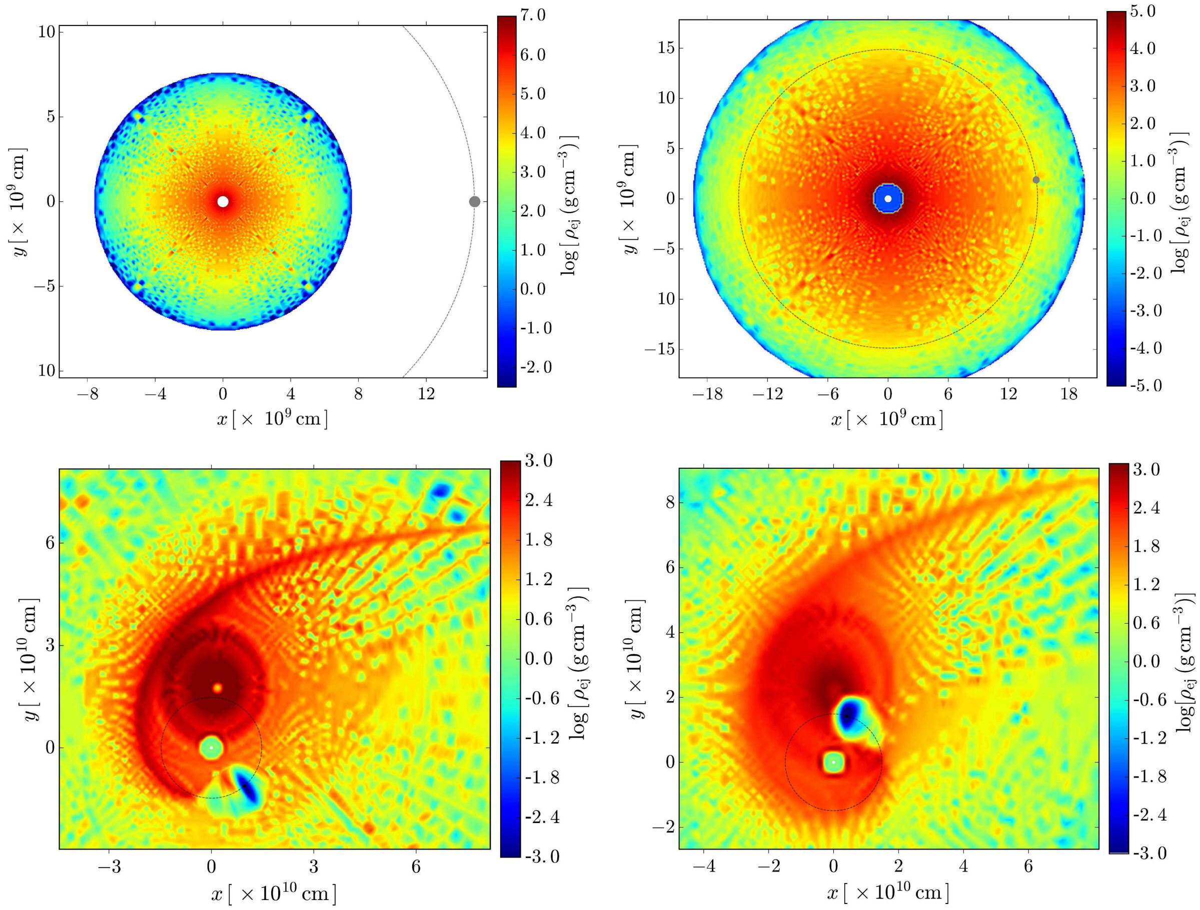

Fig. 3. Hypercritical accretion process in the IGC binary system at selected evolution times. In this example, the $\mathrm{CO_{core}}$ has a total mass of $9.44\,M_\odot$ divided in an ejecta mass of $7.94\,M_\odot$ and a νNS of $1.5\,M_\odot$ formed by the collapsed high density core. The supernova ejecta evolve homologously with outermost layer velocity $v_{0,\rm star} = 2\times10^9\,\mathrm{cm\,s^{-1}}$. The NS binary companion has an initial mass of $2.0\,M_\odot$. The binary period is $P \approx 5\,\mathrm{min}$, which corresponds to a binary separation $a \approx 1.5\times10^{10}$ cm. The system of coordinates is centered on the νNS represented by the white-filled circle at $(0,0)$. The NS binary companion, represented by the gray-filled circle, orbits counterclockwise following the thin-dashed circular trajectory. The colorbar indicates values of ejecta density in logarithmic scale. *Left upper panel*: initial time of the process. The supernova ejecta expand radially outward and the NS binary companion is at $(a,0)$. *Right upper panel*: the accretion process starts when the first supernova layers reach the Bondi–Hoyle region. This happens at $t = t_{\rm acc,0} \approx a/v_{0,\rm star} \approx 7.7\,\mathrm{s}$. *Left lower panel*: the NS binary companion reaches the critical mass by accreting matter from the SN with consequent collapse to a BH. This happens at $t = t_{\rm coll} \approx 254\,\mathrm{s} \approx 0.85\,P$. The newly-formed BH of mass $M_{\rm BH} = M_{\rm crit} \approx 3\,M_\odot$ is represented by the black-filled circle. It is here evident the asymmetry of the supernova ejecta induced by the presence of the accreting NS companion at close distance. *Right lower panel*: $t = t_{\rm coll} + 100\,\mathrm{s} = 354\,\mathrm{s} \approx 1.2\,P$, namely 100 s after the BH formation. It appears here the new binary system composed of the νNS and the newly-formed BH.

results obtained from the numerical integration explained above. Figure 3 shows the orbital plane of an IGC binary at selected times of its evolution. The NS has an initial mass of $2.0\,M_\odot$; the $\mathrm{CO_{core}}$ leads to a total ejecta mass $7.94\,M_\odot$ and a νNS of $1.5\,M_\odot$. The orbital period of the binary is $P \approx 5\,\mathrm{min}$, i.e. a binary separation $a \approx 1.5\times10^{10}\,\mathrm{cm}$. For these parameters, the NS reaches the critical mass and collapses to form a BH.

2.2. *Hydrodynamics and neutrino inside the accretion region*

We turn now to give some details on the properties of the system inside the Bondi–Hoyle accretion region. We have seen that the accretion rate onto the NS can be as high as $\sim 10^{-2}$–$10^{-1}\,M_\odot\,\mathrm{s}^{-1}$. For these accretion rates:

(1) We can neglect the effect of the NS magnetic field since the magnetic pressure remains much smaller than the random pressure of the infalling material.[11,22]
(2) The photons are trapped in the accretion flow. The trapping radius, defined at which the photons emitted diffuse outward at a slower velocity than the one of the infalling material, is[23]: $r_{\mathrm{trapping}} = \min\{\dot{M}_B\kappa/(4\pi c), R_{\mathrm{cap}}$, where κ is the opacity. For the $\mathrm{CO_{core}}$, in Ref. 12, a Rosseland mean opacity roughly $5\times 10^3\,\mathrm{cm}^2\,\mathrm{g}^{-1}$ was estimated. For the range of accretion rates, we obtain that $\dot{M}_B\kappa/(4\pi c)\sim 10^{13}$–$10^{19}$ cm, a radius much bigger than the NS capture radius which is in our simulations at most 1/3 of the binary separation. Thus, in our systems, the trapping radius extends all the way to the Bondi–Hoyle region, hence the Eddington limit does not apply and hypercritical accretion onto the NS occurs.
(3) Under these conditions, the gain of gravitational energy of the accreted material is mainly radiated via neutrino emission (see below).[11,12,22,24,25]

2.2.1. *Convective instabilities*

As the material piles onto the NS and the atmosphere radius, the accretion shock moves outward. The post-shock entropy is a decreasing function of the shock radius position which creates an atmosphere unstable to Rayleigh–Taylor convection during the initial phase of the accretion process. These instabilities can accelerate above the escape velocity driving outflows from the accreting NS with final velocities approaching the speed of light.[26,27] Assuming that radiation dominates, the entropy of the material at the base of the atmosphere is[22]: $S_{\mathrm{bubble}}\approx 16(1.4\,M_\odot/M_{\mathrm{NS}})^{-7/8}(M_\odot\,\mathrm{s}^{-1}/\dot{M}_{\mathrm{B}})^{1/4}(10^6\,\mathrm{cm}/r)^{3/8}$, in units of k_B per nucleon. This material will rise and expand, cooling adiabatically, i.e. $T^3/\rho=$ constant, for radiation dominated gas. If we assume a spherically symmetric expansion, then $\rho\propto 1/r^3$ and we obtain $k_B T_{\mathrm{bubble}} = 195\,S_{\mathrm{bubble}}^{-1}(10^6\,\mathrm{cm}/r)\,\mathrm{MeV}$. However, it is more likely that the bubbles expand in the lateral but not in the radial direction,[27] thus we have $\rho\propto 1/r^2$, i.e. $T_{\mathrm{bubble}} = T_0(S_{\mathrm{bubble}})(r_0/r)^{2/3}$, where $T_0(S_{\mathrm{bubble}})$ is given by the above equation evaluated at $r=r_0\approx R_{\mathrm{NS}}$. This temperature implies a bolometric blackbody flux at the source from the bubbles

$$F_{\mathrm{bubble}}\approx 2\times 10^{40}\left(\frac{M_{\mathrm{NS}}}{1.4\,M_\odot}\right)^{-7/2}\left(\frac{\dot{M}_{\mathrm{B}}}{M_\odot\,\mathrm{s}^{-1}}\right)\left(\frac{R_{\mathrm{NS}}}{10^6\,\mathrm{cm}}\right)^{3/2}\times\left(\frac{r_0}{r}\right)^{8/3}\mathrm{erg\,s^{-1}cm^{-2}}, \tag{6}$$

where σ is the Stefan–Boltzmann constant.

In Ref. 12, it was shown that the above thermal emission from the rising bubbles produced during the hypercritical accretion process can explain the early ($t \lesssim 50\,\mathrm{s}$) thermal X-ray emission observed in GRB 090618.[10,28] In that case, T_{bubble} drops from $50\,\mathrm{keV}$ to $15\,\mathrm{keV}$ expanding from $r \approx 10^9\,\mathrm{cm}$ to $6 \times 10^9\,\mathrm{cm}$, for an accretion rate $10^{-2}\,M_\odot\,\mathrm{s}^{-1}$.

It is interesting that also r-process nucleosynthesis can occur in these outflows.[26] This implies that long GRBs can be also r-process sites with specific signatures from the decay of the produced heavy elements, possibly similar as in the case of the *kilonova* emission in short GRBs.[29] The signatures of this phenomenon in XRFs and BdHNe, and its comparison with kilonovae, deserves to be explored.

2.2.2. *Neutrino emission*

Most of the energy from the accretion is lost through neutrino emission. For the accretion rate conditions characteristic of our models $\sim 10^{-4}$–$10^{-2}\,M_\odot\,\mathrm{s}^{-1}$, e^+e^- pair annihilation dominates the neutrino emission and electron neutrinos remove the bulk of the energy. The temperature of these neutrinos can be roughly approximated by assuming that the inflowing material generally flows near to the NS surface before shocking and emitting neutrinos. For accretion rates $\sim 10^{-4}$–$10^{-2}\,M_\odot\,\mathrm{s}^{-1}$, neutrino energies ~ 5–$20\,\mathrm{MeV}$ are obtained.[15] A detailed study of the neutrino emission will be the presented elsewhere.

For the developed temperatures (say $k_B T \sim 1$–$10\,\mathrm{MeV}$) near the NS surface, the dominant neutrino emission process is the e^+e^-annihilation leading to $\nu\bar{\nu}$. This process produces a neutrino emissivity proportional to the ninth power of the temperature. The accretion atmosphere near the NS surface is characterized by a temperature gradient with a typical scale height $\Delta r_\nu \approx 0.7\,R_{\mathrm{NS}}$.[15] Owing to the aforementioned strong dependence of the neutrino emission on temperature, most of the neutrino emission occurs in the region Δr_ν above the NS surface.

These conditions lead to the neutrinos to be efficient in balancing the gravitational potential energy gain allowing the hypercritical accretion rates. The effective accretion onto the NS can be estimated as[22]: $\dot{M}_{\mathrm{eff}} \approx \Delta M_\nu (L_\nu / E_\nu)$, where ΔM_ν and L_ν are the mass and neutrino luminosity in the emission region (i.e. Δr_ν). E_ν is half the gravitational potential energy gained by the material falling from infinity to the $R_{\mathrm{NS}} + \Delta r_\nu$. Since $L_\nu \approx 2\pi R_{\mathrm{NS}}^2 \Delta r_\nu \epsilon_{\mathrm{e^-e^+}}$ with $\epsilon_{\mathrm{e^-e^+}}$ the e^+e^- pair annihilation process emissivity, and $E_\nu = (1/2) G M_{\mathrm{NS}} \Delta M_\nu / (R_{\mathrm{NS}} + \Delta r_\nu)$, it can be checked that for $M_{\mathrm{NS}} = 1.4\,M_\odot$ this accretion rate leads to values $\dot{M}_{\mathrm{eff}} \approx 10^{-9}$–$10^{-1}\,M_\odot\,\mathrm{s}^{-1}$ for temperatures $k_B T = 1$–$10\,\mathrm{MeV}$.

2.3. *Accretion luminosity*

The gain of gravitational potential energy in the accretion process is the total one available to be released, e.g. by neutrinos and photons. The total energy released in the star in a time-interval dt during the accretion of an amount of mass dM_b with angular momentum $l\dot{M}_b$, is given by[13,30]

$$L_{\rm acc} = (\dot{M}_b - \dot{M}_{\rm NS})c^2 = \dot{M}_b c^2 \left[1 - \left(\frac{\partial M_{\rm NS}}{\partial J_{\rm NS}}\right)_{M_b} l - \left(\frac{\partial M_{\rm NS}}{\partial M_b}\right)_{J_{\rm NS}}\right]. \qquad (7)$$

This upper limit to the energy released is just the amount of gravitational energy gained by the accreted matter by falling to the NS surface and which is not spent in changing the gravitational binding energy of the NS. The total energy releasable during the accretion process, say $\Delta E_{\rm acc} \equiv \int L_{\rm acc} dt$, is given by the difference in binding energies of the initial and final NS configurations. The typical luminosity will be $L_{\rm acc} \approx \Delta E_{\rm acc}/\Delta t_{\rm acc}$ where $\Delta t_{\rm acc}$ is the duration of the accretion process.

The duration of the accretion process is given approximately by the flow time of the slowest layers of the supernova ejecta to the NS. If the velocity of these layers is $v_{\rm inner}$, then $\Delta t_{\rm acc} \sim a/v_{\rm inner}$, where a is the binary separation. For $a \sim 10^{11}$ cm and $v_{\rm inner} \sim 10^8\,{\rm cm\,s^{-1}}$, we obtain $\Delta t_{\rm acc} \sim 10^3$ s, while for shorter binary separation, e.g. $a \sim 10^{10}$ cm ($P \sim 5$ min), $\Delta t_{\rm acc} \sim 10^2$ s, as validated by the results of our numerical integrations.

For instance, the NS in the system with $P = 5$ min accretes $\approx 1\,M_\odot$ in $\Delta t_{\rm acc} \approx 100$ s. With the aid of Eq. (3), we estimate a difference in binding energies between a $2\,M_\odot$ and a $3\,M_\odot$ NS, i.e. $\Delta E_{\rm acc} \approx 13/200(3^2 - 2^2)\,M_\odot c^2 \approx 0.32\,M_\odot c^2$ leading to a maximum luminosity $L_{\rm acc} \approx 3 \times 10^{-3}\,M_\odot c^2 \approx 0.1 \dot{M}_b c^2$. This accretion power, which could be as high as $L_{\rm acc} \sim 0.1\dot{M}_b c^2 \sim 10^{47}$–$10^{51}\,{\rm erg\,s^{-1}}$ for accretion rates in the range $\dot{M}_b \sim 10^{-6}$–$10^{-2}\,M_\odot\,{\rm s^{-1}}$, necessarily leads to signatures observable in long GRBs (see, e.g. Refs. 10 and 12).

2.4. *Post-explosion orbits and formation of NS-BH binaries*

We turn now to discuss the out-states of the IGC process. The SN explosion of the $\rm CO_{core}$ leaves as a central remnant, the νNS, while the IGC process triggered by the hypercritical accretion of the SN ejecta onto the NS companion leads to the formation of a BH. Thus, the question arises if BdHNe are natural sites for the formation of NS-BH binaries or if these binaries become disrupted during the SN explosion and the consequent IGC process. The answer to this question was recently given in Ref. 14, where it was shown that indeed most of BdHN form NS-BH binaries since the high compactness of the orbit avoids the unbinding of the orbit.

In typical systems, most of the binaries become unbound during the SN explosion because of the ejected mass and momentum imparted (kick) on the newly formed compact object in the explosion of the massive star. Under the instantaneous explosion assumption, if half of the binary system's mass is lost in the SN explosion, the system is disrupted. In general, the fraction of massive binaries that can produce double compact object binaries is thought to be low: ~0.001–1%.[31–33]

The mass ejected during the SN alters the binary orbit, causing it to become wider and more eccentric. Assuming that the mass is ejected instantaneously, the post-explosion semi-major axis is $a/a_0 = (M_0 - \Delta M)/(M_0 - 2a_0 \Delta M/r)$, where a_0 and a are the initial and final semi-major axes respectively, M_0 is the total initial mass of the binary system, ΔM is the change of mass (equal to the amount of mass ejected in the SN), and r is the orbital separation at the time of explosion.[34] For circular orbits, the system is unbound if it loses half of its mass. However, for very tight binaries as the one proposed in the IGC scenario, a number of additional effects can alter the fate of the binary.

The time it takes for the ejecta to flow past a companion in a SN is roughly 10–1000 s. Although the shock front is moving above $10^4\,\mathrm{km\,s^{-1}}$, the denser, lower-velocity ejecta can be moving at $10^3\,\mathrm{km\,s^{-1}}$.[12] The broad range of times arises because the SN ejecta velocities varies from 10^2–$10^4\,\mathrm{km\,s^{-1}}$. The accretion peaks as the slow-moving (inner) ejecta flows past the NS companion. For normal (wide) binaries, this time is a small fraction of the orbital period and the "instantaneous" mass-loss assumption is perfectly valid. However, in the compact binary systems considered in the IGC scenario, the orbital period ranges from only 100–1000 s, and the mass loss from the SN explosion can no longer be assumed to be instantaneous.

We have seen how in BdHNe, the accretion process can lead to BH formation in a time-interval as short as the orbital period. We here deepen this analysis to study the effect of the SN explosion in such a scenario with a specific example of Ref. 14. Figure 4 shows as the ejecta timescale becomes just a fraction of the orbital timescale, the fate of the post-explosion binary is altered. For these models, we assumed very close binaries with an initial orbital separation of 7×10^9 cm in circular orbits. With $\mathrm{CO_{core}}$ radii of 1–4×10^9 cm, such a separation is small, but achievable. We assume the binary consists of a $\mathrm{CO_{core}}$ and a $2.0\,M_\odot$ NS companion. When the $\mathrm{CO_{core}}$ collapses, it forms a $1.5\,M_\odot$ NS, ejecting the rest of the core. We then vary the ejecta mass and time required for most of the ejected matter to move out of the binary. Note that even if 70% of the mass is lost from the system (the $8\,M_\odot$ ejecta case), the system remains bound as long as the explosion time is just above the orbital time ($T_{\mathrm{orbit}} = 180$ s) with semi-major axes of less than 10^{11} cm.

The short orbits (on ejecta timescales) are not the only feature of these binaries that alters the post-explosion orbit. The NS companion accretes both matter and momentum from the SN ejecta, reducing the mass lost from the system with respect to typical binaries with larger orbital separations and much less accretion. In addition, as with common envelope scenarios, the bow shock produced by the accreting NS transfers orbital energy into the SN ejecta. Figure 4 shows the final orbital separation of our same three binaries, including the effects of mass accretion (we assume $0.5\,M_\odot$ is accreted with the momentum of the SN material) and orbit coupling (30% of the orbital velocity is lost per orbit). With these effects, not only do the systems remain bound even for explosion times greater than 1/2 the orbital period but, if the explosion time is long, the final semi-major axis can be on par with the initial orbital separation.

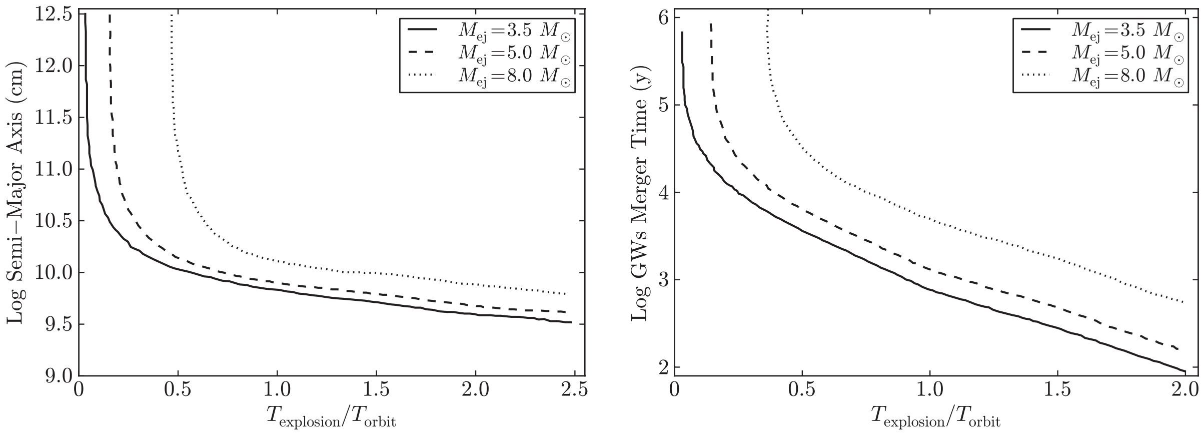

Fig. 4. Left panel: semi-major axis versus explosion time for three binary systems including mass accretion and momentum effects. Including these effects, all systems with explosion times above 0.7 times, the orbital time are bound and the final separations are on par with the initial separations. Right panel: merger time due to GW emission as a function of explosion time. Beyond a critical explosion time (0.1–0.6 $T_{\rm orbit}$ depending on the system), the merger time is less than roughly 10,000 yr. For most of our systems, the explosion time is above this limit and we expect most of these systems to merge quickly.

The tight compact binaries produced in these explosions will emit GW emission, ultimately causing the system to merge. For typical massive star binaries, the merger time is many Myr. For BdHNe, the merger time is typically 10,000 yr, or less, as shown in the right panel of Fig. 4. Since the merger should occur within the radius swept clean by the BdHN, we expect a small baryonic contamination around the merger site which might lead to a new family of events which we term ultrashort GRBs, U-GRBs. to this new family of events.

3. NS–NS/NS-BH Mergers and Short GRBs

Let us turn to short GRBs. We have mentioned that the most viable progenitors of short GRBs appear to be mergers of NS–NS and/or NS-BH binaries. Specifically, in the case of NS–NS mergers, the value of the critical mass of the NS, which crucially depends on the nuclear EOS, has been also found to be a most relevant parameter since it defines the fate of the post-merger object.[8] In this section, we discuss the conditions that determine the fate of the NS–NS binary merger by estimating the mass and angular momentum of the post-merger object. Once we know these values, we can compare the mass of the merged core with the value of the NS critical mass obtained for uniformly rotating NSs. Based on this, we can asses whether a massive NS or a BH is formed from the merger.

We proceed to estimate the mass and the angular momentum of the post-merger core via baryonic mass and angular momentum conservation of the system. We adopt for simplicity that nonrotating binary components. We first compute the total baryonic mass of the NS–NS binary $M_b = M_{b_1} + M_{b_2}$ using the relation between the gravitational mass M_i and the baryonic mass M_{b_i} $(i = 1, 2)$ recently obtained in Ref. 21 and given in Eq. (3) assuming $j_{\rm NS} = cJ_{\rm NS}/(GM_\odot^2) = 0$. The post-merger core will have approximately the entire baryonic mass of the initial binary, i.e. $M_{b,\rm core} \approx M_b$, since little mass is expected to be ejected during the coalescence process. However, the gravitational mass of the post-merger core cannot be estimated using again the above formula since, even assuming nonrotating binary components, the post-merger core will necessarily acquire a fraction $\eta \leq 1$ of the binary angular momentum at the merger point. One expects a value of η smaller than unity since, during the coalesce, angular momentum is lost, e.g. by gravitational wave emission and it can be also redistributed, e.g. into a surrounding disk.

To obtain the gravitational mass of the post-merger core, we can use again Eq. (3) relating the baryonic mass $M_{b,\rm NS}$ and the gravitational mass $M_{\rm NS}$ in this case with $j_{\rm NS} \neq 0$. The mass and angular momentum of the post-merger core, respectively $M_{\rm core}$ and $J_{\rm core}$, are therefore obtained from baryon mass and angular momentum conservation, i.e.

$$M_{\rm core} = M_{\rm NS}, \quad M_{b,\rm core} = M_{b,\rm NS} = M_{b_1} + M_{b_2}, \quad J_{\rm core} = J_{\rm NS} = \eta J_{\rm merger}, \quad (8)$$

where $J_{\rm merger}$ is the system angular momentum at the merger point. The value of $J_{\rm merger}$ is approximately given by $J_{\rm merger} = \mu r^2_{\rm merger}\Omega_{\rm merger}$, where $\mu = M_1 M_2/M$ is the binary reduced mass, $M = M_1 + M_2$ is the total binary mass, and $r_{\rm merger}$ and $\Omega_{\rm merger}$ are the binary separation and angular velocity at the merger point. If we adopt the merger point where the two stars enter into contact we have $r_{\rm merger} = R_1 + R_2$, where R_i is the radius (which depend on the EOS) of the i-component of the binary.

Given the parameters of the merging binary, the above equations lead to the merged core properties $M_{\rm core}$ and $J_{\rm core}$ (or $j_{\rm core}$). These values can be therefore confronted with the values of uniformly rotating, stable NSs to check if such a merger will lead either to a new massive NS or to an unstable merged core collapsing to a BH.

For the sake of exemplifying, let us assume a mass-symmetric binary, $M_1 = M_2 = M/2$. In this case, Eq. (8) together with the above estimate of $J_{\rm merger}$ lead to the angular momentum of the merged core $J_{\rm core} = (\eta/4)(GM^2/c)\mathcal{C}^{-1/2}$, where $\mathcal{C} \equiv GM_1/(c^2 R_1) = GM_2/(c^2 R_2)$ is the compactness of the merging binary components. Therefore, if we adopt $M_1 = 1.4\ M_\odot$ and $\mathcal{C} = 0.15$ the above equations imply a merged core mass $M_{\rm core} = (2.61, 2.65)\ M_\odot$ for $\eta = (0,1)$, i.e. for a dimensionless angular momentum of the merged core $j_{\rm core} = (0, 5.06)$. Whether or not these pairs $(M_{\rm core}, j_{\rm core})$ correspond to stable NSs depend on the nuclear EOS. A similar analysis can be done for any other pair of binary masses.

4. Detectability of GWs Produced by the GRB Progenitors

Having established the nature of the progenitors of each GRB sub-class, we turn now to briefly discuss the detectability of their associated GW emission. The minimum GW frequency detectable by the broadband aLIGO interferometer is

$f_{\rm min}^{\rm aLIGO} \approx 10\,{\rm Hz}$.[35] Since during the binary inspiral, the GW frequency is twice the orbital one, this implies that a binary enters the aLIGO band for orbital periods $P_{\rm orb} \lesssim 0.2\,{\rm s}$. Thus, $CO_{\rm core}$-NS binaries, *in-states* of XRFs and BdHNe, and $CO_{\rm core}$-BH binaries, *in-states* of BH-SN, are not detectable by aLIGO since they have orbital periods $P_{\rm orb} \gtrsim 5\,{\rm min} \gg 0.2\,{\rm s}$. Concerning their *out-states* after the corresponding hypercritical accretion processes, namely νNS–NS, *out-states* of XRFs, and νNS-BH, *out-states* of BdHNe and BH-SNe, they are not detectable by aLIGO at their birth but only when approaching the merger. Clearly, the analysis of the νNS–NS mergers is included in the analysis of the S-GRFs and S-GRBs and, likewise, the merger of νNS-BH binaries is included in the analysis of U-GRBs. In the case of NS-WD binaries, the WD is tidally disrupted by the NS making their GW emission hard to be detected (see, e.g. Ref. 36).

A coalescing binary evolves first through the *inspiral regime* to then pass over a *merger regime*, the latter composed by the plunge leading to the merger itself and by the ringdown (oscillations) of the newly formed object. During the inspiral regime, the system evolves through quasi-circular orbits and is well described by the traditional point-like quadrupole approximation.[37–39] The GW frequency is twice the orbital frequency ($f_s = 2f_{\rm orb}$) and grows monotonically. The energy spectrum during the inspiral regime is: $dE/df_s = (1/3)(\pi G)^{2/3} M_c^{5/3} f_s^{-1/3}$, where $M_c = \mu^{3/5} M^{2/5} = \nu^{3/5} M$ is the so-called *chirp mass* and $\nu \equiv \mu/M$ is the symmetric mass-ratio parameter. A symmetric binary ($m_1 = m_2$) corresponds to $\nu = 1/4$ and the test-particle limit is $\nu \to 0$. The GW spectrum of the merger regime is characterized by a GW burst.[40] Thus, one can estimate the contribution of this regime to the signal-to-noise ratio with the knowledge of the location of the GW burst in the frequency domain and of the energy content. The frequency range spanned by the GW burst is $\Delta f = f_{\rm qnm} - f_{\rm merger}$, where $f_{\rm merger}$ is the frequency at which the merger starts and $f_{\rm qnm}$ is the frequency of the ringing modes of the newly formed object after the merger, and the energy emitted is $\Delta E_{\rm merger}$. With these quantities defined, one can estimate the typical value of the merger regime spectrum as: $dE/df_s \approx \Delta E_{\rm merger}/\Delta f$. Unfortunately, the frequencies and energy content of the merger regime of the above merging binaries are such that it is undetectable by LIGO.[41]

Since the GW signal is deep inside the detector noise, the signal-to-noise ratio (ρ) is usually estimated using the matched filter technique.[42] The exact position of the binary relative to the detector and the orientation of the binary rotation plane are usually unknown, thus it is a common practice to average over all the possible locations and orientations, i.e.[42]: $\langle \rho^2 \rangle = 4\int_0^\infty \langle|\tilde{h}(f)|^2\rangle/S_n(f)df = 4\int_0^\infty h_c^2(f)/[f^2 S_n(f)]df$, where f is the GW frequency in the detector frame, $\tilde{h}(f)$ is the Fourier transform of $h(t)$, and $\sqrt{S_n(f)}$ is the one-sided amplitude spectral density of the detector noise, and $h_c(f)$ is the characteristic strain, $h_c = (1+z)/(\pi d_l)\sqrt{(1/10)(G/c^3)(dE/df_s)}$. We recall that in the detector frame, the GW frequency is redshifted by a factor $1+z$ with respect to the one in the source frame,

f_s, i.e. $f = f_s/(1+z)$ and d_l is the luminosity distance to the source. We adopt a ΛCDM cosmology with $H_0 = 71\,\mathrm{km\,s^{-1}\,Mpc^{-1}}$, $\Omega_M = 0.27$ and $\Omega_\Lambda = 0.73$.[43]

A threshold $\rho_0 = 8$ in a single detector is adopted by LIGO.[44] This minimum ρ_0 defines a maximum detection distance or GW horizon distance, say d_{GW}, that corresponds to the most optimistic case when the binary is just above the detector and the binary plane is parallel to the detector plane. In order to give an estimate, the annual number of merging binaries associated with the above GRB subclasses detectable by aLIGO, we can use the lower and upper values of the aLIGO *search volume* defined by $\mathcal{V}_s = V_{\max}^{\mathrm{GW}}\mathcal{T}$, where $V_{\max}^{\mathrm{GW}} = (4\pi/3)\mathcal{R}^3$, where $\mathcal{T}$ is the observing time and $\mathcal{R}$ is the so-called *detector range* defined by $\mathcal{R} = \mathcal{F}d_{\mathrm{GW}}$, with $\mathcal{F}^{-1} = 2.2627$ (see, Refs. 44 and 45, for details). For a $(1.4+1.4)\,M_\odot$ NS binary and the three following different observational campaigns we have[44]: 2015/2016 (O1; $\mathcal{T} = 3$ months) $\mathcal{V}_S = (0.5\text{–}4)\times 10^5\,\mathrm{Mpc^3\,yr}$, 2017/2018 (O3; $\mathcal{T} = 9$ months) $\mathcal{V}_S = (3\text{–}10)\times 10^6\,\mathrm{Mpc^3\,yr}$, and the entire network including LIGO-India at design sensitivity (2022+; $\mathcal{T} = 1$ yr) $\mathcal{V}_S = 2\times 10^7\,\mathrm{Mpc^3\,yr}$. The maximum possible sensitivity reachable in 2022+ leads to $d_{\mathrm{GW}} \approx 0.2\,\mathrm{Gpc}$, hence $V_{\max}^{\mathrm{GW}} \approx 0.033\,\mathrm{Gpc^3}$, for such a binary. One can use this information for other binaries with different masses taking advantage of the fact that d_{GW} scales with the binary chirp mass as $M_c^{5/6}$. The expected GW detection rate by aLIGO can be thus estimated as: $\dot{N}_{\mathrm{GW}} \equiv \rho_{\mathrm{GRB}} V_{\max}^{\mathrm{GRB}}$, where ρ_{GRB} is the inferred occurrence rate of GRBs shown in Table 1 computed in Ref. 6. Bearing the above in mind, it is easy to check that there is a low probability for aLIGO to detect the GW signals associated with the GRB binary progenitors: indeed in the best case of the 2022+ observing rung one obtains, respectively, $\sim$1 detection every 3 and 5 yr for U-GRBs and S-GRFs.

5. Conclusions

There is accumulated evidence on the binary nature of long and short GRBs. Such binaries are composed of $\mathrm{CO_{cores}}$, NSs, BHs and WDs in different combinations. We have here focused on the salient aspects of the NS physics relevant for the understanding of these binaries and their implications in GRB astrophysics, including their associated GW emission. We have discussed the crucial role of the NS critical mass in discriminating the GRB sub-classes. Therefore, we expect that the increasing amount of GRB high-quality data will help in constraining the NS critical mass with high accuracy with the most welcome result of constraining the NS matter content and the corresponding nuclear EOS.

Acknowledgments

M. Karlica, M. Kovacevic and Y. A. are supported by the Erasmus Mundus Joint Doctorate Program Grant Nos. 2013–1471, 2013–1471 and 2014–0707, respectively, from EACEA of the European Commission. M. M. and J. A. R. acknowledge the partial support of the Project No. 3101/GF4 IPC-11, and the target program F.0679 of the Ministry of Education and Science of the Republic of Kazakhstan. C. C. and S. F. acknowledge INdAM-GNFM for support.

References

1. E. P. Mazets, S. V. Golenetskii, V. N. Ilinskii, V. N. Panov, R. L. Aptekar, I. A. Gurian, M. P. Proskura, I. A. Sokolov, Z. I. Sokolova and T. V. Kharitonova, *Astrophys. Space Sci.* **80** (1981) 3.
2. R. W. Klebesadel, The durations of gamma-ray bursts, in *Gamma-Ray Bursts — Observations, Analyses and Theories*, eds. C. Ho, R. I. Epstein and E. E. Fenimore (Cambridge University Press, 1992).
3. J.-P. Dezalay, C. Barat, R. Talon, R. Syunyaev, O. Terekhov and A. Kuznetsov, *AIP Conference Proceedings* **265** (1991) 304–309.
4. C. Kouveliotou, C. A. Meegan, G. J. Fishman, N. P. Bhat, M. S. Briggs, T. M. Koshut, W. S. Paciesas and G. N. Pendleton, *Astrophys. J.* **413** (1993) L101.
5. M. Tavani, *Astrophys. J.* **497** (1998) L21.
6. R. Ruffini, J. A. Rueda, M. Muccino, Y. Aimuratov, L. M. Becerra, C. L. Bianco, M. Kovacevic, R. Moradi, F. G. Oliveira, G. B. Pisani and Y. Wang, *Astrophys. J.* **832** (2016) 136.
7. R. Ruffini, Y. Wang, M. Enderli, M. Muccino, M. Kovacevic, C. L. Bianco, A. V. Penacchioni, G. B. Pisani and J. A. Rueda, *Astrophys. J.* **798** (2015) 10.
8. R. Ruffini, M. Muccino, M. Kovacevic, F. G. Oliveira, J. A. Rueda, C. L. Bianco, M. Enderli, A. V. Penacchioni, G. B. Pisani, Y. Wang and E. Zaninoni, *Astrophys. J.* **808** (2015) 190.
9. R. Ruffini, M. G. Bernardini, C. L. Bianco, L. Vitagliano, S.-S. Xue, P. Chardonnet, F. Fraschetti and V. Gurzadyan, Black hole physics and astrophysics: The GRB-Supernova connection and URCA-1–URCA-2, in *The Tenth Marcel Grossmann Meeting*, eds. M. Novello, S. Perez Bergliaffa and R. Ruffini (World Scientific, Singapore, 2006).
10. L. Izzo, J. A. Rueda and R. Ruffini, *Astron. Astrophys.* **548** (2012) L5.
11. J. A. Rueda and R. Ruffini, *Astrophys. J.* **758** (2012) L7.
12. C. L. Fryer, J. A. Rueda and R. Ruffini, *Astrophys. J.* **793** (2014) L36.
13. L. Becerra, F. Cipolletta, C. L. Fryer, J. A. Rueda and R. Ruffini, *Astrophys. J.* **812** (2015) 100.
14. C. L. Fryer, F. G. Oliveira, J. A. Rueda and R. Ruffini, *Phys. Rev. Lett.* **115** (2015) 231102.
15. L. Becerra, C. L. Bianco, C. L. Fryer, J. A. Rueda and R. Ruffini, *Astrophys. J.* **833** (2016) 107.
16. J. Goodman, *Astrophys. J.* **308** (1986) L47.
17. B. Paczynski, *Astrophys. J.* **308** (1986) L43.
18. D. Eichler, M. Livio, T. Piran and D. N. Schramm, *Nature* **340** (1989) 126.
19. R. Narayan, T. Piran and A. Shemi, *Astrophys. J.* **379** (1991) L17.
20. E. Berger, *Annu. Rev. Astron. Astrophys.* **52** (2014) 43.
21. F. Cipolletta, C. Cherubini, S. Filippi, J. A. Rueda and R. Ruffini, *Phys. Rev. D* **92** (2015) 023007.
22. C. L. Fryer, W. Benz and M. Herant, *Astrophys. J.* **460** (1996) 801.
23. R. A. Chevalier, *Astrophys. J.* **346** (1989) 847.
24. Y. B. Zel'dovich, L. N. Ivanova and D. K. Nadezhin, *Sov. Astron.* **16** (1972) 209.
25. R. Ruffini and J. Wilson, *Phys. Rev. Lett.* **31** (1973) 1362.

26. C. L. Fryer, F. Herwig, A. Hungerford and F. X. Timmes, *Astrophys. J.* **646** (2006) L131.
27. C. L. Fryer, *Astrophys. J.* **699** (2009) 409.
28. L. Izzo, R. Ruffini, A. V. Penacchioni, C. L. Bianco, L. Caito, S. K. Chakrabarti, J. A. Rueda, A. Nandi and B. Patricelli, *Astron. Astrophys.* **543** (2012) A10.
29. N. R. Tanvir, A. J. Levan, A. S. Fruchter, J. Hjorth, R. A. Hounsell, K. Wiersema and R. L. Tunnicliffe, *Nature* **500** (2013) 547.
30. N. R. Sibgatullin and R. A. Sunyaev, *Astron. Lett.* **26** (2000) 772.
31. C. L. Fryer, S. E. Woosley and D. H. Hartmann, *Astrophys. J.* **526** (1999) 152.
32. M. Dominik, K. Belczynski, C. Fryer, D. E. Holz, E. Berti, T. Bulik, I. Mandel and R. O'Shaughnessy, *Astrophys. J.* **759** (2012) 52.
33. K. A. Postnov and L. R. Yungelson, *Living Rev. Rel.* **17** (2014) 3.
34. J. G. Hills, *Astrophys. J.* **267** (1983) 322.
35. LIGO Scientific Collab. (J. Aasi *et al.*), *Class. Quantum Grav.* **32** (2015) 074001.
36. V. Paschalidis, M. MacLeod, T. W. Baumgarte and S. L. Shapiro, *Phys. Rev. D* **80** (2009) 024006.
37. P. C. Peters and J. Mathews, *Phys. Rev.* **131** (1963) 435.
38. P. C. Peters, *Phys. Rev.* **136** (1964) 1224.
39. M. Rees, R. Ruffini and J. A. Wheeler, *Black Holes, Gravitational Waves and Cosmology* (Gordon and Breach Science Publishers, New York, 1974).
40. M. Davis, R. Ruffini, W. H. Press and R. H. Price, *Phys. Rev. Lett.* **27** (1971) 1466.
41. R. Ruffini, J. Rodriguez, M. Muccino, J. A. Rueda, Y. Aimuratov, U. Barres de Almeida, L. Becerra, C. L. Bianco, C. Cherubini, S. Filippi, D. Gizzi, M. Kovacevic, R. Moradi, F. G. Oliveira, G. B. Pisani and Y. Wang, arXiv:1602.03545.
42. É. É. Flanagan and S. A. Hughes, *Phys. Rev. D* **57** (1998) 4535.
43. M. Rigault, G. Aldering, M. Kowalski, Y. Copin, P. Antilogus, C. Aragon, S. Bailey, C. Baltay, D. Baugh, S. Bongard, K. Boone, C. Buton, J. Chen, N. Chotard, H. K. Fakhouri, U. Feindt, P. Fagrelius, M. Fleury, D. Fouchez, E. Gangler, B. Hayden, A. G. Kim, P.-F. Leget, S. Lombardo, J. Nordin, R. Pain, E. Pecontal, R. Pereira, S. Perlmutter, D. Rabinowitz, K. Runge, D. Rubin, C. Saunders, G. Smadja, C. Sofiatti, N. Suzuki, C. Tao and B. A. Weaver, *Astrophys. J.* **802** (2015) 20.
44. B. P. Abbott *et al.*, *Living Rev. Rel.* **19** (2016) 1.
45. L. S. Finn and D. F. Chernoff, *Phys. Rev. D* **47** (1993) 2198.